

**UNIVERSITY OF BELGRADE**

**FACULTY OF PHYSICS**

**ALEKSANDAR ĆIRIĆ**

**JUDD-OFELT THEORY AND  
THERMOMETRY OF EUROPIUM  
DOPED MATERIALS**

DOCTORAL DISSERTATION

Belgrade, 2019

**UNIVERZITET U BEOGRADU**

**FIZIČKI FAKULTET**

**ALEKSANDAR ĆIRIĆ**

**DŽAD-OFELT-OVA TEORIJA I  
TERMOMETRIJA EUROPIUMOM  
DOPIRANIH MATERIJALA**

**DOKTORSKA DISERTACIJA**

Beograd, 2019

Mentor doktorske disertacije:

***Prof. dr. Miroslav D. Dramićanin***

naučni savetnik Instituta za nuklearne nauke Vinča.

Članovi komisije za odbranu doktorske disertacije:

***Prof. dr. Miroslav D. Dramićanin***

naučni savetnik Instituta za nuklearne nauke Vinča.

***Prof. dr. Stevan Stojadinović***

redovni profesor Fizičkog fakulteta Univerziteta u Beogradu

***Prof. dr. Ivan Belča***

redovni profesor Fizičkog fakulteta Univerziteta u Beogradu

Datum odbrane doktorata: 27.05.2019.

Ova doktorska disertacija urađena je pod rukovodstvom mentora prof. dr. Miroslava D. Dramićanina, naučnog savetnika INN “Vinča”, uz značajnu pomoć od strane prof. dr. Stevana Stojadinovića i prof. dr. Ivana Belče. Iskreno im se zahvaljujem za veliku pomoć koju su mi pružili u toku istraživanja i postdiplomskih studija.

Zahvaljujem se svojoj porodici na razumevanju, podršci i strpljenju.

Aleksandar Ćirić

# Judd-Ofelt theory and thermometry of europium doped materials

## Abstract

The main topic of this research is an extension of the Judd-Ofelt theory, a theoretical model applied to the luminescence thermometry, aimed to evaluate the thermometric figures of merit through Judd-Ofelt intensity parameters. The rather expensive, complicated and lengthy conventional method for evaluating the luminescence intensity ratio thermometric properties of a given material would include recording spectra at various temperatures and subsequent data analysis. This model is capable of finding the best transitions for the given material, or various materials, from a room-temperature spectra or Judd-Ofelt parameters given in literature. The model is originally developed for  $\text{Eu}^{3+}$  doped compounds, but is extended for all lanthanide doped materials from praseodymium to thulium.

In turn, in  $\text{Eu}^{3+}$  doped compounds, the model is able to predict the dipole strength and radiative transition probability of transitions from  $^5\text{D}_1$  level, if Judd-Ofelt and luminescence intensity ratio thermometric parameters are known. Such analysis was performed on a  $\text{TiO}_2:\text{Eu}^{3+}$  sample, created by the plasma electrolytic oxidation.

Judd-Ofelt analysis requires cumbersome calculations, and calculation by hand on many materials to be tested would pose a practical problem. The solution was to create an application software that would be able to calculate Judd-Ofelt intensity parameters and derived quantities from emission spectra of  $\text{Eu}^{3+}$  doped compounds. Written in Java, JOES application software was created and tested on  $\text{TiO}_2:\text{Eu}^{3+}$ ,  $\text{ZrO}_2:\text{Eu}^{3+}$ , and  $\text{Nb}_2\text{O}_5:\text{Eu}^{3+}$ , with various europium concentrations, created by plasma electrolytic oxidation process.

Luminescence intensity ratio thermometry was tested on  $\text{TiO}_2:\text{Eu}^{3+}$ ,  $\text{ZrO}_2:\text{Eu}^{3+}$ , and  $\text{Nb}_2\text{O}_5:\text{Eu}^{3+}$  samples. Temperature of the samples during the spectroscopic measurements was controlled by the custom-made heating/cooling apparatus, consisting of a hot plate, cold plate, a control/power unit, and a RTD reference thermometer.

Since plasma electrolytic oxidation is a protective coating method, already widely employed for industrial purposes, the investigated samples obtain an additional

functionality of becoming temperature sensors, with possible applications in rotor turbines, or on vehicles for hypersonic flights.

Since the photoluminescence properties of materials are investigated, the in-depth analysis is performed on  $\text{HfO}_2:\text{Eu}^{3+}$ , prepared by plasma electrolytic oxidation, at various europium concentrations. Morphology, chemical and phase composition was investigated, since the photoluminescence is dependent those material properties. Judd-Ofelt analysis was performed on the sample, and the obtained parameter values are in accordance with the europium site symmetry.

CIE chromaticity coordinates were investigated for all the samples, identifying the material potentials for LED and display purposes, from orange-red to white.  $\text{HfO}_2:\text{Eu}^{3+}$  at low concentrations is a potential white LED phosphor.

**Keywords:** Judd-Ofelt, photoluminescence, thermometry, europium

**Scientific field:** Physics

**Research area:** Applied physics

**UDC number:** 535.371+536.51(043.3)

# Džad-Ofelt-ova teorija i termometrija europiumom dopiranih materijala

## Rezime

Glavni predmet istraživanja je proširenje Džad-Ofelt-ove teorije u vidu teorijskog modela primenjenog na fenomen luminescentne termometrije, sa ciljem predviđanja termometrijskih veličina preko Džad-Ofelt-ovih parametara. Tradicionalni metod za ispitivanje termometrijskih osobina materijala pomoću odnosa intenziteta linija uključuje snimanje spektara na različitim temperaturama i njihovu analizu. Ovaj model ima sposobnost određivanja najboljih elektronskih prelaza za dati materijal, ili za razne materijale, na osnovu spektra snimljenog na sobnoj temperaturi ili Džad-Ofelt-ovih parametara datih u literaturi. Model, isprva kreiran za  $\text{Eu}^{3+}$  dopirane materijale, proširen je na sve materijale dopiranih lantanidima, od prazeodijuma do tulijuma.

Za  $\text{Eu}^{3+}$  dopirana jedinjenja, model može da predvidi jačinu dipolnih prelaza i verovatnoće prelaza sa  $^5\text{D}_1$  nivoa, ukoliko su poznati Džad-Ofelt-ovi i termometrijski parametri dobijeni iz metode odnosa intenziteta. Takva analiza je izvršena nad  $\text{TiO}_2:\text{Eu}^{3+}$  uzorku, kreiranom plazmenom elektrolitičkom oksidacijom.

Džad-Ofelt-ova analiza zahteva kompleksna izračunavanja, tako da bi ručno računanje nad podacima sa mnogo testiranih materijala predstavljalo praktičan problem. Rešenje je u kreiranju softverske aplikacije koja bi mogla da izračuna Džad-Ofelt-ove parametre i izvedene veličine pomoću emisionih spektara  $\text{Eu}^{3+}$  dopiranih materijala. Napisana u Javi, JOES softverska aplikacija je napravljena i testirana na  $\text{TiO}_2:\text{Eu}^{3+}$ ,  $\text{ZrO}_2:\text{Eu}^{3+}$ , i  $\text{Nb}_2\text{O}_5:\text{Eu}^{3+}$ , dopiranim sa više različitih koncentracija europiuma i kreiranih plazmenom elektrolitičkom oksidacijom.

“Luminescence intensity ratio” termometrija je testirana na  $\text{TiO}_2:\text{Eu}^{3+}$ ,  $\text{ZrO}_2:\text{Eu}^{3+}$ , i  $\text{Nb}_2\text{O}_5:\text{Eu}^{3+}$  uzorcima. Temperatura uzoraka tokom spektroskopskih merenja kontrolisana je za tu svrhu napravljenim aparatom za grejanje/hlađenje, koji se sastoji od ploče za grejanje, ploče za hlađenje, kontrolne/naponske jedinice, i otpornog referentnog termometra.

Kako je plazmena elektrolitička oksidacija metod koji se u industriji koristi za kreiranje zaštitnih slojeva, ispitani uzorci dobijaju dodatnu funkcionalnost kao temperaturni senzori, sa mogućom primenom na rotoru turbina ili vozilima za hipersonični let.

Pošto su ispitivane fotoluminiscentne osobine materijala, detaljna analiza je izvršena nad  $\text{HfO}_2:\text{Eu}^{3+}$ , pripremljenim plazmenom elektrolitičkom oksidacijom, sa raznim koncentracijama europiuma. Morfologija, hemijski i fazni sastav je ispitan, pošto fotoluminiscencija pokazuje zavisnost od ovih osobina. Džad-Ofelt-ova analiza je izvršena nad uzorkom, i dobijene vrednosti parametara se slažu sa simetrijom europijuma u kristalnoj matrici.

CIELUV koordinate su izračunate za sve uzorke, identifikujući materijale pogodne za LED i primenu za ekrane, od narandžasto-crvenih do belih.  $\text{HfO}_2:\text{Eu}^{3+}$  sa niskim koncentracijama europijuma je potencijalni beli LED fosfor.

**Ključne reči:** Džad-Ofelt, fotoluminiscencija, termometrija, europium

**Naučna oblast:** Fizika

**Uža naučna oblast:** Primenjena fizika

**UDK:** 535.371+536.51(043.3)

## Table of Contents

1. Introduction .....	1
1.1. Abbreviations .....	1
1.2. XRD.....	2
1.3. Plasma electrolytic oxidation .....	4
1.4. Photoluminescence .....	7
1.4.1. Transitions .....	8
1.4.2. Configurational coordinate diagram.....	10
1.4.3. PL Measurements .....	11
1.4.3.1. Instruments .....	12
1.4.3.1.1. Light Sources.....	12
1.4.3.1.2. Wavelength selectors.....	14
1.4.3.1.3. Detectors (transducers).....	14
1.4.3.2. Spectra .....	16
1.4.3.3. Correction and compensation schemes.....	16
1.5. Lanthanides.....	18
1.6. Temperature sensing.....	22
1.6.1. Invasive techniques .....	23
1.6.2. Non-invasive.....	24
1.6.3. Semi-invasive .....	25
1.7. Judd-Ofelt theory.....	28
2. Theory.....	30
2.1. Luminescence thermometry .....	30
2.1.1. Temperature quenching of RE PL.....	30
2.1.2. Thermometric figures of merit .....	31
2.1.3. Time-integrated methods and LIR.....	32
2.1.3.1. RE utilized for LIR .....	34
2.1.3.2. LIR methods from multiple emission centers .....	35
2.1.3.3. LIR experiment.....	36
2.1.4. Time-resolved methods .....	37
2.1.4.1. Decay-time sensing.....	37
2.1.4.2. Rise-time sensing.....	38

2.1.4.3. Frequency-domain method .....	39
2.1.5. Comparison of LIR and time-resolved methods .....	40
2.2. Ti, Zr, Hf and Nb oxides doped with $\text{Eu}^{3+}$ ion .....	41
2.2.1. The importance and current applications.....	41
2.2.2. Crystal structures .....	43
2.2.2.1. $\text{TiO}_2:\text{Eu}^{3+}$ .....	44
2.2.2.2. $\text{ZrO}_2:\text{Eu}^{3+}$ and $\text{HfO}_2:\text{Eu}^{3+}$ .....	45
2.2.2.3. $\text{Nb}_2\text{O}_5:\text{Eu}^{3+}$ .....	49
2.2.3. PEO.....	49
2.2.3.1. $\text{ZrO}_2:\text{Eu}^{3+}$ .....	50
2.2.3.2. $\text{Nb}_2\text{O}_5:\text{Eu}^{3+}$ .....	52
2.2.3.3. $\text{TiO}_2:\text{Eu}^{3+}$ .....	53
2.2.4. PL .....	54
2.2.4.1. $\text{ZrO}_2:\text{Eu}^{3+}$ .....	57
2.2.4.2. $\text{TiO}_2:\text{Eu}^{3+}$ .....	57
2.2.4.3. $\text{Nb}_2\text{O}_5:\text{Eu}^{3+}$ .....	57
2.3. Judd-Ofelt theory.....	59
2.3.1. The complete Hamiltonian .....	59
2.3.2. Electrostatic interaction of a free ion.....	59
2.3.3. Time-integrated perturbation theory.....	60
2.3.4. First order interactions.....	61
2.3.4.1. Coefficients.....	62
2.3.4.1.1. Coefficients of fractional parentage .....	62
2.3.4.1.2. Wigner 3j symbol .....	63
2.3.4.1.3. Wigner 6j symbol .....	63
2.3.4.2. Electrostatic (Coulomb) interaction .....	64
2.3.4.2.1. Slater integrals .....	64
2.3.4.2.2. Matrix elements for the ES interaction.....	66
2.3.4.3. Spin-orbit interaction.....	67
2.3.4.3.1. Spin-orbit tensor operator.....	68
2.3.4.3.2. Spin-orbit interaction matrix elements .....	68
2.3.4.4. Experimentally obtaining the parameters .....	69
2.3.5. Intermediate Coupling approximation.....	70
2.3.5.1. Intermediate coupling wavefunctions.....	71

2.3.5.2. IC 4f energy levels.....	71
2.3.5.3. The Crystal Field (CF) interaction .....	73
2.3.5.3.1. CF Hamiltonian .....	75
2.3.5.3.2. Symmetry groups.....	78
2.3.5.4. IC induced ED tensor operator .....	80
2.3.5.5. IC reduced matrix elements (RME) .....	82
2.3.5.6. IC ED matrix elements .....	83
2.3.6. Transition mechanisms for RE [55].....	84
2.3.6.1. Experimental dipole and oscillator strengths .....	85
2.3.6.2. Theoretical dipole and oscillator strengths.....	86
2.3.6.3. Comparing experimental and theoretical values .....	87
2.3.6.4. Review of the experimental and theoretical values .....	88
2.3.6.5. MD transitions .....	88
2.3.6.6. Mixed ED and MD transitions .....	90
2.3.6.7. Spontaneous radiative transitions .....	90
2.3.7. JO parametrization scheme, electric dipole and oscillator strengths.....	92
2.3.7.1. Additivity of intensity parameters .....	93
2.3.7.2. Experimental JO parameters from europium emission spectrum.....	94
2.3.8. JO derived quantities .....	94
2.3.9. JO parameters interpretation.....	97
2.4. Europium .....	100
2.4.1. Uniqueness of europium.....	100
2.4.2. Energy level structure of trivalent europium.....	100
2.4.2.1. Configuration.....	100
2.4.2.2. Terms .....	101
2.4.2.3. Levels .....	102
2.4.2.4. Sublevels – Stark levels.....	107
2.4.3. PL .....	108
2.4.3.1. Excitation spectra .....	108
2.4.3.2. Emission spectra .....	110
2.4.3.3. PL quenching.....	112
2.4.4. Europium as a spectroscopic probe .....	116
2.5. Nanoscale PL structures .....	118
3. Experimental.....	120

3.1. PEO.....	120
3.2. XRD, SEM, EDS, PL .....	121
3.3. Heating/Cooling apparatus .....	121
3.3.1. Hot-plate in the range from room temperature to 400 °C.....	122
3.3.2. Hot/cold plate in the range from 0 °C to 80°C .....	123
3.3.3. Control/power unit.....	124
3.3.4. Oven .....	126
3.3.5. RTD thermometer.....	126
3.3.6. Fiber optic bundle.....	127
4. Results and discussion .....	128
4.1. Morphology, chemical and phase compositions .....	128
4.1.1. HfO <sub>2</sub> :Eu <sup>3+</sup> .....	128
4.1.2. Nb <sub>2</sub> O <sub>5</sub> :Eu <sup>3+</sup> and ZrO <sub>2</sub> :Eu <sup>3+</sup> .....	131
4.1.3. TiO <sub>2</sub> :Eu <sup>3+</sup> .....	132
4.2. PL .....	133
4.2.1. HfO <sub>2</sub> :Eu <sup>3+</sup> .....	133
4.2.2. TiO <sub>2</sub> :Eu <sup>3+</sup> , Nb <sub>2</sub> O <sub>5</sub> :Eu <sup>3+</sup> and ZrO <sub>2</sub> :Eu <sup>3+</sup> .....	138
4.3. Heating/Cooling apparatus .....	140
4.4. LIR.....	142
4.4.1. Nb <sub>2</sub> O <sub>5</sub> :Eu <sup>3+</sup> and ZrO <sub>2</sub> :Eu <sup>3+</sup> .....	142
4.4.2. TiO <sub>2</sub> :Eu <sup>3+</sup> .....	144
4.5. JOES application software.....	146
4.5.1. Introduction .....	146
4.5.2. Refractive index.....	146
4.5.3. Derived Quantities.....	147
4.5.4. UI.....	147
4.5.5. JO analysis of HfO <sub>2</sub> , TiO <sub>2</sub> , ZrO <sub>2</sub> and Nb <sub>2</sub> O <sub>5</sub> doped with Eu <sup>3+</sup> .....	149
4.5.6. Additional Features .....	150
4.5.6.1. Spectroscopic probe.....	150
4.5.6.2. Chromaticity .....	151
4.6. LIR and thermometry .....	155
4.6.1. Radiative transition probability and ED strength of <sup>5</sup> D <sub>1</sub> emissions .....	155
4.6.2. LIR thermometric JO model.....	155
5. Conclusion.....	160

6. References .....	163
7. Biografija .....	182
8. Prilog .....	183

# 1. Introduction

## 1.1. Abbreviations

- JO – Judd-Ofelt theory
- RE – Rare Earth
- ES – electrostatic
- EM - electromagnetic
- ED – electric dipole
- MD – magnetic dipole
- s-o – spin-orbit
- CF – crystal field
- PEO – plasma electrolytic oxidation
- IC – intermediate coupling
- RME – reduced matrix elements
- XRD – X-ray diffraction
- PL – photoluminescence
- AC – alternating current
- DC – constant current
- CTB – charge transfer band
- RTD - resistive temperature detector
- RT - radiative transition probability

## 1.2. XRD

Knowledge of how atoms are arranged into crystal structures is the basis of our understanding of the properties and the structure of materials and X-ray diffraction experiment is the most powerful experimental technique for the investigations of the crystal structures. The wave in the diffraction experiment is directed into material and a detector is typically moved to record the direction and intensities. Then the constructive or destructive interference occurs as scattered waves are emitted by atoms of different types and positions. Geometrical relationship between the constructive waves and the crystal gives a diffraction pattern [1].

The crystals that have precise periodicities give sharp and clear peaks in their diffraction patterns. The occurrence of defects gives less precisely periodic, with broadened, distorted and weakened peaks. Amorphous structures do not give sharp diffraction peaks.

The most basic example of the method for obtaining the crystal lattice parameter is for the highest symmetry. In a cubic crystal the constructive interference occurs at  $d_{hkl} = \frac{a_0}{\sqrt{h^2+k^2+l^2}}$ , thus the diffraction peak must occur at Bragg angle of  $2\theta_{hkl} = 2 \arcsin \frac{\lambda\sqrt{h^2+k^2+l^2}}{2a_0}$ , where  $hkl$  are the Miller indices, and the  $a_0$  is the lattice parameter.

For identifying crystals in a sample one must match the positions and intensities of the peaks to a known pattern. ICDD [2] has a vast database of diffraction patterns and a software to match them.

Experimental approaches for observing diffractions are: single crystal monochromatic method, Laue method (uses the distribution of wavelengths in polychromatic radiation and a single crystal sample), and the method that will be used in this thesis, the Debye-Scherrer's method (see Fig. 1). The Debye-Scherrer's method uses monochromatic light and a distribution of planes as provided by a polycrystalline sample. The equipment is being used to control the  $2\theta$  angle, as presented in Fig. 2. Even when  $\theta$  is the Bragg angle, X-rays are at the wrong angle for most of the crystallites, but some are oriented adequately. The result is the creation of diffraction cones, as given in Fig. 3.

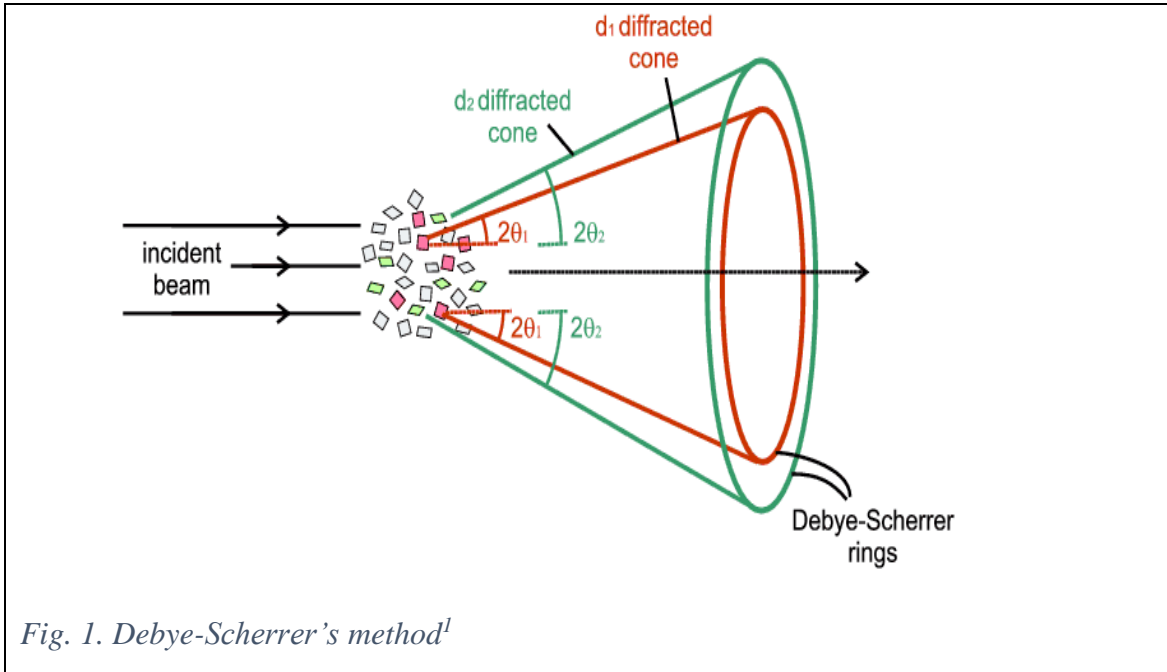


Fig. 1. Debye-Scherrer's method<sup>1</sup>

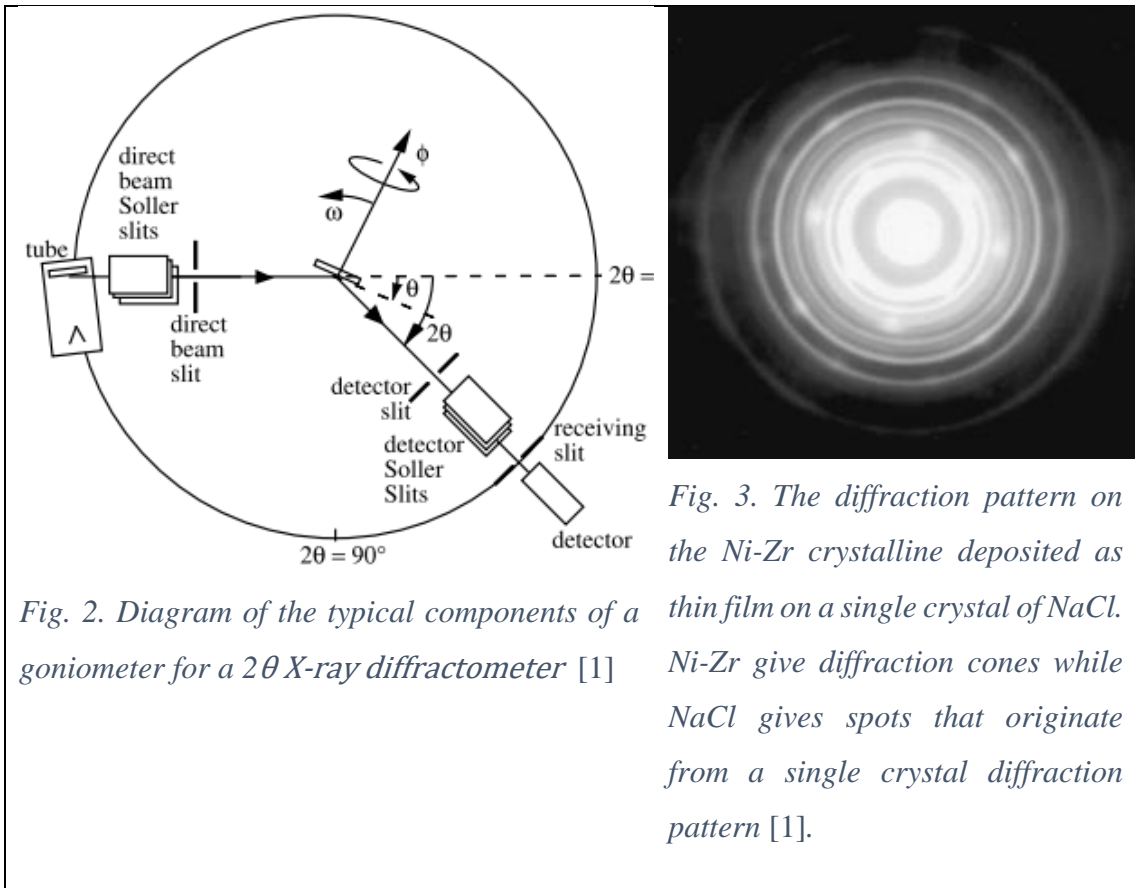


Fig. 2. Diagram of the typical components of a goniometer for a  $2\theta$  X-ray diffractometer [1]

Fig. 3. The diffraction pattern on the Ni-Zr crystalline deposited as thin film on a single crystal of NaCl. Ni-Zr give diffraction cones while NaCl gives spots that originate from a single crystal diffraction pattern [1].

<sup>1</sup> Image acquired from <http://pd.chem.ucl.ac.uk/pdnn/diff2/kinemat2.htm>

### 1.3. Plasma electrolytic oxidation

By the industry demand, in the spotlight is a creation of modern materials with better properties than the base metal and its alloys. Oxide coatings on non-ferrous metals have proven itself to provide both physical and chemical protection to the base metal. Traditionally, an electrochemical process, anodizing, is being used to convert the metal surface into a decorative and durable finish. However, those desired properties depend on the barrier layer thickness, and the anodization is a slow process that creates thin protective coatings. Thus, an industry demand appeared for the novel method that would create thicker layer of ceramics and by much shorter production time. PEO is a relatively new surface treatment method for generating strong oxide films (up to 500  $\mu\text{m}$  thick [3]) on various metals and alloys [4], similar to anodizing, but by employing higher potentials than the dielectric breakdown potential [5]. In literature, the process is sometimes referred to as micro-arc oxidation (MAO) or anodic spark deposition (ASD). The advantages of the method are numerous: the apparatus is cheap and the process is very fast and relatively simple, making it a perfect candidate for industrial applications [6]. PEO created oxide ceramic coatings are often superior to the original anodic oxides in mechanical characteristics and superior to plasma sprayed coatings in adhesive strength [7,8]. The process is efficient and environmentally friendly, and oxide coatings have controllable morphology and composition [5]. In most research of the method, it has been proven that it is adequate for creating metal oxides doped with rare-earth elements, and that the final product has good luminescent properties [6,9–11]. Other methods that are suited for production of RE luminescent films are the sol-gel method, physical vapor deposition, and chemical vapor deposition. Their drawbacks include more complicated and expensive equipment or low adhesion of the created film [12].

PEO is very universal in a means that it can be employed on various materials and their alloys, and prepared in a wide range of electrolytes with various concentrations. Thus the morphology and the chemical composition of the product can be fine-tuned. However, the most often used electrolytes are  $\text{H}_3\text{BO}_3$ ,  $\text{NaOH}$ ,  $\text{Na}_2\text{SiO}_3$ ,  $\text{Na}_3\text{PO}_4$ ,  $\text{Na}_2\text{WO}_4 \cdot 2\text{H}_2\text{O}$  and  $\text{H}_4\text{SiW}_{12}\text{O}_{40}$  [3]. Although oxide coatings obtained by PEO have porous microstructure, their composition is modified by the incorporation of species from the electrolyte, providing them with high hardness, adhesion, strength and wear resistance [9].

At the beginning of the anodization, the voltage linearly increases with time, producing the thin barrier oxide layer until the critical voltage value. Breakdown voltage is determined by the used electrolyte and material of the anode [3]. After dielectric breakdown (due to the strong electric field [7]), voltage keeps increasing at a slower rate. When the breakdown voltage is reached, a large number of evenly distributed small discharges start appearing (see Fig. 4) on the anode surface, followed by the low anodic luminescence (galvanoluminescence). The spatial density of micro-discharges is the highest in the early stage of the PEO process [5]. Further anodization results in relatively stable value of the voltage of anodization [13]. Discharge characteristics determine thermal and chemical conditions on the oxidizing surface and play an important role in the phase formation and structure of the oxide coatings [6]. Distribution and microdischarge type have significant influence on formation mechanism, chemical composition, morphology, and other characteristics of obtained oxide films [13].

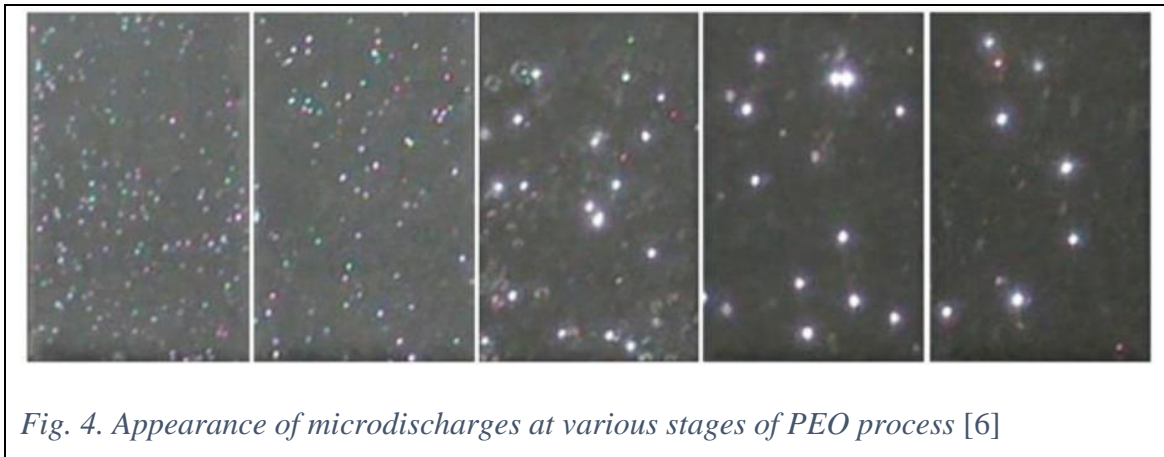


*Fig. 4. Appearance of microdischarges at various stages of PEO process [6]*

In the first step, a discharge channel is formed in the oxide layer as a result of the loss of its dielectric stability in a region of elevated conductivity. The region is heated by electron avalanches. Strong electric field drives electrolyte in the channel, and high temperature melts the substrate which enters the channel. Thus, a plasma column (plasmoid) is being formed. In the second step, plasma chemical reactions take place in the channel, which leads to the pressure increase within the channel (~100 MPa [11]), resulting in a volumetric expansion. The third step is the cooling by the surrounding electrolyte and a subsequent volumetric quenching [7].

Oxide coatings obtained by PEO usually contain both crystalline and amorphous phases where constituent species can originate both from metal and the electrolyte [11]. Additionally, if RE powder is added in the electrolyte, the result can be creation of a thin film phosphor. Thin film phosphors have a great potential in integrated optical and optoelectronic devices such as waveguides, LEDs, solar panels, X-ray imaging and displays. E.g. they present better properties than powder screens: higher contrast, better resolution, better thermal stability and conductivity, higher uniformity, better adhesion, and a longer life (but are usually less bright) [14].

## 1.4. Photoluminescence

The phenomena which involve absorption of energy and subsequent emission of light are classified under the term luminescence [15]. Photoluminescence is a member of the luminescence family of processes, and occurs when emission of light follows the absorption of photons. Photoluminescence further divides into fluorescence and phosphorescence, depending on the electronic configuration of the excited state and the emission path [16].

Phosphorescence occurs when the energy passes from the singlet excited state to the triplet state (rarely triplet to triplet) via nonradiative transfer called intersystem crossing [16], with the radiative emission from the triplet state to the ground state. During the transition to the triplet state, and during the radiative transition from the triplet state, the spin of the electron changes orientation [17]. Changing of the spin is forbidden, which is why the fluorescence is the more probable process, and why the phosphorescence has much larger lifetime.

Fluorescence occurs when the electron is excited to a singlet state, and radiatively returns to the ground state. Most often is the downshifting emission: the excitation is done by a single photon, then the electron moves to the lowest vibrational level from which it radiatively decays to the ground state [18]. If the material absorbs two photons it may ultimately emit the photon of lower wavelength than the absorbed ones, in a process called upconversion (see Fig. 5) [19].

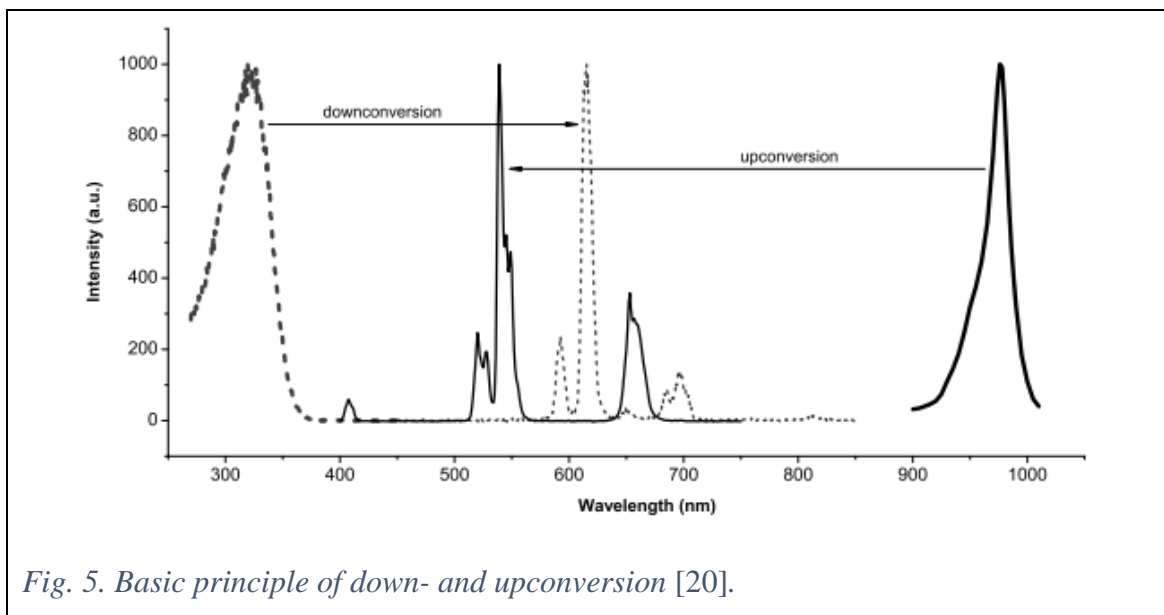


*Fig. 5. Basic principle of down- and upconversion [20].*

Since the emission of fluorescence always takes place from the lowest vibrational level, the emission spectrum is always of the same shape for the given material, independent of the excitation wavelength [21].

#### 1.4.1. Transitions

The processes, or types of transitions can be classified in two groups: radiative and non-radiative (with or without photon emissions, respectively). Radiative transfers include PL and a radiative transfer to another ion. Non-radiative mechanisms are far more complex, and they can be classified into the following types [15] (see Fig. 6):

- Internal conversion: transfer from a higher to a lower energy state of same multiplicity.
- External conversion: result of a collision with the solvent molecules.
- Intersystem crossing: crossover of states with different multiplicity, enhanced if the states' vibrational levels overlap.
- Cross relaxation: the original system loses energy while the other system acquires it, a major mechanism for quenching in high concentrations of RE. It can also happen between different elements which have the same energy level separation.
- Vibrational relaxation: a fast transition to the lower vibrational state of the same level.

Overall, the favored route to the ground state is the one that minimizes the lifetime of the excited state, being that a non-radiative or a radiative process. The fluorescence is favored in rigid structures, where high-energy vibrations are suppressed [20]. Vibrational relaxation is very fast, in order of  $10^{-12}$  s, thus the fluorescence from a solution always involves a transition from the lowest vibrational level of an excited electronic state, with the consequent production of the several closely spaced emission lines. The transition can terminate at any of the ground state vibrational levels. A consequence is the displacement of the PL band for a given transition to the longer wavelengths (see Fig. 7), i.e. lower energy [16]. If the absorption originates from the lowest vibrational level of the ground electronic state, to the lowest vibrational level of the excited state and back, the transition is called 0-0 transition and the emission and the absorption lines have the same wavelengths (see Fig. 8).

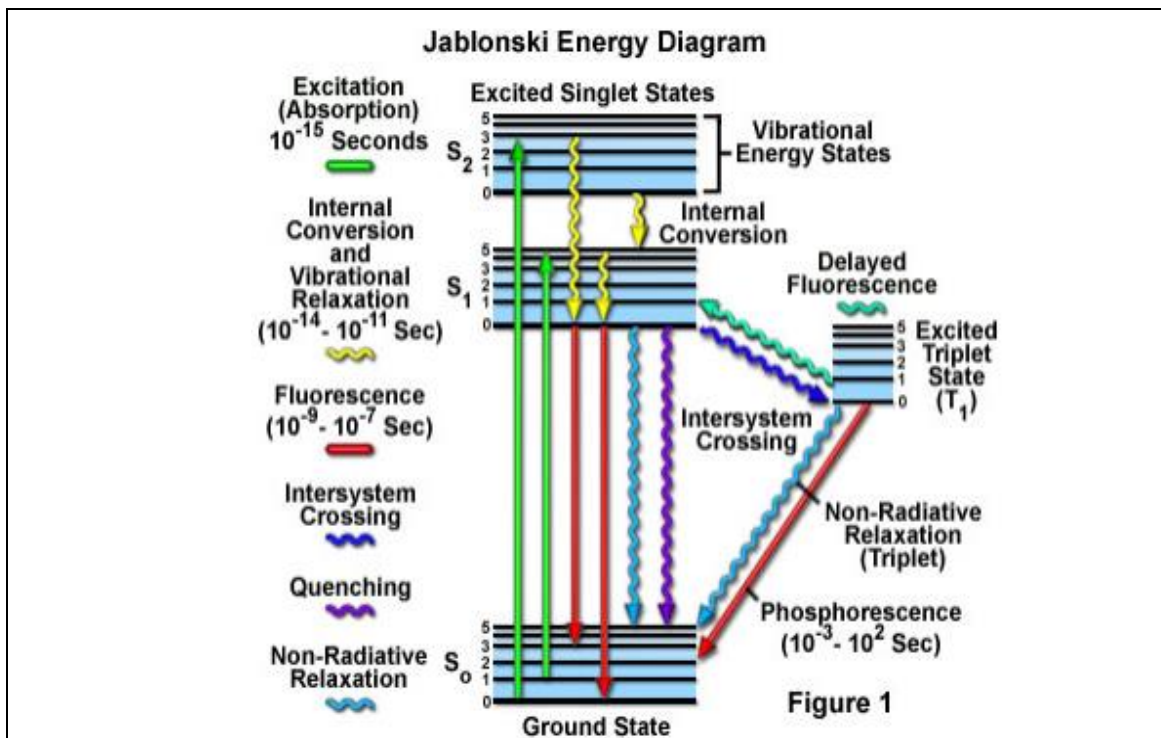


Fig. 6. Jablonski Energy diagram of radiative and non-radiative processes [22]

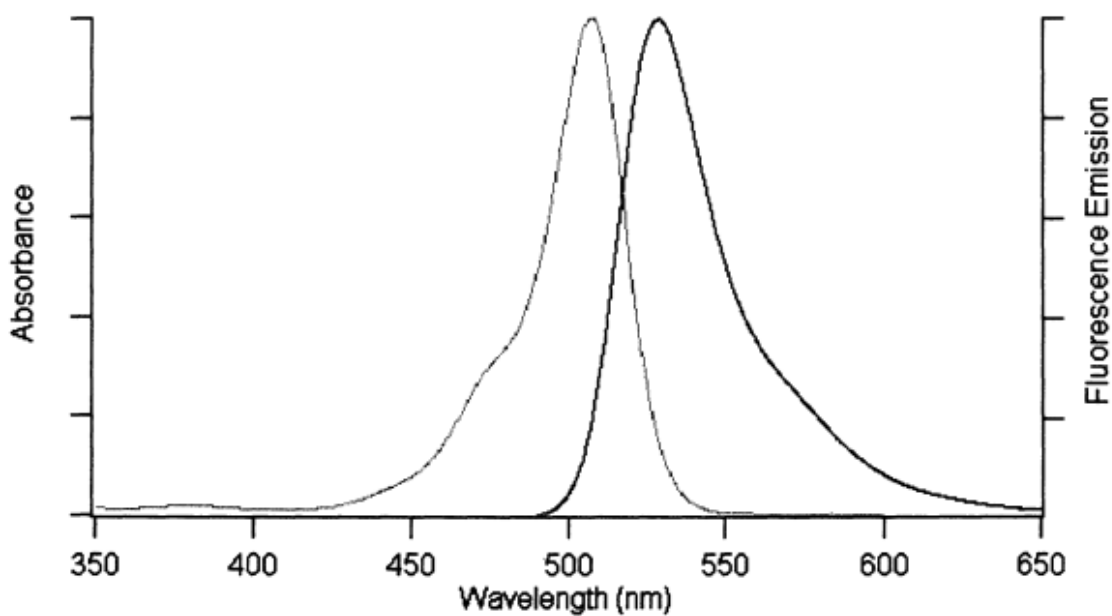


Fig. 7. Absorption (left) and PL (right) spectrum of Rhodamine-123 in methanol [18].

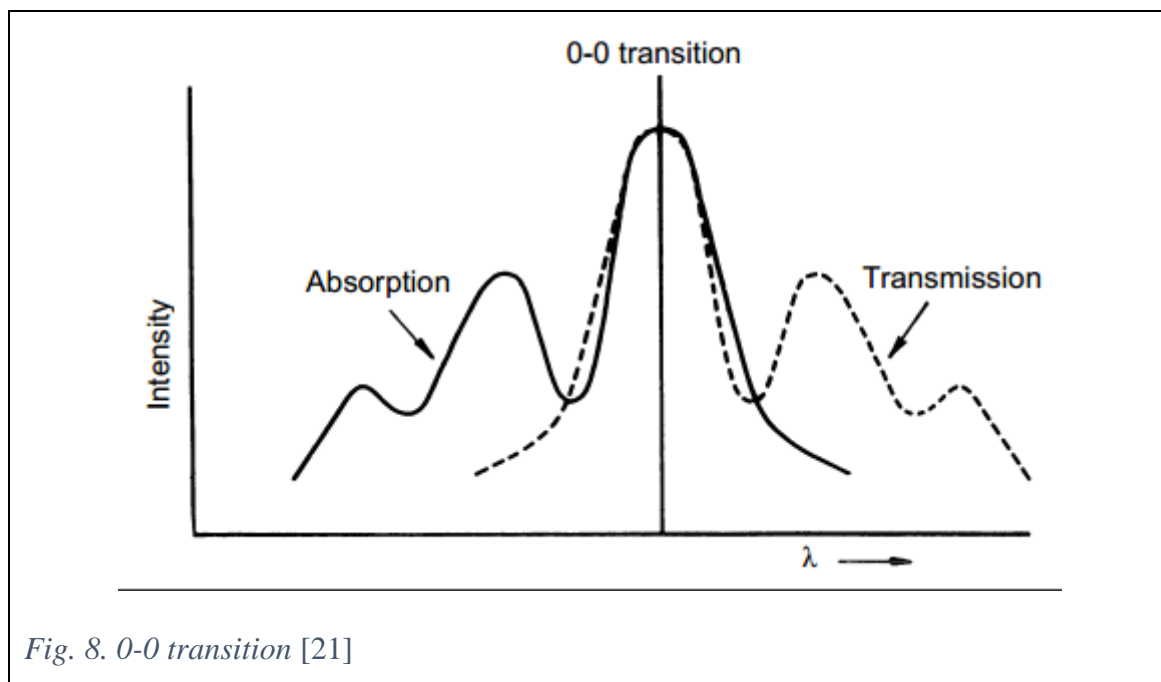


Fig. 8. 0-0 transition [21]

The long-range (Forster) quenching occurs without collisions between molecules, but by the dipole-dipole coupling between the excited phosphor and the quencher. Resonance energy transfer is a process when the excited molecule transfers the energy to a nearby molecule through near-field electromagnetic interaction. Static quenching occurs by forming a complex with another molecule that as a whole does not fluorescence. After some excitation time, the fluorescent molecules can change their structure so that they fluorescence no more, in a process called photo-bleaching [18]. RE PL is efficiently quenched through vibrational quenching of O-H vibrations, thus the water should be expelled from the coordination sphere of RE [20].

#### 1.4.2. Configurational coordinate diagram

Detecting bands instead of isolated absorption or emission lines is very common in solids. The configurational coordinate model explains the width of bands in solids (see Fig. 9). For small displacements the central ion approximatively behaves as a harmonic oscillator, and the electronic states are represented by parabolas. The vibrational levels are shown by the horizontal lines on the diagram, split by ca.  $100 \text{ cm}^{-1}$  [23]. The equilibrium distance is denoted by  $R_0$ . An emission starts from the lowest vibrational level of the excited state to the ground state. At 0 K, only the 0-0 transition would be

observed. After excitation the nuclei adjust their positions in a process called relaxation. Then the system can return non-radiatively or radiatively to the ground level. The energy difference between the absorption and emission lines is called the Stokes shift, and the difference is equal to that of the relaxation process [24]. The Frank-Condon principle states that the vibrational levels are not significantly altered during electronic transitions. The similarity of the vibrational level structures in the ground and excited states often results in absorption and emission spectra having mirrored features [23].

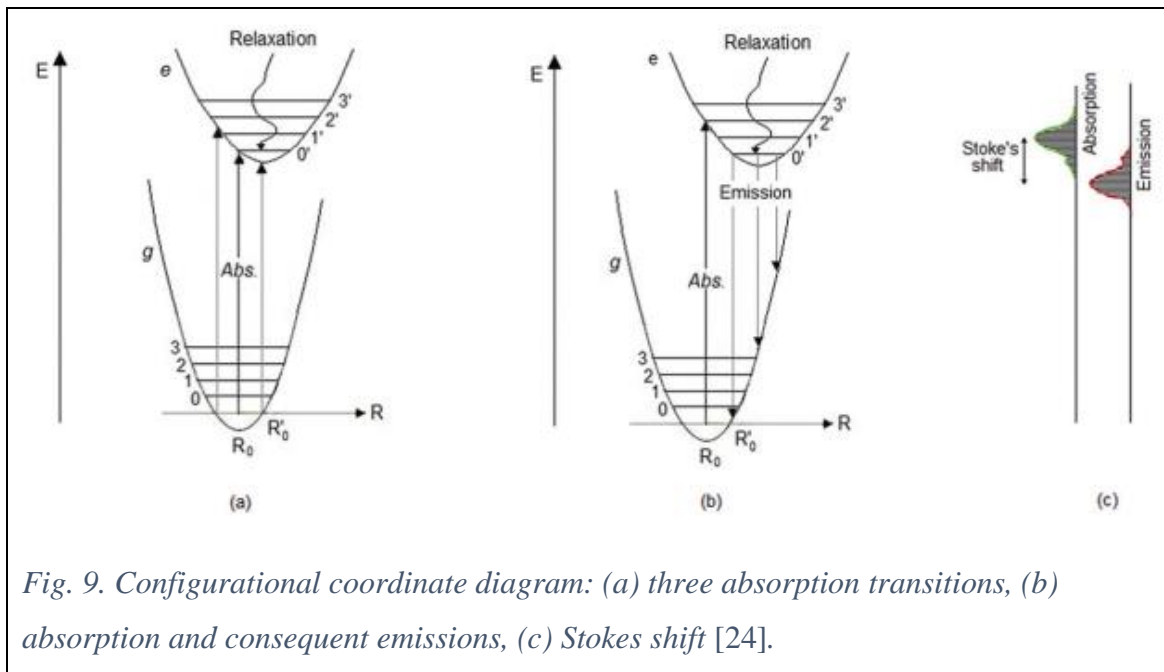


Fig. 9. Configurational coordinate diagram: (a) three absorption transitions, (b) absorption and consequent emissions, (c) Stokes shift [24].

In RE, since CF weakly affects RE ion, the displacement is small, thus the narrow emission lines will be observed.

#### 1.4.3. PL Measurements

Spectroscopy is a study of interaction of EM radiation with matter. Luminescence spectroscopy measures the energy levels of the luminescence centers, whose luminescence intensity is a function of their concentration, absorbing power at the excitation wavelength, their quantum yield of the emission wavelength, and sometimes on orientation in relation to the crystallographic directions in the mineral [25].

PL spectra are commonly measured by a spectrofluorometer. The obtained raw emission and excitation spectra must be corrected before submitting them to theoretical

analysis. Lifetime measurements require pulse excitation with period negligible compared to the emission lifetime.

#### 1.4.3.1. Instruments

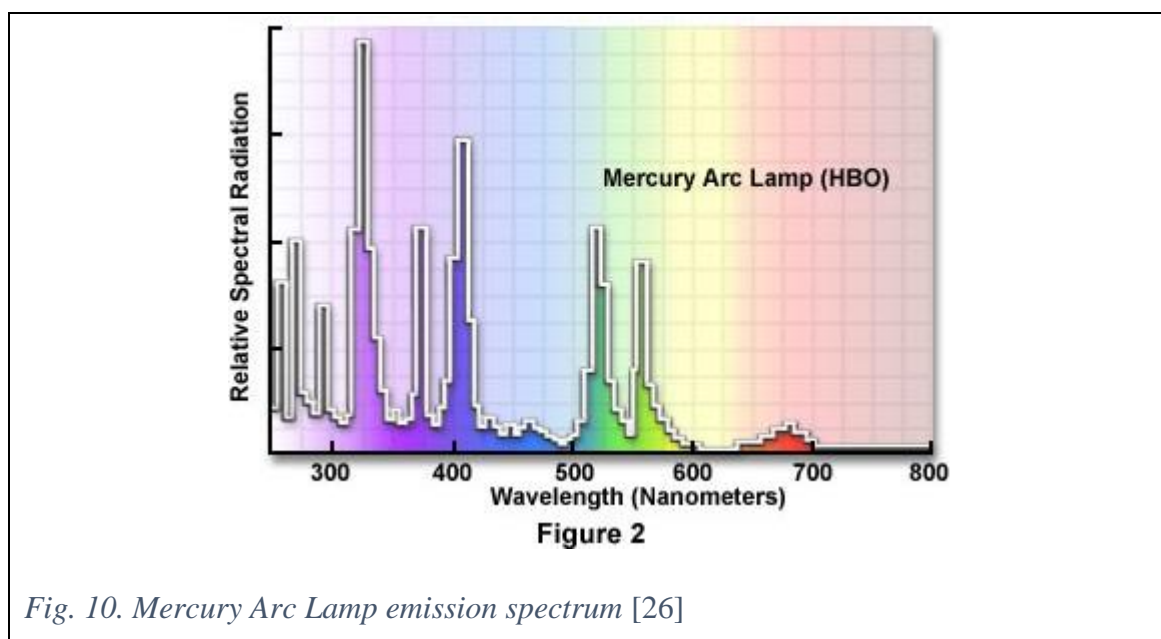
A sample for PL measurements must be irradiated by an ideally monochromatic light source. The PL from the sample is measured one wavelength step at a time, at the desired wavelength resolution. The intensity of the light at the measured wavelength is obtained by a detector.

If only filters are employed for wavelength selection, the instrument is called a fluorometer, while spectrofluorometers employ two monochromators for that purpose. Some instruments are hybrids, employing a filter for selecting the excitation wavelength and a monochromator for choosing the emission wavelength [16]. The schematic diagram of a typical spectrofluorometer is presented in Fig. 18.

##### 1.4.3.1.1. Light Sources

Light sources used for sample irradiation should ideally have an equal intensity on the whole spectrum. In practice no such light source exists, and the right light source should be selected for the task.

The typically used lamp in fluorometers is a Mercury arc lamp. It can be used for exciting fluorescence at 254, 302, 313, 546, 578, 691 and 773 nm (Fig. 10).



Xenon lamps are a source of continuum radiation in the broad wavelength range (see Fig. 11), thus they are the most common light source in spectrofluorometers. In some instruments, a capacitor is discharged through the lamp at constant frequency to provide flashes in order to obtain higher peak PL intensities.

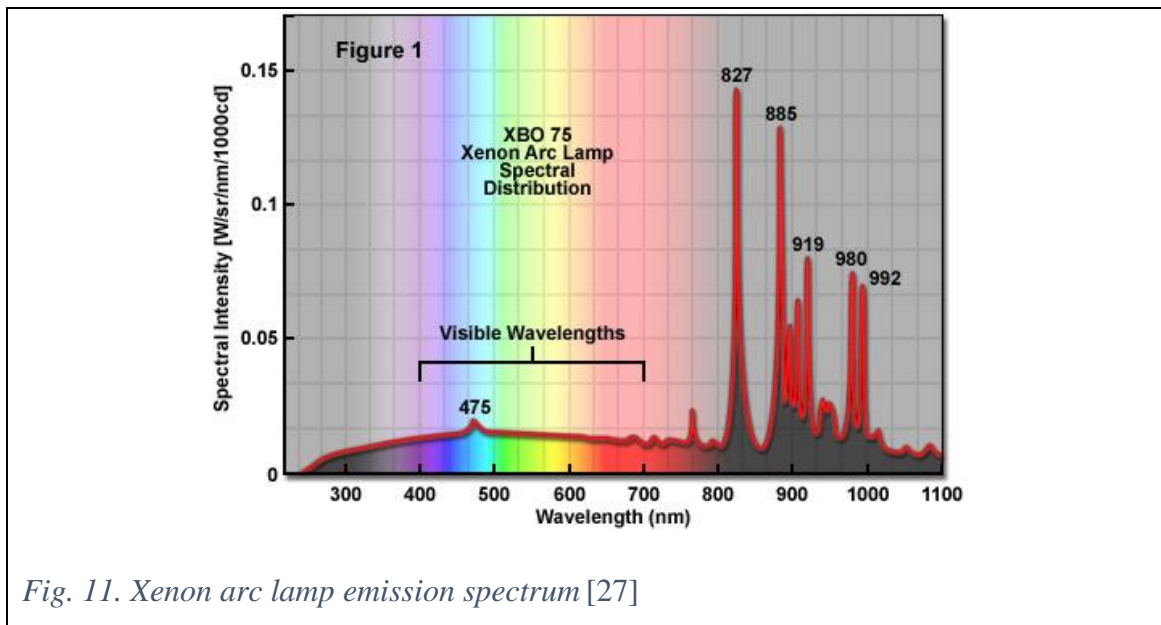


Fig. 11. Xenon arc lamp emission spectrum [27]

LEDs are a relatively novel device for sample illumination. Their features include narrow and well defined peaks, low cost, high intensity, and ease of operation. The emission spectra of several LEDs is given in Fig. 12.

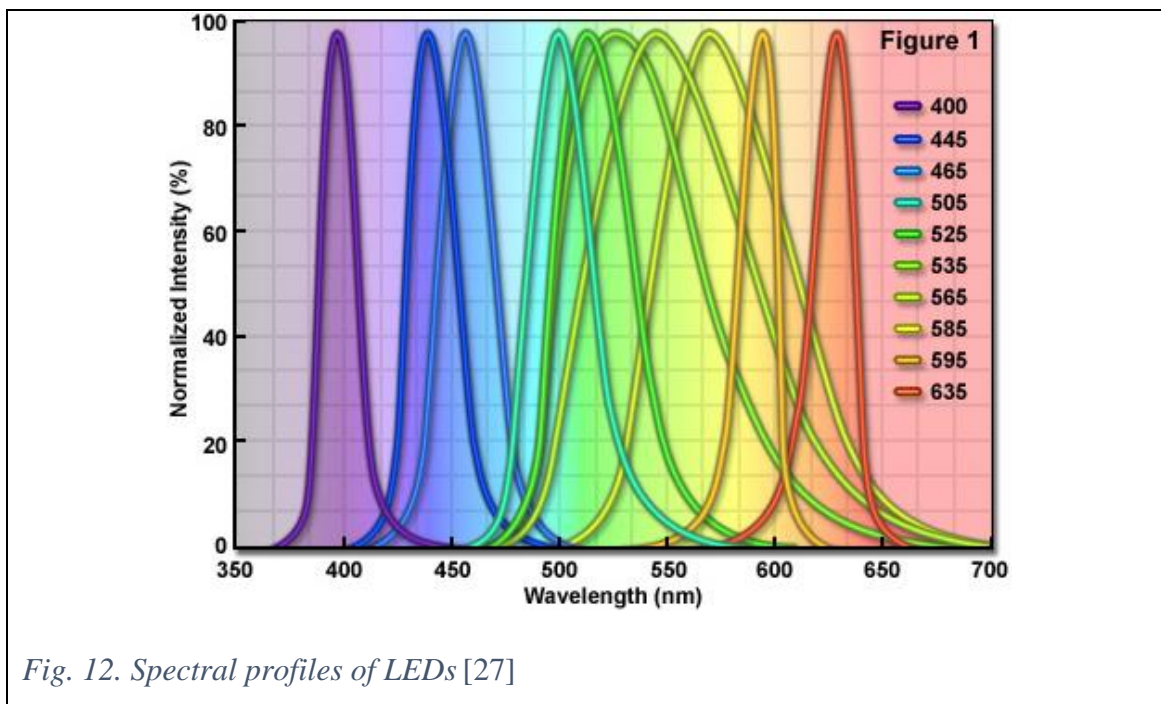


Fig. 12. Spectral profiles of LEDs [27]

Lasers witness an increasing use in the recent years, despite the high cost. Each laser provides an unique emission spectrum (Fig. 13) [26].

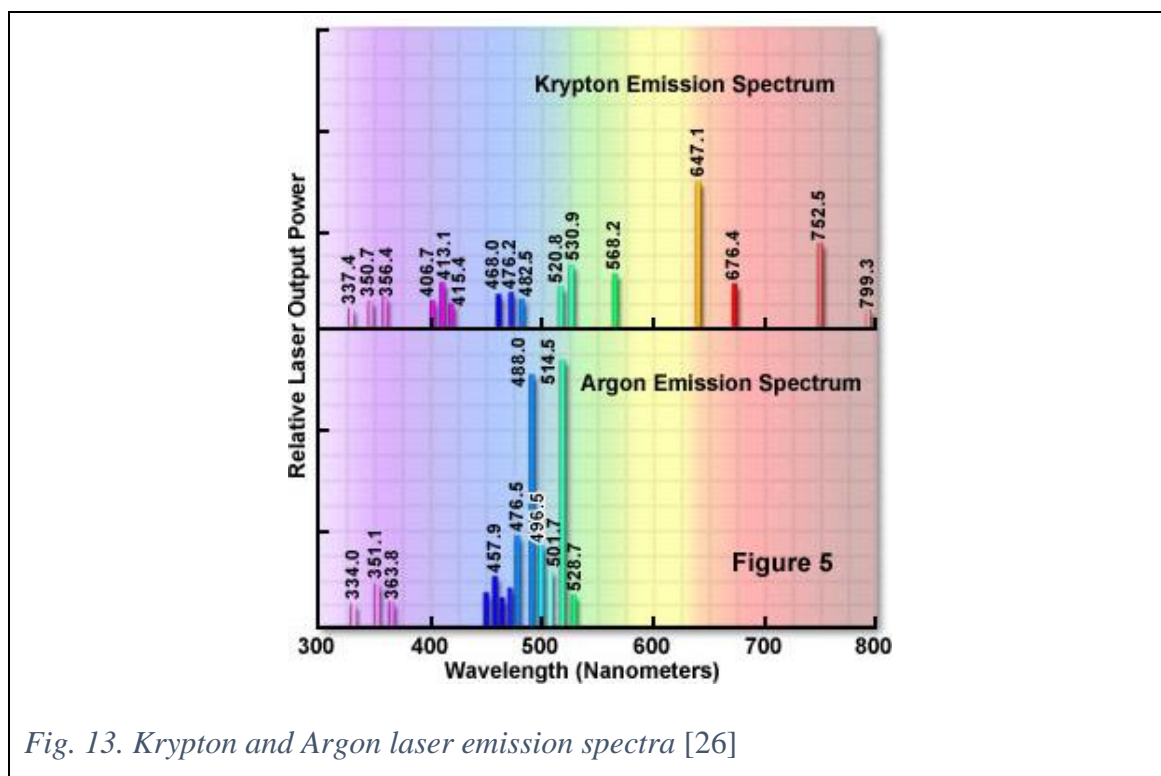


Fig. 13. Krypton and Argon laser emission spectra [26]

#### 1.4.3.1.2. Wavelength selectors

The selection of desired wavelength can be done by the interference or absorption filters in the case of the fluorimeters. The monochromators employed in spectrofluorometers select wavelengths by the prism or the diffraction grating.

#### 1.4.3.1.3. Detectors (transducers)

The typical detectors used in spectroscopy are a photomultiplier tube (PMT), diodes (Fig. 14), or a charge coupled device (CCD) (see Fig. 15).

Instrumental sensitivity can be expressed as the signal to noise ratio of the instrument or the minimum detectable quantity. The limit of sensitivity of a PMT is governed by a dark current (a signal from PMT with no incident light). The spectral response of a detector is also wavelength dependent [21] (see Fig. 16 and Fig. 17).

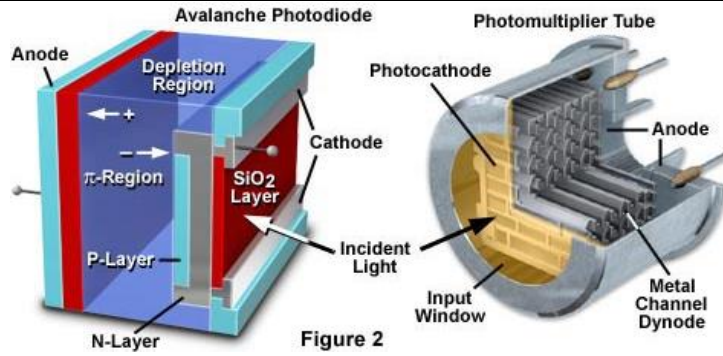


Fig. 14. Photodiode (left), PM tube (right) [22]

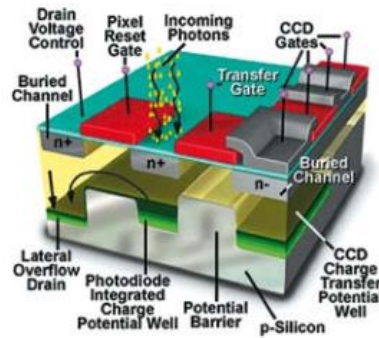


Fig. 15. The principle behind and anatomy of a CCD sensor [22]

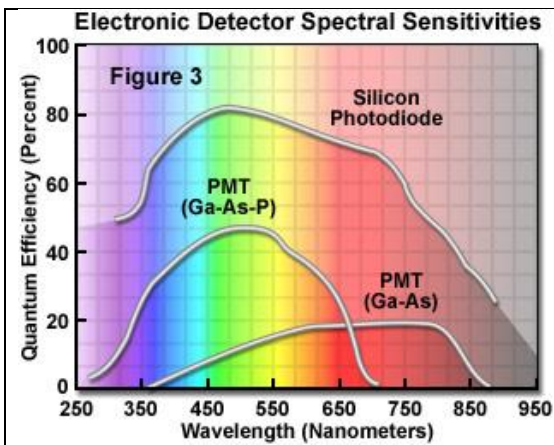


Fig. 16. PMT and silicon photodiode spectral sensitivities<sup>2</sup>

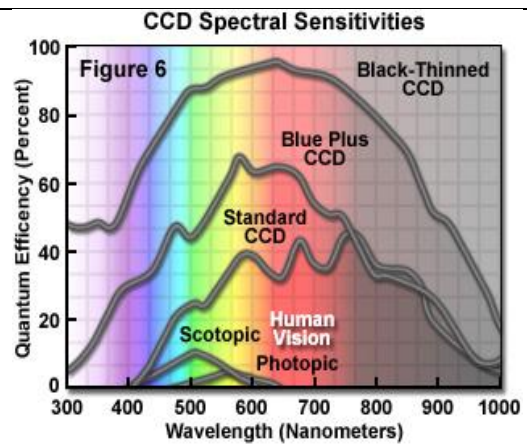


Fig. 17. CCD spectral sensitivities<sup>3</sup>

<sup>2</sup> Image acquired from: <https://www.olympus-lifescience.com/en/microscope-resource/primer/techniques/confocal/detectorsintro/>

<sup>3</sup> Ibid.

#### *1.4.3.2. Spectra*

The spectra used in PL studies can be divided into three types. In absorbency spectrum the sample is irradiated by all the wavelengths, and the wavelength of interest is monitored. The absorbency shows which wavelengths are absorbed by the solution. The excitation spectrum is used to show the wavelengths of the incident light responsible for the fluorescence. The material is excited through a group of consecutive wavelengths, and fluorescence emission is monitored at the wavelength of maximum intensity. Emission spectrum is measured by the excitation by the narrow band of incident light, as determined by the excitation spectrum, and by monitoring the fluorescence at a desired wavelength range [15]. In multisite systems the excitation spectrum can uncover the bands responsible for the energy storage and subsequent emission of radiative energy [28].

PL spectroscopy is among the most sensitive analytical techniques available. Background luminescence and signals from scattering and other sources determine the limits of detection. PL has 1-3 orders of magnitude better detection limits than the absorption spectroscopy, however the precision and accuracy is poorer by a factor 2 to 5 [16], due to the source flicker noise and drift or the presence of the contaminants.

Fluorescence is emitted from the sample in all directions, but is most conveniently observed at right angles to the excitation beam. This minimizes contributions contribution from scattering and from the source radiation [16].

#### *1.4.3.3. Correction and compensation schemes*

The effects that influence the obtained spectrum are: source stability and spectral distribution, inner filter effects, efficiencies of optical components and spectral responses of detectors. Hence, fluorescence measurements of the same sample at different instruments will produce different spectra [29]. The source compensation is best done by monitoring intensity via a reference photomultiplier (Fig. 18).

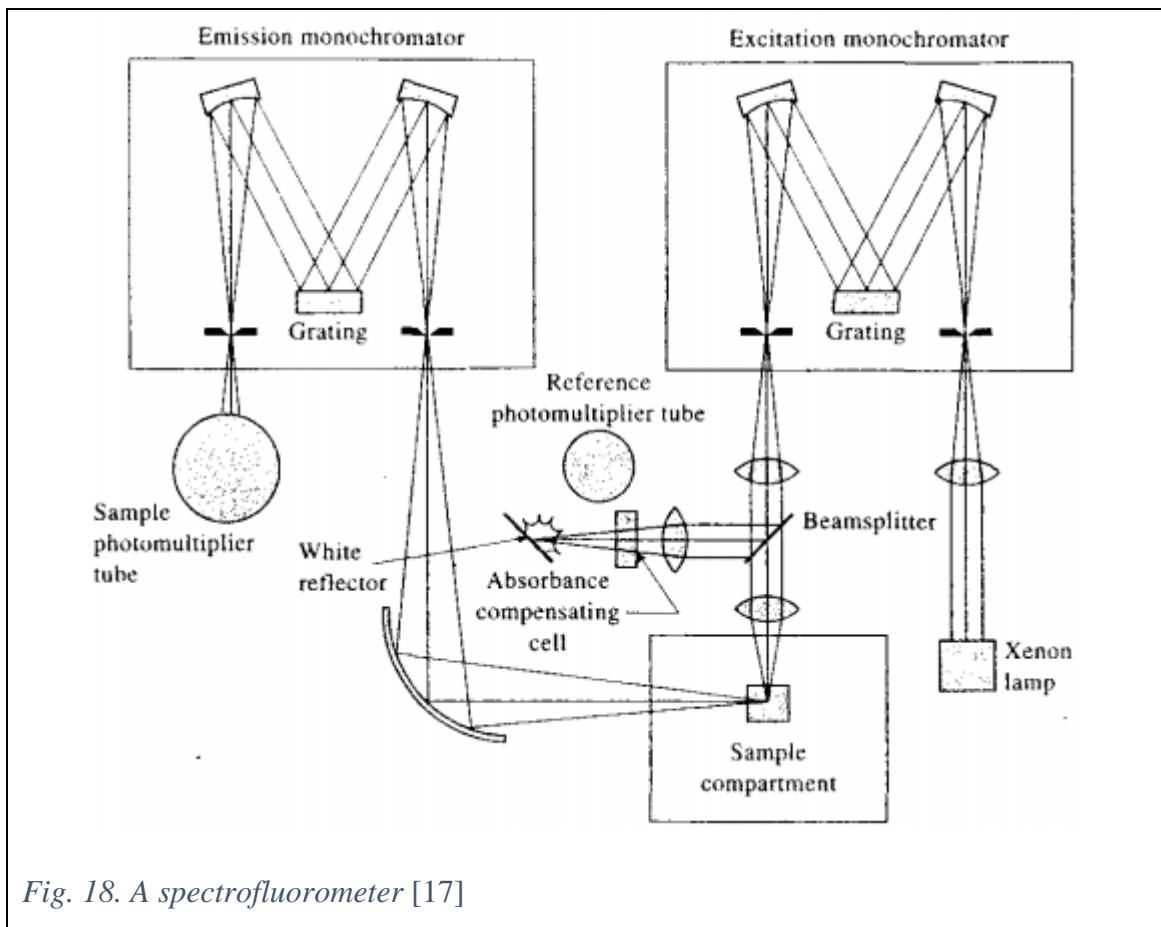


Fig. 18. A spectrofluorometer [17]

However, source compensation does not correct for the other effects. For the wavelength dependence of the source or the efficiencies of the optical components and excitation monochromator, a correction can be made by comparing with a reference spectrum [16]. To correct the emission spectrum, calibration factors for the emission monochromator and detector must be determined by placing a calibrated light source, and the resultant spectrum is then multiplied by the correction factors. In other words, technically corrected spectra can be obtained by measuring the wavelength dependency of the whole instrument [29].

## 1.5. Lanthanides

Lanthanides are the most fascinating group of chemical elements, noteworthy due to both their similarity and their diversity [30]. The term RE and Lanthanides are usually taken as synonyms in the literature. Lanthanides make a series of chemical elements with atomic numbers 57 through 71, from Lanthanum through Lutetium. RE elements are comprised of Lanthanides with addition of Yttrium and Scandium. The name rare-earth is due their high abundance in nature and difficulty of chemically extracting a pure element [31].

RE resemble each other in view of their chemical properties. RE are characterized by the general  $[\text{Xe}]4f^n5d^16s^2$  electronic configuration, with the outer configuration  $5s^25p^66s^2$ , where n represents the number of electrons from 0 to 14 (from La to Lu). However, La, Ce, Gd and Lu take  $[\text{Xe}]4f^{n-1}5d^16s^2$  electronic configuration, and the rest of RE take  $[\text{Xe}]4f^n6s^2$  [20].

Some RE can exist as divalent, and some can exist as  $\text{RE}^{4+}$  ions, however, the most stable ionization state is the trivalent one, with configuration  $[\text{Xe}]4f^N$ : 5s and 5p electrons remain untouched and they are screening the 4f electrons from the surrounding environment [28]. The  $\text{RE}^{3+}$  ions have the maximum possible numbers of unpaired electrons, and exhibit a complex magnetic behavior because the electrons in the unfilled shells provide a net magnetic moment [24]. As the 4f orbitals have low radial expansion, no matter that the 5s and 5p electrons are lower in energy, their sub-shells are located outside the 4f orbitals [20], as presented in Fig. 19. Because of the shielding, the 4f-4f transitions have characteristic sharp peaks and long lifetimes [32]. The exceptions are La and Lu, because their 4f orbital is empty and full, respectively, therefore these ions do not feature any 4f-4f transition [33].

Optical properties of RE arise from the inner f-electrons. The transition probabilities of 4f-4f are sensitive to the ions surrounding the RE. The emission colors of RE range from UV to visible to NIR. Trivalent Eu, Tb and Gd have the strongest luminescence, which is due to their long lifetime. Gd emits in the UV region. Trivalent Dy and Sm have inferior PL quantum yields and shorted lifetimes. Trivalent Nd, Er and Yb have found their use in the NIR region. The upconversion is demonstrated by the trivalent Tm, Dy, Er and Ho, sensitized by  $\text{Yb}^{3+}$  [20].

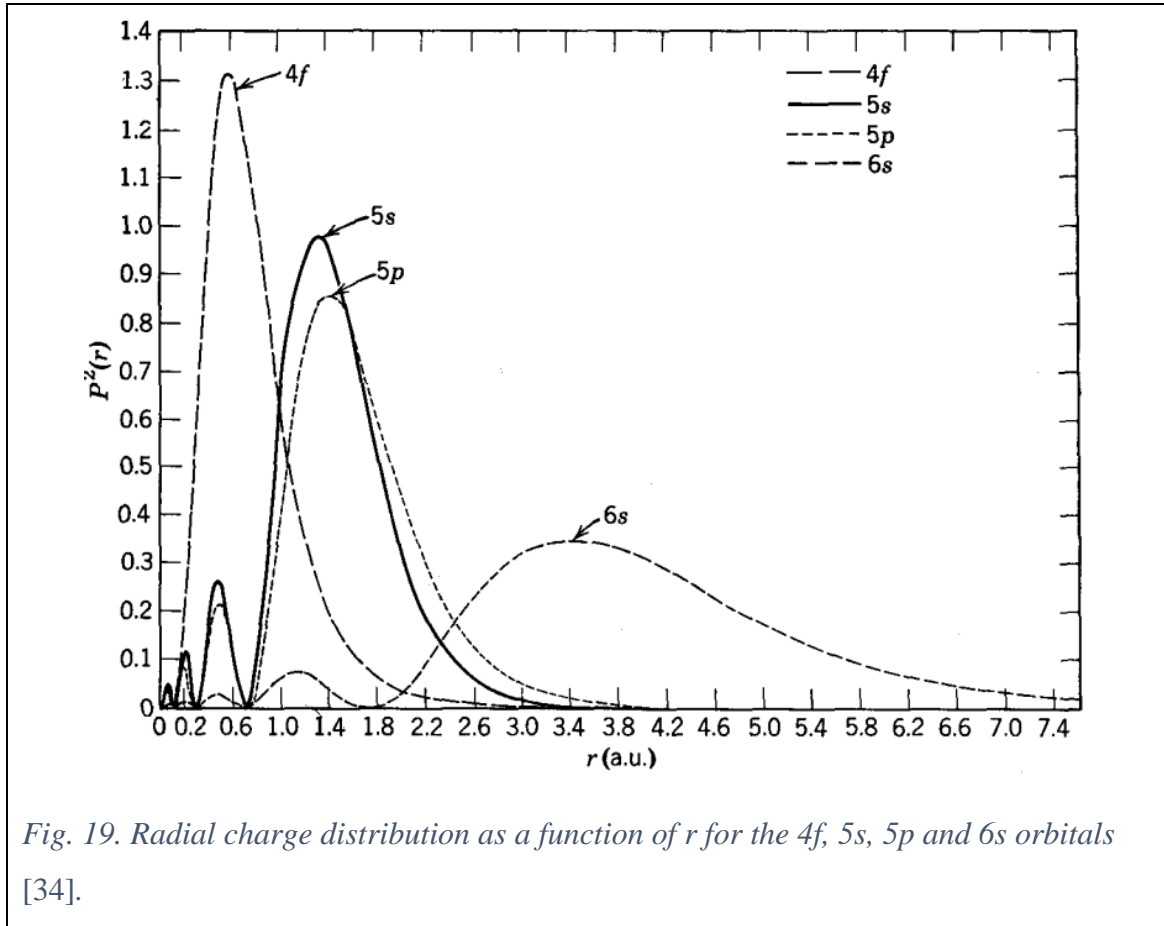


Fig. 19. Radial charge distribution as a function of  $r$  for the  $4f$ ,  $5s$ ,  $5p$  and  $6s$  orbitals [34].

The energy levels of lanthanides are given in Fig. 20. Free ion energies are described by configurations, terms and levels. Sub-levels occur when the ion feels some external field (in our case the CF of the host matrix). The Coulomb repulsion between electrons splits the degeneracy of the  $4f^N$  electronic configuration into LS terms. The terms are further split into J levels by the spin-orbit (s-o) interaction. This free ion state is represented by the  $^{2S+1}L_J$ , where  $2S+1$  is the spin multiplicity. In the coordinating environment, J levels can be split to sublevels, called Stark levels, due to the effects of the crystal field (CF) (see Fig. 21). The number of possible orientations of the orbitals is given by the number of possible values of the magnetic quantum number, and is equal to 7 for f orbitals according to the  $(2l+1)$  rule. In a totally symmetric surrounding all orientations of the orbitals are equivalent and are thus degenerate [25].

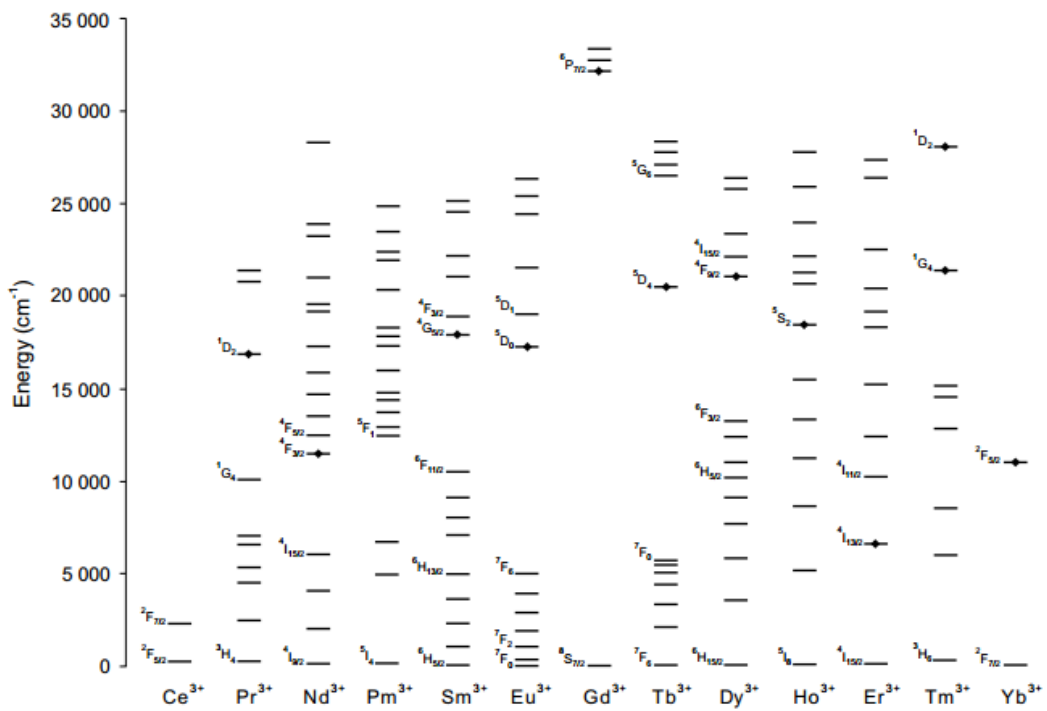


Fig. 20. Energy levels of trivalent RE [20]

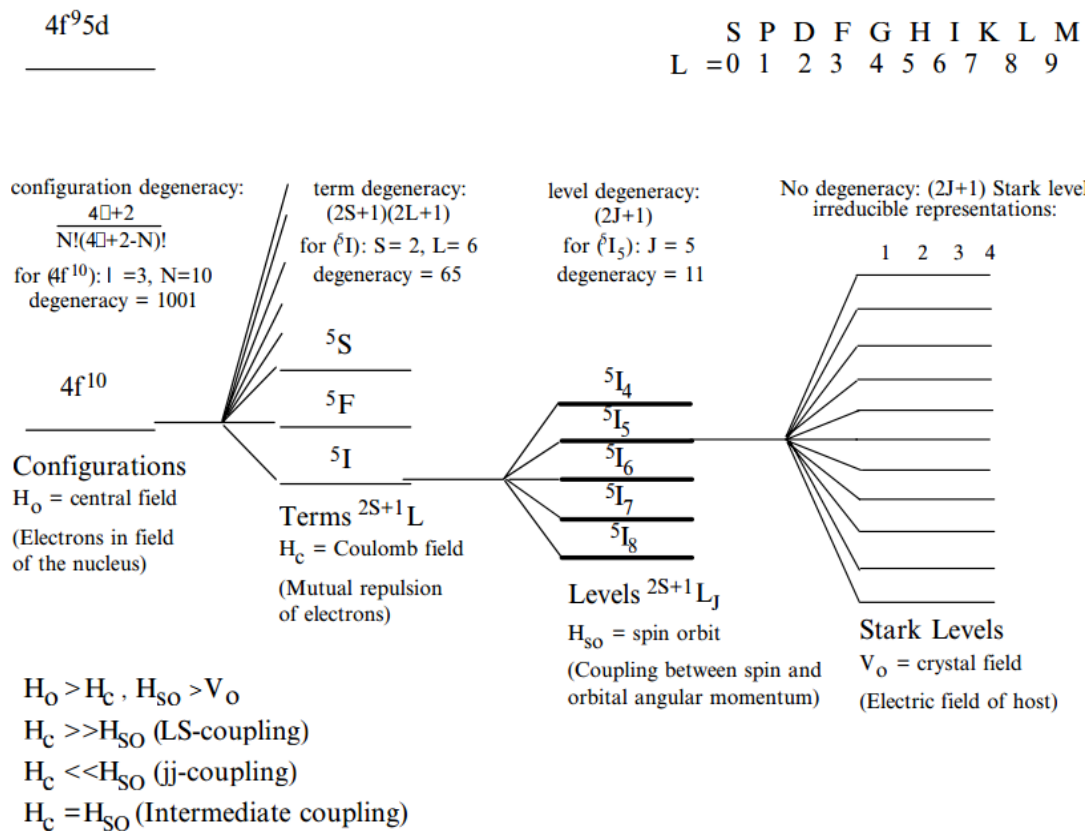


Fig. 21. RE ion atomic structure [31].

The Hund's rule can help in evaluating the ground state [24], in the following order:

1. the term of lowest energy will have the highest spin multiplicity,
2. the greatest L,
3. for RE with less than a half filled shell, minimum J; with more than a half filled, with maximum J.

The characteristic absorption and emission spectra of RE compounds are attributed to transitions between 4f levels and their sharp lines with oscillator strengths typically of order of  $10^{-6}$  [35].

The 4f-4f ED transitions are forbidden by the Laporte rule, while MD transitions are parity-allowed. The consequence is the low level of 4f-4f transition intensity. In a coordinated environment the forbidden transitions become partly allowed, and the resulting transitions are called induced ED transitions. Although the relative intensities are mostly sensitive to the environment, the 4f-4f transitions of RE have mostly unchanged wavelengths.

RE often require indirect excitation, the so called sensitization or antenna effect [20]. There are two main mechanisms for intermolecular energy transfer from the triplet state of the ligand to the central ion: Dexter (electron exchange) and Forster (dipole-dipole). Additionally, the charge transfer transitions exist, but they require high energies and are more probable for the  $\text{Eu}^{3+}$ ,  $\text{Sm}^{3+}$ , and  $\text{Yb}^{3+}$  than the other  $\text{RE}^{3+}$  [20]. Another type are the f-d transitions, however, although they are allowed, they require high energies.

## 1.6. Temperature sensing

Temperature affects even the tiniest detail of the daily lives of all living beings [36], thus it is no wonder that it is the second most measured physical quantity, second only to time [37]. Of all the sensors the ones for temperature measurement account for up to 80% of the sensor market. The industry requires specialized sensors for specific purposes since no sensor is suitable for all situations. Thus, the comparison of the available sensor types and measurement techniques is of particular value in the development and selection of the best sensor for the given task [38]. The choice of the proper sensor for the task is not a straightforward task. Many parameters must be taken into the consideration, such as: the accuracy, sensitivity, size, life, cost, various constraints, dynamic response, range of operation etc. [39]. Here will be reviewed only the most notable devices.

The accuracy of the device might depend on a calibration against the absolute temperature scale. The current international temperature scale, ITS-90, is defined in ranges [39,40]:

1. 0.65 – 5 K, by He vapor pressures,
2. 3 - 24.5 K, by a constant volume gas thermometer,
3. 13.9 – 273.16 K, by platinum resistance thermometer calibrated against various triple points,
4. 273.16 – 1235 K, via platinum resistance thermometer calibrated at fixed freezing and melting points,
5. above 1235 K, by using the Plank law of radiation.

Temperature measurement techniques can be classified depending on the nature of contact between the measuring device and the medium of interest [39]:

1. invasive: the measuring device is in direct contact with the medium,
2. semi-invasive: the medium is altered in a manner to enable remote observation,
3. noninvasive: the medium is observed remotely.

### 1.6.1. Invasive techniques

The use of invasive instrumentation necessary involves disturbing the measured substance, since the thermal contact can be achieved by surface adhesion of the sensor head, or by inserting it inside the measured object [41]. The traditional invasive measuring devices are gas thermometers or liquid-in-glass thermometers. Gas thermometers measure pressure or volume change of encapsulated gas in order to obtain the temperature. The accuracy of the method can be very high, but the method is generally restricted to detailed scientific experiments and can be very expensive. Liquid-in-glass thermometers can achieve accuracies of 5 mK, and the existing instrumental error is only due to the manufacturing imperfections [39]. However, there is a trend of substituting the traditional liquid thermometers by alternative sensors [42]. Bimetallic strips are an example of one alternative. They can achieve accuracies of 1 K.

Thermocouples are the most widely used temperature measurement sensors in industry [41]. Thermocouples are nontoxic, easy to use, precise, have a wide operating range (from 3 K to 3300 K), and signals can be easily digitized, since the basis of their operation is the Seebeck effect (electromotive force produced in a circuit of two different conductors experiencing a thermal gradient). They have a fast response, and an adequate accuracy. The drawbacks are the requirement of an electrical link to the sensor, limitation in corrosive environments and are affected strongly by the electromagnetic fields. Contact measurements require convective heat transfer, thus there is a need of thermal equilibrium between the sensor and the measurand. This can disturb the environment, thus the invasive measurements are not adequate for small samples [42]. They require an independent measurement of junction temperature (called cold junction compensation). A drift caused by annealing of thermocouple materials is a constant problem and all thermocouples require an often recalibration. The most commonly used pair of metals is nickel chromium – aluminum alloy, which carries the standardized letter designation “K”. The K type thermocouple is operable on the -250 °C to 1100 °C, creates a ca. 40  $\mu\text{V}/^\circ\text{C}$  output, is a low cost but also a low stability sensor. The constant use over 800 °C causes oxidation on the K type thermocouple sensor surface, which causes drift. Furthermore, they are unstable with hysteresis between 300 °C and 600 °C, which can result in error of a several degrees.

Semiconductors can be used for temperature measurements. In the temperature range from -55 to 150 °C, a transistor or a diode can be used with a good accuracy within 0.8 °C. Thermistors are semiconductors whose resistance is sensitive to temperature. They can be used in lower temperature ranges than platinum RTDs and thermocouples. The accuracy of the industrial sensors is ca. 1 K. Their advantage is the low price and the simple and inexpensive read-out instrumentation. The disadvantage is susceptibility to de-calibration and drift.

The motion of the electrons inside a solid is dependent of the lattice vibrations, thus the conductor resistance increases with the temperature. Any conductor can be used as a resistive temperature detector (RTD), however, since platinum has higher resistivity than copper, gold or silver, is relatively unreactive and has a well-established temperature coefficient of  $3.85 \cdot 10^{-3} \text{ K}^{-1}$ , it is a material of choice for RTDs. Its operating range is from -260 °C to 962 °C. Their accuracies and operating ranges are defined in the classes: Class A devices have uncertainty of  $0.15 + 0.002 \cdot |T|$ , while Class B have  $0.3 + 0.005 \cdot |T|$ . Although with lower accuracy, Class B sensors usually have larger operating range than the Class A detectors. The standard platinum resistance thermometer (SPRT) can achieve an accuracy of 2 mK. RTDs feature an almost linear resistance to temperature dependence [41]. This dependence is better approximated by a quadratic equation on the positive Celsius scale, and by cubic equation for measurements on the negative Celsius scale [39]. Overall, RTDs suffer from much smaller drifts, have greater accuracies, but slower responses than the thermocouples. RTSs are more expensive than the thermocouple and require a generally more expensive equipment.

### 1.6.2. Non-invasive

Optical sensors have an advantage of contactless measurements and large scale imaging. Radiation that exists solely due to the object's temperature is called incandescence [21,24]. Optical pyrometers or IR thermometers, based on the black-body radiation, have fast recording, but lack good spatial resolution and suffer from the dependence of the precision upon the sample properties. Another drawback is the need for a reliable calibration. As IR radiation is attenuated by glass, the sensors cannot be used for thermometry in combination with microscopes [42]. The accuracy of the

commercial devices lies between 1 and 5 °C [39]. The another drawback is that pyrometry requires the exact knowledge about the emissivity of the measured surface, and the emissivity is dependent upon wavelength, detection angle and surface properties. The sighting path must be clear as well as the optics and the measured surface. There are also no industry accepted calibration standards for optical pyrometers as there are for thermocouples and RTDs [43].

Optical methods can be classified in two groups: passive, where the natural radiative properties of the material is observed, and active, where an excitation source is used [42]. While IR thermometry is a passive method, another popular non-invasive method are spontaneous Rayleigh and Raman scattering, where an EM radiation is absorbed and re-emitted. Rayleigh scattering is the elastic scattering of light by small particles, where the temperature is derived from the ideal gas law. Upon the irradiation, if a molecule is promoted to a higher vibrational state and returns to the original state, the process is called Rayleigh scattering. If it returns to a different vibrational state, then that is the case of Raman scattering. In other words, Rayleigh and Raman scatterings are the cases of the elastic and inelastic scatterings. Their range of operation is from room temperature to ca. 2200 °C, and accuracies of 1% to 7%, respectively. Applications include measuring temperatures of plasma or gases [39]. Their another drawback is the use of the expensive equipment.

### 1.6.3. Semi-invasive

Liquid sensors, bimetallic strips, thermocouples, pyrometers and thermistors cannot be easily miniaturized and therefore are not suitable for measurement of temperature at a spatial resolution  $<10\ \mu\text{m}$ . Thus, they cannot be employed for temperature measurements e.g. inside cells [42]. Another example are gas turbines where the development trend is in increasing the turbine entry temperatures for increasing the engine efficiency. These temperature increases require a protective coatings and accurate temperature measurements [44]. The application of pyrometry in gas turbines is problematic due to the stray light caused by flames, reflections, changes in the emissivity of the observed surface and the cleanliness. Thermocouples are intrusive and suffer from high installation costs where rotating components are concerned, and their coverage is limited to pre-installed points and cannot be changed during operation [44]. The

thermographic phosphors and luminescence thermometry does not suffer from those drawbacks, and out of all the semi-invasive methods it has attracted the most attention. Other methods such as semi-invasive diagnostics based on thermo-chromic liquid crystals or temperature sensitive paints are generally limited to temperatures less than 100 °C [12]. The probes and sensors for luminescence thermometry can be incorporated in the sample, deposited on the surface (with sufficient thickness for producing high enough luminescence [12]), used for single-point measurements or imaging [42]. Thermographic phosphors can be incorporated inside, or on the surface of the fiber optic cables, allowing the contact measurements in hostile environments, where the access is restricted, or in high fields [45].

Luminescence thermometry exploits the dependence of the luminescence properties on the temperature of certain materials. Generally, multiphonon relaxation, energy transfers and cross-over processes are regarded as the main reasons for the thermal quenching of PL [46]. Out of the materials of choice for luminescence thermometry (such as semiconductors, organic-inorganic hybrids, organic dyes, polymers [36]) the lanthanides, due to the narrow emission lines and long lifetimes, are favored in most instances. Even more, RE luminescence provides materials with the ability to perform multiple functions, such as adding the thermometric functionality to materials already chosen for a specific application [36].

The application of RE for temperature sensing includes choosing a RE of choice, incorporating it in a host of choice, selecting a temperature-read-out method and finally, a sensor calibration. The most important criterion for phosphor selection is its sensitivity on the desired temperature range [12]. The others are its dynamic temperature range and stability [45].

PL intensity of these sensors generally decreases with increasing temperature, while at high temperatures the contribution of the black-body radiation increases [44]. As presented in Fig. 22, even at the elevated temperatures PL signal is dominant. Even so, blue emitting materials are preferable for high temperature measurements, since the interference with blackbody radiation is minimized [12].

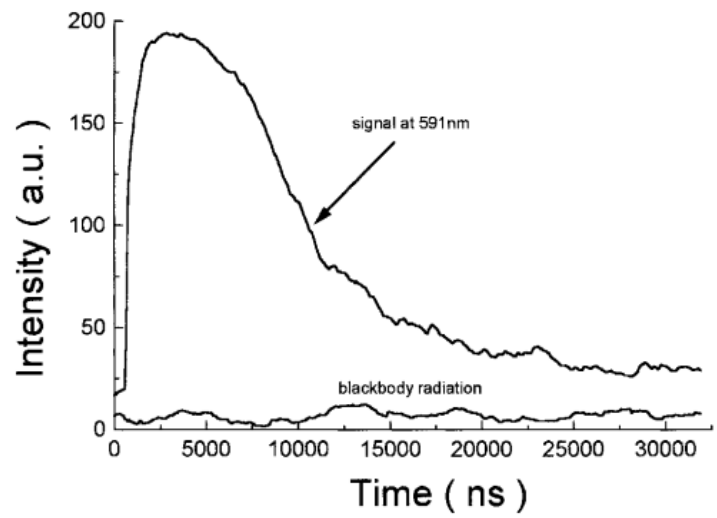


*Fig. 22. Phosphor response signal and blackbody radiation at 800 °C [44].*

## 1.7. Judd-Ofelt theory

*“The Judd-Ofelt theory marked a turning point in our understanding of the fascinating spectroscopic properties of the rare earths. It has been in a very real sense the first step in the journey to an understanding of the rare earths and their much heavier cousins, the actinides, but like many journeys into the unknown, the end is not in sight.”*

*Brian G. Wybourne, The fascination of the rare earths - then, now and in the future (2003)*

RE elements posed a trouble for chemists and physicists in the first half of the 20<sup>th</sup> century. Their abundance and hard separation meant that most of them could not be obtained in adequate purity for spectroscopic analysis, and their complex spectra could not be analyzed. The low intensities of the absorption lines indicated the presence of the forbidden transitions that would agree with the rearrangement within the 4f shell. In 1949 Racah introduced an application of group theory and tensor operators of complex spectra, which found its use in CF calculations and free ion calculations. Soon the development of computers solved the problem of diagonalizing the large matrices. In 1962 the end of a long search for a consistent theory of the intensities of 4f-4f transitions of lanthanides and actinides represented a beginning of their understanding [30]. The theory of the intensities of induced electric dipole 4f-4f transitions is originally introduced simultaneously in separate research papers by Judd [47] and Ofelt [48]. Judd-Ofelt (JO) theory has the ability to predict oscillator strengths in both absorption and luminescence, luminescence branching ratios, excited state radiative lifetimes, energy-transfer probabilities and estimates of quantum efficiencies by using only three parameters. JO parameters thus represent the overall picture of important mechanisms that affect the electron transitions within 4f shell of rare earth ions.

Its predictive qualities are responsible for its widespread use in all fields regarding luminescence of rare earths [33]. Rapid increase of the importance of the field of lanthanide materials is followed by an increasing trend of number of research papers mentioning the theory [49,50]. Judd-Ofelt is the only tool that is used in *ab initio* type calculations of lanthanides and actinides. Its main aim is not to reproduce the

measurements by a fitting procedure but rather to understand the physical mechanisms [50].

The original JO theory is based on the static, free-ion and single configuration approximations. In the static model, the environment affects the central ion by a static electric field. Because of the screening effect of 4f orbitals in RE, it may be observed as a free-ion, thus the environment fields effect on the central ion can be observed as a perturbation of the free-ion Hamiltonian. The interactions between different configurations are neglected, i.e. only 4f-4f transitions are being observed [31].

## 2. Theory

### 2.1. Luminescence thermometry

#### 2.1.1. Temperature quenching of RE PL

In order to understand the effects of temperature on PL intensity, it is necessary to first consider the processes that start once the electron is being excited. In a process of de-excitation, the energy can be lost radiatively or by a number of nonradiative ways. If the population of optically active electrons of the excited state is labeled as  $N$ , the de-excitation is given by [36,51]:

$$\frac{dN}{dt} = -(A_R + A_{NR})N(t) \quad (2.1.1)$$

where  $A_R$  and  $A_{NR}$  are the frequencies of radiative and non-radiative transitions, respectively. This gives an exponential decay of the excited state, with an observed lifetime [23]:

$$\tau_{obs} = \frac{1}{A_R + A_{NR}} = \frac{1}{\frac{1}{\tau} + A_{NR}} \quad (2.1.2)$$

where  $\tau$  is the radiative lifetime, which can be measured from the spectra or from the ratio of the observed lifetime and quantum efficiency:  $\tau = \tau_{obs}/\eta$ .

The quantum efficiency is defined as the ratio of number of molecules that luminescence to the ratio of excited electrons, i.e. the number of photons emitted to the total number of photons involved in the process [17]:

$$\eta = \frac{A_R}{A_R + A_i + A_{ec} + A_{ic} + A_{pd} + A_d} = \frac{A_R}{A_R + A_{NR}} \quad (2.1.3)$$

where  $i$  labels intersystem crossing,  $ec$  stays for an external conversion,  $ic$  for internal conversion,  $pd$  is pre-dissociation (the transition without emission from a stable excited state to an unstable excited state that leads to dissociation) and  $d$  stands for dissociation (splitting of the molecule). All the non-radiative processes, called quenching, are observed as one.

The radiative lifetime values calculated from the equation above and obtained from spectroscopy measurements differ in many cases, however, it is far more important

that the radiative lifetime can be considered as temperature independent in most cases [36]. Thus the temperature dependence of PL results from the temperature dependence of quenching mechanisms, and the emission intensity can be represented as:

$$I(T) = CA_R\tau_{obs} = C\eta = C \frac{A_R}{A_R + A_{NR}} \quad (2.1.4)$$

where  $C$  is the temperature independent constant comprised of many physical parameters.

Depending on the temporal nature of temperature induced changes of luminescence, the measurement methods can be classified as time-integrated or time-resolved [51].

### 2.1.2. Thermometric figures of merit

The luminescence thermometry measurements do not directly provide the value of the temperature. The other measurable quantity that can be converted to temperature is called an indication ( $Q$ ). The dynamic range is defined as the range between the lowest and highest  $T$  that can be determined with adequate precision. An accuracy of a measurement is a degree of accordance of the measured with the true value, expressed in %. Precision is based upon the reproducibility of a measurement by means of the relative standard deviation [42].

The most frequently reported figure of merit is the absolute sensitivity, defined as a rate of change of indication with temperature [52]:

$$S = \left| \frac{\partial Q}{\partial T} \right| \quad (2.1.5)$$

Since the absolute sensitivity is dependent on the indication, it is not suitable for comparison of results. The normalized value of sensitivity with respect to its indication is called a relative sensitivity, given by [36]:

$$S_R [\%K^{-1}] = \left| \frac{1}{Q} \frac{\partial Q}{\partial T} \right| \cdot 100\% \quad (2.1.6)$$

The temperature resolution is the smallest change in temperature that causes an observable change in indication:

$$\Delta T_{\min} = \frac{\sigma}{S} \quad (2.1.7)$$

where  $\sigma$  is the standard deviation.

Spatial resolution is the minimum distance between points of measurement that can be resolved:

$$\Delta x_{\min} = \left| \frac{dx}{dT} \right| \Delta T_{\min} \quad (2.1.8)$$

In analogy with the spatial resolution, the temporal resolution is given by:

$$\Delta t_{\min} = \left| \frac{dt}{dT} \right| \Delta T_{\min} \quad (2.1.9)$$

### 2.1.3. Time-integrated methods and LIR

Time-integrated methods are observed by a constant illumination and observation. Single band observations include monitoring of the temperature dependent intensity, energy shifts, or peak bandwidth. Measurements of a single-band intensity depend upon the excitation energy, homogeneity of the phosphor layer, alignment, impurities in and on the optics, phosphor or detector [12]. The spectral line shift has not proved to be a consistent method due to the small shifts over a wide range of temperatures. Thus, all those schemes are almost completely abandoned in favor of LIR, which exploits the independence of the ratio of two emission peaks on the fluctuations in excitation and detection [53]. The parameters limiting the use of the single-band methods are compensated by the normalization of one band's measured luminescence intensity to the other [12]. LIR does not suffer from the concentration dependence, geometry, source intensity [42], and temperature changes of excitation bands [54]. However, background fluorescence, light scattering and reflections are not compensated for.

The use of two thermally coupled levels for LIR has several advantages over the use of two non-coupled levels: the theory of the relative changes in PL intensity is well understood and easier to predict, the population of each level is proportional to the total population, thus the changes in excitation power will affect the individual levels to the same extent. This helps in reducing the dependence of the technique on the excitation

power. The use of relatively closely spaced energy levels means that the wavelength dependent effects of the optical elements will be reduced [52].

The criteria for levels to be used for LIR are: less than 2000  $\text{cm}^{-1}$  energy separation (as larger energy differences have extremely low upper level populations for the temperature ranges of interest), and more than 200  $\text{cm}^{-1}$  (to avoid overlapping) [32,52]. Using pairs of energy levels with larger energy differences would increase the sensitivity, but as the energy difference widens, the population from the upper thermalizing level would decrease, which would pose a problem due to the low light intensities [52].

At 0 K only the lowest energy level is populated. The fractional thermal population of the level from which the emission starts at temperature  $T$  can be calculated from the Boltzmann distribution [55]:

$$\frac{N_i(T)}{N} = \frac{g_i \exp\left(-\frac{\Delta E_i}{kT}\right)}{\sum_j g_j \exp\left(-\frac{\Delta E_j}{kT}\right)} \quad (2.1.10)$$

where  $N_i$  labels the number of optically active ions at level  $i$  [28],  $N$  is the total population, hence the summation of all the levels (labeled by  $j$ ), and  $\Delta E$  is the energy difference between the level  $j$  and the ground state,  $k = 0.695 \text{ cm}^{-1} \text{ K}^{-1}$  is the Boltzmann constant,  $T$  is temperature in kelvins and  $g = 2J + 1$  labels the level degeneracy. Then the ratio of populations of the higher (H) to the lower (L) excited level is also given by the Boltzmann distribution [38]:  $N_H/N_L = g_H/g_L \cdot \exp(-\Delta E/kT)$ , where,  $\Delta E$  now means the energy difference between the two emitting levels. Given that the emission intensity is equal to:

$$I = h\nu NA \quad (2.1.11)$$

LIR of two thermally coupled levels is given by [38,52,56]:

$$LIR(T) = \frac{I_H}{I_L} = B \exp\left(-\frac{\Delta E}{kT}\right) \quad (2.1.12)$$

where  $B = A_H \nu_H g_H / A_L \nu_L g_L$  is the approximately temperature independent value.

At low temperatures the higher state might not be populated because electrons do not have enough thermal energy to bridge the gap between two emitting levels, and if

they do for the closely separated levels, the  $A_{NR}$  and thus their depopulation is very high. Thus, LIR has a low temperature bound: the smaller  $\Delta E$  the lower is the temperature from which LIR can be employed. An increase of temperature is followed by the population increase of H level and a consequent rise of its emission intensity. This happens at the expense of the L level's population. However, as the temperature increases, the overall emission decreases in intensity because of the rise of the temperature quenching, all until one of the emissions becomes undetectable. The upper bound is dependent upon the material properties and the detection system. The consequence of limits are larger measurement uncertainties in their vicinity.

For LIR, the absolute and relative sensitivity are given by, respectively [52,57–60]:

$$S(T) = \frac{\Delta E}{kT^2} LIR(T), S_R(T) = \frac{\Delta E}{kT^2} \cdot 100\% \quad (2.1.13)$$

The crucial dependence of the relative sensitivity on the energy level difference is evident. Since the energy difference depends weakly on the host matrix, but is rather a property of a doped RE ion, the relative sensitivities of the same RE will be approximately the same in any host.

#### *2.1.3.1. RE utilized for LIR*

RE ions commonly utilized for LIR and their thermally coupled energy levels are presented in Fig. 23. The energy gap of ca.  $1750 \text{ cm}^{-1}$  of  $\text{Eu}^{3+}$  ion is the largest among  $\text{RE}^{3+}$ , and consequently the hosts doped with it have the largest relative sensitivities.

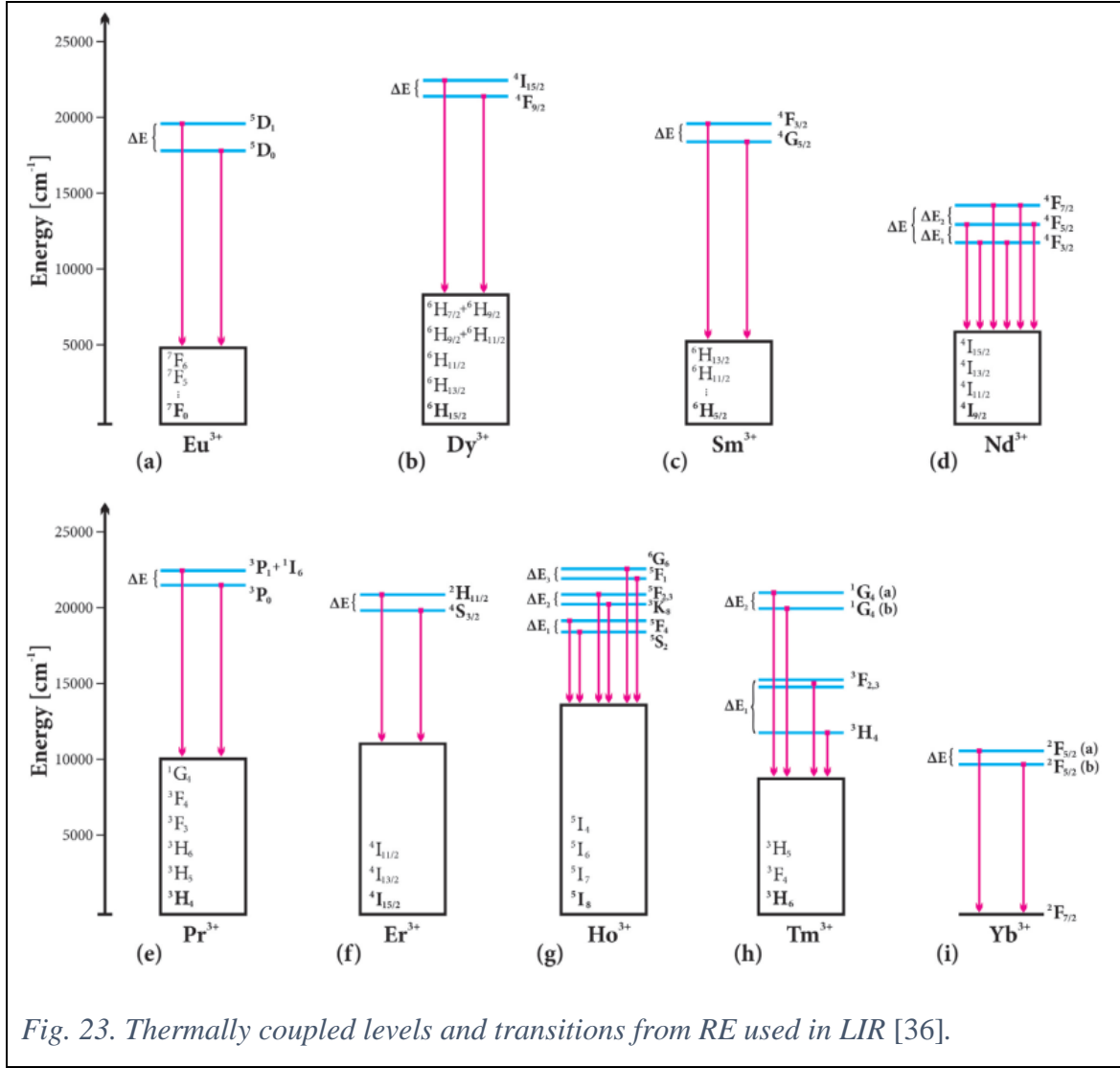


Fig. 23. Thermally coupled levels and transitions from RE used in LIR [36].

### 2.1.3.2. LIR methods from multiple emission centers

LIR can be used with any combination of emissions that originate from one or more emission centers (but without the powerful theoretical tool that lies in employing the Boltzmann distribution on the thermally coupled levels). The simplest case would be if one transition has a relatively constant intensity with temperature, thus it may be used as a reference transition ( $I_R$ ). Then LIR would have the same trend as a temperature dependence of the excited-state lifetime [59]:

$$LIR(T) = \frac{I(T)}{I_{ref}} = \frac{C}{I_{ref}} A_R \tau_{obs} = \frac{C}{I_{ref}} \frac{A_R}{A_R + A_{NR}} \quad (2.1.14)$$

This can be achieved in host materials whose trap emission can serve as a reference.

### 2.1.3.3. LIR experiment

LIR thermometry requires only a simple instrumentation which usually consists of a spectrofluorometer, and a heating/cooling apparatus. Heating and cooling during testing can be achieved by placing a sample on a hot/cold plate or inside an oven/refrigerator. The temperature of the sample should be monitored independently by a reference thermometer [52,61]. Since luminescence thermometry needs to be calibrated against a temperature standard, its accuracy is limited by this reference. Most often, a thermocouple is used as a reference sensor [12], but better results can be obtained by using an RTD. This is most often performed in a temperature controlled calibration cell. Instead of the spectrofluorometer, the two photodiodes with filters can be employed for measuring the peak intensities of interest. The commercial fiber optic solution of that type is presented in Fig. 24.

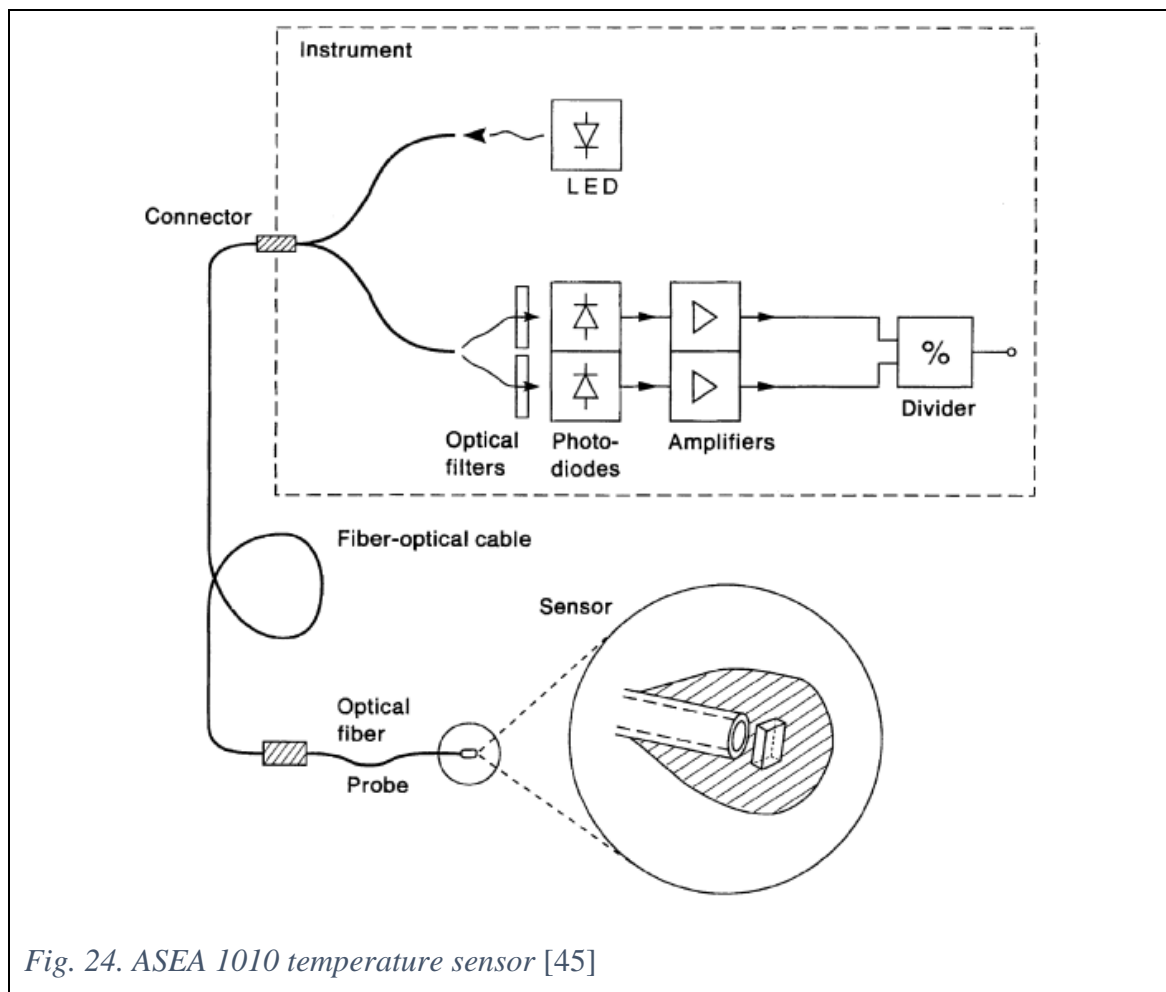


Fig. 24. ASEA 1010 temperature sensor [45]

In the ratiometric intensity measurements the reference intensity of the second band ideally responds to temperature in the opposite direction than the other observed transition [42]. The ratio of the intensities then follows the Boltzmann distribution as stated in equation 2.1.12. In practice, several effects can cause a deviation of the measured LIR from the Boltzmann distribution: overlapping of fluorescence peaks of the two individual thermally coupled levels, and stray light from other energy levels or the excitation source. Then the experimental data can be analyzed by adding an offset to the Boltzmann distribution [52]:

$$LIR = \frac{n_H}{n_L} B \exp\left(-\frac{\Delta E}{kT}\right) + \frac{m_L}{n_L} \quad (2.1.15)$$

where  $n_i$  is the fraction of the total fluorescence intensity of the transition originating from level  $i$  actually measured by the detector, and  $m_L$  is the fraction of the total intensity from the lower level measured by the detector for the other thermalizing level.

Frequently the experimentally estimated value of energy difference deviates from the theoretically obtained value. The large difference would imply a measurement error or that some other mechanism apart from the Boltzmann distribution takes place as the temperature increases, such can be energy transfers between thermally coupled levels or other levels or CTB [36].

#### 2.1.4. Time-resolved methods

The time-resolved measurements of interest are the measurements of emission decay and rise times or the phase shift. The former belongs to the time-domain, which uses pulsed excitation sources, and the latter to the frequency-domain method, which uses the intensity-modulated continuous wave light sources (see Fig. 27).

##### 2.1.4.1. Decay-time sensing

The luminescence intensity following a pulsed excitation ideally can be approximated by a mono-exponential decay [12,44]:  $I=I_0 \cdot \exp(-t/\tau_{obs})$ . The temperature dependence of the observable lifetime can be obtained from equation 2.1.2 [56].

Starting at low temperatures,  $A_{NR}$  approaches zero, thus the observable lifetime is approximately equal to the radiative lifetime. By rising temperature, radiative lifetime slightly changes by:

$$\tau = \tau_0 \exp(-\alpha T) \quad (2.1.16)$$

where  $\alpha$  is the phenomenological parameter of order less than  $10^{-4} \text{ K}^{-1}$ . This read-out method is unusable at that temperature range. At some point, the non-radiative rates increase drastically, which leads to a fast decline of the observable lifetime, with a very high sensitivity values. The temperature of that point depends upon the energy difference between RE excited level and the closest lower energy level or CTB, and on the phonon energy of the host material. Lifetimes as a function of temperature in various materials are given in Fig. 25.

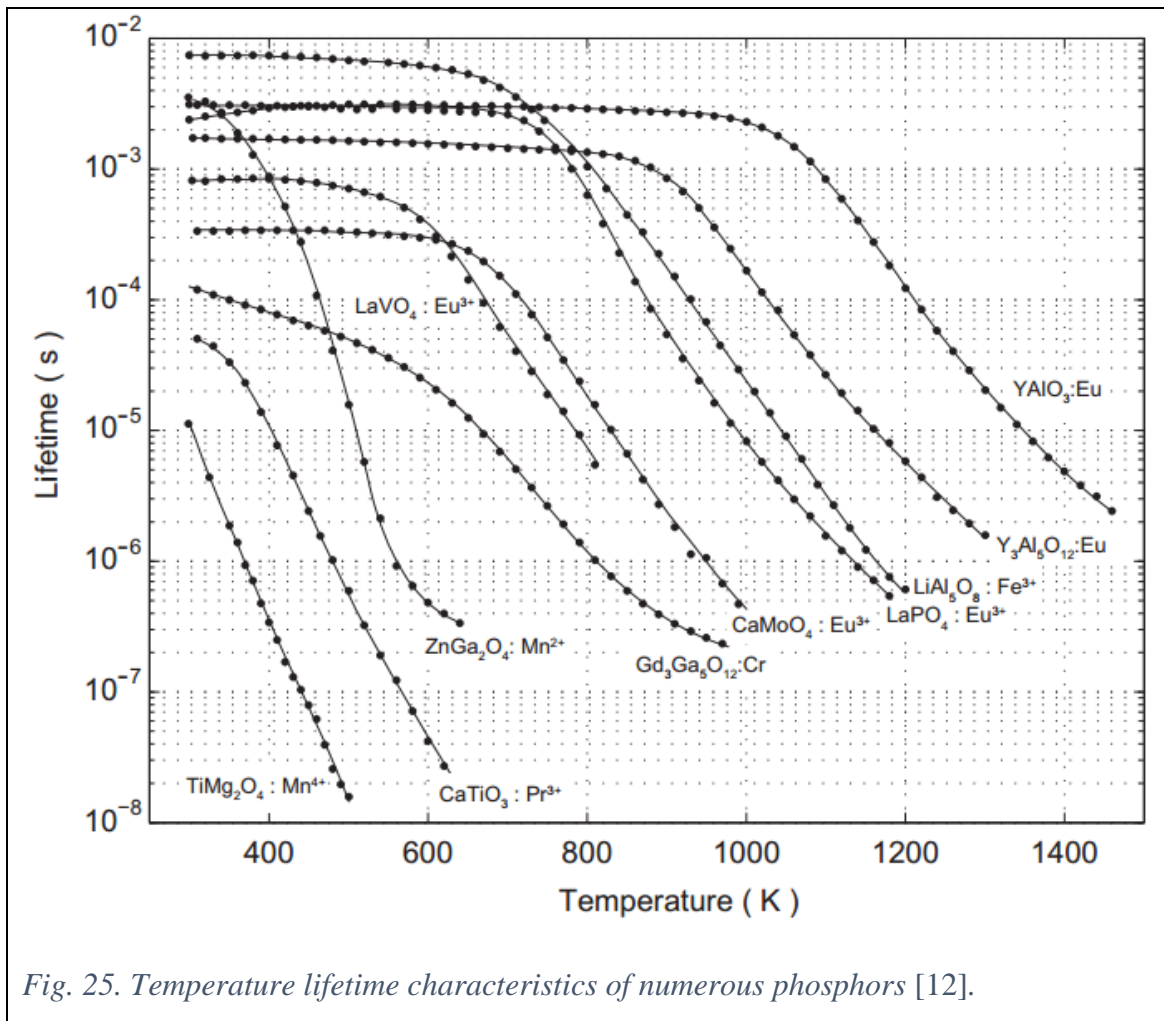


Fig. 25. Temperature lifetime characteristics of numerous phosphors [12].

#### 2.1.4.2. Rise-time sensing

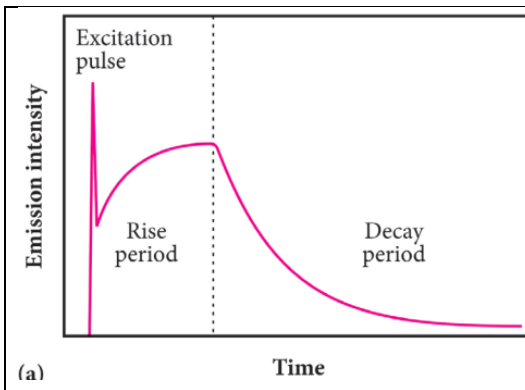
Emission following pulse excitation has shape as presented in Fig. 26. In the first time period the emission resembles the excitation pulse, in second, the emission rises because of the rise of population in the excited level, and the third period is marked by an

exponential decay. The first and the second period together mark a rise-time, which is temperature dependent.

The population can be described as:

$$N = N_0 + N_1 \left( 1 - \exp\left(-\frac{t}{\tau_r}\right) \right) \quad (2.1.17)$$

where  $N_0$  is the population directly excited within the ion,  $N_1$  the population obtained from the neighboring ions, and  $\tau_r$  is a rise-time constant. The rise-time constant is the time until the emission intensity reaches  $1-1/e$  of its maximum value.



(a) Fig. 26. Emission intensity following the excitation pulse [36].

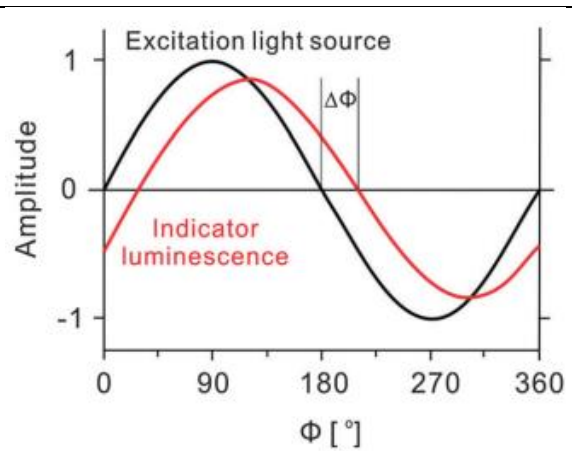


Fig. 27. Frequency domain method [42].

#### 2.1.4.3. Frequency-domain method

In this method the excitation is done with sinusoidal amplitude modulated light source with modulation frequencies ranging from  $0.1$  to  $10 \cdot \tau_{obs}$ . Then the emission follows the excitation, but with a phase shift (Fig. 27). The decay time can be determined from the phase shift by:

$$\tau_{obs} = \frac{\tan \Delta\Phi}{2\pi f_{mod}} \quad (2.1.18)$$

where the phase shift is given by  $\Delta\Phi$  and  $f_{mod}$  is the modulation frequency of the excitation. This method can provide accurate measurements.

### 2.1.5. Comparison of LIR and time-resolved methods

Both LIR and time-resolved techniques show considerable promise and have been studied in detail for a range of materials [38]. Both techniques result in a quantity independent of the source intensity.

#### **Pro's for LIR:**

- Lifetime methods are intrinsically referenced and concentration independent, however they require a more sophisticated read-out apparatus [42], i.e. LIR needs a cheaper equipment [61,62].
- Another complication is the multi-exponential dependence of the decay times of many phosphors.
- LIR is better for fast moving objects and for creating temperature maps. For creating temperature maps a high speed cameras would be necessary for a time-resolved methods [12].
- LIR have larger relative sensitivities than time-integrated methods [62].
- LIR has a greater dynamic temperature range [62].

#### **Pro's for time-resolved:**

- Time-resolved transient signal waveforms are detectable with greater reproducibility than the LIR, which is due to the better controllable temporal functions of the detection system comparing to the spectral ones [12]. In other words, the uncertainties in decay times are generally smaller than in emission intensities, thus the decay-time methods have better temperature resolutions and higher high-temperature bound [42].
- Pulsed excitation and subsequent temperature dependent fluorescence decay from the excited level can be monitored by a single detector [38].
- By using delayed detections the problems that compromises LIR can be overcome, such as a strong background luminescence [62].

## 2.2. Ti, Zr, Hf and Nb oxides doped with $\text{Eu}^{3+}$ ion

### 2.2.1. The importance and current applications

The choice of the base metals for creating samples by PEO had fallen on titanium, zirconium, hafnium and niobium, for creating the  $\text{TiO}_2$ ,  $\text{ZrO}_2$ ,  $\text{HfO}_2$  and  $\text{Nb}_2\text{O}_5$  oxides, respectively, because of their excellent chemical, physical, electrical, mechanical and optical properties [63,64], high dielectric constant, high melting point, low thermal conductivity, high pH stability, high refractive indexes, large band-gaps, low optical loss and high transparency in the visible and NIR regions [4,11]. They are used in solar cell applications, structural ceramics, biocompatible materials [6], as optical coatings, sensors or catalysts [9].

Titanium dioxide has a great potential to be employed for ecological purposes, due to its high photocatalytic activity. Niobium pentoxide is being used in capacitors and optical glasses. Zirconium and hafnium dioxides are studied as possible high- $\kappa$  oxide materials for future microelectronic circuits [65]. Zirconia is additionally used for optical filters and laser mirrors [66].

At hypersonic speeds the metal alloys undergo drastic reductions in strength and oxidize rapidly. The selection of materials for the task is influenced mainly by the temperature profile the vehicle experiences (see Fig. 28.) in order to maintain the structural integrity. The only materials that satisfy the given conditions are ceramics (see Fig. 29), the protective coatings resulting from the oxidation of the base metal. The extreme temperatures limit the oxides that can be used to thoria, hafnia and zirconia. They have the highest melting temperatures among the oxides and low reactivity with most metals [67].

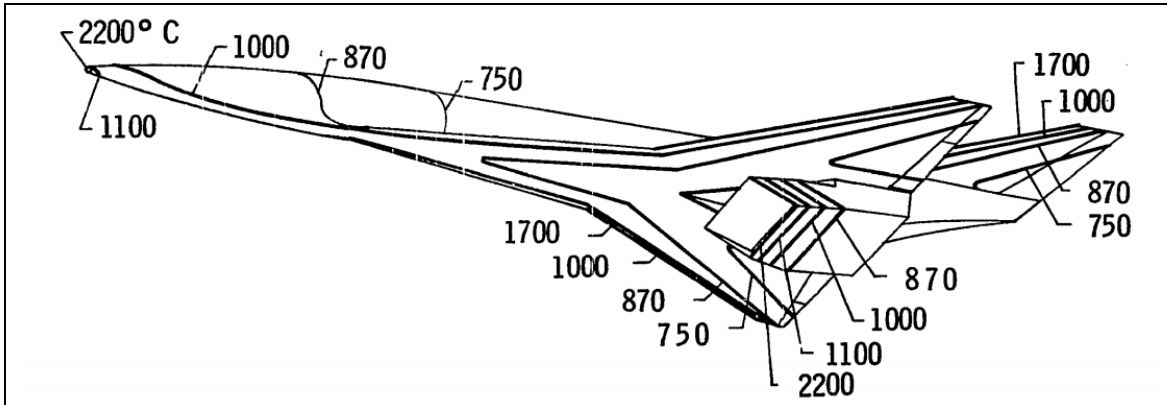


Fig. 28. Surface temperatures during flight at hypersonic speeds [67]

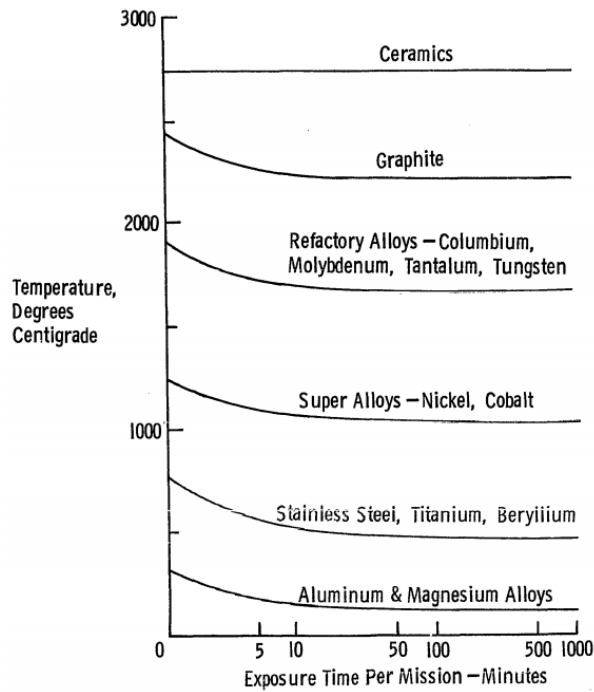


Fig. 29. Temperature capabilities for various structural materials [67]

Hafnia has even higher melting point, greater thermal conductivity and lower thermal expansion than zirconia. It exhibits a phase transformation from monoclinic to tetragonal at much higher temperatures, at ca. 1700 °C, followed by the increase in density by 3.4%, while zirconia density increases by 7.5%. Thus, hafnia has less destructive volume change with temperature related phase transformation. Because of its superior properties, hafnia has become more and more interesting material since the dawn of the space age [67].

Furthermore, HfO<sub>2</sub> enhances the capacitive density of capacitors by reducing the leakage current, which is due its high thermal stability, high breakdown electric field (ca. 8.5 MV/cm), high dielectric constant and wide energy gap. Its high refractive index and large band gap have been utilized for optical coatings for astronomical CCD [68] and IR optical devices. As a high-κ dielectric it is employed as a replacement for SiO<sub>2</sub> in CMOS applications [68,69] as the gate dielectric material [70]. It is also an efficient absorbent of the gamma rays and X-rays [71,72].

Niobium pentoxide is suitable for a wide range of applications in the construction of gas sensing, electro-chromic displays and photoelectrodes, as well as in field-emission displays and microelectronics. It also has remarkable photocatalytic properties [73].

Relatively low phonon frequency of the materials in question makes them an ideal matrix component for preparation of highly luminescent materials by doping with rare earth metals.

### 2.2.2. Crystal structures

Each of the chosen oxides exhibits different phases under different conditions (temperature and doping concentration of impurities). Each phase is represented by a different space group. The valence of the metal ions in oxides are as follows: dioxides formed with group 4 elements are 4-valent in bulk, and 3-valent on the surface, pentoxides with group 5 elements are 5-valent in bulk. By substituting the host metal ion by an impurity, the mismatch of the ionic radii and charge balance perturb the crystal lattice. Thus, another symmetry is attributed to the site symmetry of the host metal ion.

The percentage difference in ion radii between doped and substituted ions must not exceed 30%. The radius percentage difference ( $D_r$ ) between the Eu<sup>3+</sup> and the substituted host metal ion can be calculated by the following formula [74]:

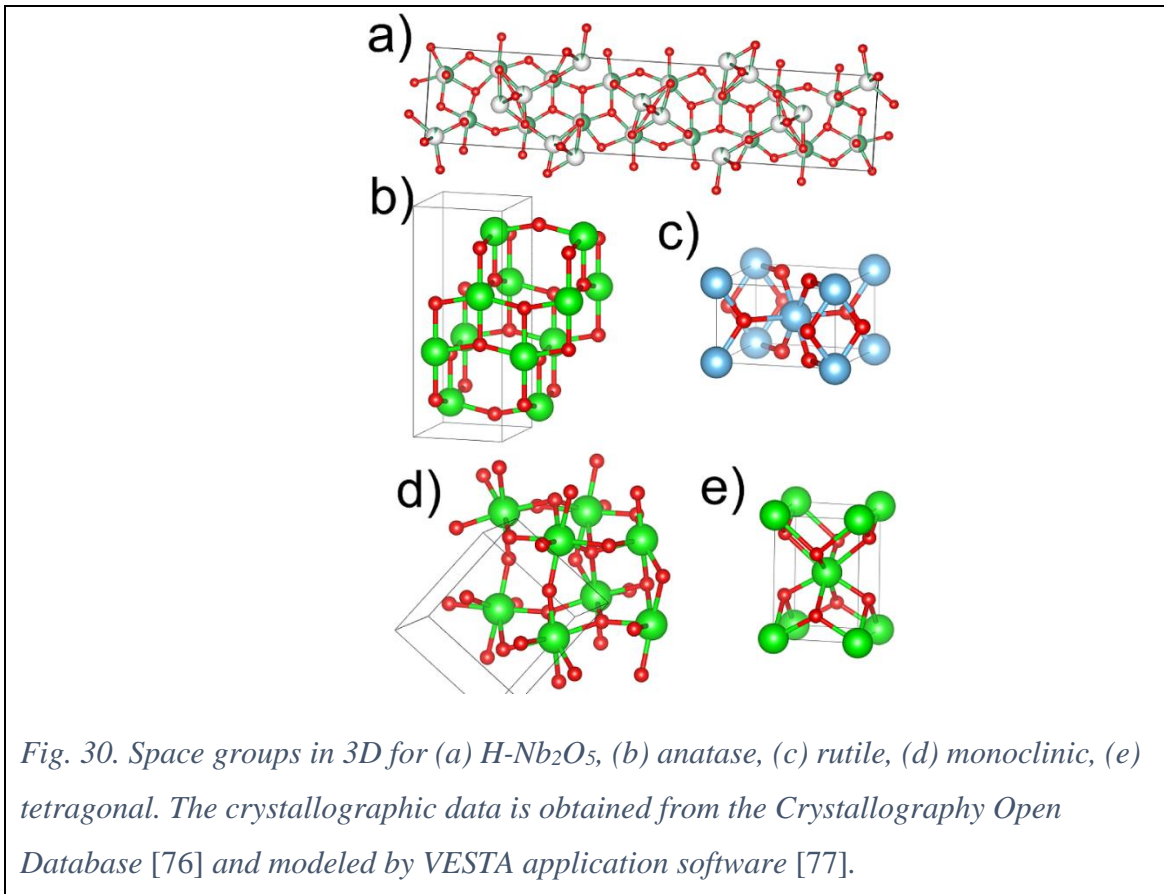
$$D_r = \frac{R_m(CN) - R_d(CN)}{R_m(CN)} \quad (2.2.1)$$

where  $CN$  is the coordination number,  $R_m$  is the host ion radius, and  $R_d$  is the doped ion radius.

Europium ion has larger ionic radii than host metal ions of the investigated oxides. Thus, when it substitutes the host metal in its site, due to the mismatch of the radii and charge imbalance, the symmetry of the  $\text{Eu}^{3+}$  site gets lowered than the symmetry of the host metal site, lattice parameters change, and the transformation is followed by the creation of the oxygen vacancies.

#### 2.2.2.1. $\text{TiO}_2:\text{Eu}^{3+}$

Titanium dioxide applications highly depend on its crystalline structure and morphology. Three most abundant crystalline phases are anatase (tetragonal space group  $I4_1/amdm$ , in Schoenflies notation  $D_{4h}$ ), rutile (tetragonal  $P4_2/mnm$ , in Schoenflies notation  $D_{4h}$ ) and brookite ( $Pbca$ , in Schoenflies notation  $D_{2d}$ ) (see Fig. 30bc). Rutile phase is denser and thermodynamically more stable than anatase, but is not favorable for formation of nanoparticles. In contrast, anatase has better photocatalytic properties [75].



At terminal planes of the crystal, titanium ions are trivalent, while in crystal volume they are  $Ti^{4+}$ . Surface Ti atoms adjust their coordination environment, favoring the formation of  $Ti^{3+}$ , which becomes apparent more with decreasing the particle's size to nanoparticles. In anatase phase,  $Ti^{4+}$  ions have 6-fold ligand coordination number and are at the center of the  $D_{2d}$  distorted octahedron. There are three possible sites that can incorporate  $Eu^{3+}$  ion. Two sites are reduced from original  $D_{2d}$  symmetry to either  $D_2$ , when  $Eu^{3+}$  substitutes  $Ti^{4+}$ , and to  $C_{2v}$  when it substitutes a vacancy. The third site is with  $C_1$  symmetry at the surface, when  $Ti^{3+}$  is replaced by  $Eu^{3+}$  [75].

#### 2.2.2.2. $ZrO_2:Eu^{3+}$ and $HfO_2:Eu^{3+}$

The structures formed by zirconium dioxide and hafnium dioxide (even when doped with RE), are almost identical [78], the main difference is in larger ionic radius of the latter. Thus they exhibit the same phases (although at different temperatures). Zirconium and hafnium are often found in the same ore, and in our samples they represent the most of the impurities (especially in hafnium foil, which is 97% pure hafnium and almost 3% zirconium) [10].

The main structural difference between their phases is given by the displacements of the lattice oxygen atoms [79]. Zirconium<sup>4</sup> dioxide main phases are monoclinic ( $P2_1/c$ , in Schoenflies notation  $C_{2h}$ ) m- $ZrO_2$ , tetragonal ( $P4_2/nmc$  [80], in Schoenflies notation  $D_{4h}$ ) t- $ZrO_2$ , and ( $Fm\bar{3}m$  [81], Schoenflies  $O_h$ ) cubic c- $ZrO_2$ . Orthorhombic phase ( $Pca2_1$ , Schoenflies  $C_{2v}$  [82]) o- $ZrO_2$  is a metastable phase [83].

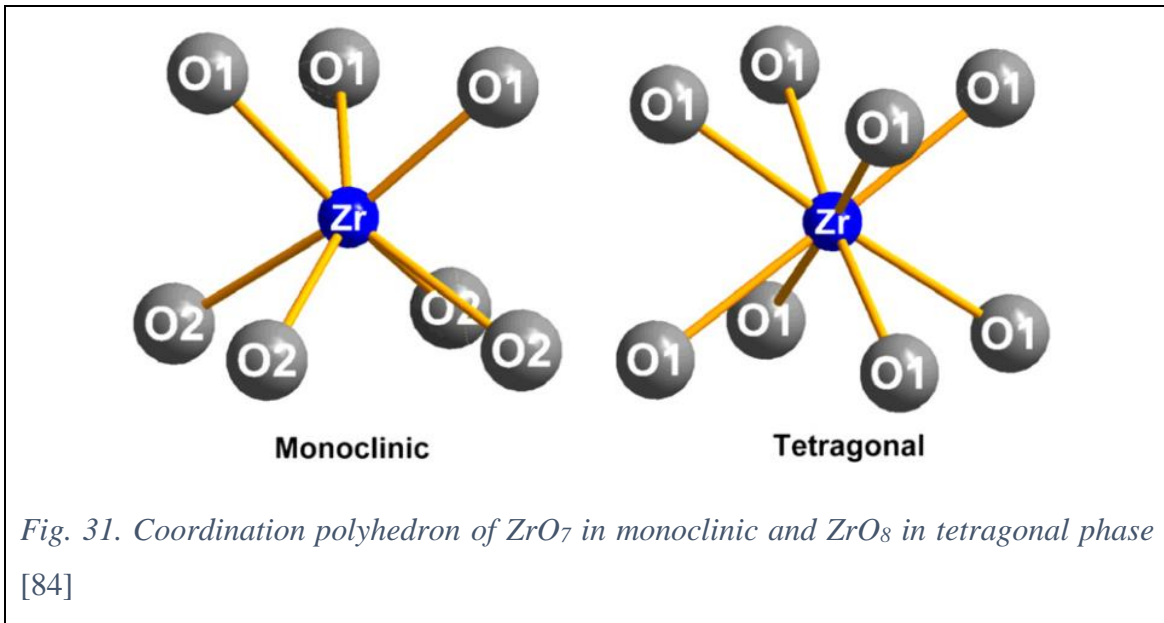
At ambient pressure zirconia cubic phase appears at temperatures above 2370 °C, tetragonal between 1170 °C and 2370 °C, and monoclinic below 1170 °C [4]. As for the hafnia, tetragonal phase appears by heating above 1700 °C, while the cubic phase appears at 2200 °C [10].

In the crystal structure of tetragonal zirconia,  $Zr^{4+}$  ions are 8-fold coordinated to oxygen atoms in  $D_{2d}$  symmetry, with inversion symmetry [81,84]; in monoclinic, each  $Zr^{4+}$  is in 7-fold coordination [85] ( $C_s$  symmetry) with oxygen atoms [83], as shown in Fig. 31.  $Zr^{4+}$  cations are surrounded by a tetrahedron with four oxygen atoms and a trigon with three oxygen atoms, all of them with different bond lengths and angles. The shortest

---

<sup>4</sup> The same applies for hafnia, here and in further text, unless stated otherwise.

Zr-O distance in the coordination polyhedron lies in range from 204 pm to 226 pm [86]. In tetragonal, it is a distorted octahedron structure with four oxygen atoms at a distance 245 pm, and another four at 206 pm from the central ion [87]. For both hafnia and zirconia, monoclinic phase is the most stable [72]. The structure of the amorphous  $ZrO_2$  is similar to that of the disordered monoclinic phase [79]. Tetragonal zirconia has cations at 2b positions (0.75, 0.25, 0.25) and the anions in the 4d positions (0.25, 0.25, 0.45), with unit cell volume of pure t- $ZrO_2$  ca. 0.067 nm<sup>3</sup>[88].

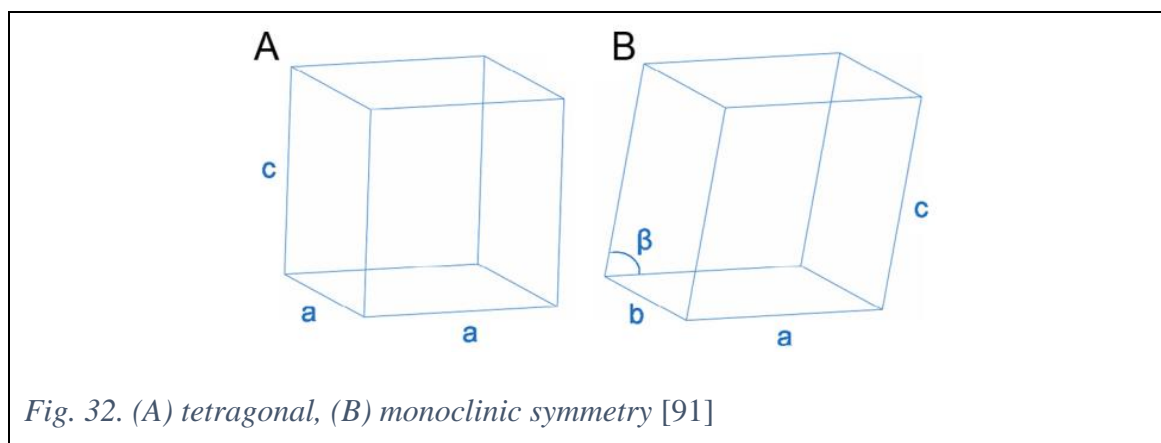


Due to the mismatch of ionic radii and the charge imbalance between  $Zr^{4+}$  (89 pm) and  $Eu^{3+}$  (107 pm) the substitution creates oxygen vacancies and causes a lattice distortion [4]. Stark splitting for  $^5D_0 \rightarrow ^7F_1$  4f-4f transition of europium are 200 cm<sup>-1</sup> and 20 cm<sup>-1</sup> for m- $ZrO_2:Eu^{3+}$  and t- $ZrO_2:Eu^{3+}$ , respectively. Because the CF splitting of J-manifolds is a linear function of the CF strength parameters, these values evidence for different CF strengths of different symmetries [79]. Zirconia and hafnia doped with europium species morph from the  $C_s$  to the low  $C_1$  local symmetry [79]. In c- $ZrO_2$   $Eu^{3+}$  occupy  $D_{2h}$  or  $D_{4h}$  sites [89].

Doping concentration with rare-earths is proportional to the amount of tetragonal zirconia [89] stabilized at room temperature, at the expense of the monoclinic zirconia. Up to 8 mol% the  $ZrO_2$  has both phases, while above it features a pure tetragonal phase [81]. The stabilization of structures from monoclinic to tetragonal is attributed to the

substitution of  $Zr^{4+}$  by  $Eu^{3+}$ , i.e. by the oxygen vacancy created because of the charge difference compensation [90].

Both hafnia and zirconia belong to the same space groups and show relatively small differences in their lattice constants. The parameters in Ref. [67] state the lattice parameters for monoclinic zirconia:  $a = 521$  pm,  $b = 526$  pm,  $c = 537$  pm,  $\beta = 99^\circ 58'$ ; for hafnia:  $a = 511$  pm,  $b = 514$  pm,  $c = 528$  pm,  $\beta = 99^\circ 44'$ . The tetragonal hafnia has lattice parameters  $a = 514$  pm,  $b = 525$  pm, and density  $10.01$  g/cm<sup>3</sup>. Cubic hafnia  $a = 530$  pm. According to another reference, monoclinic lattice constants are:  $a = 515$  pm,  $b = 521$  pm,  $c = 531$  pm,  $\beta = 80.77^\circ$ , tetragonal:  $a = 507$  pm,  $b = 516$  pm (see Fig. 32) [91]. According to the Ref. [81] the lattice parameters of  $800^\circ\text{C}$  annealed sample based on  $m\text{-ZrO}_2$  has lattice parameters  $a = 527$  pm,  $b = 503$  pm,  $c = 547$  pm,  $\beta = 95.0^\circ$  while annealed at  $1000^\circ\text{C}$  has  $a = 514$  pm,  $b = 521$  pm,  $c = 531$  pm,  $\beta = 99.2^\circ$  [81]. Orthorhombic lattice parameters are  $a = 526$  pm,  $b = 507$  pm and  $c = 508$  pm [82]. See Fig. 33. for visual representation of the various phases of zirconia and hafnia, and Table 1 for parameters depending on the concentration of doped europium. By doping with europium the average volume of the unit cell increases, e.g. volume of the unit cell of  $\text{HfO}_2:\text{Eu}^{3+}$  is higher than the pure hafnia, which happens because of the larger ionic radii of the  $\text{Eu}^{3+}$  comparing to the  $\text{Hf}^{4+}$  (76 pm) [92].



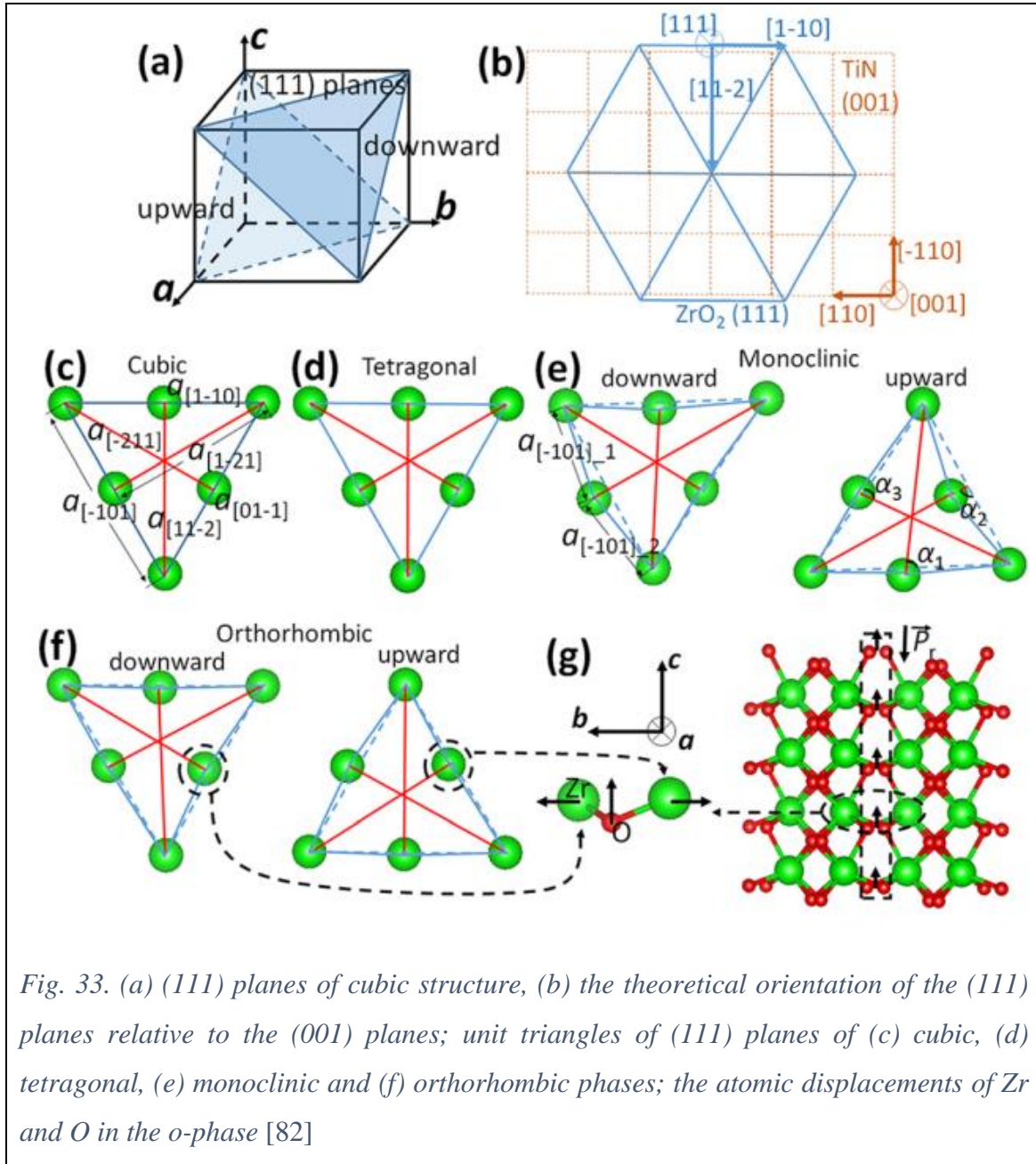


Fig. 33. (a) (111) planes of cubic structure, (b) the theoretical orientation of the (111) planes relative to the (001) planes; unit triangles of (111) planes of (c) cubic, (d) tetragonal, (e) monoclinic and (f) orthorhombic phases; the atomic displacements of Zr and O in the o-phase [82]

Table 1. Lattice parameters depending on various concentrations of doped europium in tetragonal and monoclinic phases [93]

$a$ (Å)	Tetragonal phase				Monoclinic phase				
	$c$ (Å)	%wt	$2V_{\text{cell}}$	% <sub>at</sub> Eu	$a$ (Å)	$b$ (Å)	$c$ (Å)	$\beta$ (°)	%wt
3.6047 (2)	5.1841 (4)	100. ± 0.0	134.72 (2)	3.92 (9)	–	–	–	–	0.0 ± 0.0
3.6053 (1)	5.1843 (2)	70.0 ± 1.0	134.77 (1)	4.15 (9)	5.164 (1)	5.206 (1)	5.325 (1)	98.70 (1)	30.0 ± 0.1
3.6055 (1)	5.1841 (3)	58.8 ± 0.3	134.78 (3)	4.19 (9)	5.1623 (7)	5.2052 (9)	5.3229 (8)	98.630 (8)	41.2 ± 0.1
3.6059 (2)	5.1838 (4)	45.9 ± 0.3	134.80 (2)	4.28 (9)	5.1595 (7)	5.2069 (8)	5.3223 (8)	98.780 (7)	54.1 ± 0.1
3.6062 (3)	5.1841 (6)	37.3 ± 0.7	134.84 (3)	4.4 (1)	5.1604 (7)	5.2072 (8)	5.3208 (8)	98.822 (7)	62.7 ± 0.1
3.612 (1)	5.172 (3)	18.9 ± 0.8	134.9 (1)	5.0 (3)	5.1603 (6)	5.2086 (7)	5.3211 (7)	98.912 (6)	81.1 ± 0.1

### 2.2.2.3. $Nb_2O_5:Eu^{3+}$

The main phases of niobium pentoxide are the low temperature pseudo-hexagonal TT-Nb<sub>2</sub>O<sub>5</sub>, orthorhombic T-Nb<sub>2</sub>O<sub>5</sub> ( $\gamma$ -Nb<sub>2</sub>O<sub>5</sub>) at 600 °C - 800°C and monoclinic H-Nb<sub>2</sub>O<sub>5</sub> ( $\alpha$ -Nb<sub>2</sub>O<sub>5</sub>) (Fig. 30a) and M-Nb<sub>2</sub>O<sub>5</sub> ( $\beta$ -Nb<sub>2</sub>O<sub>5</sub>) at above 1173 °C. The H-Nb<sub>2</sub>O<sub>5</sub> is the only stable structure [73,94].

T-Nb<sub>2</sub>O<sub>5</sub> net parameters are: a = 617 pm, b = 293 pm, c = 394 pm. Its crystalline structure consists of 4 x 4 blocks of corner-shared NbO<sub>6</sub> octahedron [73]. Monoclinic phase is of space group P2 (in Schoenflies notation C<sub>2</sub>), with 14 formula units in the cell with parameters: a = 2116 pm, b = 382 pm, c = 1935 pm and  $\beta = 119^\circ 50'$  [95].

The pseudo-hexagonal TT-Nb<sub>2</sub>O<sub>5</sub> phase, is a less crystalline form of orthorhombic T-Nb<sub>2</sub>O<sub>5</sub> phase. The TT-Nb<sub>2</sub>O<sub>5</sub> phase can be stabilized by doping with rare earth elements [9].

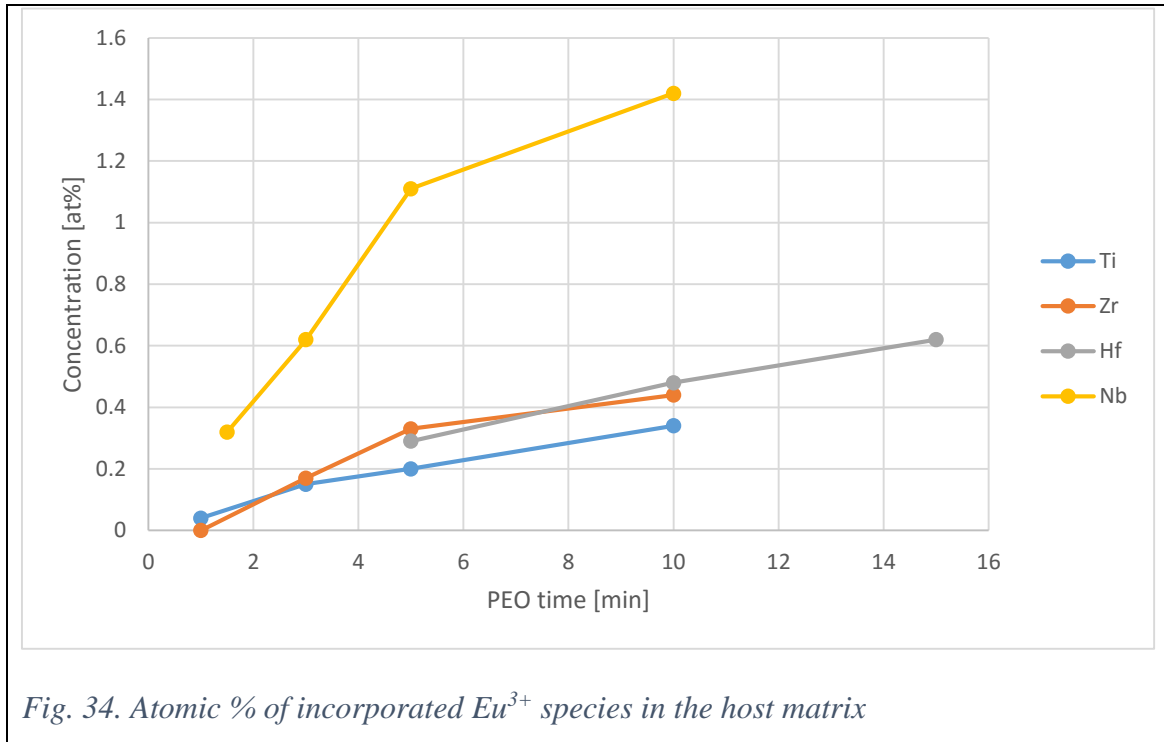
### 2.2.3. PEO

The beginning of the PEO process is related to the classical anodization and growth of barrier oxide coating, characterized by almost linear increase of voltage up to ca. 270 V. Oxide coatings are formed at metal/oxide and oxide/electrolyte fronts due to migrations of host metal cations at the metal/oxide front and O<sup>2-</sup>/OH<sup>-</sup> at the oxide/electrolyte front.

Initial oxide layer forms on the surface of titanium as a result of the following overall reaction:  $Ti + 2H_2O \rightarrow TiO_2 + 4H^+ + 4e^-$  [6]. Analogous process goes for other group IV elements. The overall reaction of the process on niobium is:  $2Nb + 5H_2O \rightarrow Nb_2O_5 + 10H^+ + 10e^-$  [9].

The uniform thickening is terminated by dielectric breakdown, and further anodization results in a stable voltage while discharging continues. Due to the strong electric fields, anionic components of electrolyte are drawn into the channels. Metal substrate is melted out and gets oxidized, while Eu<sub>2</sub>O<sub>3</sub> particles melt inside the discharge channels (Eu<sub>2</sub>O<sub>3</sub> melting point is at ca. 2620 K, much lower than the temperature of the plasma at microdischarge channels (ca. 10<sup>4</sup> K)). Molten Eu<sub>2</sub>O<sub>3</sub> reacts with other components from the electrolyte and the substrate to form mixed-oxide coatings. After

the short-living discharging, molten regions rapidly cool in contact with the surrounding electrolyte and the quenching leads to the formation of oxides composed of the substrate and electrolyte [4]. By the repetition of the process, the oxide thickness increases, at the growth rate of ca. 1.5  $\mu\text{m}/\text{min}$  [6]. After ca. 200 s, voltage reaches a stable value of 460 V. The number of microdischarges reduces with increasing PEO time [9]. Eu content in the coatings increases with PEO time (Fig. 34.).



SEM images clearly show the morphologies of the oxide surfaces (see Fig. 35.).

### 2.2.3.1. $\text{ZrO}_2:\text{Eu}^{3+}$

At the beginning of PEO, microdischarges are very intense. At high temperatures at the microdischarge sites the cubic phase is created. During the cooling process, molten material undergoes phase transformations from cubic to tetragonal, and from tetragonal to monoclinic. Microdischarges generate high concentration of defects, such as oxygen vacancies, which could lead to the stabilization of the tetragonal phase. As the time progresses, the number of microdischarges decreases, which results in lowering the local temperature around microdischarge sites – a condition suitable for the formation of the monoclinic phase [4], with a consequence of overall toughening of the material (with the volumetric expansion of about 4%) [85]. RE can stabilize the tetragonal phase, but if the

concentration is low, not whole sample will be stabilized [4], and the fraction of the tetragonal phase which is poorer in europium undergoes the transformation process to the monoclinic phase first [85]. The crystallite size of m-ZrO<sub>2</sub> increases with PEO time [4].

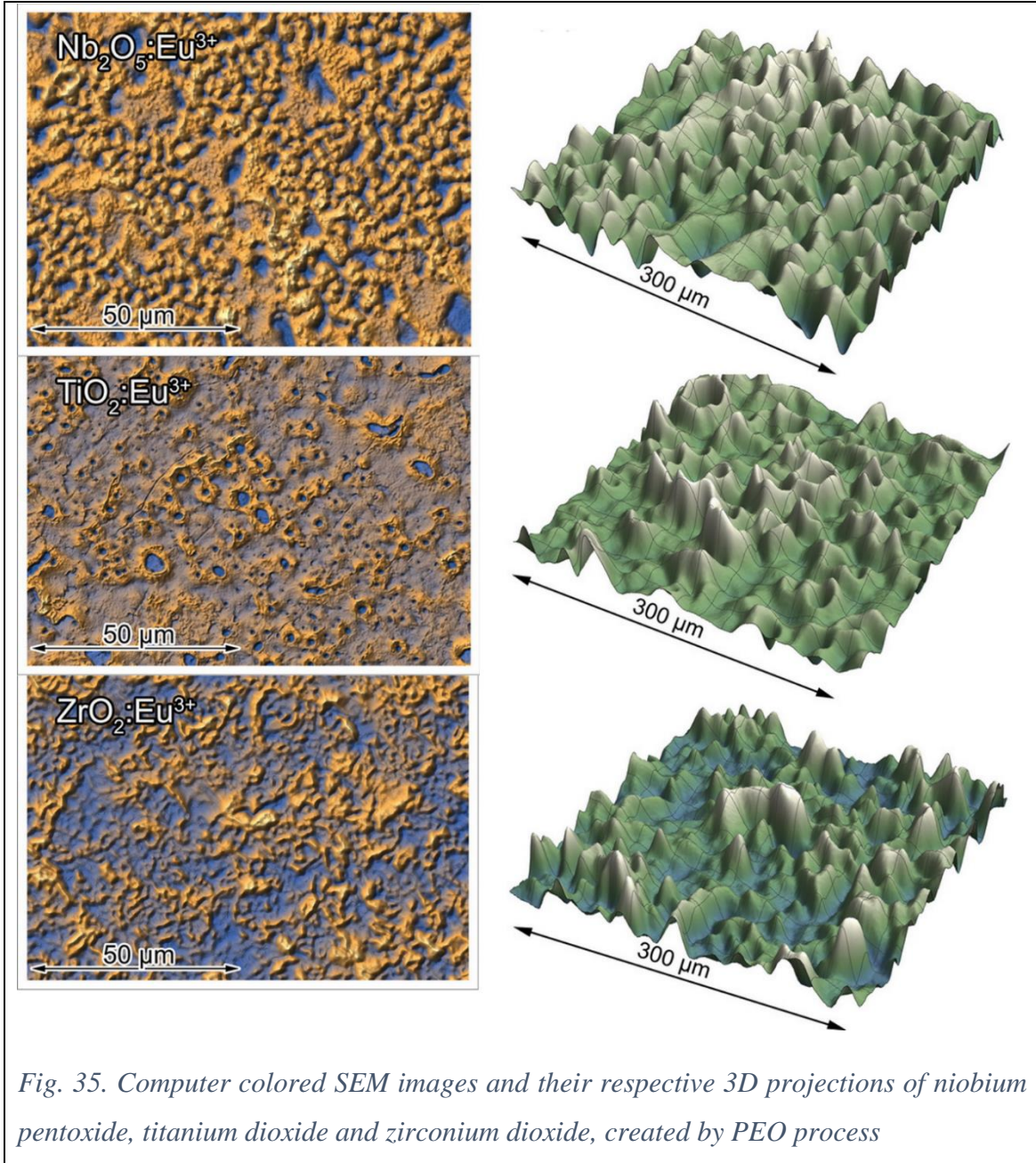


*Fig. 35. Computer colored SEM images and their respective 3D projections of niobium pentoxide, titanium dioxide and zirconium dioxide, created by PEO process*

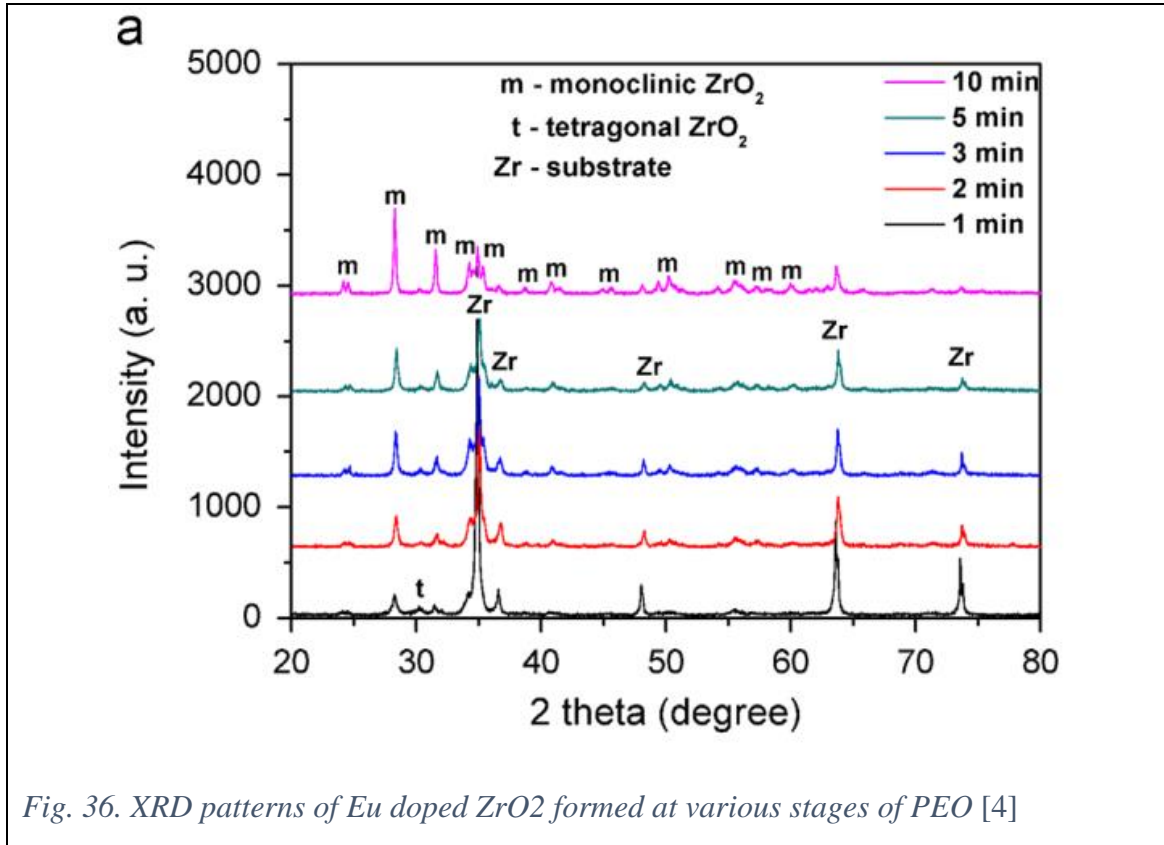


Fig. 36. XRD patterns of Eu doped ZrO<sub>2</sub> formed at various stages of PEO [4]

The main observed phase is monoclinic (m-ZrO<sub>2</sub>) and there is one peak for the tetragonal (t-ZrO<sub>2</sub>) phase for zirconia created by 10 min PEO process [81]. The cubic ZrO<sub>2</sub> phase (c-ZrO<sub>2</sub>) was not detected. The main monoclinic peaks are centered at 28.17° (-1 1 1)<sub>m</sub> and 31.38° (1 1 1)<sub>m</sub>. The tetragonal peak is observed at 30.93° (1 0 1)<sub>t</sub> [96] (see Fig. 36). The monoclinic fraction is defined by the following equation [96]:

$$X_m = \frac{I(1\ 1\ \bar{1})_m + I(1\ 1\ 1)_m}{I(1\ 1\ \bar{1})_m + I(1\ 1\ 1)_m + I(1\ 1\ 1)_t} \quad (2.2.2)$$

#### 2.2.3.2. Nb<sub>2</sub>O<sub>5</sub>:Eu<sup>3+</sup>

The niobium pentoxide coatings created by the PEO process are partially crystallized and composed of pseudo-hexagonal TT-Nb<sub>2</sub>O<sub>5</sub> phase, which is a less crystalline form of orthorhombic T-Nb<sub>2</sub>O<sub>5</sub> phase (see Fig. 37.).

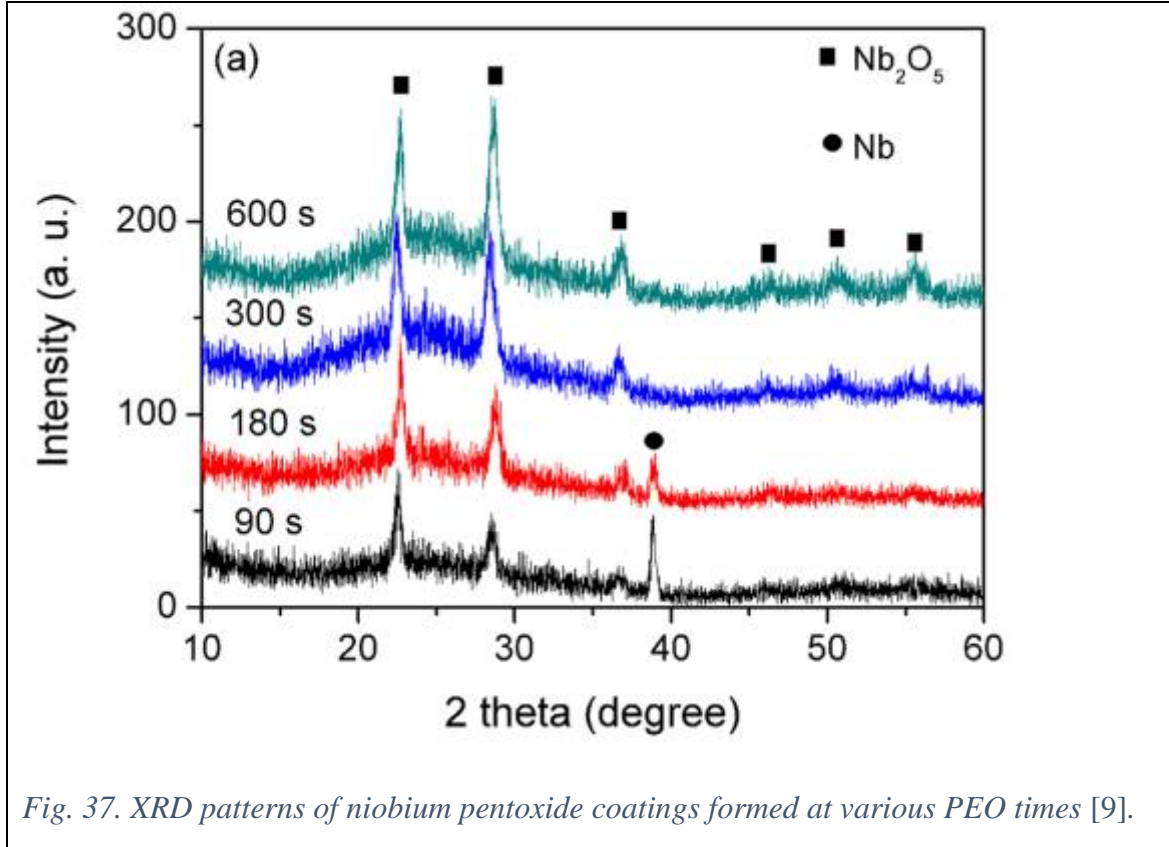


Fig. 37. XRD patterns of niobium pentoxide coatings formed at various PEO times [9].

### 2.2.3.3. $TiO_2:Eu^{3+}$

From the XRD analysis of PEO created titanium dioxide coatings (see Fig. 38), evident is the existence of anatase and rutile phases, anatase being the dominant phase. Rutile content increases with PEO time, which suggests that the crystallization increases with PEO time. Incorporation of  $Eu^{3+}$  does not significantly change the phase structure. The weight function of rutile phase is given by [6]:

$$W_R = \frac{I_R}{0.884 I_A + I_R} \quad (2.2.3)$$

Crystallite sizes can be calculated by the Scherrer's equation:

$$D = \frac{0.94 \lambda}{\beta \cos \theta} \quad (2.2.4)$$

where  $\beta$  is a full width at half maximum, in radians, and  $\theta$  is Bragg angle, and  $\lambda$  is the wavelength of the incident X-rays. The phase content and crystallite sizes for different PEO times of titanium dioxide are given in Table 2.

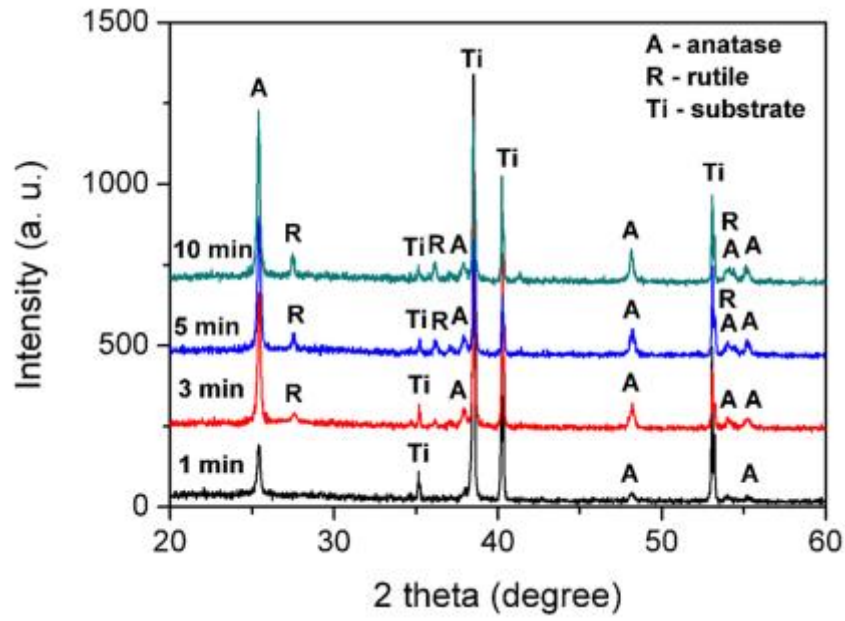


Fig. 38. XRD patterns of  $TiO_2:Eu^{3+}$  formed at various PEO times [6]

Table 2. Weight fractions of anatase and rutile phase and crystallite sizes at various PEO times [6].

PEO time	$W_A$ (%)	$W_R$ (%)	$D_A$ (nm)	$D_R$ (nm)
1 min	100	0	41.7	/
3 min	95.5	4.5	43.3	30.5
5 min	91.1	8.9	46.2	35.6
10 min	87.1	12.9	48.1	44.9

#### 2.2.4. PL

In order to begin a spontaneous emission, some EM field is needed to perturb the electron to induce the charge oscillations and to initiate the radiation process. If the transition is initiated by applied photons the emission is stimulated. The rate at which atoms in some state  $k$  decay to state  $l$  is proportional to the number of photons supplied by the radiation field, which is proportional to photon energy density  $u(\nu)$  and the number of atoms in that state. Since the spontaneous process occurs without supplying radiation, its rate of decay is determined purely by the number of atoms in that state,  $N_k$  [97]:

$$W_{kl} = (A_{kl} + B_{kl}u(\nu))N_k = \omega_{kl}N_k \quad (2.2.5)$$

where  $A$  and  $B$  are the Einstein coefficients.

An interesting behavior of the lanthanide ions is the strong dependence of their luminescence on the site they occupy – the more symmetrical is the site the less allowed their f-f transitions are [85]. Higher symmetry leads to degeneration, while lower symmetry removes the degeneracy and leads to the observation of additional spectral lines [98], which is the case in the investigated oxides.

Excitation spectra of  $\text{Eu}^{3+}$  doped oxides can be divided into two regions (see Fig. 39): one is intense and broad band ranging from 200 nm to 350 nm (with maximum at ca. 250 nm), and another is composed of several sharp peaks from 350 nm to 600 nm. The high-energy band is assigned to the charge-transfer band (CTB), originating from the transition from the completely filled 2p orbital of the oxygen ligands ( $\text{O}^{2-}$ ) to the empty states of 4f configuration of europium ion [55,99,100]. The high intensity of the CTB band indicates a very efficient energy transfer mechanism. The position of CT band is related closely to the covalence between  $\text{O}^{2-}$  and  $\text{Eu}^{3+}$ : a decrease in CTB energy represents an increase in covalence, i.e. the decrease in ionicity between oxygen and europium ions. Eu-O bond length becomes larger when europium ion is 8-fold coordinated, which decreases the ionicity and causes the red shift of the CT band. Zhang et al. reported that the CTBs of  $\text{Eu}^{3+}$  are centered at 242 nm, 240 nm and 237 nm, corresponding to tetragonal, mixture of tetragonal and monoclinic and monoclinic phase, respectively [87]. The sharp excitation bands are due to the direct excitation of  $\text{Eu}^{3+}$  ion. The strongest excitation bands originating from the  ${}^7\text{F}_0$  are at the following approximate positions: 363, 383, 395, 415, 466, and 528 nm for transitions to  ${}^5\text{D}_4$ ,  ${}^5\text{L}_7$ ,  ${}^5\text{L}_6$ ,  ${}^5\text{D}_3$ ,  ${}^5\text{D}_2$ ,  ${}^5\text{D}_1$  out of which the absorption band at ca. 395 nm is the strongest one. Due to the thermal population of the  ${}^7\text{F}_1$  level at room temperature, the  ${}^7\text{F}_1 \rightarrow {}^5\text{D}_1$  transition can be observed in the excitation spectra. After the excitation, the excited electrons most often migrate to the  ${}^5\text{D}_0$  level, following the radiative transition to the  ${}^7\text{F}_1$  multiplet.

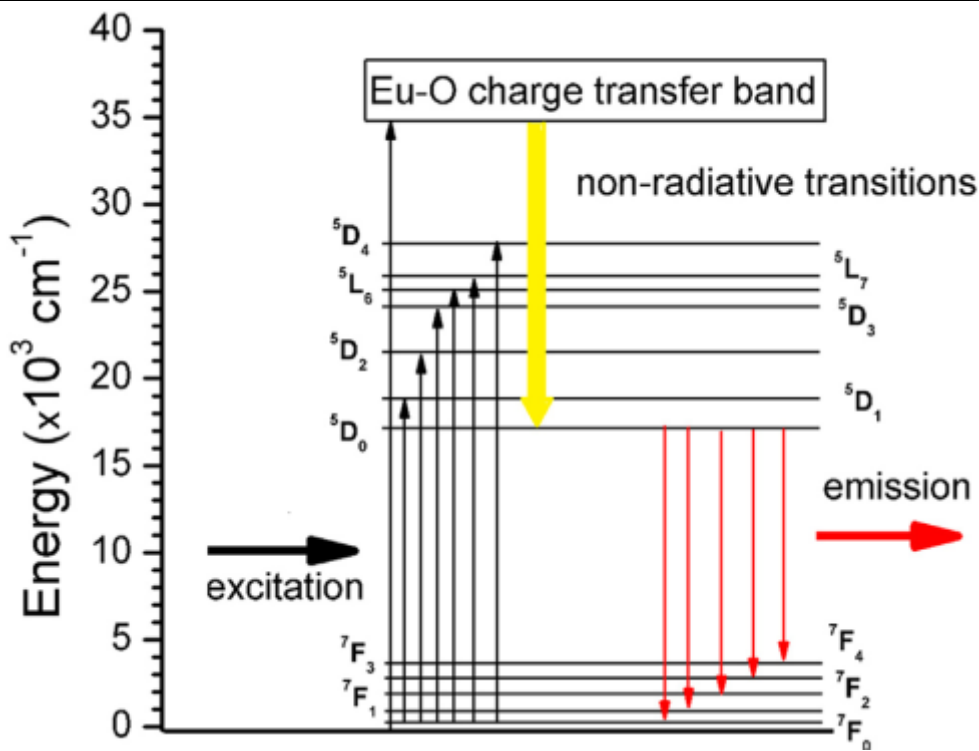


Fig. 39. Schematic representation of energy level diagram and proposed mechanism of CT pathways involved in the PL of Eu doped coatings [9].

The total PL intensity is a sum of PL originating from the host matrix and Eu<sup>3+</sup> ion. Emissions in the 420 - 575 nm range originate from the higher excited levels of europium, while above 575 nm are from the  $5D_0$  level. The hypersensitive transition  $5D_0 \rightarrow 7F_2$  is very sensitive to ligand field and is proportional to the increase of covalency [96]. Magnetic dipole transitions weakly vary with the crystal field strength around the europium ion in matrix, and can be taken as a reference. Therefore, the asymmetric ratio, a ratio of intensities of  $5D_0 \rightarrow 7F_2$  to  $5D_0 \rightarrow 7F_1$  transition, gives a measure of the degree of distortion from the inversion symmetry of the local environment of the Eu<sup>3+</sup> ion in matrix [96].  $5D_0 \rightarrow 7F_0$  at 577 nm is strictly forbidden by the selection rules, and the appearance of this transition is an indication that Eu<sup>3+</sup> ion occupies a site with  $C_{nv}$ ,  $C_n$  or  $C_s$  symmetry. The emission peaks that originate from the f-f transitions show variation in intensities with change of crystalline phase [81].

#### 2.2.4.1. $ZrO_2:Eu^{3+}$

Emission spectra features two distinct regions: the broad band with maximum at ca. 490 nm, which originates from the  $ZrO_2$  [81] substrate, and a series of sharp peaks which are due to f-f transitions of Eu ion [4]. The variation of peak intensities of magnetic and hyperfine dipole transitions and different lifetimes has been reported in different crystalline structures of zirconia [81]. Furthermore, europium will experience a different crystal field in different phases, which determines a shift of the hypersensitive transition [85]. In tetragonal phase magnetic dipole transition has higher intensity than the hypersensitive transition, while in monoclinic, where europium ion does not occupy the inversion symmetry site, the hypersensitive dominates all other transitions. Thus, the emission peak at 613 nm originates from  $Eu^{3+}$  in m- $ZrO_2$ , and the peak at ca. 606 nm is from tetragonal site [79]. Changes in the intensity ratio  $R_f = I(613 \text{ nm})/I(606 \text{ nm})$  is a tool to analyze changes in the m/t phase composition [101]. Radiative emission rates are higher for the sites of low symmetry, thus they are higher for monoclinic compared to the more symmetric tetragonal sites [79].  ${}^5D_0 \rightarrow {}^7F_4$  transition comes exclusively from monoclinic sites. Peaks at 625 nm and 630 nm of the  ${}^5D_0 \rightarrow {}^7F_2$  can be associated with lower local symmetry of  $Eu^{3+}$  ions in m- $ZrO_2$  [4].

#### 2.2.4.2. $TiO_2:Eu^{3+}$

The site symmetry of  $Ti^{4+}$  (ionic radii 68 pm) ions in anatase lattice are  $D_{2d}$ . Due to the large mismatch in ionic radii and the charge imbalance, the substitution by  $Eu^{3+}$  creates oxygen vacancies and causes the lattice distortion, lowering the site symmetry. Its MD transition can be observed with two peaks at 591 and 596 nm.

#### 2.2.4.3. $Nb_2O_5:Eu^{3+}$

The substitution of Nb with Eu ions causes local disordering, resulting in reduced local symmetry. The substitution creates oxygen vacancies and causes the lattice distortion. In asymmetric environment the hypersensitive transition dominates the MD transition [9], such is the case of  $Nb_2O_5:Eu^{3+}$ . The MD transition  ${}^5D_0 \rightarrow {}^7F_1$  can be resolved by three Gaussian components with maxima at 585 nm, 589 nm and 595 nm as presented in Fig. 40. The MD transition directly reflects the CF splitting of the  ${}^7F_1$  level and is an indication of the Eu site symmetry.

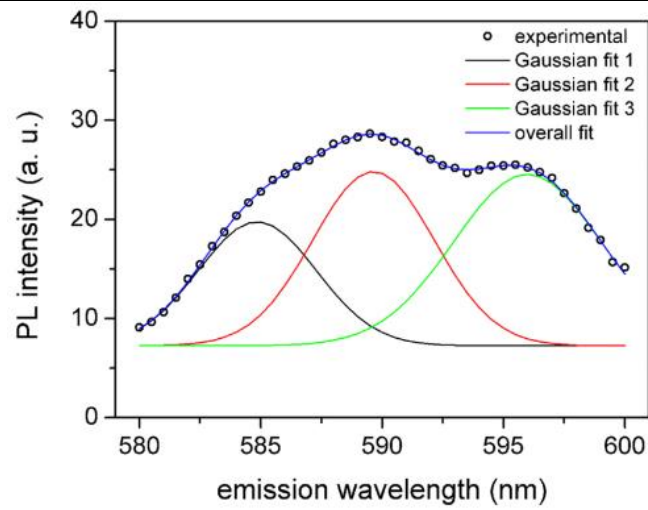


Fig. 40.  $Nb_2O_5:Eu^{3+}$  MD peak resolved by three Gaussian fits [9].

## 2.3. Judd-Ofelt theory

### 2.3.1. The complete Hamiltonian

The complete Hamiltonian of an N-electron ion in a crystal field (CF) is given by [102–105]:

$$\begin{aligned}
 H = E_{\text{ave}} + \sum_{k=2,4,6} F^k f_k + \zeta_{4f} A_{SO} + \alpha L(L+1) + \beta G(G_2) + \gamma F(R_7) + \\
 + \sum_{i=2,3,4,6,7,8} T^i t_i + \sum_{k=0,2,4} M^k m_k + \sum_{k=2,4,6} P^k p_k + \sum_{i=0}^N \sum_{k=0}^{\infty} \sum_{q=-k}^k B_q^k C_q^k(i) \quad (2.3.1)
 \end{aligned}$$

where  $E_{\text{ave}}$  takes into account the kinetic energy of the electrons and their interaction with the nucleus, and only shifts the barycenter of the whole 4f configuration. The second and the third term represent the ES and s-o interactions, respectively. The Trees configuration interaction parameters are given by  $\alpha$ ,  $\beta$ , and  $\gamma$ ;  $G$  and  $F$  are the Casimir operators for groups  $G_2$  and  $R_7$ .  $M^k$  parameters are due to the spin-spin and spin-other-orbit interactions, and  $P^k$  parameters describe the higher order magnetic interactions.  $T^i$  are the 3-body interaction parameters. The last term represents the CF interaction. The higher-order interactions, however, are not of interest here, but the Hamiltonians that are concerned with electrostatic repulsion, the s-o interaction and the CF will be discussed in detail.

### 2.3.2. Electrostatic interaction of a free ion

For an N-electron ion the non-relativistic Hamiltonian with only electrostatic interactions can be written as [106]:

$$H_{ES} = \sum_{i=1}^N \frac{p_i^2}{2m} - \frac{1}{4\pi\epsilon_0} \sum_{i=1}^N \frac{Ze^2}{r_i} + \frac{1}{4\pi\epsilon_0} \sum_{i<j}^N \frac{e^2}{r_{ij}} \quad (2.3.2)$$

The first term represents the kinetic energy, the second term is the potential energy of electrons in the field of nucleus, and the third term represents the repulsive Coulomb potential between pairs of electrons. In the central field approximation each electron is moving independently in an unknown spherically symmetric potential  $U(r)$ , and the following equation is a zeroth order approximation to the previous Hamiltonian, a central field Hamiltonian [106]:

$$H_0 = \sum_{i=1}^N \left( \frac{p_i^2}{2m} + U(r_i) \right) \quad (2.3.3)$$

with eigenfunctions [106]:

$$\psi_{\alpha}(\mathbf{r}) = \frac{1}{r} R_{nl}(r) Y_l^{m_l}(\theta, \varphi) \chi_{m_s}, \alpha = nlm_l m_s \quad (2.3.4)$$

The solution to the N-electron operator  $H_0$  can be found in the form of the Slater determinants:

$$\psi_{\alpha_1 \dots \alpha_N}(\mathbf{r}_1, \dots, \mathbf{r}_N) = \frac{1}{\sqrt{N!}} \begin{vmatrix} \psi_{\alpha_1}(\mathbf{r}_1) & \dots & \psi_{\alpha_N}(\mathbf{r}_1) \\ \vdots & \ddots & \vdots \\ \psi_{\alpha_1}(\mathbf{r}_N) & \dots & \psi_{\alpha_N}(\mathbf{r}_N) \end{vmatrix} \quad (2.3.5)$$

This antisymmetric wavefunctions are the eigenfunctions of the central field Hamiltonian, and their eigenvalues depend only on quantum numbers  $n$  and  $l$ . Thus, all eigenstates of  $H_0$  within a given configuration, as defined by all possible sets  $i = \alpha_1 \dots \alpha_N$ , are completely degenerate:

$$H_0 |\psi_i^c\rangle = E_0^c |\psi_i^c\rangle \quad (2.3.6)$$

### 2.3.3. Time-integrated perturbation theory

Optically active 4f electrons of RE are shielded from the environment by the 5s and 5p shells, and at the same time they are the outermost, i.e. the valence electrons. Thus, 4f electrons are responsible for the spectroscopic properties of RE doped compounds. The tri-positive RE embedded in any structure retains its free-ionic properties, and its properties are slightly modified by the environment that can be treated as a second-order perturbation [50].

The corrections to the  $H_0$  are given in the form  $H_k$ , where  $k$  is an integer. The smaller the value of  $k$ , the larger the correction is. Let all corrections be given as  $W = \sum H_k$ , and the real Hamiltonian can then be presented as  $H = H_0 + W$ .  $H_I$  is the Hamiltonian of the remaining electrostatic interactions:  $H_I = H_{ES} - H_0$ .

Let's assume an eigenstate  $\psi^c$  (where  $c$  represents a configuration, in the case of  $\text{Eu}^{3+} c = 4f^6$ ) of  $H_0$  with non-degenerate eigenvalue  $E_0^c = \langle \psi^c | H_0 | \psi^c \rangle$ . Then the corrected eigenvalue,  $E^c$ , by the first and the second order corrections is:

$$E^c = E_0^c + \langle \psi^c | W | \psi^c \rangle + \sum_{\substack{p,k \\ p \neq c}} \frac{|\langle \psi_k^p | W | \psi^c \rangle|^2}{E_0^c - E_0^p} \quad (2.3.7)$$

where  $k$  labels the eigenstates of the possibly degenerated eigenvalue  $E_0^p$  of  $H_0$ . However,  $H_0$  is completely degenerated inside our configuration, thus the previous equation gets modified to a set of matrix elements:

$$E_{ij}^c = E_0^c \delta_{ij} + \langle \psi_i^c | W | \psi_j^c \rangle + \sum_{\substack{p,k \\ p \neq c}} \frac{\langle \psi_i^c | W | \psi_k^p \rangle \langle \psi_k^p | W | \psi_j^c \rangle}{E_0^c - E_0^p} \quad (2.3.8)$$

The first term in this equation is the center of mass and it can be set to zero for the ground level. The second term describes the inter-configurational interactions. The third term takes account the interaction of configuration  $c$  with all other configurations  $p$ .

In order to calculate the energy levels, the diagonalization of all the energy matrices  $E_{ij}^c$  is needed. For the case of europium trivalent ion, that is needed only for the configuration  $c=4f^6$ . Equation 2.3.8 then can be reduced to (for inter-configurational interactions):

$$E_{ij}^c = \sum_k \langle \psi_i^c | H_k | \psi_j^c \rangle \quad (2.3.9)$$

$H_k$  can be separated to radial and axial components:  $H_k = H_{k,r} H_{k,\Omega}$ , where the general radial integral is:

$$(\forall i, j) \langle \psi_i^c | H_{k,r} | \psi_j^c \rangle = \int \dots \int R_{nl}^N H_{k,r} R_{nl}^N dr_1 \dots dr_N \quad (2.3.10)$$

#### 2.3.4. First order interactions

Hamiltonian operator corresponds to the total energy of the system, thus the energies of the  $^{2S+1}L_J$  multiplets are found by solving the time-independent Schrodinger



$$A = r \sqrt{\prod_{i=1}^{12} p_i^{k_i}} \quad (2.3.12)$$

where  $p_i$  are the prime numbers  $\{1,2,3,5,7,11,13,17,19,23, 29, 31, 37\}$ , and  $k_i$  are written in a form  $\{0, \dots, 9, A, \dots, Z\}$ , with values ranging from 1 to 36. The coefficients of fractional parentage can be easily evaluated by RELIC application software [111].

#### 2.3.4.1.2. Wigner 3j symbol

The other coefficients used are the Wigner 3j and 6j symbols. Wigner 3j is a mathematical treatment of coupling two angular momenta, an alternative to the Clebsch-Gordan coefficients, and is explicitly given by:

$$\begin{aligned} \begin{pmatrix} a & b & c \\ \alpha & \beta & \gamma \end{pmatrix} &= \frac{(-1)^{a-b-\gamma}}{\sqrt{2c+1}} \underbrace{\langle \alpha\alpha\beta\beta | c(-\gamma) \rangle}_{\text{CG}} = (-1)^{a-b-\gamma} \cdot \\ &\sqrt{\Delta(a,b,c)(a+\alpha)!(a-\alpha)!(b+\beta)!(b-\beta)(c+\gamma)!(c-\gamma)!} \sum_t \frac{(-1)^t}{\chi(t)} \end{aligned} \quad (2.3.13)$$

where

- $\chi(t) = t!(c-b+t+\alpha)!(c-a+t-\beta)!(a+b-c-t)!(a-t-\alpha)!(b-t+\beta)!$
- $t \in \{(c-b+t+\alpha), (c-a+t-\beta), (a+b-c-t), (a-t-\alpha), (b-t+\beta)\} \geq 0\}$
- $\Delta(a,b,c) = \frac{(a+b-c)!(a-b+c)!(-a+b+c)!}{(a+b+c+1)!}$

#### 2.3.4.1.3. Wigner 6j symbol

The 6-j coefficients are used for coupling 3 angular momenta, and are given by:

$$\begin{Bmatrix} j_1 & j_2 & j_3 \\ J_1 & J_2 & J_3 \end{Bmatrix} = \sqrt{\Delta(j_1, j_2, j_3)\Delta(j_1, J_2, J_3)\Delta(j_1, j_2, J_3)\Delta(j_1, J_2, j_3)} \sum_t \frac{(-1)^t (t+1)!}{f(t)} \quad (2.3.14)$$

where:

- $f(t) = (t-j_1-j_2-j_3)!(t-j_1-J_2-J_3)!(t-J_1-j_2-J_3)!(t-J_1-J_2-j_3)!(j_1+j_2+J_1+J_2-t)!(j_2+j_3+J_2+J_3-t)!(j_3+j_1+J_3+J_1-t)!$

- $t \in \{(t - j_1 - j_2 - j_3), (t - j_1 - J_2 - J_3), (t - J_1 - j_2 - J_3), (t - J_1 - J_2 - j_3), (j_1 + j_2 + J_1 + J_2 - t), (j_2 + j_3 + J_2 + J_3 - t), (j_3 + j_1 + J_3 + J_1 - t)\} \geq 0\}$

#### 2.3.4.2. Electrostatic (Coulomb) interaction

The ES interaction Hamiltonian is given by:

$$H_{ES} = H_0 + H_1 \quad (2.3.15)$$

As already mentioned, for the ground state  $H_0$  can be set to 0, thus the ES interaction Hamiltonian reduces to the electron-electron repulsion term:

$$H_1 = \frac{1}{4\pi\epsilon_0} \sum_{i < j}^N \frac{e^2}{r_{ij}} \quad (2.3.16)$$

The inverse distance between electrons can be expanded in terms of the spherical harmonics:

$$\frac{1}{r_{ij}} = \sum_{k=0}^{\infty} \frac{r_{<}^k}{r_{>}^{k+1}} \sum_{q=-k}^k (-1)^q \left( c_{-q}^{(k)} \right)_i \left( c_q^{(k)} \right)_j \quad (2.3.17)$$

where  $r_{<}$  and  $r_{>}$  are the smaller and the larger distance, respectively, of  $r_i$  and  $r_j$ , and

$c_q^{(k)} = \sqrt{\frac{4\pi}{2k+1}} Y_q^k$  is an element of the tensor operator  $C^{(k)}$ . By substituting equation 2.3.17

into the equation for ES Hamiltonian 2.3.16:

$$H_1 = \frac{e^2}{4\pi\epsilon_0} \sum_k \sum_{i < j} \frac{r_{<}^k}{r_{>}^{k+1}} C_i^k C_j^k \quad (2.3.18)$$

##### 2.3.4.2.1. Slater integrals

Expansion of electrostatic interactions in terms of Legendre polynomials allows separation of variables, and the equation can be split into its radial and angular parts [107].

The radial parameters are the Slater integrals<sup>5</sup>, which for the RE are defined by [35]:

---

<sup>5</sup> While the energy levels can be obtained from the analysis of the free ion spectra, theoretical calculations are a necessity for interpretation of empirical results and are the only way of obtaining the eigenvectors. The methods for dealing with this problem were developed by Slater [35].

$$F^k(4f) = \frac{e^2}{4\pi\epsilon_0} \iint_0^\infty \frac{r_<^k}{r_>^{k+1}} R_{4f}^2(r_i) R_{4f}^2(r_j) dr_i dr_j \quad (2.3.19)$$

where  $r_>$  is greater and  $r_<$  is smaller than  $r_i$  and  $r_j$ .

Note that the Slater integrals have different values depending on the position of  $k$ , written in the subscript or superscript. The relations between the two are given by:  $F_2=F^2/225$ ,  $F_4=F^4/1089$ ,  $F_6=25F^6/184041$ .

$F_0$  is usually omitted since it produces only a uniform shift of the energies of all the states of the configuration. Since the energies are referenced to the ground state, this shift is irrelevant.

With the Slater integrals and the tabulated coefficients, the matrix elements of  $H_I$  can be evaluated. From the exact equation, all Slater integrals can be evaluated by using the Hartree-Fock method. However, Hartree-Fock calculations provide Slater integrals with significant error in the case of RE ions, thus they must be obtained semi-empirically (adjusted to the experimentally observed energies) [112].

An approximate value for the Slater integrals is given in a form  $F_2=12.4(Z-34)$  [35,107]. Thus, the  $F_2$  parameter shows a linear increase with increasing number of electrons in the 4f shell, as presented in Fig. 41. Other parameters are approximately related as:  $F_4/F_2=148(4)$ ,  $F_6/F_2=0.016(1)$ . Carnall et al stated slightly different values [107]:  $F_4/F_2=148$ ,  $F_6/F_2=0.016$ .

In the many electron atom the coefficients at the Slater parameters in the multipole expansion of the Coulomb interaction depend explicitly on the many-electron SL term [113]. The angular operators can now be defined as:

$$f_k = \sum_{i<j} C_i^k C_j^k \quad (2.3.20)$$

The electrostatic Hamiltonian is then given by:

$$H_1 = \sum_k F^k f_k \quad (2.3.21)$$

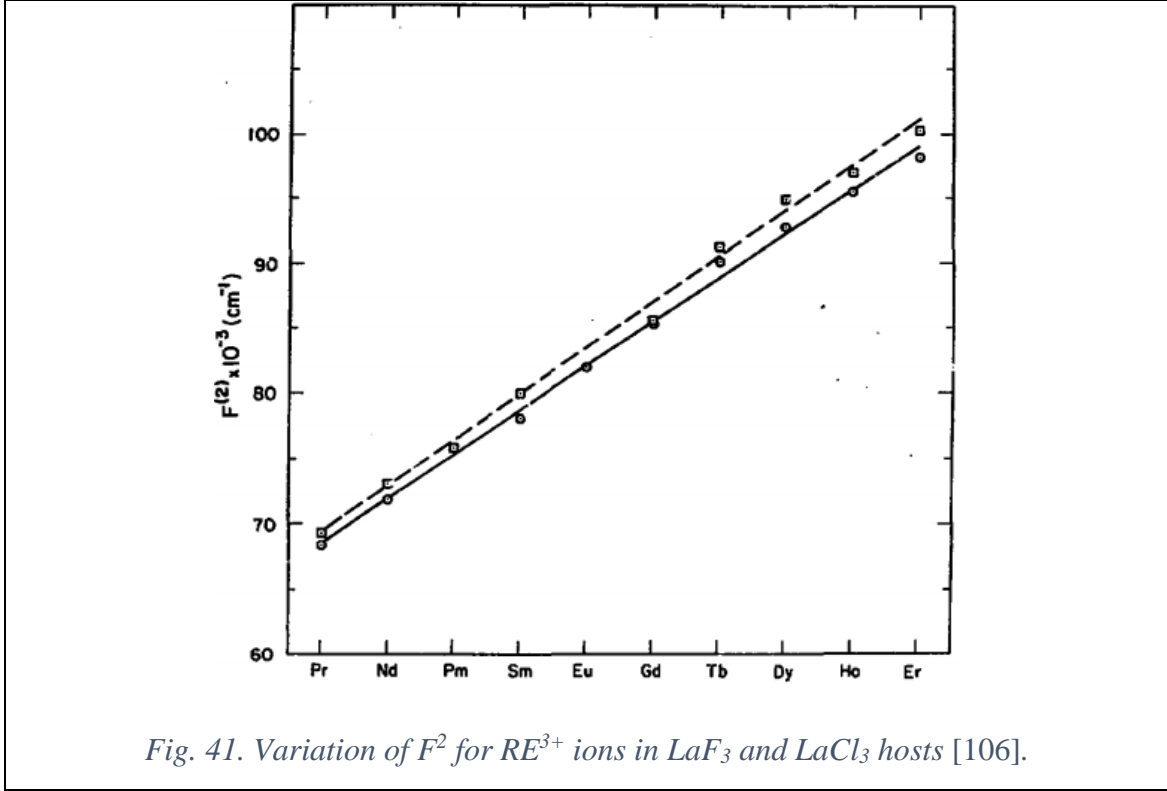


Fig. 41. Variation of  $F^2$  for  $RE^{3+}$  ions in  $LaF_3$  and  $LaCl_3$  hosts [106].

#### 2.3.4.2.2. Matrix elements for the ES interaction

To proceed any further, we must switch to the matrix elements forms of the operators, by multiplying them with the interacting states  $\langle 4f^N SL |$  and  $|4f^N S' L' \rangle$ . Thus, the matrix elements of the angular operator  $f_k$  are:  $\langle 4f^N SL | f_k | 4f^N S' L' \rangle$ , and the electrostatic Hamiltonian matrix elements are now given by:  $\langle 4f^N SL | H_1 | 4f^N S' L' \rangle$ . The definition of the tensor operator  $C_q^{(k)}$  is equivalent to [114]:

$$\langle \Psi' | C^k | \Psi \rangle = (-1)^l \sqrt{(2l' + 1)(2l + 1)} \begin{pmatrix} l' & k & l \\ 0 & 0 & 0 \end{pmatrix} \quad (2.3.22)$$

$H_1$  is an electric interaction and cannot act on the spin, therefore the matrix element is zero unless  $S=S'$  and  $L=L'$ . For the  $l=3$  and  $l'=3$ , and because the  $3j$  and  $6j$  symbols would be zero unless  $k = 0, 2, 4, 6$ , the electrostatic matrix element takes a form [33]:

$$\begin{aligned} \langle 4f^N SL | H_1 | 4f^N S' L' \rangle &= \langle 4f^N SL | C_i^k C_j^k | 4f^N S' L' \rangle F_k = \\ &= \delta_{SS'} \delta_{LL'} 49 (-1)^L \sum_{k=0,2,4,6} \begin{pmatrix} 3 & k & 3 \\ 0 & 0 & 0 \end{pmatrix}^2 \begin{Bmatrix} 3 & 3 & k \\ 3 & 3 & L \end{Bmatrix} F_k \end{aligned} \quad (2.3.23)$$

The additional complication for the electrostatic matrix elements arises for some L and S which are distinguished only by the seniority quantum number (thus producing the off-diagonal matrix elements). The solution is given in the form [33,107]:

$$\langle 4f^N SL | H_1 | 4f^N S' L' \rangle = \sum_{k=0}^3 e_k E^k \quad (2.3.24)$$

where  $e_k$  are the coefficients tabulated in Ref. [109], and  $E^k$  are related to the Slater integrals as [106]:  $E^0 = F_0 - 10F_2 - 33F_4 - 286F_6$ ,  $E^1 = (70F_2 + 231F_4 + 2002F_6)/9$ ,  $E^2 = (F_2 - 3F_4 + 7F_6)/9$ ,  $E^3 = (5F_2 + 6F_4 - 91F_6)/3$ .

### 2.3.4.3. Spin-orbit interaction

The second perturbation operator is the most important relativistic correction given by the:

$$H_2 = \frac{1}{2m^2c^2} \sum_i \mathbf{s}_i (\nabla_i U(r_i) \times \mathbf{p}_i) = \frac{1}{2m^2c^2} \sum_i \frac{1}{r_i} \frac{d}{dr_i} U(r_i) (\mathbf{s}_i \cdot \mathbf{l}_i) \quad (2.3.25)$$

where  $s_i$  and  $l_i$  are the spin and orbital angular momentum, respectively.  $H_2$  can be further divided into the radial  $\xi$  and angular parts [106]:

$$H_2 = \sum_i \xi(r_i) (\mathbf{s}_i \cdot \mathbf{l}_i) \quad (2.3.26)$$

where  $\xi(r_i) = \frac{\hbar^2}{m^2c^2} \frac{1}{r_i} \frac{d}{dr_i} U(r_i)$ .

Now we can introduce the spin-orbit coupling parameter for a 4f configuration, which is a constant for all the states of a given 4f configuration (thus, it is a material dependent value):

$$\zeta_{4f} = \int_0^\infty R_{4f}^2(r) \xi(r) dr \quad (2.3.27)$$

For RE from  $\text{Pr}^{3+}$  to  $\text{Gd}^{3+}$  the s-o coupling parameter can be approximately given by [107]:  $\zeta_{4f} = 142 \cdot Z - 7648$ , which equals to ca. 1300 for  $\text{Eu}^{3+}$ .

### 2.3.4.3.1. Spin-orbit tensor operator

In order to calculate matrix elements of the s-o interaction operator  $V^{(lx)}$  tensor operator must be introduced. Its RME are given by:

$$\begin{aligned} & \langle l^N SL \| V^{lx} \| l^N S' L' \rangle = \\ & = N \sqrt{s(s+1)(2s+1)(2S+1)(2L+1)(2S'+1)(2L'+1)} \cdot \\ & \cdot \sum_{\psi(l^{N-1})} (l^{N-1} \bar{S} \bar{L} | l^N SL) \begin{Bmatrix} S & S' & 1 \\ s & s & \bar{s} \end{Bmatrix} \begin{Bmatrix} L & L' & x \\ l & l & \bar{l} \end{Bmatrix} (-1)^{\bar{s}+\bar{l}+S+L+s+l+x+1} \end{aligned} \quad (2.3.28)$$

For the case of RE, the tensor operator with  $x = 1$ ,  $s = 1/2$  and  $l = 3$  is given by:

$$\begin{aligned} \langle 4f^N SL \| V^{11} \| 4f^N S' L' \rangle & = N \sqrt{\frac{3}{2}(2S+1)(2L+1)(2S'+1)(2L'+1)} \\ & \sum_{\psi(4f^{N-1})} (4f^{N-1} \bar{S} \bar{L} | 4f^N SL) \begin{Bmatrix} S & S' & 1 \\ 1 & 1 & \bar{s} \end{Bmatrix} \begin{Bmatrix} L & L' & 1 \\ 3 & 3 & \bar{l} \end{Bmatrix} (-1)^{\bar{s}+\bar{l}+S+L+5\frac{1}{2}} \end{aligned} \quad (2.3.29)$$

And for the case of  $\text{Eu}^{3+}$ :

$$\begin{aligned} \langle 4f^6 SL \| V^{11} \| 4f^6 S' L' \rangle & = 6 \sqrt{\frac{3}{2}(2S+1)(2L+1)(2S'+1)(2L'+1)} \\ & \sum_{\psi(4f^5)} (4f^5 \bar{S} \bar{L} | 4f^6 SL) \begin{Bmatrix} S & S' & 1 \\ 1 & 1 & \bar{s} \end{Bmatrix} \begin{Bmatrix} L & L' & 1 \\ 3 & 3 & \bar{l} \end{Bmatrix} (-1)^{\bar{s}+\bar{l}+S+L+5\frac{1}{2}} \end{aligned} \quad (2.3.30)$$

### 2.3.4.3.2. Spin-orbit interaction matrix elements

Now the spin-orbit interaction matrix elements for the  $\text{Eu}^{3+}$  can be calculated [33]:

$$\begin{aligned} \langle 4f^N SLJ | \mathcal{H}_{so} | 4f^N S' L' J' \rangle & = \zeta (-1)^{J+L+S'} \sqrt{l(l+1)(2l+1)} \begin{Bmatrix} S & S' & 1 \\ L' & L & J \end{Bmatrix} \cdot \\ & \cdot \langle l^N SL \| V^{11} \| l^N S' L' \rangle = |l=3, N=6| = \\ & = \zeta (-1)^{J+L+S'} \sqrt{84} \begin{Bmatrix} S & S' & 1 \\ L' & L & J \end{Bmatrix} \langle 4f^6 SL \| V^{11} \| 4f^6 S' L' \rangle \end{aligned} \quad (2.3.31)$$

These matrix elements will contribute off-diagonally to the  $H$ -matrix, and can be calculated with the knowledge of the spin-orbit coupling parameter. As well as with the Slater integrals, the spin-orbit coupling parameter can be calculated by Hartree-Fock method, but in practice is adjusted to the experimentally observed energies. However, it is approximately in relation with the  $F_2$  [115]:  $\zeta_{4f} \approx 3.5 F_2$ .

#### 2.3.4.4. Experimentally obtaining the parameters

Weak interactions of RE ion with the host matrix affect the ES and s-o coupling strengths, with characteristic parameters given by Slater integrals and s-o coupling parameter. Thus, for obtaining the IC wavefunctions it is necessary to first obtain the values of these parameters. As Hartree-Fock method has been proven to be inaccurate for the RE, the values are best obtained semi-empirically. Another benefit in obtaining the experimental values lies in the small dependence of Slater integrals and to a lesser degree s-o parameter on the host matrix [106].

As already mentioned, CF causes partial or complete splitting of each multiplet to  $2J+1$ . The degeneracy-weighted average energy, barycenter energy, of each  $^{2S+1}L_J$  is then given by [33]:

$$E_B(^{2S+1}L_J) = \frac{1}{2J+1} \sum g_i E_i \quad (2.3.32)$$

where  $i$  counts energy levels,  $g_i$  is the degeneracy of the  $i^{\text{th}}$  level, and  $E_i$  is the energy of the  $i^{\text{th}}$  level.

There are two methods for obtaining  $E_B$ :

1. The exact method: by determining the energy and degeneracy of each CF level of each multiplet using low-temperature polarized absorption and luminescence spectroscopy, and then using the equation 2.3.32 to calculate  $E_B$ .
2. The approximate method: from high-temperature polarized absorption spectra where all crystal-field levels of the initial state are thermally populated (approximately equally, thus all CF transitions contribute to the observed absorption spectrum  $\varepsilon(E)$ ),  $E_B$  can be estimated as the barycenter of the given transition, as presented in Fig. 42:  $\int_0^{E_B} \varepsilon(E) dE = 0.5$ .

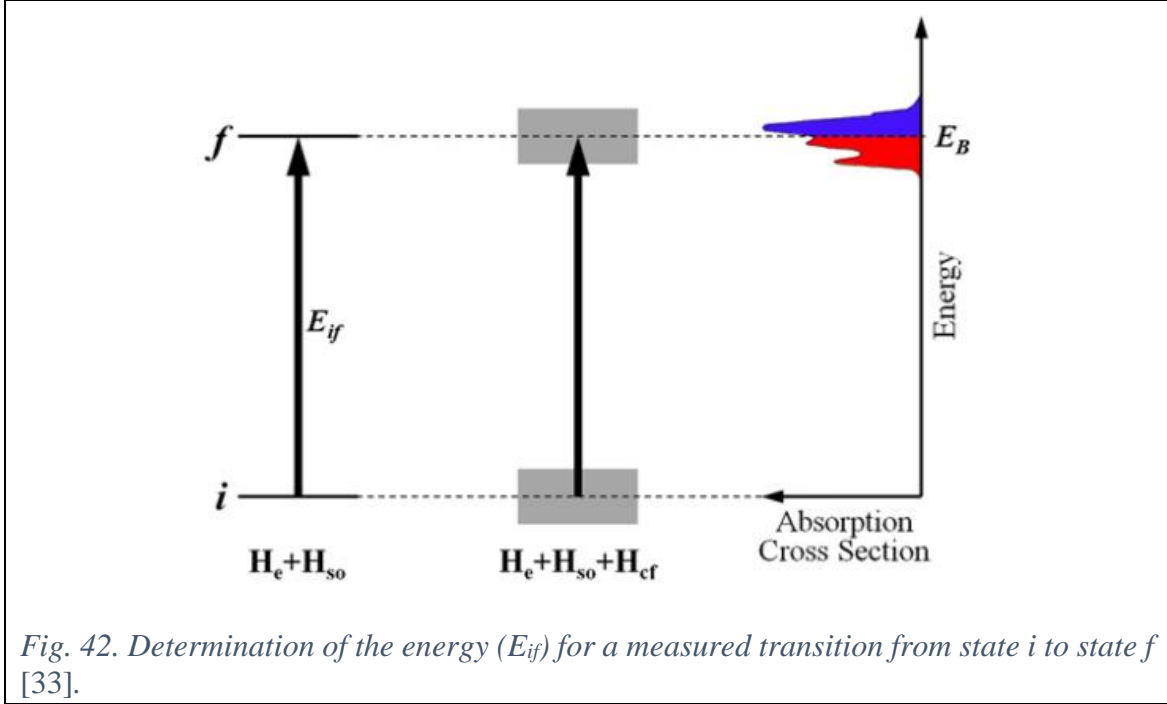


Fig. 42. Determination of the energy ( $E_{if}$ ) for a measured transition from state  $i$  to state  $f$  [33].

$\{F_k, \zeta, c_i\}$  set of parameters can be obtained by fitting the calculated  $E_B$  to a set of experimental  $E_B$ , by a Downhill Simplex Algorithm (implemented in RELIC), by minimizing relative root mean square for 4 parameters (where  $n = \#(E_i^{\text{exp}})$ ):

$$RMS_{rel} = \sqrt{\frac{1}{n-4} \sum_{i=1}^n \left( \frac{E_i^{\text{exp}} - E_i^{\text{th}}}{E_i^{\text{exp}}} \right)^2} \quad (2.3.33)$$

The average values, obtained experimentally in various oxides for the Slater integrals and the spin-orbit coupling parameter are [112,115]:  $F_2 = 381 \text{ cm}^{-1}$ ,  $F_4 = 56 \text{ cm}^{-1}$ ,  $F_6 = 6 \text{ cm}^{-1}$ ,  $\zeta = 1331 \text{ cm}^{-1}$ . These values can be used in some cases as an approximation in case the method given by equation 2.3.33 is not at a disposal.

### 2.3.5. Intermediate Coupling approximation

In the problem of quenching of an orbital momenta, three basic interactions should be taken into account [113]: ES, s-o and CF. For a weak CF, the relative intensity of s-o and ES determine the coupling scheme to be used. LS (Russell-Saunders) coupling is the result of ES (Coulomb) interaction between electrons, with the total angular momentum given by:  $J = L + S$ , where  $S = \sum s_i$ ,  $L = \sum l_i$ . In the case of dominant s-o interaction, due to

the large  $Z$ , the individual spins and orbital angular momenta are coupled first in a so-called jj coupling scheme, defined as:  $j_i = s_i + l_i, J = \sum j_i$ .

ES and s-o interactions are dominant in  $RE^{3+}$  (they account for 80-90% of all interactions). Considering just them offers a useful first-order description known as intermediate coupling (IC) approximation [33], where CF can be considered as a perturbation.

### 2.3.5.1. Intermediate coupling wavefunctions

With Coulomb and spin-orbit interaction matrix elements calculated, all the elements of the  $H$  matrix can be obtained. However, such  $H$ -matrix will have the off-diagonal elements in  $|4f^N SLJ\rangle$  basis set. Diagonalizing is equivalent to finding the matrix eigenvalues, which turn out to be the entries of the diagonalized matrix. The eigenvectors make up the new set of axes corresponding to the diagonalized matrix. Thus, by diagonalizing the  $H$ -matrix the IC energy levels and wavefunctions are obtained. Diagonalization yields the IC wavefunctions expressed as a linear combination of all other states in the configuration having the same  $J$  and being mixed by s-o interaction [31,33,103,116]:

$$|4f^N SLJ\rangle = \sum_i c_i |4f^N S'L'J\rangle, \quad \sum_i c_i^2 = 1 \quad (2.3.34)$$

### 2.3.5.2. IC 4f energy levels

The eigenvalues, i.e. energies, are originally given by the Dieke diagram [117]. However, the energies vary from host to host, thus the Dieke diagram can be used only as a first-order energy-level description.

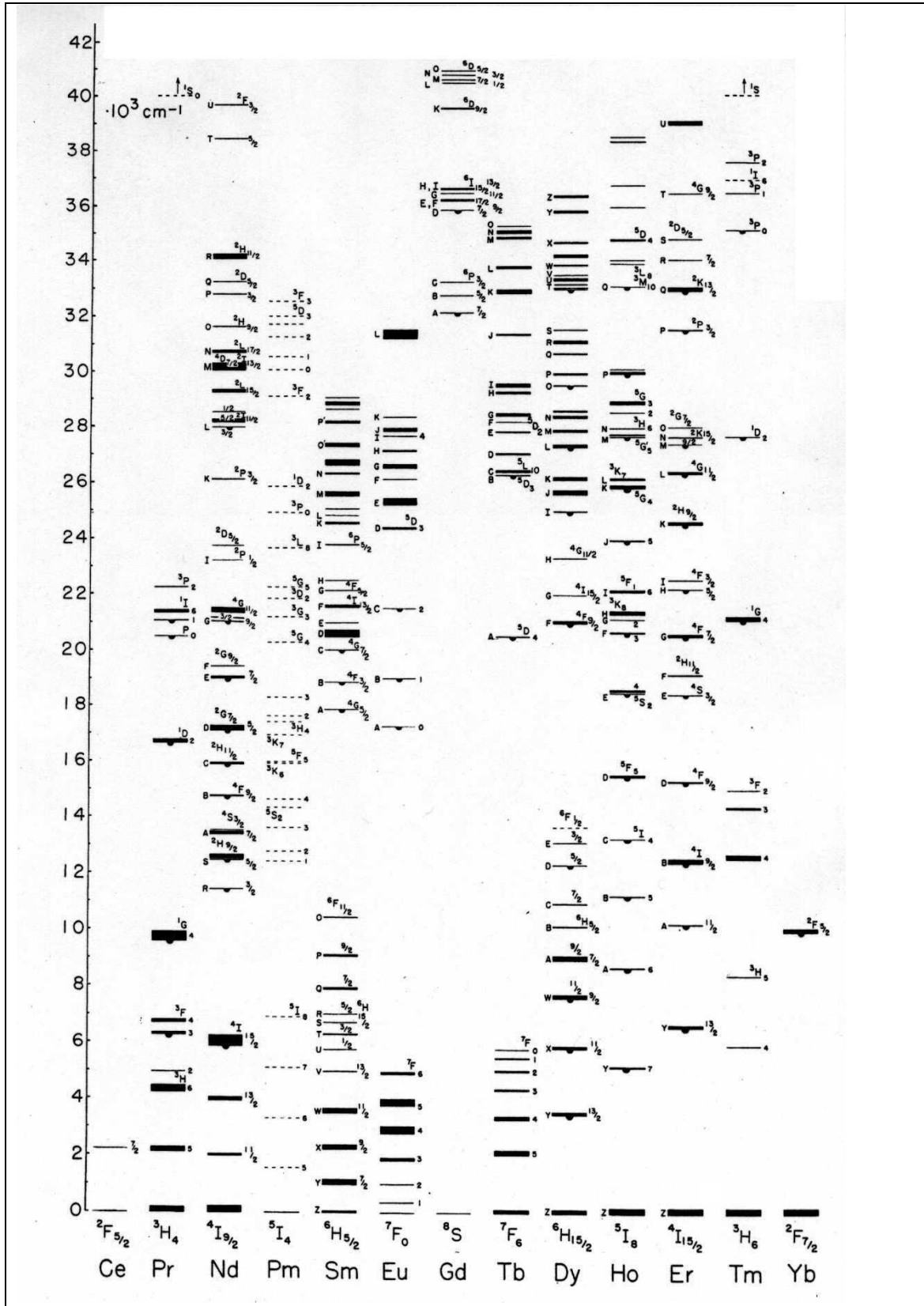


Fig. 43. The original Dieke RE energy diagram [117].

### 2.3.5.3. The Crystal Field (CF) interaction

In a crystal the  $2J+1$  degeneracy of a free atom is destroyed, reducing the spherical symmetry to the point symmetry at the ion site. Degree to which degeneracy is removed will depend on the point symmetry surrounding the ion, which is why the host material plays a fundamental role in determining the nature of spectra of impurity (dopant) ions. Screening effect (of 4f by outer shells, see Fig. 44) protects the optically active electrons from the influence of CF. Because of this, RE exhibit similar spectra to free ion spectra, with sharp and well defined spectral features.

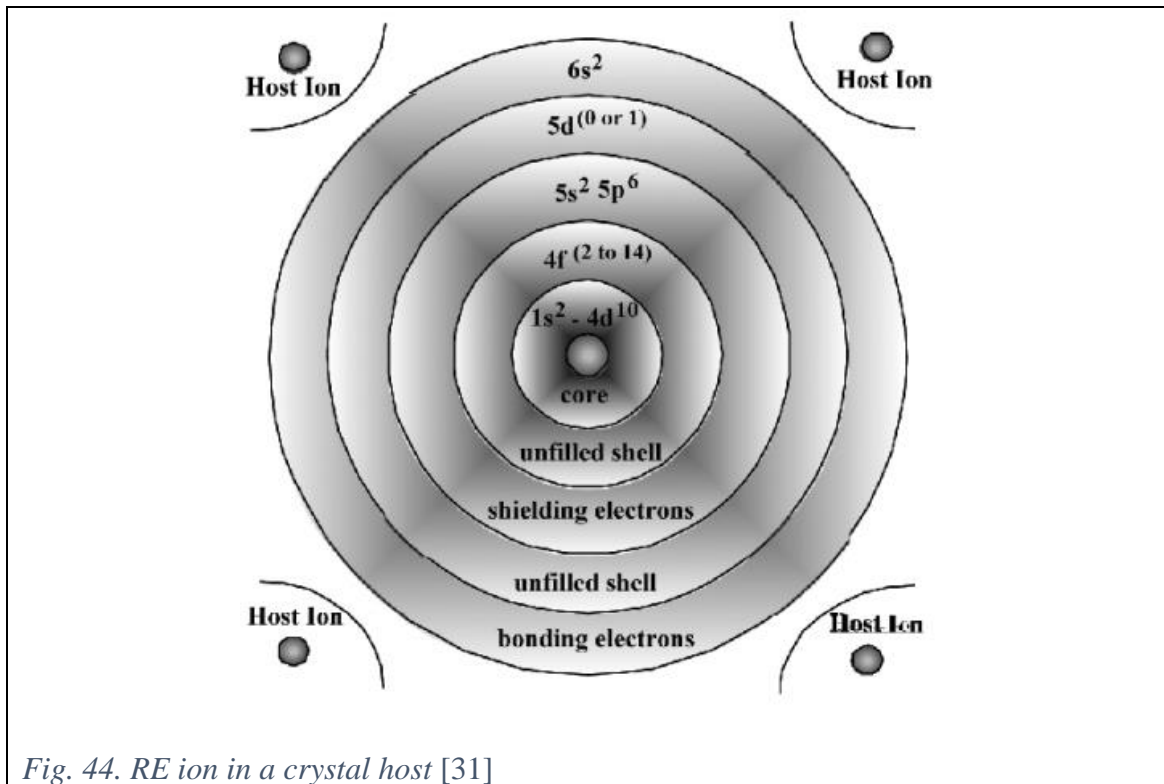


Fig. 44. RE ion in a crystal host [31]

Crystal field can be seen as a perturbation, which splits levels into Stark levels. The total Hamiltonian is given by:

$$H = H_e + H_{so} + H_{CF} \quad (2.3.35)$$

Orders of splitting a RE ion experiences in a CF are of following magnitudes: due to ES,  $10^4 \text{ cm}^{-1}$ , s-o  $10^3 \text{ cm}^{-1}$ , CF  $10^2 \text{ cm}^{-1}$ .

Not all transitions between atomic states are allowed (energetically feasible). Forbidden transitions can occur, but they are not probable. Transition selection rules

depend on the type of transition, whether it is electric dipole (ED), electric quadrupole (E2) or magnetic dipole (MD) transition.

Transition operators  $\mu \in \{\mathbf{P}, \mathbf{M}, \mathbf{Q}\}$ , are given by:

- $\mathbf{P} = -e \sum \mathbf{r}_i$  – ED operator is an odd operator (ungerade (u) inversion symmetry),
- $\mathbf{M} = -\frac{e\hbar}{2mc} \sum (\mathbf{l}_i + 2\mathbf{s}_i)$  – MD operator, even operator (gerade (g) inversion symmetry),
- $\mathbf{Q} = -\frac{1}{2} \sum (\mathbf{k} \mathbf{r}_i) \times \mathbf{r}_i$  – E2 operator, even operator.

For the transitions the selection rules given in Table 3. apply [118].

*Table 3. Selection rules for various transition processes.*

	$\Delta S$	$\Delta L$	$\Delta J$	<b>P</b>
<b>ED</b>	0	0, $\pm 1$	0, $\pm 1$	opposite
<b>MD</b>	0	0	0, $\pm 1$	same
<b>E2</b>	0	0, $\pm 1, \pm 2$	0, $\pm 1, \pm 2$	opposite
<b>Vibronic</b>			0, $\pm 2$	
<b>Phonon processes</b>	0	$\pm 1$	$< 7$ ; if J or J'=0 then 2,4,6	

The probability of a transition is given by  $\langle f | \mu | i \rangle$ . Laporte selection rule states that only the opposite parity states can be connected by an electric dipole (E1) transitions. Parity of a system is the product of parities of the individual components. The parity of photon is given by the radiation field, if it is ED it is thus equal to -1, for MD transition it equal to +1. The algebraic sum of the angular momenta of the electrons in the initial and final state must change by an odd integer. For transitions within 4f shell, the ED transitions are forbidden since the initial and the final state have the same parity and the ED operator has the odd parity, which can be presented as:  $u \otimes u \otimes u = u$ . From Fig. 45 can be seen that 4f shells clearly have an odd parity (ungerade), since there is a change in sign on reflection about the origin.

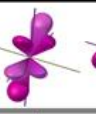
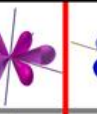
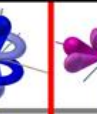
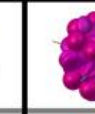
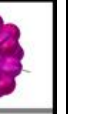
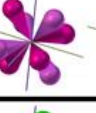
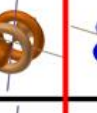
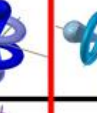
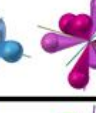
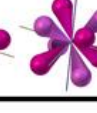
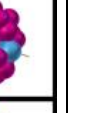
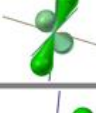
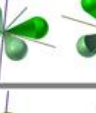
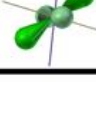
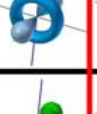
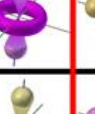
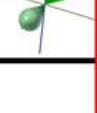
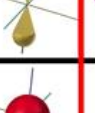
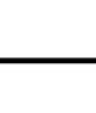
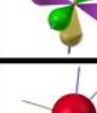
TYPE	SET	INDIVIDUAL ORBITALS						COLLECTIVE	
f	Cubic								
	General								
d	Common								
	"Tri-torus"								
p									
s									

Fig. 45. *spdf orbitals*<sup>6</sup>.

#### 2.3.5.3.1. CF Hamiltonian

The observed spectral lines of 4f-4f transitions have a meaning that for the RE in CF matrix the selection rules for ED transitions, stated in Table 1, no longer apply<sup>7</sup>. In order to allow the transitions, the CF must be non-centrosymmetric (lacking a center of symmetry at the equilibrium position). ED transitions can be forced through parity mixing and result from the perturbation caused by the odd-order terms of the crystal field. In other words, the occurrence and weakness of the ED intra-configurational transitions is explained by small mixing with other opposite parity configurations by the surrounding host material, i.e. CF interaction. The CF interaction lifts the J-degeneracy of the free ion states if the external charge distribution is not invariant under rotations.

For transition metals in a CF the states may be more influenced by the CF than the ES electron repulsion, which is known as the strong field scheme [97]. The weak field scheme applies for RE where 4f-shells are strongly screened from the CF by s, p, d shells, and the value of the s-o component is significant due to the large nuclear charge Z [113].

<sup>6</sup> Image acquired from <http://vixra.org/pdf/1308.0130v1.pdf>

<sup>7</sup> Better interpretation is the introduction of the new transition type, induced ED transitions, for which new selection rules apply.

The main influence of the host material is that the rotational invariance is released, which leads to the splitting of the degenerated  $J$  state into the maximum of  $2J+1$  Stark levels.

The CF Hamiltonian with the charge distribution of the host matrix  $e \cdot \rho(\mathbf{R})$  is:

$$H_{CF} = -\frac{e^2}{4\pi\epsilon_0} \sum_i \int \frac{\rho(R)}{|r_i - R|} dV \quad (2.3.36)$$

where

$$\frac{1}{|r_i - R|} = \sum_{k=0}^{\infty} \frac{r_i^k}{R^{k+1}} \frac{4\pi}{2k+1} \sum_{q=-k}^k Y_q^{k*}(\theta, \phi) Y_q^k(\theta_i, \phi_i) \quad (2.3.37)$$

If we introduce the structural parameters (CF parameters) in the static crystal field expansion, the CF Hamiltonian can be written in the reduced form. The CF structural parameters are given by:

$$A_q^k = -\frac{e^2}{4\pi\epsilon_0} \sqrt{\frac{4\pi}{2k+1}} \int \frac{\rho(R)}{R^{k+1}} Y_q^k(\theta, \phi) dV \quad (2.3.38)$$

Thus, the perturbing CF Hamiltonian represents the inter-shell interactions via the CF potential, and couples the states of the ground and excited configurations, which represents the origin of the JO theory. The CF Hamiltonian is given by:

$$H_{CF} = \sum_{k,q} A_q^k \sum_i r_i^k (c_q^k)_i \quad (2.3.39)$$

The structural parameters depend only on the crystal host and can be calculated in a point charge lattice integral by using the crystallographic data and charges of the host lattice.

The coefficients of the CF expansions can now be defined as a functions of the radial distances, termed crystal field parameters:

$$B_q^k = A_q^k \langle r^k \rangle \quad (2.3.40)$$

CF Hamiltonian is equal to [104]:  $H_{CF} = \sum_{k,q} B_q^k C_q^k$ , which describes the anisotropic components of the CF interactions.

$B_q^k$  terms are generally determined semi-empirically, since the radial parts cannot be calculated exactly [119], and it is the only reliable method for even-rank parameters (the odd-rank terms do not contribute to the energy, therefore their values cannot be adjusted) [50]. With the knowledge of the point symmetry and the CF it is possible to construct the CF energy matrix. The number of non-zero crystal field parameters depends on the site symmetry and increases with lowering the symmetry of the RE ion site [105], i.e. the non-zero crystal field parameters can be determined by checking which of the coefficients contain the same symmetry elements as the point group in question. The matrix is then diagonalized using the set of starting  $B_q^k$  parameters. By fitting them to the experimentally obtained values, the best fit of  $B_q^k$  parameters can be found.

CF strength in any host can be expressed by an overall scalar CF strength parameter, given by [104]:

$$S = \sqrt{\frac{1}{3} \sum_k \frac{1}{2k+1} \left( |B_0^k|^2 + 2 \sum_{q>0} |Re B_q^k|^2 + |Im B_q^k|^2 \right)} \quad (2.3.41)$$

CF potential is represented by one-particle effective operators of even or odd ranks, depending on the coordinates [50]. For 4f-4f transitions the  $k$  can take values  $k = 0, \dots, 7$ . If the initial and final states have the same parity  $k$  must be even, if opposite,  $k$  must be odd. Even  $k$  values are responsible for CF splitting, while odd  $k$  are responsible for the intensity of induced ED transitions for f-f transitions [119]. However, if states of the  $4f^N$  configuration are coupled to states of opposite parity in higher lying configurations, such as  $4f^{N-1}5d$ , then  $k$  must take values  $k = 1, 3, 5$ . Values of  $q$  are limited by the point group of the RE site, since the  $H_{CF}$  must be invariant under all symmetry operations of the point group, and it transforms as the totally symmetric representation, because symmetry operations cannot change the energy of the ion. By grouping crystal field parameters as:

$$B_0^k = \sqrt{\frac{4\pi}{2k+1}} Y_k^0 \sum_L (-Ze)_L \frac{r^k}{R_L^{k+1}} \quad (2.3.42)$$

$$B_q^k = \sqrt{\frac{4\pi}{2k+1}} (-1)^q \text{Re } Y_k^q \sum_L (-Ze)_L \frac{r^k}{R_L^{k+1}} \quad (2.3.43)$$

$$B_q^{k'} = \sqrt{\frac{4\pi}{2k+1}} (-1)^q \text{Re } Y_k^q \sum_L (-Ze)_L \frac{r^k}{R_L^{k+1}} \quad (2.3.44)$$

CF Hamiltonian can be rewritten as [119]:

$$H_{CF}(r_i) = \sum_k \left( B_0^k (C_0^k)_i + \sum_{q=1}^k \left( B_q^k \left( (C_{-q}^k)_i + (-1)^q (C_q^k)_i \right) + B_q^{k'} i \left( (C_{-q}^k)_i - (-1)^q (C_q^k)_i \right) \right) \right) \quad (2.3.45)$$

### 2.3.5.3.2. Symmetry groups

Because Hamiltonian must be invariant under operations of the point symmetry group,  $k$  and  $q$  values are also limited by the point group symmetry. Equating CF expansion with the expansion that has been transformed through operations of the point symmetry group gives the allowed CF parameters for a particular point symmetry.  $B_0^0$  are spherically symmetric and result only in a uniform shift of all levels of a given configuration, and can be ignored as far as the CF splitting is concerned. Since the terms with  $k$ -odd vanish for configurations containing solely equivalent electrons,  $4f^N$  configuration CF matrix elements are given by [34]:

$$\langle f^N \alpha SLJM | H_{CF} | f^N \alpha' SL'J'M' \rangle = \sum_{k,q} B_q^k \langle f^N \alpha SLJM | U_q^k | f^N \alpha' SL'J'M' \rangle \langle f || C^k || f \rangle \quad (2.3.46)$$

Point groups may be classified under different symmetry groups [31,34,119]:

1. Cubic:  $O_h$ ,  $O$ ,  $T_d$ ,  $T_h$ ,  $T$
2. Hexagonal:  $D_{6h}$ ,  $D_6$ ,  $C_{6v}$ ,  $C_{6h}$ ,  $C_6$ ,  $D_{3h}$ ,  $C_{3h}$ ; Trigonal subgroup:  $D_{3d}$ ,  $D_3$ ,  $C_{3v}$ ,  $S_6 = C_{3i}$ ,  $C_3$
3. Tetragonal:  $D_{4h}$ ,  $D_4$ ,  $C_{4v}$ ,  $C_{4h}$ ,  $C_4$ ,  $D_{2d}$ ,  $S_4$
4. Lower symmetry:
  - a. Orthorhombic:  $D_{2h}$ ,  $D_2$ ,  $C_{2v}$ ,
  - b. Monoclinic:  $C_{2h}$ ,  $C_2$ ,  $C_s$ ,

c. Triclinic:  $S_2 = C_i, C_1$

In hexagonal symmetry  $q = 6$ , in tetragonal  $q = 4$ , trigonal  $q = 3$ , orthorhombic  $q = 2$ , monoclinic  $q = 2$ , and triclinic  $q = 1$ . The difference between orthorhombic and monoclinic CF is that for orthorhombic only real CF parameters have to be considered.

The number of levels a state of given  $J$  will be split for each of the 32 crystallographic point groups is given in Table 4 and Table 5.

Table 4. CF splitting for integral  $J$ .

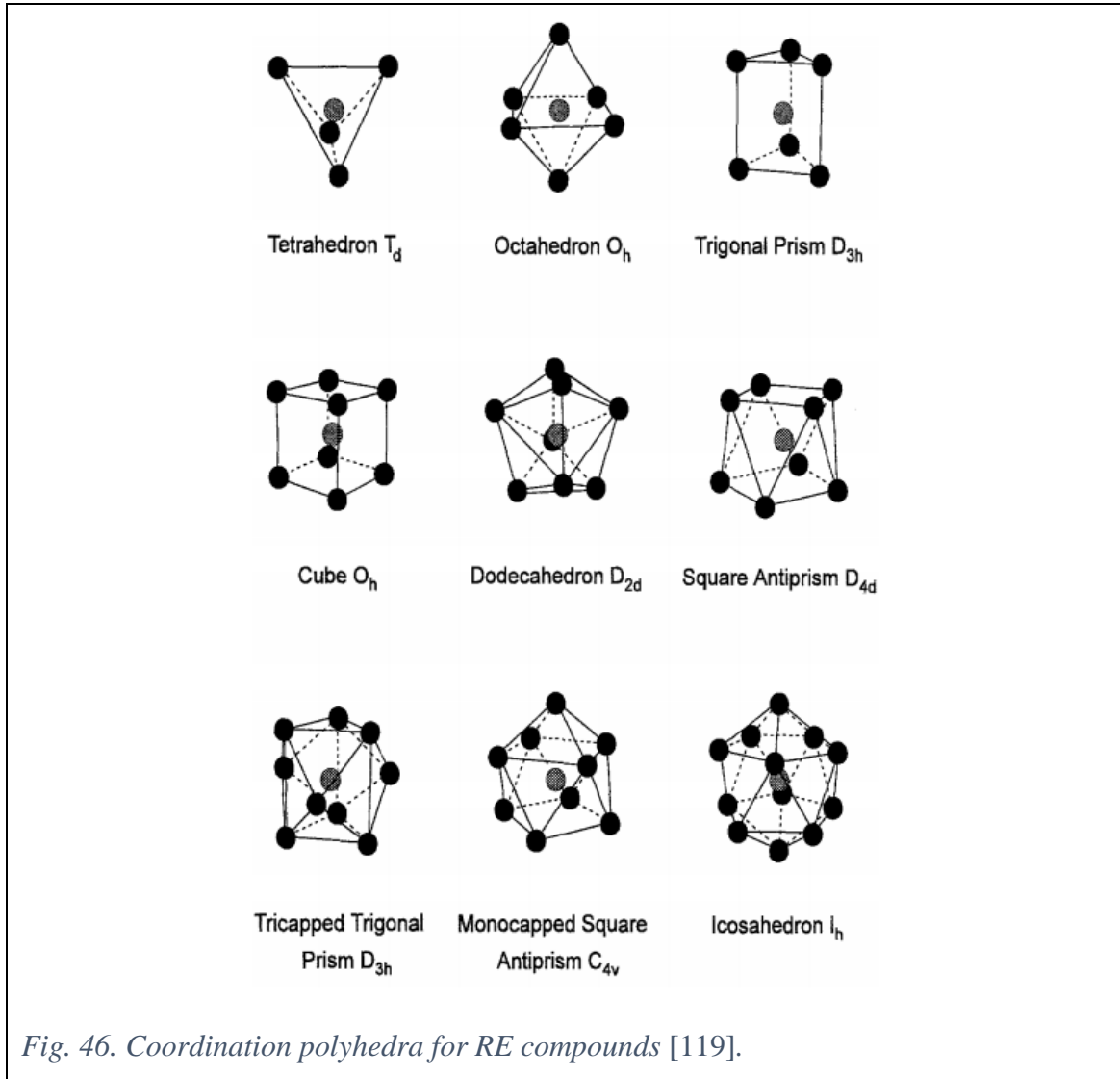
<b>J</b>	<b>0</b>	<b>1</b>	<b>2</b>	<b>3</b>	<b>4</b>	<b>5</b>	<b>6</b>	<b>7</b>	<b>8</b>
<b>Cubic</b>	1	1	2	3	4	4	6	6	7
<b>Hexagonal</b>	1	2	3	5	6	7	9	10	11
<b>Tetragonal</b>	1	2	4	5	7	8	10	11	13
<b>Lower symmetry</b>	1	3	5	7	9	11	13	15	17

Table 5. CD splitting for half-integral  $J$ .

<b>J</b>	<b>1/2</b>	<b>3/2</b>	<b>5/2</b>	<b>7/2</b>	<b>9/2</b>	<b>11/2</b>	<b>13/2</b>	<b>15/2</b>
<b>Cubic</b>	1	1	2	3	3	4	5	5
<b>All other symmetries</b>	1	2	3	4	5	6	7	8

Out of those 32 point groups, 21 are non-centrosymmetric:  $C_{6v}, C_6, D_6, D_{3h}, D_3, C_{3v}, C_{3h}, C_3, D_4, C_{4v}, C_4, S_4, D_{2d}, D_2, C_{2v}, C_2, C_s, C_1, O, T_d$  and  $T$ , while 11 are centrosymmetric:  $O_h, T_h, D_{6h}, C_{6h}, D_{4h}, C_{4h}, D_{3d}, C_{3i}, D_{2h}, C_{2h}$  and  $C_i$  [119]. JO theory limits the induced ED transitions to the point groups with no center of symmetry, since then the odd part of the CF potential will be non-zero and intensity can be achieved by mixing configurations of opposite parity into the 4f wave functions. If ED transitions are observed in centrosymmetric systems, their existence is attributed to the vibronic coupling. MD transitions are allowed in any symmetry, since MD operator has the gerade parity.

Coordination geometries for RE compounds in some symmetries is given in Fig. 46 as a visual aid.



#### 2.3.5.4. IC induced ED tensor operator

It is useful to introduce tensor forms of CF and ED operators. ED operator  $\mathbf{P} = -e \sum \mathbf{r}_i$  has the tensor form:

$$D_q^1 = -e \sum_i r_i^k (c_q^k)_i \quad (2.3.47)$$

and CF tensor operator is equal to the CF Hamiltonian:

$$D_q^k = \sum_{k,q} A_q^k \sum_i r_i^k (c_q^k)_i \quad (2.3.48)$$

Let us now define the notation for the states. The initial and final states of single parity are given by  $\langle \varphi_a |$  and  $|\varphi_b \rangle$ , respectively. The initial and the final states of higher

energy, opposite parity configurations are given by  $\varphi_\beta$ . The initial and final mixed parity states are labeled by  $|\psi_a\rangle$  and  $|\psi_b\rangle$ , respectively.

If the symmetry of the CF is different from the eigenstates involved, then degenerate states will split. In this case  $E_n^{(0)} - E_i^{(0)} = 0, n \neq i$ . In order to determine the eigenstates and eigenvalues, first the matrix element  $\langle \phi_i^{(0)} | H' | \phi_n^{(0)} \rangle$  must be set to zero when  $E_n^{(0)} - E_i^{(0)} = 0$ , which can be accomplished by diagonalizing the submatrix of  $H'$  in which contains the degenerate states, and the energy splittings may be obtained [97].

Since the CF is small, it can be taken as a first-order perturbation.  $\langle \varphi_a |$  and  $|\varphi_b\rangle$  and the respective energies are known, thus the time-independent perturbation theory to the first order is given by:

$$|\psi_b\rangle = |\varphi_b\rangle + \sum_{\beta} \frac{\langle \varphi_\beta | D_q^k | \varphi_b \rangle}{E_b - E_\beta} |\varphi_\beta\rangle, \langle \psi_a | = \langle \varphi_a | + \sum_{\beta} \frac{\langle \varphi_a | D_q^k | \varphi_\beta \rangle}{E_a - E_\beta} \langle \varphi_\beta | \quad (2.3.49)$$

For ED transition between the states  $\psi_a$  and  $\psi_b$ , matrix elements of the electric dipole moment are:

$$\langle \psi_a | D_q^1 | \psi_b \rangle = \sum_{\beta} \left( \frac{\langle \varphi_a | D_q^1 | \varphi_\beta \rangle \langle \varphi_\beta | D_q^k | \varphi_b \rangle}{E_a - E_\beta} + \frac{\langle \varphi_a | D_q^k | \varphi_\beta \rangle \langle \varphi_\beta | D_q^1 | \varphi_b \rangle}{E_b - E_\beta} \right) \quad (2.3.50)$$

In order to solve this equation, two approximations must be made [33,50,55]:

1. States of  $\varphi_\beta$  are taken to have the same average energy, i.e. the states of  $\varphi_\beta$  are completely degenerate in J. This is justified by the large distance to the ground configuration, so that from the point of the ground state, the higher-configuration states all look close.
2. The difference of the average energy of the higher-configuration states and the initial and the final state are approximately equal:  $E_a - E_\beta = E_b - E_\beta$ .

The assumption No.2 allows the removal of the energy denominators. The approximation No.1 allows the closure relation  $\sum_{\beta} |\varphi_\beta\rangle \langle \varphi_\beta| = 1$  to be used, thus  $D_q^1$  and  $D_q^k$  can be united to a single operator, i.e. the angular parts  $C_q^k =$

$(-1)^{l'} \sqrt{(2l'+1)(2l+1)} \begin{pmatrix} l & 1 & l' \\ 0 & 0 & 0 \end{pmatrix} U_q^k = \langle l \| C^k \| l' \rangle U_q^k$  of the electric dipole operator and CF:

$$U_q^t U_p^t = \sum_{\lambda} (-1)^{1+t+\lambda+Q} (2\lambda+1) \left\{ \begin{matrix} 1 & t & \lambda \\ l & l & l' \end{matrix} \right\} \begin{pmatrix} 1 & t & \lambda \\ q & p & Q \end{pmatrix} U_Q^\lambda \quad (2.3.51)$$

where  $Q = -q - p$  and  $\lambda = 1 + t$ .

### 2.3.5.5. IC reduced matrix elements (RME)

Matrix elements of spherical tensor operators on the basis of angular momentum eigenstates can be expressed as the product of two factors: one is independent of angular momentum orientation, and the other is Clebsch-Gordan coefficients, by the Wigner-Eckart theorem:

$$\begin{aligned} \langle j'm'\alpha' | T_q^k | jm\alpha \rangle &= \langle jm\alpha \ kq | j'm'\alpha' \rangle \langle j'\alpha' \| T^k \| j\alpha \rangle = \\ &= (-1)^{j'-m'} \begin{pmatrix} j' & k & j \\ -m' & q & m \end{pmatrix} \langle j'\alpha' \| T^k \| j\alpha \rangle \end{aligned} \quad (2.3.52)$$

where:

- $T^k$  is a tensor operator of rank  $k$ , which transforms like the spherical harmonics  $Y_{kq}(\theta, \phi)$ ,
- $\langle jm\alpha \ kq | j'm'\alpha' \rangle$  are Clebsch-Gordan coefficients, for coupling  $j$  and  $k$  in order to obtain  $j'$ ,
- $\langle j'\alpha' \| T^k \| j\alpha \rangle$  is RME; it depends neither on the magnetic quantum numbers ( $m$  and  $m'$ ), nor on  $q$ -component of the tensor operator.
- $\alpha$  is just some other quantum number.

Operating with a spherical tensor operator of rank  $k$  on an angular momentum eigenstate  $|jm\alpha\rangle$  is like adding angular momentum  $k$  to the state.

The main advantage is that any matrix element of a tensor operator can be calculated by multiplying 3j-symbol with the corresponding RME, which has to be calculated only once for a particular combination of  $T_q^k, j'$  and  $j$ . Wigner-Eckart theorem thus separates the geometry (3j-symbol) from physics (RME).

Now tensor operators  $U^k$  and  $L+gS$ , can be introduced, which are a single electron tensor for ED 4f-4f transition intensities and MD transition intensities, respectively. Their RME are given by the following equations [33,103]:

$$\langle 4f^6 SL \| U^k \| 4f^6 SL' \rangle = 6\sqrt{(2L+1)(2L'+1)} \sum_{\psi(4f^5)} (4f^5 \bar{S} \bar{L} | 4f^6 SL) \begin{Bmatrix} L & l & \bar{L} \\ l & L' & k \end{Bmatrix} (-1)^{\bar{L}+L+l+k} \quad (2.3.53)$$

Equation 2.3.53 is expressing the states of a  $4f^6$  configuration as a linear combination of the states of the preceding  $4f^5$  electron configuration angular-momentum-coupled to the additional 4f electron. By coupling S and L to J:

$$\langle 4f^6 SLJ \| U^k \| 4f^6 SL'J' \rangle = (-1)^{S+L'+J+k} \sqrt{(2J+1)(2J'+1)} \begin{Bmatrix} J & J' & k \\ L & L & S \end{Bmatrix} \langle 4f^6 SL \| U^k \| 4f^6 SL' \rangle \quad (2.3.54)$$

The IC RME of an arbitrary tensor operator X between two IC wavefunctions is given by:

$$\langle 4f^N SLJ \| X \| 4f^N S' L' J' \rangle = \sum_i \sum_j c_i c_j \langle 4f^N SLJ \| X \| 4f^N S' L' J' \rangle, X \in \{U^k, V^{11}, L + gS\} \quad (2.3.55)$$

RME are responsible for the CF splitting of a J level, with splitting magnitude proportional to the RME, i.e. levels with large values of RME show a greater CF splitting. Since RME are relatively insensitive to the chemical nature and symmetry of the host matrix, they can be regarded as constants for a given trivalent ion [119].

### 2.3.5.6. IC ED matrix elements

The effective tensor operator can be further simplified by utilizing the Wigner-Eckart theorem:

$$\langle JM | U_Q^\lambda | J' M' \rangle = (-1)^{J-M} \begin{pmatrix} J & \lambda & J' \\ -M & Q & M' \end{pmatrix} \langle J \| U^\lambda \| J' \rangle \quad (2.3.56)$$

where J, M and J', M' are the quantum numbers of the  $\psi_a$  and  $\psi_b$ , respectively.

The geometry of the angular momentum transformations is contained in the 3j symbol, while the physics of the dynamics is in the RME of  $U^\lambda$ . Now the matrix elements of ED transition can be given as:

$$\langle \psi_a | D_q^1 | \psi_b \rangle = -e \sum_{t,p,\lambda,Q} (-1)^{-Q} A_q^t \Xi(t, \lambda) (2\lambda + 1) \begin{pmatrix} 1 & \lambda & t \\ q & Q & p \end{pmatrix} \langle \psi_a | U_Q^\lambda | \psi_b \rangle \quad (2.3.57)$$

where

$$\Xi(t, \lambda) = 2 \sum_{\beta} \begin{Bmatrix} 1 & t & \lambda \\ l & l & l' \end{Bmatrix} \langle l \| C^1 \| l' \rangle \langle l' \| C^t \| l \rangle \frac{\langle \psi_a | r | \psi_b \rangle \langle \psi_a | r^t | \psi_b \rangle}{E_{\frac{\beta}{b}} - E_{\beta}} \quad (2.3.58)$$

In the summations above,  $t$  takes only odd values, since only the odd-order terms in the multipole expansion of the CF contribute to the parity mixing, while the even-order terms are only responsible for shifting and splitting of the energy levels. The matrix element of  $D_q^1$  is non-vanishing only if  $1 + \lambda + t$  is even; thus  $\lambda$  takes even values. The 3j and 6j symbols give the selection rules for ED transition:

- The spin cannot change, i.e.  $\Delta S=0$ ,
- $\Delta L \leq 6$ ,
- $J = 0 \rightarrow J' = 0$  transition is forbidden,
- $\Delta J \leq 6$ ,
- if  $J = 0$  or  $J' = 0$ , then  $\Delta J = 2, 4, 6$

and limit  $\lambda$  to values 2, 4, or 6 [50].

It is possible to derive another selection rule [120]:  $\Delta J \leq \lambda$ . This means that for  $\lambda = 2$ ,  $\Delta J \leq 2$ , i.e. for transitions in which  $\Delta J > 2$ ,  $U^2$  is equal to zero. Analogous goes for  $\lambda = 4, 6$ . This selection rule can ease the estimation of the RME by quick estimation of the zero value RME. E.g. in the case of  $\text{Eu}^{3+}$ , this limits the allowed ED transitions from the first excited state  $^5D_0$  only to  $^7F_{2,4,6}$ .

### 2.3.6. Transition mechanisms for RE [55]

A resonant transfer of energy from a radiation field to matter is called absorption. An absorption has as a consequence the creation of the induced dipole moment. The transfer of energy from matter to the field is called emission, or luminescence.

MD transition occurs when the RE ion interacts with the magnetic field component of the photon through MD. The transition will possess MD component if

during a transition the electron is displaced over a curved path, i.e. a rotational displacement of charge occurs. Because the rotation is not reversed through inversion center, MD transition has even parity and is thus allowed in the 4f-4f transitions.

Induced ED transitions follow the creation of an ED by the linear movement of charge, and a transition has odd parity. Induced ED transitions occur when non-centrosymmetric interactions allow the mixing of opposite parity electronic states.

The notation used for electric dipole strength is  $D$  for randomly oriented systems, and  $D'$  for the oriented ones, and the relations between them are simple:  $D=3D'$ , meaning that the in the randomly oriented systems  $D$  is the sum of  $D'$  over the three orientations. Oscillator strength  $P$  is equal to  $P'$ . Theoretical values will not be emphasized, while the experimental ones will be labeled by *exp*.

#### 2.3.6.1. Experimental dipole and oscillator strengths

Molar absorptivity  $\varepsilon$  can be calculated from the absorbance  $A$  by the Beer's law [103]:  $A[\text{dim: } /]=\varepsilon Cd=\ln(I_0/I)$ , where  $C$  is the concentration, and  $d$  is the optical pathlength. The area under the peak is, however, a better measure of the intensity:  $\int \varepsilon(\tilde{\nu})d\tilde{\nu}$ , where  $\tilde{\nu}$  is the wavenumber or energy in  $\text{cm}^{-1}$ .

Instead of the molar absorptivity for the measure of intensity, the dipole strength  $D$  or oscillator strength  $P$  are being used. Molar absorptivity and dipole strength are related by:

$$\varepsilon(\tilde{\nu}) = \frac{8\pi^3}{hc} \frac{N_A}{2303} f(\tilde{\nu})\tilde{\nu}D'_{\text{exp}} \quad (2.3.59)$$

where  $f$  represents the line shape function, which integral can be greatly simplified by:  $\int f(\tilde{\nu})\tilde{\nu}d\tilde{\nu} = \tilde{\nu}_0$ , where  $\tilde{\nu}_0$  is the wavenumber of the absorption maximum. Thus the integral of the molar absorptivity is given by:

$$\int \varepsilon(\tilde{\nu})d\tilde{\nu} = \frac{8\pi}{hc} \frac{N_A X_A(T)}{2303} \tilde{\nu}_0 D'_{\text{exp}} = 3 \cdot 108.9 \cdot 10^{36} \cdot X_A \cdot (T) \tilde{\nu}_0 D'_{\text{exp}} \quad (2.3.60)$$

where  $X_A(T)$  is the fractional thermal population of the initial level, given by:

$$X_A(T) = \frac{g_A e^{-\frac{\Delta E_A}{kT}}}{\sum_i g_i e^{-\frac{\Delta E_i}{kT}}} \quad (2.3.61)$$

where  $\Delta E_A$  is the energy difference between the initial level and the ground level,  $\Delta E_i$  is between the level  $i$  and the ground level,  $g_A$  is the degeneracy of the initial level, and  $g_i$  is the degeneracy of the level  $i$ . The summation runs over all energy levels of the  $4f^N$  configuration, but may be truncated at  $2000 \text{ cm}^{-1}$ , since a contribution of higher energy levels are small.

For the symmetric line function, and for the general shape of  $f$ :

$$\int \frac{\varepsilon(\tilde{\nu})}{\tilde{\nu}} d\tilde{\nu} = 3 \cdot 108.9 \cdot 10^{36} X_A(T) \tilde{\nu}_0 D'_{\text{exp}} \quad (2.3.62)$$

$D'_{\text{exp}}$  is related to  $P_{\text{exp}}$  by:

$$P_{\text{exp}} = \frac{8\pi^2 mc}{he^2} \tilde{\nu}_0 D'_{\text{exp}} = 1.41 \cdot 10^{30} \cdot \tilde{\nu}_0 D', D'_{\text{exp}} = 7.089 \cdot 10^{-31} \frac{P_{\text{exp}}}{\tilde{\nu}_0} \quad (2.3.63)$$

thus  $P$  is related to molar absorptivity by [103]:

$$P'_{\text{exp}} = \frac{4.32 \cdot 10^{-9}}{X_A(T)} \int \varepsilon(\tilde{\nu}) d\tilde{\nu} \quad (2.3.64)$$

$P$  are usually of the order of  $10^{-6}$ . For the same dipole strengths, transitions in the IR have larger oscillator strengths than the transitions in the UV region. Since it is directly proportional to the integrated molar absorptivity it is convenient for comparing experimental intensities. The dipole strength is wavelength independent and has much simpler definition, thus it is preferred figure for theoretical calculations.

### 2.3.6.2. Theoretical dipole and oscillator strengths

$D'$  is defined as the absolute square of the matrix element in the dipole operator  $X$  (which stands for ED or MD operator) between the wavefunctions of the initial and the final state:

$$D' [esu^2 cm^2] = |\langle \psi_i | X_\rho^1 | \psi_f \rangle|^2, D = |\langle \psi_i | X | \psi_f \rangle|^2 \quad (2.3.65)$$

where  $\rho$  can be  $x$ ,  $y$  or  $z$  orientation.

An oscillator strength is a measure of the strength of a transition, and it is described by the ratio of the actual intensity to the intensity radiated by one electron oscillating harmonically in 3D. Thus, for a 3D harmonic oscillator  $P$  equals 1.

$D'$  is related to  $P$  by:

$$P = \frac{8\pi^2 mc}{he^2} \tilde{\nu}_0 D' = 1.41 \cdot 10^{30} \cdot \tilde{\nu}_0 D', D' = 7.089 \cdot 10^{-31} \frac{P}{\tilde{\nu}_0} \quad (2.3.66)$$

### 2.3.6.3. Comparing experimental and theoretical values

In a single crystal of non-cubic symmetry, no CF degeneracy higher than  $g_A = 2$  is found. For randomly oriented systems the degeneracy of the ground state is  $g = 2J+1$ . The addition of degeneracy factor is due the summation of the matrix elements over all the  $M$  components of the ground state, with assumption of equal population of all the Stark levels.

In order to compare the theoretical and the experimental values it is necessary to introduce the corrections due to the effects of the dielectric medium. The factor  $\chi$  takes into account that the local electric field,  $E_{loc}$ , at the site of the ion undergoing an optical transition is generally different from the macroscopic field in the medium  $E$ . The local field is a total field consisting of the electric field of the incident light  $E$ , plus the electric field of dipoles. The exact correction is given by  $(E_{loc}/E)^2$ . The virtual-cavity or Lorentz model is appropriate for RE doped crystals to introduce the necessary corrections to a first approximation. For an ED-induced absorption it is given by  $\chi_{ED}^{abs} = \frac{(n^2+2)^2}{9}$ , while in the case of emission  $\chi_{ED}^{em} = n\chi_{ED}^{abs}$ , where the absorption coefficient has been multiplied by a refractive index to account for the speed of light in matter.  $\chi_{MD}^{abs} = n$  and  $\chi_{MD}^{em} = n^3$ .

The refractive index values should be given at the wavelength of the barycenter of a transition. Usually, they can be evaluated by the Sellmeier's dispersion relation [121]:

$$n(\lambda) = \sqrt{1 + \sum_{i=1}^3 \frac{B_i \lambda^2}{\lambda^2 - C_i}} \quad (2.3.67)$$

Thus, the experimental dipole and oscillator strengths are related to theoretical values by:

$$D'_{\text{exp}} = \frac{\chi}{g_A} D', P'_{\text{exp}} = \frac{\chi}{g_A} P', D_{\text{exp}} = \frac{\chi D}{2J+1}, P_{\text{exp}} = \frac{\chi P}{2J+1} \quad (2.3.68)$$

It should be noted that these correction factors are valid only for low concentrations so that the interactions between neighboring RE ions can be neglected.

#### 2.3.6.4. Review of the experimental and theoretical values

To sum up, the theoretical dipole strengths can be calculated from the squared matrix elements of the dipole operator. The theoretical oscillator strength can be calculated from the theoretical dipole strengths. Dipole strengths are preferred in the theoretical, and oscillator in the experimental approach. Experimental values in the absorption spectrum are obtained from the integral of the molar absorptivity.

Theoretical values:

$$D' [esu^2 cm^2] = |\langle \psi_i | X_\rho^1 | \psi_f \rangle|^2, D = |\langle \psi_i | X | \psi_f \rangle|^2, P = \frac{8\pi mc}{he^2} \frac{1}{3} \tilde{\nu}_0 D \quad (2.3.69)$$

Experimental values:

$$D_{\text{exp}} = \frac{1}{108.9 \cdot 10^{36} \cdot X_A(T)} \int \frac{\varepsilon(\tilde{\nu})}{\tilde{\nu}} d\tilde{\nu}, D'_{\text{exp}} = \frac{D_{\text{exp}}}{3} \quad (2.3.70)$$

$$\begin{aligned} P_{\text{exp}} &= \frac{8\pi^2 mc \tilde{\nu}_0}{he^2} \frac{1}{3} D_{\text{exp}} = \frac{4.702 \cdot 10^{29}}{108.9 \cdot 10^{36} \cdot X_A(T)} \int \varepsilon(\tilde{\nu}) d\tilde{\nu} = \\ &= 4.32 \cdot 10^{-9} \int \varepsilon(\tilde{\nu}) d\tilde{\nu} \end{aligned} \quad (2.3.71)$$

#### 2.3.6.5. MD transitions

MD tensor operator is given by:

$$\mathbf{M} = -\frac{e\hbar}{2mc} \sum (\mathbf{l}_i + g_S \mathbf{s}_i), \mathbf{M}_\rho^1 = -\frac{e\hbar}{2mc} (\mathbf{L} + g_S \mathbf{S})_\rho^1 \quad (2.3.72)$$

where  $\frac{e\hbar}{2mc} = 9.273 \cdot 10^{-21} \text{ esu cm}$ ,  $\rho$  is the polarization number or component, and 1 represents the tensor rank. Then the matrix element of the oriented MD is given by:

$$\langle \psi_i | \mathbf{M}_\rho^1 | \psi_f \rangle = -\frac{e\hbar}{2mc} \langle \psi_i | (\mathbf{L} + g_S \mathbf{S})_\rho^1 | \psi_f \rangle \quad (2.3.73)$$

This matrix element can be calculated by the application of the Wigner-Eckart theorem to remove the  $\rho$  dependence:

$$\begin{aligned} & \langle 4f^N SLJM | (\mathbf{L} + g_S \mathbf{S})^1 | 4f^N S' L' J' M' \rangle = \\ & = (-1)^{J-M} \begin{pmatrix} J & 1 & J' \\ -M & \rho & M' \end{pmatrix} \langle 4f^N SLJ || (\mathbf{L} + g_S \mathbf{S})^1 || 4f^N S' L' J' \rangle \end{aligned} \quad (2.3.74)$$

RME in equation 2.3.74 can be calculated by splitting the  $\mathbf{L}$  and  $\mathbf{S}$  components [31]:

$$\delta_{SS'} \delta_{LL'} (-1)^{S+L+J+1} \begin{Bmatrix} L & J & S \\ J' & L & 1 \end{Bmatrix} \sqrt{(2L+1)(2J+1)(2J'+1)L(L+1)} \quad (2.3.75)$$

$$\delta_{SS'} \delta_{LL'} (-1)^{S+L+J+1} \begin{Bmatrix} S & J & L \\ J' & S & 1 \end{Bmatrix} \sqrt{(2S+1)(2J+1)(2J'+1)S(S+1)} \quad (2.3.76)$$

3j and 6j coefficients in previous equations limit the number of allowed transitions. The resulting selection rules for the MD transition are [119]:

- $\Delta S = 0, \Delta L = 0$  – only in the Russell-Saunders coupling scheme,
- $J = 0 \rightarrow J' = 0$  is forbidden,
- $\Delta J = 0, \pm 1$ .

In the IC coupling scheme only  $J$  remains a good quantum number. From the selection rules, the three different cases can be distinguished for MD matrix elements [103]:

- $J = J'$ :  $\langle 4f^N SLJ || (\mathbf{L} + g_S \mathbf{S})^1 || 4f^N S' L' J \rangle = g \sqrt{J(J+1)(2J+1)}$
- $J' = J - 1$ :  $\langle 4f^N SLJ || (\mathbf{L} + g_S \mathbf{S})^1 || 4f^N S' L' (J - 1) \rangle = \sqrt{\frac{(S+L+J+1)(S+L+J-1)(J+S-L)(J+L-S)}{4J}}$
- $J' = J + 1$ :  $\langle 4f^N SLJ || (\mathbf{L} + g_S \mathbf{S})^1 || 4f^N S' L' (J + 1) \rangle = \sqrt{\frac{(S+L+J+2)(S-L+J+1)(J-S+L+1)(-J+L+S)}{4(J+1)}}$

where  $g$  is the Lande  $g$ -factor which describes the effective magnetic momentum, given by:  $g = 1 + \frac{J(J+1) - L(L+1) + S(S+1)}{2J(J+1)}$ .

MD RME in IC coupling scheme is then given by [33]:

$$\langle 4f^N SLJ || (\mathbf{L} + g_S \mathbf{S})^1 || 4f^N S' L' J' \rangle = \sum_i \sum_j c_i c_j \langle 4f^N SLJ || (\mathbf{L} + g_S \mathbf{S})^1 || 4f^N S' L' J' \rangle \quad (2.3.77)$$

The calculated MD strength can now be evaluated, but it is expressed in the Bohr magneton squared [ $\beta^2$ ]. The conversion to the units used for dipole strength is:  $1\beta = 9.273 \cdot 10^{-21}$  esu cm. Thus the values for theoretical dipole and oscillator strength are, respectively [116]:

$$D_{MD} [esu^2 cm^2] = \frac{e^2 \hbar^2}{4m^2 c^2} |\langle 4f^N SLJ || (\mathbf{L} + g_S \mathbf{S})^1 || 4f^N S' L' J' \rangle|^2 \quad (2.3.78)$$

$$P_{MD} = \frac{8\pi^2 mc \tilde{\nu}_0}{3he^2} D_{MD} \quad (2.3.79)$$

The intensity of an MD transition is relatively independent of the surroundings. Europium is unique element due its pure MD transitions  ${}^5D_0 \rightarrow {}^7F_1$ ,  ${}^5D_1 \rightarrow {}^7F_0$ , and almost pure  ${}^5D_2 \rightarrow {}^7F_1$ , with dipole strengths  $9.4 \cdot 10^{-42}$  esu<sup>2</sup> cm<sup>2</sup>,  $1.8 \cdot 10^{-42}$  esu<sup>2</sup> cm<sup>2</sup> and  $0.9 \cdot 10^{-42}$  esu<sup>2</sup> cm<sup>2</sup> [122], respectively. Ref. [55] also states value  $9.4 \cdot 10^{-42}$  esu<sup>2</sup> cm<sup>2</sup>, which is due to the temperature correction at a room temperature, while in literature is most commonly found temperature uncorrected value of  $9.6 \cdot 10^{-42}$  esu<sup>2</sup> cm<sup>2</sup> [123].

#### 2.3.6.6. Mixed ED and MD transitions

In general, a transition is not a pure induced ED or MD. Experimental dipole strength can be compared with the total calculated dipole strength by:

$$D'_{\text{exp}} = \frac{1}{g_A} (\chi_{ED} D'_{MD} + \chi_{ED} D'_{ED}), D_{\text{exp}} = \frac{1}{2J+1} (\chi_{ED} D_{MD} + \chi_{ED} D_{ED}) \quad (2.3.80)$$

with analogues equations are for the oscillator strengths.

#### 2.3.6.7. Spontaneous radiative transitions

Types of EM interactions with matter can be classified as absorption, induced emission and spontaneous emission, with coefficients  $B_{12}$ ,  $B_{21}$  and  $A$ , respectively. In order for decay to begin, followed by a photon release, something is needed to perturb the excited electrons, otherwise the transitions would not be initiated. There is always some EM field present in the vicinity of an atom, at whatever frequency is required to

induce the charge oscillations and to initiate the radiation process, called *spontaneous emission*. Alternatively, if the transition is initiated by the external EM field the resulting decay is called a *stimulated emission* [97]. The population equilibrium is then given by:

$$N_1 B_{12} \rho_\nu = N_2 (B_{21} \rho_\nu + A) \quad (2.3.81)$$

where  $N = N_1 + N_2$  is the total number of electrons,  $\rho_\nu$  is the spectral energy density of the radiation field at frequency  $\nu$ . The Plank's law gives the energy density in thermal equilibrium:

$$\rho_\nu d\nu = \frac{8\pi\nu^2 n^3}{c^3} \frac{h\nu}{e^{kT} - 1} d\nu \quad (2.3.82)$$

The population of the states, i.e. the occupation numbers are then given by:

$$\frac{N_2}{N_1} = \frac{g_2}{g_1} e^{-\frac{h\nu}{kT}} \quad (2.3.83)$$

where  $g$  is the degeneracy of a level given in its subscript, given by  $g_i = 2J_i + 1$ .

The spontaneous emission is then given in relation to the absorption coefficient by the radiative transition probability (RT):

$$A = \frac{8\pi h \nu^3 n^3 g_2}{c^3 g_1 B_{12}} \quad (2.3.84)$$

The spontaneous emission is equal to the sum of all spontaneous emissions from the higher, to the lower J-multiplet, i.e. it is a sum of transitions originating from all Stark levels of the upper level to all the Stark levels of the final lower level (factor 1/3 and sum over  $q$  exist to average the polarization modes):

$$A(J \rightarrow J') = \frac{1}{3g_2} \sum_{M_1, M_2, q} A(M_1, M_2, q) \quad (2.3.85)$$

The spontaneous emission is the classical equivalent to the line strength and is given by [103,104,124]:

$$A(J \rightarrow J') = \frac{64\pi^4 \tilde{\nu}^3}{3h(2J+1)} (\chi_{ED} D_{ED} + \chi_{MD} D_{MD}) \quad (2.3.86)$$

Where it is assumed that the transition has a mixed ED and MD character. For the pure transitions of europium, starting from the  $^5D_0$  level and finishing at the  $^7F_{1,2,4,6}$ , equation 2.3.86 equals to:

$$\begin{aligned} A_{\lambda}(^5D_0 \rightarrow ^7F_{\lambda}) &= \frac{64\pi^4 \tilde{\nu}_{\lambda}^3 n_{\lambda} (n_{\lambda}^2 + 2)^2}{3h \cdot 9} D_{ED}^{\lambda}, \\ A_1(^5D_0 \rightarrow ^7F_1) &= \frac{64\pi^4 \tilde{\nu}_1^3}{3h} n_1^3 D_{MD} \end{aligned} \quad (2.3.87)$$

for  $\lambda=2,4,6$ . In JO model  $A(^5D_0 \rightarrow ^7F_J, J = 0, 3, 5) = 0$ , since those transitions are forbidden by the selection rules.

As in the absorption process, there is an assumption that all CF component of the initial state are equally populated. If fluorescence can be detected, the lifetime of the state is long compared to the rate at which it is populated in the excitation process, thus the thermal equilibrium at the temperature of the system can be achieved prior to emission [103].

### 2.3.7. JO parametrization scheme, electric dipole and oscillator strengths

For the randomly-oriented system and the IC wavefunctions, ED dipole strength is given by:

$$D = e^2 |\langle 4f^N SLJ || D_{\rho}^1 || 4f^N S' L' J' \rangle|^2 \quad (2.3.88)$$

Axe's slightly modified parametrization scheme from that of Judd can now be presented. ED strength, also known as the line strength (and often an alternative notation  $S_{ED}$  is used) is given by (theoretical and experimental, respectively):

$$D_{ED} = e^2 \sum_{\lambda=2,4,6} \Omega_{\lambda} |\langle 4f^N SLJ || U^{\lambda} || 4f^N S' L' J' \rangle|^2 \quad (2.3.89)$$

$$D_{\text{exp}} = \frac{\chi_{ED}}{2J + 1} D_{ED} \quad (2.3.90)$$

This expression should be read as a possibility of determining the line strengths of various transitions by three parameters, limited to even unit tensor operators [50].

Now the experimental oscillator strength, gained from the theoretical ED strength, can be calculated and compared with the experimental oscillator strength obtained from the molar absorptivity, respectively:

$$P_{ED}^{\text{exp}} = \frac{8\pi^2 mc \tilde{\nu}_0}{3h} \frac{1}{e^2} D_{ED}^{\text{exp}} = 1.085 \cdot 10^{11} \frac{\chi_{ED} \tilde{\nu}_0}{2J+1} \sum_{\lambda=2,4,6} \Omega_{\lambda} |\langle 4f^N SLJ || U^{\lambda} || 4f^N S'L'J' \rangle|^2 \quad (2.3.91)$$

$$P_{ED}^{\text{exp},\varepsilon} = \frac{4\varepsilon_0 mc^2}{e^2} \frac{10 \ln 10}{N_A} \int \varepsilon(\tilde{\nu}) d\tilde{\nu} = 4.32 \cdot 10^{-9} \frac{\text{mol} \cdot \text{cm}^2}{L} \int \varepsilon(\tilde{\nu}) d\tilde{\nu} \quad (2.3.92)$$

where the theoretical JO parameters are given by [35,103,125]:

$$\Omega_{\lambda} [\text{cm}^2] = (2\lambda + 1) \sum_{k,q} |B_{\lambda kq}|^2 \frac{1}{2k+1} \quad (2.3.93)$$

where

$$B_{\lambda kq} = A_{kq} \Xi(k, \lambda) \quad (2.3.94)$$

By comparing the experimental oscillator strengths and minimizing with the relative root-mean-square (RMS) deviation [33,126,127]:

$$RMS_{rel} = \sqrt{\frac{1}{n-3} \sum_{i=1}^n \left( \frac{P_{ED,i}^{\text{exp},\varepsilon} - P_{ED,i}^{\text{exp}}}{P_{ED,i}^{\text{exp},\varepsilon}} \right)^2} \quad (2.3.95)$$

the values for the JO intensity parameters are obtained, from which, in turn, ED dipole strength can be calculated.

### 2.3.7.1. Additivity of intensity parameters

In the presence of the several non-equivalent sites in the host matrix, one obtains an average value for each of the  $\Omega_{\lambda}$  parameters [55]. Also, if the transitions overlap, the complex band is integrated as a whole:  $D_{ED}(A+B) = e^2 \sum_{\lambda=2,4,6} \Omega_{\lambda} (U_A^{\lambda} + U_B^{\lambda})$ , where RME have been abbreviated as:  $|\langle 4f^N SLJ || U^{\lambda} || 4f^N S'L'J' \rangle|^2 \equiv U^{\lambda}$ .

### 2.3.7.2. Experimental JO parameters from europium emission spectrum

For the calculation of JO parameters of  $\text{Eu}^{3+}$  the JO theory is not needed if the corrected emission spectrum is available. This experimental calculation of JO parameters is not possible for other RE, due to no single MD transition to serve as a reference [128]. Additionally, the  $U^{2,4,6}$  are the only non-zero RME for  ${}^5\text{D}_0 \rightarrow {}^7\text{F}_{2,4,6}$  transitions [104].

Emission intensity,  $I$ , of a given transition is proportional to the area under the emission curve, and is given by [129]:  $I = h\nu A_{\kappa} N$ , where  $N$  is the population of the emitting level. Thus, the radiative transition probability of a given transition is proportional to the surface of the emission peaks that correspond to that transition:  $A_{\kappa} \sim J_{\kappa} = \int I_{\kappa}(\tilde{\nu}) d\tilde{\nu}$ , where  $\kappa$  can take values 1, 2, 4, 6. Thus, it can be said that  $\frac{J_{\lambda}}{J_1} \propto \frac{A_{\lambda}}{A_1}$  [124,129], which by using the equations 2.3.87:

$$\frac{A_{\lambda}}{A_1} = \frac{\tilde{\nu}_{\lambda}^3 \chi_{ED} D_{ED}^{\lambda}}{\tilde{\nu}_1^3 \chi_{MD} D_{MD}} \quad (2.3.96)$$

From the fact that the  $D_{ED}^{\lambda} = e^2 \Omega_{\lambda} U^{\lambda}$  for europium emissions  ${}^5\text{D}_0 \rightarrow {}^7\text{F}_{\lambda}$ , since its RME are zeros except on the diagonal [100], the JO intensity parameters can be obtained directly from the europium spectrum [102,129]:

$$\Omega_{\lambda}^{\text{exp}} = \frac{D_{MD} \tilde{\nu}_1^3}{e^2 \tilde{\nu}_{\lambda}^3 U^{\lambda}} \frac{9n_1^3}{n_{\lambda}(n_{\lambda}^2 + 2)^2} \frac{J_{\lambda}}{J_1} \quad (2.3.97)$$

Thus the intensities of the  ${}^5\text{D}_0 \rightarrow {}^7\text{F}_2$ ,  ${}^5\text{D}_0 \rightarrow {}^7\text{F}_4$ , and  ${}^5\text{D}_0 \rightarrow {}^7\text{F}_6$  depend solely on  $\Omega_2$ ,  $\Omega_4$ , and  $\Omega_6$  parameters, respectively [130].

### 2.3.8. JO derived quantities

Obtaining the derived quantities from the JO is the main goal of the theory, since they provide the information about the practical applications of the investigated material. The quantities calculated here are: radiative lifetime, branching ratios, stimulated emission cross section, luminescence quantum efficiency, optical gain, quantum yield and the sensitization efficiency.

The lifetime is the time after which the population of an excited state has decayed to  $1/e$  i.e. 36.8%, of the initial population [25]. Higher emission probabilities and more transitions from a level lead to faster decay and shorter lifetimes.

Following the excitation, the relaxation may occur by a purely radiative process or by the energy transfer to lattice vibrations. Experimentally observed lifetime,  $\tau_{\text{obs}}$ , also called the total fluorescence lifetime, takes into account both radiative and non-radiative rates:

$$\frac{1}{\tau_{\text{obs}}} = A_R + A_{NR} \quad (2.3.98)$$

where  $A_R = \sum A_k$  is the total radiative relaxation rate [103]. This radiation rate does not take into account the transitions that are not allowed in the JO theory. Without this approximation, the total RT is given by:  $A_R = \sum A_{J'}$ . The JO forbidden transitions  ${}^5D_0 \rightarrow {}^7F_{0,3,5}$  gain their intensity through J-mixing mechanism [116,120,131], i.e. they borrow the intensity from the  ${}^5D_0 \rightarrow {}^7F_{2,4,6}$  through higher-order perturbations of the CF [128]. J-mixing is caused by the non-diagonal matrix elements of CF interaction between different J multiplets [105]. Observable lifetime can be determined from the emission intensity decay following pulse excitation, i.e. by the time-domain method [132]. The width of the pulse should be made as short as possible and should be ideally shorter than the lifetime of the excited state. For lifetime measurements of  $\text{Eu}^{3+}$  compounds, typically a microsecond flash lamp is used. It is recommended to excite  $\text{Eu}^{3+}$  in the level of interest, whenever possible. The appropriate wavelength of the incident lamp can be obtained from the excitation spectra.

For  $\text{Eu}^{3+}$  doped compounds the part of the measured decay closest to the excitation pulse is excluded from the analysis (“tail fitting”). In the case of single-exponential decay, the emission intensity is equal to:

$$I(t) = I(0)e^{-\frac{t}{\tau_{\text{obs}}}} \quad (2.3.99)$$

The observable lifetime can now be calculated from the slope of a plot of  $\ln I(t)$ . In case that the decay is not a single exponential, the lifetime can be numerically evaluated by the average lifetime [123]:

$$\tau_{\text{obs}} = \frac{\int_0^{\infty} tI(t)dt}{\int_0^{\infty} I(t)dt} \quad (2.3.100)$$

The total RT is equal to the inverse of the radiative lifetime of the measured level [102]. An approximate estimation of RT and radiative lifetime from  $\text{Eu}^{3+}$  corrected spectrum can be used instead of JO theory [128]:

$$A_R \approx 14.65 \text{ s}^{-1} \cdot n_1^3 \frac{J_{\text{tot}}}{J_1} \quad (2.3.101)$$

where  $J_{\text{tot}} = \sum_{i=0}^6 J_i$  is the total integrated area of the corrected emission spectrum. Stronger emission probabilities and more transitions from a level lead to faster decay and shorter lifetimes [100]. Theoretical radiative lifetime is an inverse of equation 2.3.101 [128]:

$$\tau_R^{\text{th}} = \frac{n_1^{-3} J_1}{14.65 J_{\text{tot}}} \quad (2.3.102)$$

However, note that this is just a theoretical model for which the real values might slightly vary, and the two values for the radiative lifetime should be compared.

Branching ratios can be used to predict the relative intensities of all emission lines originating from a given excited state [100]. Theoretical branching ratio is obtained from the JO theory:

$$\beta_{\kappa}^{\text{th}} = \frac{A_{\kappa}}{\sum A_{\kappa}} \quad (2.3.103)$$

where  $\kappa = 1, 2, 4, 6$ . These branching ratios do not include transitions other than to  ${}^7\text{F}_{\kappa}$ , and this is justified by the analysis that indicates that these transitions “borrow” intensity from the hypersensitive transition through higher order perturbations of the crystal field [128]. Branching ratios can also be obtained directly from the emission spectra as a ratio of integrated intensities:

$$\beta_{\kappa}^{\text{exp}} = \frac{J_{\kappa}}{J_{\text{tot}}} \quad (2.3.104)$$

and the two types of branching ratios should be compared. Emission level with  $\beta > 50\%$  is a potential laser emission transition [33]. The most important parameter determining the potential laser performance is the stimulated emission cross section, given by [55,100,133,134]:

$$\sigma_{\kappa}(\lambda_p) = \frac{\lambda_p^4}{8\pi c n_p^2} \frac{\max I_{\kappa}}{\int I_{\kappa} d\lambda} A_{\kappa} \quad (2.3.105)$$

where  $\lambda_p$  is the wavelength of the peak  $\kappa$ , and  $n_p$  is the refractive index at  $\lambda_p$ , which is in most cases approximately equal to  $n_{\kappa}(\tilde{\nu}_{\kappa})$ . The emission cross-section describes the maximum spatial amplification of intensity  $I(x)$  for a given population inversion  $N$  is given by:  $I(x) = I_0 e^{\sigma_{\kappa} N x}$  [118].

Luminescence quantum efficiency (or intrinsic quantum yield),  $\eta$ , is by definition the ratio of the number of photons emitted to the number of photons absorbed [25,135]. For RE ions it is also equal to the ratio of the observed lifetime to the radiative lifetime [102,124,128,134]:

$$\eta = \frac{\tau_{\text{obs}}}{\tau_R} = \frac{A_R}{A_R + A_{NR}} \quad (2.3.106)$$

where  $A_{NR} = 1/\tau_{\text{obs}} - 1/\tau_R$ . Overall quantum yield ( $\Phi$ ) can be determined if the quantum yield of the investigated sample ( $u$ ) is compared with that of a reference sample ( $ref$ ) [128]:

$$\Phi_u = \frac{n_u^2 I_u A_{ref}}{n_{ref}^2 I_{ref} A_u} \Phi_{ref} \quad (2.3.107)$$

A good reference sample is  $Y_2O_3:Eu^{3+}$ . The knowledge of  $\Phi$  can give us the sensitization efficiency:

$$\eta_{\text{sens}} = \Phi/\eta \quad (2.3.108)$$

An amplifier device is often characterized by the optical gain, a figure of merit for gain defined as the product of the lifetime and the emission cross-section [100,136]:

$$P = \sigma \tau_{\text{obs}} \quad (2.3.109)$$

### 2.3.9. JO parameters interpretation

While the original JO is based on the static coupling approximation, in reality not only the central ion is perturbed by the environment, but also the ligands. The dipoles on the ligands induce, in turn, the multi-poles on the central ion. This is known as the dynamic coupling, and adds additional contributions to the intensity parameters.

However, in the semi-empirical approach, dynamic coupling contribution is included within the JO intensity parameters. Thus, the JO is successful when used in a fitting procedure, but fails in the ab initio calculations due to the imperfections of the theory [50]. Even more, the fitted values also contain the electron correlation effects, s-o interaction at the third order, mass polarization shift, hyperfine interactions, and the relativistic effects. In general, the JO parameters represent the overall picture of mechanisms that affect the 4f-4f transitions.

JO intensity parameters contain the angular and the radial terms, coefficients of coupling and re-coupling of angular momenta. The genealogy of the energy states is included within the RME of the unit tensor operator  $U^\lambda$  [50]. JO parameters contain the CF strengths, the energy separation of the two opposite-parity configurations and the inter-configurational radial integrals and include contribution from both static and vibrationally induced ED transitions [116].

The effect of the CF applied to the RE ion is the removal of the degeneracy of the free-ion levels and a shift of the barycenter positions, the latter being called nephelauxetic effect. Nephelauxetic means cloud expanding, the name given because of the increase of the electron cloud around the RE ion by transferring electron density to bonding molecular orbitals, which results in a decrease of the inter-electronic repulsion. Thus, it is caused by a covalent contribution to the bonding between the RE ions and ligands. The consequence is lowering the Slater integral values comparing to the free ion [119]. The nephelauxetic effect depends not only on the covalency of the metal-ligand bond, but is also inversely proportional to the coordination number. The  $\Omega_2$  parameter is associated with short-range coordination effects. The higher the polarization and less symmetry, the larger  $\Omega_2$  value is expected [130].  $\Omega_2$  is closely related to the hypersensitive transitions, and hypersensitivity is related to the covalency parameter through the nephelauxetic effect and is attributed to the increasing polarizability of the ligands around the RE ions [127]. High  $\Omega_2$  values are thus due the high covalency of the Eu-O bond [134]. The high polarizability of oxygen ions, due to the lower electronegativity, favor high values of  $\Omega_2$ . Thus in Eu<sup>3+</sup> doped compounds,  $^5D_0 \rightarrow ^7F_2$  intensity is enhanced when the Eu-O chemical bond is more covalent, and the asymmetric ratio can be used as a measure of covalency [136].  $\Omega_4$  and  $\Omega_6$  depend on long-range effects [130]. They are related to the viscosity and

rigidity of the host material [100].  $\Omega_4$  is not directly related to symmetry around europium ion, but it depends on electron density around the ligands. Its value increases with  $\text{Eu}^{3+}$  concentration, which indicates that the electron density on the ligand decreases [137].

$\Omega_6$  is less dependent on the environment than  $\Omega_2$ , but is more dependent on the overlap integrals of 4f and 5d orbitals [127].

The spectroscopic quality factor, the ratio of  $\Omega_4$  vs  $\Omega_6$  [127], can only be used for the  $\text{Nd}^{3+}$  doped compounds. Its use for other RE such is europium is often in literature and should be disregarded as an error [55].

The lack of site symmetry of RE ion in a host is reflected by the stronger hypersensitive transition. Since the MD transition is host independent, the higher is the ratio of intensities of  ${}^5\text{D}_0 \rightarrow {}^7\text{F}_2$  to  ${}^5\text{D}_0 \rightarrow {}^7\text{F}_1$ , the lower is the symmetry and larger the covalence [100]. The parameter describing this is often called the asymmetry ratio R, and is proportional to the  $\Omega_2$  parameter:

$$R = \frac{I({}^5\text{D}_0 \rightarrow {}^7\text{F}_2)}{I({}^5\text{D}_0 \rightarrow {}^7\text{F}_1)} \propto \Omega_2 \quad (2.3.110)$$

## 2.4. Europium

### 2.4.1. Uniqueness of europium

Among the  $\text{RE}^{3+}$  used to optically activate the glass matrices,  $\text{Eu}^{3+}$  is the mostly used choice due to its narrow emission bands, almost monochromatic light with long lifetimes of optically active states. Europium doped phosphors are commonly used as a red phosphor for LED, due to the higher luminescence efficiency compared with other materials [104]. E.g. commercial white LEDs are usually produced by combining the InGaN blue electroluminescence, which partially excites the  $\text{YAG}:\text{Ce}^{3+}$  phosphor, and the combined transmitted and PL light resembles the white light. However, such LEDs lack the red-emitting component. The problem can be resolved with addition of a phosphor that has  $\text{Eu}^{3+}$ , that would be excited by the blue light from the InGaN [99].

The  $\text{Eu}^{3+}$  ion has been forever an object of fascination, and shows a likelihood of becoming of even greater interest in the future [30]. The transitions  ${}^7\text{F}_{0,3,5}\leftrightarrow{}^5\text{D}_0$  are forbidden in the standard JO theory and their observation in spectra enables extensions of the original JO theory to be developed [30].  ${}^7\text{F}_0\leftrightarrow{}^5\text{D}_0$  is highly forbidden by the selection rules, but is observed in spectra of  $\text{Eu}^{3+}$  doped materials, and is often used as a benchmark for providing a detailed insight into the structure of europium doped compounds. Transitions  ${}^7\text{F}_1\leftrightarrow{}^5\text{D}_0$  and  ${}^7\text{F}_0\leftrightarrow{}^5\text{D}_1$  are pure MD transitions and are mostly independent on the environment.

### 2.4.2. Energy level structure of trivalent europium

Free ion energies are described with the configurations, terms and levels. Sub-levels become apparent in the presence of an external field, such as CF of the host matrix.

#### 2.4.2.1. Configuration

RE ions can exist in 2+, 3+, and 4+ oxidation states. Eu can exist in 2+ and 3+, 2+ giving blue luminescence, and 3+, the most common, with orange-red luminescence. 3+ is the only oxidation state that is of interest here. Electronic configuration of Eu is  $[\text{Xe}]4\text{f}^76\text{s}^2$ , and of  $\text{Eu}^{3+}$  is  $[\text{Xe}]4\text{f}^6$ , i.e. trivalent europium has 64 electrons in the same closed shells as the Xenon atom and 6 electrons in the 4f shell. Those electrons can be arranged in 3003 different ways into the 7 4f orbitals. Thus, the total degeneracy of  $\text{Eu}^{3+}$

is equal to  $\binom{14}{6} = \frac{14!}{6!(14-6)!} = 3003$ , which is a number of different electronic arrangements, called microstates [102].

#### 2.4.2.2. Terms

Terms start appearing when the ES interaction between 4f electrons is taken into account, which lifts the degeneracy in L and S. Six 4f spins  $s_i$  combine into total spin angular momentum  $S = \sum s_i$ , and orbital angular momenta  $l_i$  combine into total orbital angular momenta  $L = \sum l_i$ , with quantum numbers  $M_S = -6/2, \dots, 6/2$  and  $M_L = -3 \cdot 6, \dots, 3 \cdot 6$ , respectively, giving the total number of 119 LS states (see Table 6).

All combinations of states that have the same angular momentum and spin can be under the same term  $^{2S+1}L$ . As ES interaction removes degeneracy in S and L, the  $^{2S+1}L$  is a term symbol for Coulomb interaction only.  $^{2S+1}L$  terms are found by successively subtracting states from LS matrix. If there are terms having the same L and S, a seniority quantum number  $\tau$  is added to distinguish them:  $^{2S+1}L(\tau)$  [138]. Spin multiplicity in the  $^{2S+1}L$  terms can be defined as:

$$2S + 1 = \left\{ \begin{array}{ccccc} 1 & 2 & 3 & 4 & 5 \\ \text{singlet} & \text{doublet} & \text{triplet} & \text{quartet} & \text{quintet} \end{array} \right\}$$

and the labels for the orbitals are given in letters:  $L = \left\{ \begin{array}{cccccccccccc} 0 & 1 & 2 & 3 & 4 & 5 & 6 & 7 & 8 & 9 & 10 & 11 & 12 \\ S & P & D & F & G & H & I & K & L & M & N & O & Q \end{array} \right\}$ .

Hund's rule determines the ground term as having the greatest spin multiplicity and the greatest value of L. For europium this is the term with  $2S+1 = 7$  and  $L = 3$ , i.e.  $^7F$  term.

The existence of orbital magnetic moment should result in number of important effects in solids, such as the occurrence of the orbital magnetism with large magnetic momenta and strong anisotropy, which is the case in RE systems, where magnetism is determined by the total angular momentum  $\mathbf{J} = \mathbf{L} + \mathbf{S}$  [113].

Table 6 The 119 LS terms of the  $4f^6$  configuration of trivalent europium [102]

${}^7F$	${}^3K(6)$	${}^3F(8)$	${}^1I(6)$
${}^5L$	${}^3I(1)$	${}^3F(9)$	${}^1I(7)$
${}^5K$	${}^3I(2)$	${}^3D(1)$	${}^1H(1)$
${}^5I(1)$	${}^3I(3)$	${}^3D(2)$	${}^1H(2)$
${}^5I(2)$	${}^3I(4)$	${}^3D(3)$	${}^1H(3)$
${}^5H(1)$	${}^3I(5)$	${}^3D(4)$	${}^1H(4)$
${}^5H(2)$	${}^3I(6)$	${}^3D(5)$	${}^1G(1)$
${}^5G(1)$	${}^3H(1)$	${}^3P(1)$	${}^1G(2)$
${}^5G(2)$	${}^3H(2)$	${}^3P(2)$	${}^1G(3)$
${}^5G(3)$	${}^3H(3)$	${}^3P(3)$	${}^1G(4)$
${}^5F(1)$	${}^3H(4)$	${}^3P(4)$	${}^1G(5)$
${}^5F(2)$	${}^3H(5)$	${}^3P(5)$	${}^1G(6)$
${}^5D(1)$	${}^3H(6)$	${}^3P(6)$	${}^1G(7)$
${}^5D(2)$	${}^3H(7)$	${}^1Q$	${}^1G(8)$
${}^5D(3)$	${}^3H(8)$	${}^1N(1)$	${}^1F(1)$
${}^5P$	${}^3H(9)$	${}^1N(2)$	${}^1F(2)$
${}^5S$	${}^3G(1)$	${}^1M(1)$	${}^1F(3)$
${}^3O$	${}^3G(2)$	${}^1M(2)$	${}^1F(4)$
${}^3N$	${}^3G(3)$	${}^1L(1)$	${}^1D(1)$
${}^3M(1)$	${}^3G(4)$	${}^1L(2)$	${}^1D(2)$
${}^3M(2)$	${}^3G(5)$	${}^1L(3)$	${}^1D(3)$
${}^3M(3)$	${}^3G(6)$	${}^1L(4)$	${}^1D(4)$
${}^3L(1)$	${}^3G(7)$	${}^1K(1)$	${}^1D(5)$
${}^3L(2)$	${}^3F(1)$	${}^1K(2)$	${}^1D(6)$
${}^3L(3)$	${}^3F(2)$	${}^1K(3)$	${}^1P$
${}^3K(1)$	${}^3F(3)$	${}^1I(1)$	${}^1S(1)$
${}^3K(2)$	${}^3F(4)$	${}^1I(2)$	${}^1S(2)$
${}^3K(3)$	${}^3F(5)$	${}^1I(3)$	${}^1S(3)$
${}^3K(4)$	${}^3F(6)$	${}^1I(4)$	${}^1S(4)$
${}^3K(5)$	${}^3F(7)$	${}^1I(5)$	

#### 2.4.2.3. Levels

Levels appear when the degeneracy of terms is lifted by the spin-orbit interaction [139]. s-o is an interaction between intrinsic magnetic moment of  $e^-$  with the magnetic field created by its motion around the nucleus. s-o interaction intensity is proportional to  $Z^4$ . It removes degeneracy in J, but the  $M_J$  degeneracy remains. Thus, it causes the  ${}^{2S+1}L$  terms to split to  ${}^{2S+1}L_J$ ,  $J = |L-S|, \dots, |L+S|$ . For  $\text{Eu}^{3+}$  the number of  ${}^{2S+1}L_J$  multiplets is equal to 295 [140].

The possible J values for the  ${}^7F$  term are 0, ...,6. According to the Hund's rule, the ground state has the lowest J value, thus the ground state level is  ${}^7F_0$ . The energy level diagram (for RE, often called "Dieke diagram") of trivalent europium ion is given in Fig. 47, and free-ion levels end their calculated energies are presented in Table 6. These diagrams are useful because the energies of the J multiplets vary by only a small amount in different hosts [141].

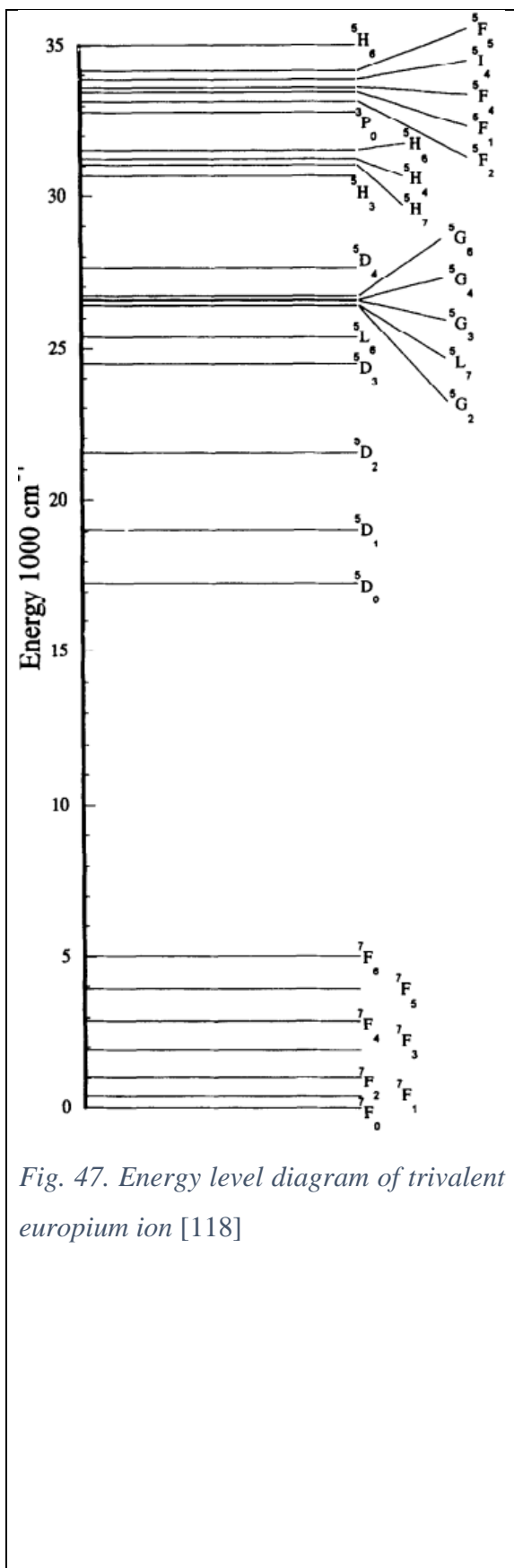


Fig. 47. Energy level diagram of trivalent europium ion [118]

Table 7. Calculated energies of free-ion levels of trivalent europium ion. Yellow color marks the most important levels for PL.

${}^7F_0$	0
${}^7F_1$	379
${}^7F_2$	1043
${}^7F_3$	1896
${}^7F_4$	2869
${}^7F_5$	3912
${}^7F_6$	4992
${}^5D_0$	17,227
${}^5D_1$	18,973
${}^5D_2$	21,445
${}^5D_3$	24,335
${}^5L_6$	25,125
${}^5L_7$	26,177
${}^5G_2$	26,269
${}^5G_3$	26,493
${}^5G_4$	26,611
${}^5G_5, {}^5G_6$	26,642
${}^5L_8$	27,095
${}^5D_4$	27,583
${}^5L_9$	27,844
${}^5L_{10}$	28,341
${}^5H_3$	30,870
${}^5H_7$	31,070
${}^5H_4$	31,292
${}^5H_6, {}^5H_5$	31,511
${}^3P_0$	32,790
${}^5F_2$	33,055
${}^5F_3$	33,092
${}^5F_1$	33,366
${}^5F_4$	33,513
${}^5F_5$	34,040
${}^5I_4$	34,057
${}^5I_5$	34,388
${}^5I_6$	34,966
${}^5I_7$	35,429
${}^5I_8$	35,453
${}^5K_5$	36,168
${}^5K_6$	37,320
${}^3P_1$	38,132
${}^5K_7$	38,247
${}^5G_2$	38,616
${}^5K_8$	38,667
${}^3K_6, {}^3I_6$	38,780
${}^5G_3$	39,143
${}^5K_9$	39,518
${}^5G_4$	39,726

A special care must be taken with the  ${}^5D_J$  multiplet, as the levels must be distinguished by a seniority quantum number with values from 1 to 3. E.g.  ${}^5D(3)_0$  lies at ca.  $17200\text{ cm}^{-1}$  (and is most commonly labeled without the seniority quantum number), while  ${}^5D(2)_0$  and  ${}^5D(1)_0$  are at ca.  $42000\text{ cm}^{-1}$  and  $75000\text{ cm}^{-1}$ , respectively [142].

These free-ion states are not pure, since the mixing of different SL states where S or L differ by at most by 1, with the same J manifold, is determined by the s-o coupling parameter. IC states of  $\text{Eu}^{3+}$  free ion, for the average Slater integrals and s-o intensity parameter, are calculated by RELIC application software:

- $|{}^7F_0\rangle' = 0.969521 \cdot |7F(0)\rangle - 0.179160 \cdot |5D1(0)\rangle + 0.010675 \cdot |5D2(0)\rangle + 0.159908 \cdot |5D3(0)\rangle - 0.023086 \cdot |3P1(0)\rangle + 0.000556 \cdot |3P2(0)\rangle + 0.025161 \cdot |3P3(0)\rangle + 0.000085 \cdot |3P4(0)\rangle + 0.003985 \cdot |3P5(0)\rangle + 0.031863 \cdot |3P6(0)\rangle - 0.002268 \cdot |1S1(0)\rangle - 0.005168 \cdot |1S2(0)\rangle + 0.000129 \cdot |1S3(0)\rangle + 0.004212 \cdot |1S4(0)\rangle$
- $|7F(1)\rangle' = +0.975168 \cdot |7F(1)\rangle - 0.003436 \cdot |5P(1)\rangle - 0.162930 \cdot |5D1(1)\rangle + 0.014007 \cdot |5D2(1)\rangle + 0.141667 \cdot |5D3(1)\rangle + 0.017683 \cdot |5F1(1)\rangle + 0.028770 \cdot |5F2(1)\rangle - 0.016268 \cdot |3P1(1)\rangle + 0.000026 \cdot |3P2(1)\rangle + 0.016475 \cdot |3P3(1)\rangle - 0.000416 \cdot |3P4(1)\rangle + 0.003340 \cdot |3P5(1)\rangle + 0.021976 \cdot |3P6(1)\rangle - 0.001367 \cdot |3D1(1)\rangle + 0.004099 \cdot |3D2(1)\rangle + 0.001867 \cdot |3D3(1)\rangle - 0.001260 \cdot |3D4(1)\rangle - 0.005418 \cdot |3D5(1)\rangle - 0.000046 \cdot |1P(1)\rangle$
- $|7F(2)\rangle' = +0.982028 \cdot |7F(2)\rangle + 0.000648 \cdot |5S(2)\rangle - 0.005397 \cdot |5P(2)\rangle - 0.135399 \cdot |5D1(2)\rangle + 0.018474 \cdot |5D2(2)\rangle + 0.111739 \cdot |5D3(2)\rangle + 0.030633 \cdot |5F1(2)\rangle + 0.050328 \cdot |5F2(2)\rangle + 0.016326 \cdot |5G1(2)\rangle - 0.004307 \cdot |5G2(2)\rangle - 0.015394 \cdot |5G3(2)\rangle - 0.008256 \cdot |3P1(2)\rangle - 0.000444 \cdot |3P2(2)\rangle + 0.006624 \cdot |3P3(2)\rangle - 0.000876 \cdot |3P4(2)\rangle + 0.002549 \cdot |3P5(2)\rangle + 0.010570 \cdot |3P6(2)\rangle - 0.002184 \cdot |3D1(2)\rangle + 0.006307 \cdot |3D2(2)\rangle + 0.002799 \cdot |3D3(2)\rangle - 0.002079 \cdot |3D4(2)\rangle - 0.008280 \cdot |3D5(2)\rangle - 0.003490 \cdot |3F1(2)\rangle - 0.000989 \cdot |3F2(2)\rangle - 0.004051 \cdot |3F3(2)\rangle + 0.002916 \cdot |3F4(2)\rangle - 0.000358 \cdot |3F5(2)\rangle - 0.001937 \cdot |3F6(2)\rangle + 0.001653 \cdot |3F7(2)\rangle - 0.005765 \cdot |3F8(2)\rangle -$

- $0.000565*|3F9(2)\rangle + 0.000589*|1D1(2)\rangle - 0.000504*|1D2(2)\rangle -$   
 $0.000557*|1D3(2)\rangle + 0.001230*|1D4(2)\rangle + 0.000201*|1D5(2)\rangle -$   
 $0.001305*|1D6(2)\rangle$
- $|7F(3)\rangle = +0.986983*|7F(3)\rangle - 0.005052*|5P(3)\rangle - 0.100501*|5D1(3)\rangle$   
 $+0.020645*|5D2(3)\rangle + 0.076591*|5D3(3)\rangle + 0.041332*|5F1(3)\rangle$   
 $+0.069443*|5F2(3)\rangle + 0.036137*|5G1(3)\rangle - 0.010363*|5G2(3)\rangle -$   
 $0.034274*|5G3(3)\rangle + 0.001516*|5H1(3)\rangle + 0.002793*|5H2(3)\rangle -$   
 $0.002214*|3D1(3)\rangle + 0.005844*|3D2(3)\rangle + 0.002414*|3D3(3)\rangle -$   
 $0.002253*|3D4(3)\rangle - 0.007482*|3D5(3)\rangle - 0.005673*|3F1(3)\rangle -$   
 $0.001380*|3F2(3)\rangle - 0.006424*|3F3(3)\rangle + 0.004912*|3F4(3)\rangle -$   
 $0.000921*|3F5(3)\rangle - 0.003402*|3F6(3)\rangle + 0.002214*|3F7(3)\rangle -$   
 $0.009058*|3F8(3)\rangle - 0.000177*|3F9(3)\rangle + 0.000087*|3G1(3)\rangle$   
 $+0.000976*|3G2(3)\rangle + 0.001851*|3G3(3)\rangle - 0.000552*|3G4(3)\rangle$   
 $+0.001670*|3G5(3)\rangle + 0.001161*|3G6(3)\rangle + 0.001623*|3G7(3)\rangle -$   
 $0.000575*|1F1(3)\rangle + 0.000036*|1F2(3)\rangle - 0.000385*|1F3(3)\rangle$   
 $+0.000285*|1F4(3)\rangle$
  - $|7F(4)\rangle = +0.988686*|7F(4)\rangle - 0.060171*|5D1(4)\rangle + 0.016918*|5D2(4)\rangle$   
 $+0.040925*|5D3(4)\rangle + 0.046550*|5F1(4)\rangle + 0.081956*|5F2(4)\rangle$   
 $+0.061545*|5G1(4)\rangle - 0.020710*|5G2(4)\rangle - 0.058993*|5G3(4)\rangle$   
 $+0.003738*|5H1(4)\rangle + 0.006428*|5H2(4)\rangle - 0.000345*|5I1(4)\rangle -$   
 $0.000578*|5I2(4)\rangle - 0.005544*|3F1(4)\rangle - 0.001136*|3F2(4)\rangle -$   
 $0.006345*|3F3(4)\rangle + 0.005508*|3F4(4)\rangle - 0.001591*|3F5(4)\rangle -$   
 $0.003384*|3F6(4)\rangle + 0.001881*|3F7(4)\rangle - 0.008806*|3F8(4)\rangle$   
 $+0.001254*|3F9(4)\rangle + 0.001184*|3G1(4)\rangle + 0.001524*|3G2(4)\rangle$   
 $+0.005003*|3G3(4)\rangle - 0.001397*|3G4(4)\rangle + 0.003861*|3G5(4)\rangle$   
 $+0.001665*|3G6(4)\rangle + 0.004049*|3G7(4)\rangle - 0.001558*|3H1(4)\rangle -$   
 $0.000275*|3H2(4)\rangle + 0.001960*|3H3(4)\rangle + 0.001547*|3H4(4)\rangle -$   
 $0.000030*|3H5(4)\rangle - 0.000127*|3H6(4)\rangle + 0.000452*|3H7(4)\rangle$   
 $+0.001249*|3H8(4)\rangle + 0.002483*|3H9(4)\rangle + 0.000649*|1G1(4)\rangle$   
 $+0.000207*|1G2(4)\rangle + 0.000802*|1G3(4)\rangle - 0.000119*|1G4(4)\rangle -$   
 $0.000147*|1G5(4)\rangle - 0.000428*|1G6(4)\rangle + 0.000971*|1G7(4)\rangle -$   
 $0.000428*|1G8(4)\rangle$

- $|^7F(5)\rangle = +0.986733|^7F(5)\rangle +0.041387|^5F1(5)\rangle +0.079019|^5F2(5)\rangle$   
 $+0.091836|^5G1(5)\rangle -0.038363|^5G2(5)\rangle -0.089574|^5G3(5)\rangle$   
 $+0.007078|^5H1(5)\rangle +0.010408|^5H2(5)\rangle -0.000723|^5I1(5)\rangle -$   
 $0.001333|^5I2(5)\rangle +0.000237|^5K(5)\rangle +0.002998|^3G1(5)\rangle$   
 $+0.001119|^3G2(5)\rangle +0.008346|^3G3(5)\rangle -0.001944|^3G4(5)\rangle$   
 $+0.005708|^3G5(5)\rangle +0.001266|^3G6(5)\rangle +0.006714|^3G7(5)\rangle -$   
 $0.004363|^3H1(5)\rangle -0.001362|^3H2(5)\rangle +0.005782|^3H3(5)\rangle$   
 $+0.004627|^3H4(5)\rangle -0.000293|^3H5(5)\rangle -0.000637|^3H6(5)\rangle$   
 $+0.000608|^3H7(5)\rangle +0.003337|^3H8(5)\rangle +0.007617|^3H9(5)\rangle$   
 $+0.000140|^3I1(5)\rangle +0.000954|^3I2(5)\rangle +0.000057|^3I3(5)\rangle -$   
 $0.000526|^3I4(5)\rangle +0.000966|^3I5(5)\rangle -0.000304|^3I6(5)\rangle$   
 $+0.000041|^1H1(5)\rangle +0.000522|^1H2(5)\rangle -0.000487|^1H3(5)\rangle -$   
 $0.000752|^1H4(5)\rangle$
- $|^7F(6)\rangle = +0.981062|^7F(6)\rangle +0.125814|^5G1(6)\rangle -0.067290|^5G2(6)\rangle -$   
 $0.126947|^5G3(6)\rangle +0.010618|^5H1(6)\rangle +0.012523|^5H2(6)\rangle -$   
 $0.000857|^5I1(6)\rangle -0.002102|^5I2(6)\rangle +0.000425|^5K(6)\rangle -0.000204|^5L(6)\rangle -$   
 $0.008642|^3H1(6)\rangle -0.003636|^3H2(6)\rangle +0.014169|^3H3(6)\rangle$   
 $+0.010294|^3H4(6)\rangle -0.001574|^3H5(6)\rangle -0.003231|^3H6(6)\rangle$   
 $+0.000681|^3H7(6)\rangle +0.005524|^3H8(6)\rangle +0.017586|^3H9(6)\rangle$   
 $+0.000534|^3I1(6)\rangle +0.002169|^3I2(6)\rangle +0.000200|^3I3(6)\rangle -$   
 $0.001493|^3I4(6)\rangle +0.002289|^3I5(6)\rangle -0.001011|^3I6(6)\rangle -0.000397|^3K1(6)\rangle$   
 $-0.000375|^3K2(6)\rangle -0.000047|^3K3(6)\rangle -0.000142|^3K4(6)\rangle -$   
 $0.000481|^3K5(6)\rangle +0.000107|^3K6(6)\rangle +0.001329|^1I1(6)\rangle -$   
 $0.000264|^1I2(6)\rangle +0.001458|^1I3(6)\rangle +0.000128|^1I4(6)\rangle -0.000185|^1I5(6)\rangle$   
 $-0.001658|^1I6(6)\rangle -0.001055|^1I7(6)\rangle$

The  $^7F_0$  state is of 94% purity,  $^7F_1$  is of 95%, etc. This indicates that the LS states of the ground multiplet can be used as an approximation to the IC states, since they are fairly pure.

#### 2.4.2.4. Sublevels – Stark levels

The  $2J+1$  degeneracy of the energy levels in the free ion is lifted by an external field, giving rise to the 3003 SLJM  $\text{Eu}^{3+}$  CF levels, labeled by  $^{2S+1}L(M_J)$  [31,33,102,141], i.e. for each  $J$  value there are  $2J+1$  microstates [142]. The energy level diagram of  $\text{Eu}^{3+}$  and the splitting of degeneracy is presented in Fig. 48. At a crystalline site, the energy levels may split into maximally  $2J+1$  CF components for even number of trivalent RE ions, and those levels are identified by the irreducible representations of the site point group symmetry [142], as given in Table 8. In the case of  $\text{RE}^{3+}$  with odd number of electrons in the 4f shell, the levels might be split to maximally  $J + \frac{1}{2}$  components [117]. In most cases the total splitting is of order of a few hundred  $\text{cm}^{-1}$ , in general small compared to the spacing between multiplet components.

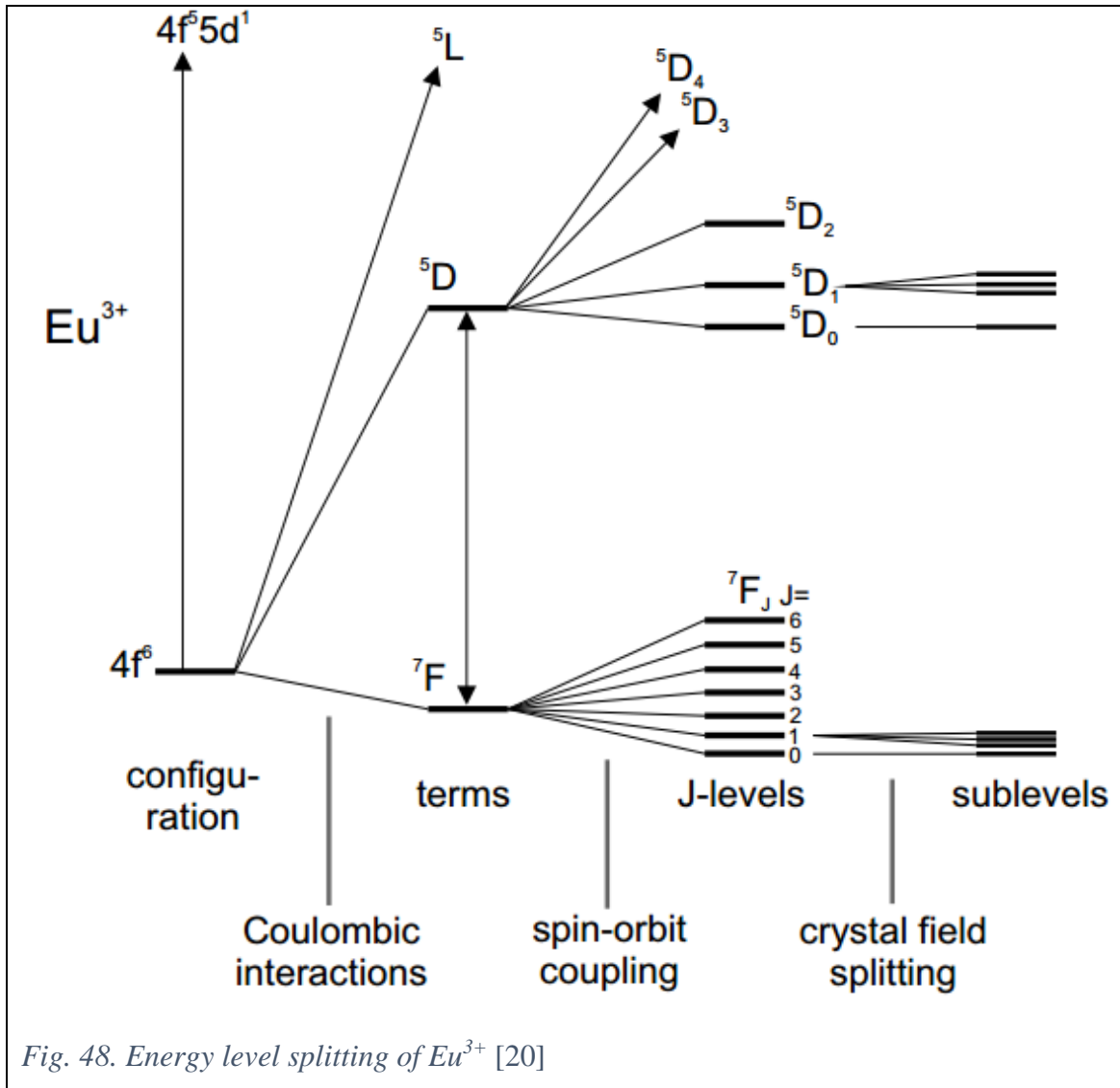


Fig. 48. Energy level splitting of  $\text{Eu}^{3+}$  [20]

Table 8. Number of CF levels into which free-ion levels split for a different symmetry group [142].

$J$	$2J + 1$	Point group				$2J$	$2J + 1$	Point group	
		Cubic <sup>a</sup>	Hexagonal <sup>b</sup>	Tetragonal <sup>c</sup>	Lower <sup>d</sup>			Cubic <sup>a</sup>	Other <sup>b,c,d</sup>
0	1	1	1	1	1				
1	3	1	2	2	3	1	2	1	1
2	5	2	3	4	5	3	4	1	2
3	7	3	5	5	7	5	6	2	3
4	9	4	6	7	9	7	8	3	4
5	11	4	7	8	11	9	10	3	5
6	13	6	9	10	13	11	12	4	6

<sup>a</sup> Cubic:  $O_h, O, T_d, T_h, T$ . <sup>b</sup> Hexagonal:  $D_{6h}, D_6, C_{6v}, C_{6h}, C_6, D_{3h}, C_{3h}$ , and trigonal:  $D_{3d}, D_3, C_{3v}, C_{3i}, C_3$ . <sup>c</sup> Tetragonal:  $D_{4h}, D_4, C_{4h}, C_4, D_{2d}, S_4$ . <sup>d</sup> Lower: rhombic:  $D_{2h}, D_2, C_{2v}$ , monoclinic  $C_2, C_{2h}, C_s$ , triclinic:  $C_i, C_1$ .

Wavefunctions of different J-multiplets can mix when their irreducible representations are the same, as defined by the CF. J-mixing might be important for  ${}^7F_J$  multiplet, depending on the site symmetry (e.g. at  $C_2$  site, where  ${}^7F_2$  states with  $M_J = \pm 2$  are mixed into  ${}^7F_0$ ; while at an octahedral site J-mixing of  ${}^7F_0$  with  ${}^7F_2$  is not permitted). The wavefunction of  ${}^7F_0$  is thus complicated by IC and J-mixing and its labeling does not convey the complete description of the state. In contrast, J-mixing is not important for the  ${}^5D_0$  state because it is widely separated from other states [142].

### 2.4.3. PL

#### 2.4.3.1. Excitation spectra

Material absorbs light according to the Beer-Lambert law:  $I(\lambda) = I_0(\lambda) \cdot \exp(-\alpha(\lambda)L)$ , where  $I$  is the intensity measured after an optical path length  $L$ ,  $I_0$  is the intensity of light before entering the sample, and  $\alpha$  is the absorption coefficient. The absorption coefficient is related to the imaginary part of the refractive index  $n_i$  by:  $\alpha = 4\pi \cdot n_i / \lambda$ . The transmission is given by:  $T = I/I_0$ , absorbance by:  $-\log(T)$ , extinction coefficient:  $\varepsilon = \alpha/C$ , absorption cross-section  $P = \sigma I$ , extinction coefficient and the cross-section are related by:  $\varepsilon = \sigma N_A / \ln 10$  [28].

The determination of quantum yield requires the correction of emission spectrum by referencing it on the integrated areas under a spectrum of the standard material and under identical conditions of incident irradiance. However, there are no suitable standards for spectral correction in the far red and NIR regions [132]. Thus, the quantum yield of unknown is related to that of standard by:

$$\phi_u = \frac{A_s F_u n^2}{A_u F_s n_0^2} \phi_s \quad (2.4.1)$$

where  $u$  and  $s$  refer to unknown and standard, respectively,  $A$  is absorbance at the excitation wavelength,  $F$  is the integrated emission area,  $n$  is refractive index,  $n_0$  is the standard refractive index at the sodium D line and temperature of the emission measurement [132].

An excitation spectrum can be considered a product of an absorption spectrum and a plot of the wavelength dependent quantum yield [102]. It is recorded by monitoring the luminescence intensity as a function of the excitation wavelength, i.e. the detection wavelength is fixed and the excitation wavelength is scanned.

In complicated PL spectra, single levels can be excited by a monochromatic illumination, which helps in the analysis of such spectra [117]. Since 4f-4f transitions within the ion are forbidden by the Laporte rule, the luminescence cannot be generated from the direct excitation of the free ion. Asymmetries in the ligand field, due to the different spatial arrangement of the ligands around the RE ion, due to the mixed ligand coordination, thermal vibrations, etc., all make the 4f-4f transitions more probable [143].

Excitation 4f-4f bands of  $\text{Eu}^{3+}$  in a host are on following positions [14,137]:  ${}^7\text{F}_{0,1} \rightarrow {}^5\text{H}_{3,6}$  at ca. 322 nm,  ${}^5\text{D}_4$  and  ${}^5\text{L}_{9,10}$  at ca. 362 nm,  ${}^5\text{L}_{7,8}$  and  ${}^5\text{G}_{2-8}$  at ca. 383 nm,  ${}^5\text{L}_6$  at ca. 393 nm,  ${}^5\text{D}_3$  at ca. 412 nm,  ${}^5\text{D}_2$  at ca. 463 nm and  ${}^5\text{D}_1$  at ca. 530 nm.  ${}^5\text{L}_6 \leftarrow {}^7\text{F}_0$  is the most intense 4f-4f excitation transition.

However, in the host matrix, the coordinated ligands may effectively absorb and transfer the energy to the RE ion in a process known as the antenna effect. Broad band at ca. 250 nm is attributed to charge transfer band (CTB). UV radiation is absorbed by the CTB, then to a higher excited  $\text{Eu}^{3+}$  levels, which then nonradiatively decays to lower levels [144]. Unlike other  $\text{RE}^{3+}$  ions, CTB of  $\text{Eu}^{3+}$  lies much nearer the 4f levels [145]. For  $\text{Eu}^{3+}$  doped materials the CTB energy can be estimated by equation by Jørgensen [146]:

$$\sigma[\text{cm}^{-1}] = 3 \cdot 10^4 (\chi(x) - \chi(M)) \quad (2.4.2)$$

where  $\sigma$  is the position of the CTB,  $\chi(x)$  and  $\chi(M)$  are the optical electronegativity of the anion and the central ion, respectively. For oxygen ligands and  $\text{Eu}^{3+}$  those values are equal to:  $\chi(\text{O}) = 3.2$  and  $\chi(\text{Eu}^{3+}) = 1.75$ . Electronegativity of  $\text{S}^{2-}$  and  $\text{F}^-$  are 2.8 and 3.9, respectively [145]. Therefore, CTB position depends primarily on the nearest ligands of  $\text{Eu}^{3+}$  ion.

Another broad absorption band  $4f^N \leftrightarrow 4f^{N-1}5d$  is due to the intra-configurational transition that in the case of  $\text{Eu}^{3+}$  in oxide hosts occur in the UV and VUV region [147] in the range 100-200 nm. Electrons in a 6p and 6s orbits are only loosely coupled to the core, and  $6p \leftrightarrow 6s$  transitions lie in the range 170-280 nm [117].

#### 2.4.3.2. Emission spectra

Luminescence of europium in the host matrix is entirely dependent on the ligands and their geometry [143]. However, since the energies of the 4f levels are mostly host independent in  $\text{RE}^{3+}$ , the spectral positions of 4f-4f positions are approximately at the same positions for the given RE ion. The spectral positions of transitions  ${}^5D_{J'=3,2,1,0} \rightarrow {}^7F_J$  are presented in Fig. 49. Evident is the decreasing of inter-level distance for each  $J'$  multiplet as the  $J'$  increases, and an increase of inter-level distance as  $J$  increases.

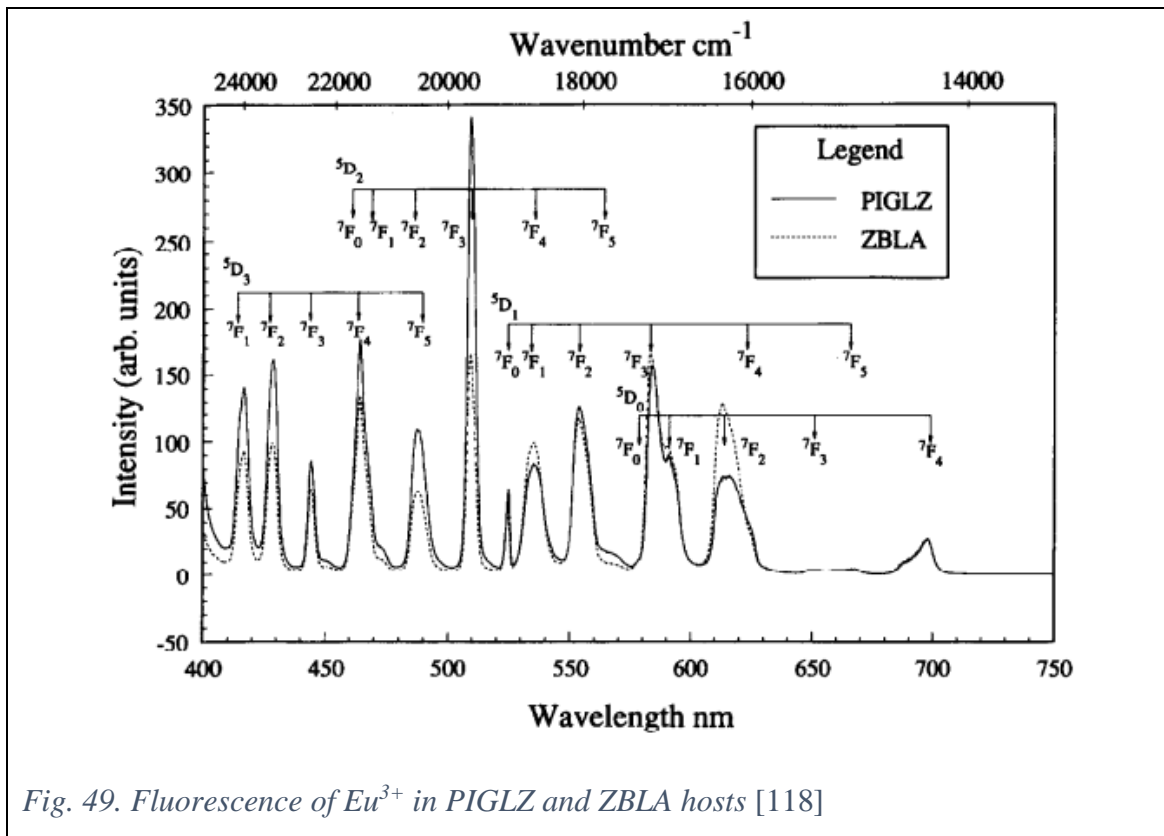


Fig. 49. Fluorescence of  $\text{Eu}^{3+}$  in PIGLZ and ZBLA hosts [118]

PL transition types from the  $^5D_0$  level are summed in Fig. 50. Although  $^5D_0 \rightarrow ^7F_0$  is strictly forbidden in JO theory, it may exist due to the J-mixing in  $C_s$ ,  $C_n$  or  $C_{nv}$  symmetries. In most  $Eu^{3+}$  spectra, it is very weak, and occurs in the region from 570 nm to 585 nm. MD transition  $^5D_0 \rightarrow ^7F_1$  can be seen from 585 nm to 600 nm, and its intensity is mostly environment independent.  $^5D_0 \rightarrow ^7F_2$  at 600 nm to 640 nm range is a hypersensitive transition (intensity strongly dependent on the environment), with highest intensities in the lower symmetry sites.  $^5D_0 \rightarrow ^7F_3$  from 640 nm to 660 nm is weak because it is forbidden in both ED and MD schemes, and exists due to the J-mixing.  $^5D_0 \rightarrow ^7F_4$  at 680 nm to 710 nm ED transition depends on the environment, but is not hypersensitive.  $^5D_0 \rightarrow ^7F_5$  from 740 nm to 770 nm is also forbidden as  $^5D_0 \rightarrow ^7F_3$  and also exists due the J-mixing.  $^5D_0 \rightarrow ^7F_6$  from 810 nm to 840 nm can feature a weak ED transition that can be observed in the NIR region in the host matrices with rigid structure.

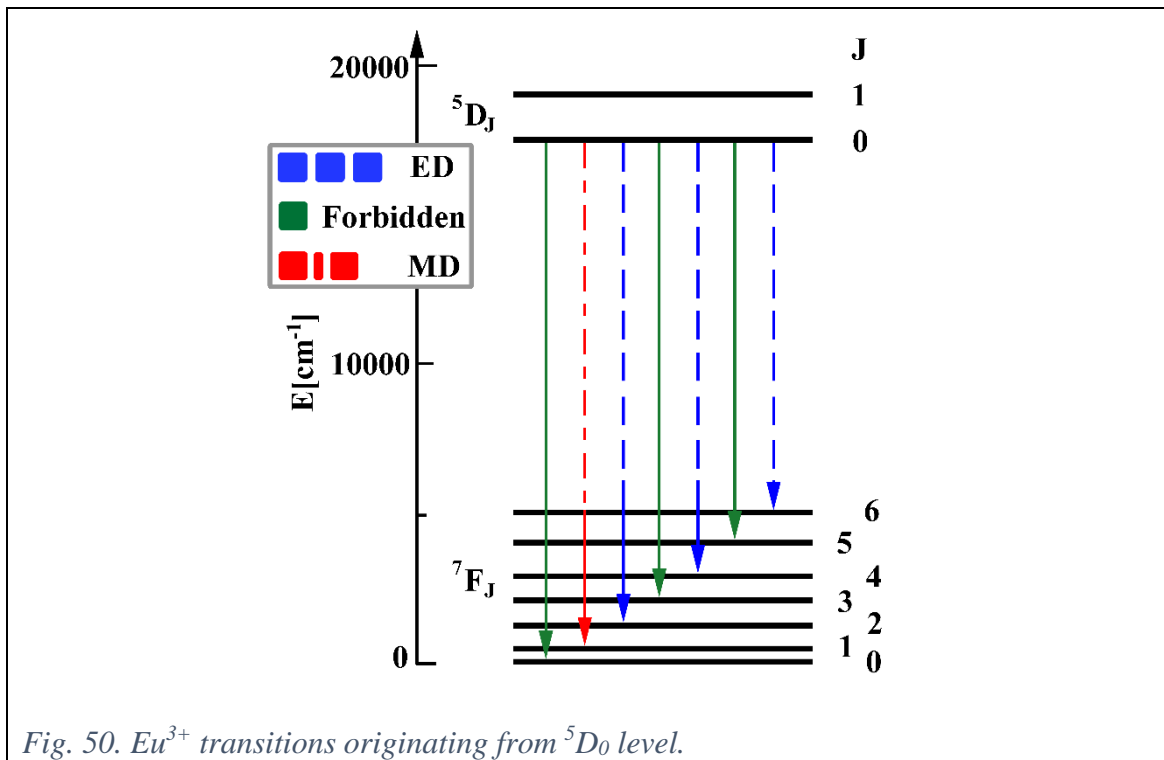


Fig. 50.  $Eu^{3+}$  transitions originating from  $^5D_0$  level.

In some materials PL can originate from the higher excited levels. Many transitions are overlapping, but due to the low intensity some of them can be neglected. Overlaps have been observed between  $^5D_0 \rightarrow ^7F_0$  and  $^5D_2 \rightarrow ^7F_5$ ,  $^5D_0 \rightarrow ^7F_2$  and  $^5D_1 \rightarrow ^7F_4$ ,  $^5D_0 \rightarrow ^7F_3$  and  $^5D_1 \rightarrow ^7F_5$ ,  $^5D_1 \rightarrow ^7F_0$  and  $^5D_2 \rightarrow ^7F_4$ ,  $^5D_1 \rightarrow ^7F_1$  and  $^5D_2 \rightarrow ^7F_4$ ,  $^5D_1 \rightarrow ^7F_2$  and  $^5D_2 \rightarrow ^7F_4$ ,  $^5D_0 \rightarrow ^7F_4$  and  $^5D_1 \rightarrow ^7F_6$ . Because the decay times of the higher excited levels is much

shorter than of  ${}^5D_0$ , the differentiation between the transitions is possible by the time-gated luminescence (by employing a pulsed excitation source, and detection after a given delay, when the higher states have been depopulated). The other method would be to directly excite the material to the  ${}^5D_0$  level or by recording materials with higher  $\text{Eu}^{3+}$  concentrations [102].

#### 2.4.3.3. PL quenching

Multiphonon relaxation between  ${}^5D_0$  and  ${}^7F_J$  can be neglected at room temperature, due to the large energy gap [99]. Fluorescence from the higher excited levels  ${}^5D_{3,2,1}$ , observed with high intensity in many glasses, are often not observed in most oxide or phosphate hosts due to the fast phonon assisted depopulation of these levels [118]. Emission from the  ${}^5D_3$  is observed only in host matrices with very low phonon energies, so that the radiative decay to the lower excited levels is very slow [102].

However, nonradiative energy transfer usually occurs as a result of exchange interaction, radiation reabsorption or multipole-multipole interaction. The exchange interaction of  $\text{Eu}^{3+}$ - $\text{Eu}^{3+}$  is generally responsible for the energy transfer of forbidden transitions whose distance is relatively low. The critical distance is thus defined as the separation between the donor and a quenching ion at which the nonradiative rate equals that of the internal single ion relaxation. The critical distance can be evaluated by:  $R_c = 2\sqrt[3]{3V/4\pi X_c N}$ , where  $X_c$  is the critical concentration,  $V$  is the volume of the unit cell and  $N$  is the number of cations per unit cell [137]. The critical transfer distance usually varies from 4 to 8 Å. The smaller energy transfer rate indicate low self-quenching luminescence [148]. The larger critical distance is an indication of the multipolar interaction involved in the energy transfer [149].

With increasing concentration of doped RE, the spacing between the adjacent RE ions decreases, and the probability for the energy transfer between them increases [28]. The energy transfer rate for dipole-dipole interaction between the acceptor (A) and sensitizer (S) ion (see Fig. 51) is given by [150]:

$$p_{SA} = \frac{8\pi^2}{3hg_Sg_A} R_{SA}^{-6} S D_S(J_S, J'_S) D_A(J_A, J'_A) \quad (2.4.3)$$

where  $J$  and  $J'$  are the ground and the excited state,  $S$  is the overlap integral,  $R_{SA}$  is the interionic distance,  $g$  is degeneracy, and  $D$  is the dipole strength. The field falls off as

$1/r^3$ , thus the energy density in the electric field  $u(\nu)=1/2 \epsilon_0 E^2$  falls off as  $1/r^6$ , resulting in an energy transfer rate from S to A depending on  $R_{SA}^{-6}$  [97].

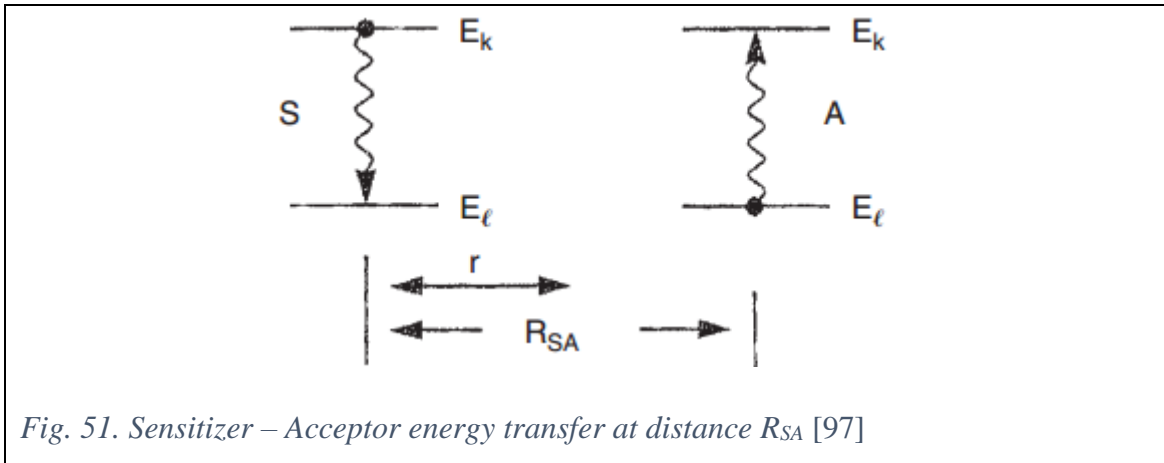
Van Uitert's equation that links the PL intensity with a concentration of RE is given by [99]:

$$I(C) = \frac{C}{K \left(1 + \beta C^{\frac{Q}{3}}\right)} \quad (2.4.4)$$

where  $K$  and  $\beta$  are constants for a certain system, and  $Q$  has values 6, 8, or 10, for dipole-dipole, dipole-quadrupole and quadrupole-quadrupole type of transition, respectively. By fitting the previous equation to the emission spectrum, it is possible to find the values of  $Q$  for each transition, indicating the type of mechanism behind it. The concentration can be calculated by:

$$C \left[ \frac{mol}{L} \right] = \frac{10^{27}}{V_u N_A} Z \delta \quad (2.4.5)$$

where  $V_u$  is the volume of the crystallographic unit cell in  $\text{\AA}^3$ ,  $Z$  is the number of formula units per unit cell, and  $\delta$  is the doping fraction.



Fluorescence power is linearly dependent on the concentration of emitting species at low concentrations [17]. The effect of concentration on fluorescence intensity is then given by:

$$F \approx 2.303 \phi_f K'' \epsilon b c P_0 \quad (2.4.6)$$

where  $K''$  is a geometry dependent constant,  $P_0$  is incident beam power,  $\varepsilon$  is molar absorptivity,  $c$  is the concentration,  $b$  is the path length of the beam through the sample, and  $\varepsilon bs$  represents the absorbance. Plot  $\phi_f(c)$  should be linear at low concentrations; at high concentrations this approximation does not hold because of the secondary absorption.

Thus, with increasing  $RE^{3+}$  concentration, the luminescence intensity increases up to the point (usually at several at%) where the concentration quenching prevails and the luminescence experiences a rapid drop with further increase in concentration. E.g. In  $LiGd_5P_2O_{13}:Eu^{3+}$ , Zhang et al. [149] have reported a maximum intensity with a high doping concentration of 0.2. In anatase  $TiO_2$ , Brik et al. [124] reported quantum efficiency of 0.84 for samples with low concentration of doped  $Eu^{3+}$ , and 0.63 for 10 at% europium concentration, with conclusion that the increase in concentration enhances non-radiative losses due to the reabsorption and energy transfers between closely located impurity ions.

$Eu^{3+}$  concentration has a large effect on the higher excited states. At Eu-Eu separation of ca. 40 Å the intensities of the higher excited states quickly fall off. This is the reason behind the color shift from blue to red with increasing concentration in glass hosts and the lack of such shift in oxide hosts [118].

The cross-relaxation increases with increasing concentration. The pairwise energy transfer mechanisms that are most probable for europium ion are [118]:

- a.  ${}^5D_3 \rightarrow {}^5D_2 \Rightarrow {}^7F_0 \rightarrow {}^7F_4, {}^7F_2 \rightarrow {}^7F_5, {}^7F_3 \rightarrow {}^7F_6$
- b.  ${}^5D_3 \rightarrow {}^7F_5 \Rightarrow {}^7F_2 \rightarrow {}^5D_2$
- c.  ${}^5D_3 \rightarrow {}^7F_4 \Rightarrow {}^7F_0 \rightarrow {}^5D_2$
- d.  ${}^5D_2 \rightarrow {}^5D_1 \Rightarrow {}^7F_1 \rightarrow {}^7F_4$
- e.  ${}^5D_2 \rightarrow {}^7F_4 \Rightarrow {}^7F_1 \rightarrow {}^5D_1$
- f.  ${}^5D_1 \rightarrow {}^5D_0 \Rightarrow {}^7F_2 \rightarrow {}^7F_4$

Co-doping  $Eu^{3+}$  compounds with other  $RE^{3+}$  that emit in the NIR region (e.g.  $Nd^{3+}$ ), quenches the  $Eu^{3+}$  luminescence, due to the energy transfer from  $Eu^{3+}$  to the nearest NIR emitting  $RE^{3+}$ , especially if that ion has resonant energy levels with  ${}^5D_0$  [102].

The radiative transition probability, branching ratios, the stimulated emission cross-section and the radiative lifetime are independent of the  $\text{Eu}^{3+}$  concentration [100], as can be seen in Table 9.

Table 9. JO intensity parameters, experimental lifetimes and non-radiative transition rates, quantum efficiencies and asymmetry ratios of  $\text{Y}_2\text{Hf}_2\text{O}_7:\text{Eu}^{3+}$  nanoparticles, at various concentrations of doped europium [131].

Conc.(at%)	$\Omega_2 (10^{-20} \text{ cm}^{-2})$	$\Omega_4 (10^{-20} \text{ cm}^{-2})$	$\tau$ (ms)	$A_R (s^{-1})$	$A_{NR} (s^{-1})$	$\eta$ (%)	R
1	7.03	3.64	1.53	454.39	199.20	69.52	4.38
2	6.88	3.65	1.54	444.61	204.73	68.47	4.25
4	7.01	3.87	1.47	458.25	226.67	66.91	4.37
8	6.78	4.06	1.45	452.65	246.64	64.73	4.23
12	6.51	4.16	1.38	442.75	281.88	61.11	4.06

PL intensity originating from the  $^5\text{D}_0$  level decreases with increasing temperature. The intensity of transitions originating from the  $^5\text{D}_1$  appear to initially decrease with temperature at low temperatures, before increasing at ca. 80 °C (see Fig. 52), which in contrast with the theory that predicts that if the populations are governed by a Boltzmann distribution the intensity from the upper level should always increase as the temperature is raised. The cause for this variation is due to the reduction in thermalizing rates from the  $^5\text{D}_0$  to the  $^5\text{D}_1$  level at lower temperatures due to the large energy gap. The other radiative and non-radiative rates dominate to such extent that the two levels cannot be considered as fully thermally coupled [52].

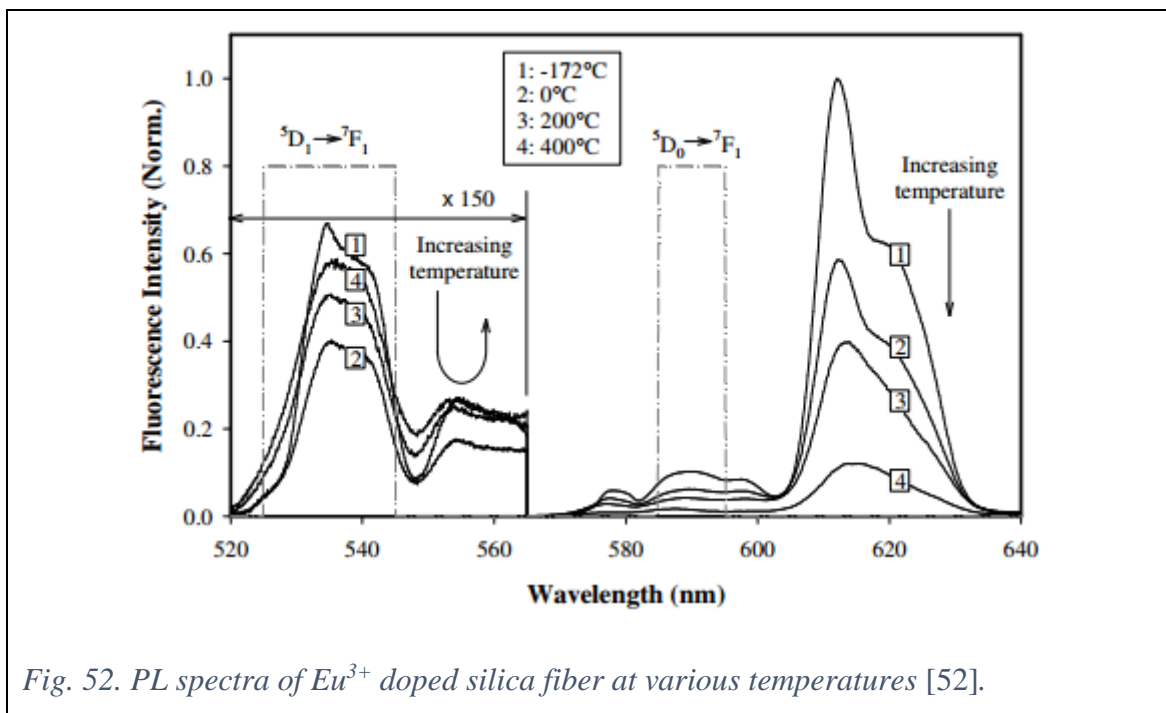


Fig. 52. PL spectra of  $\text{Eu}^{3+}$  doped silica fiber at various temperatures [52].

The lifetime of  ${}^5D_0$  does not vary significantly below room temperature. The measurements of fluorescence lifetime of the  ${}^5D_{0,1}$  levels as a function of temperature exhibited a slow and fast components of order ca. 1 ms and 4  $\mu$ s, respectively, as reported by Wade et al. in silica fiber [52]. The magnitude of the slow component increases with respect to the fast component as the temperature was raised. The fast initial decay has been related to the relaxation from the  ${}^5D_1$  to  ${}^5D_0$ , which is followed by a longer decay due to thermalization. Unlike the  ${}^5D_1$  fluorescence, only a slow decay component was observed for the  ${}^5D_0$  fluorescence.

#### 2.4.4. Europium as a spectroscopic probe

Not all RE are suitable as a probe for the site symmetry around the central metal ion, and the best RE for the job is the  $\text{Eu}^{3+}$  ion, because [119]:

1. The ground state,  ${}^7F_0$ , is non-degenerate, thus if  ${}^5D_0 \leftrightarrow {}^7F_0$  transition is observed in  $C_s$ ,  $C_n$ , and  $C_{nv}$  symmetries, it is possible to determine the number of non-equivalent sites in the host matrix, as for each site one transition is expected.
2. The straightforward relation between the CF splitting and CF parameters exists for  $J=1, 2$  values, and  $\text{Eu}^{3+}$  has levels with those values in spectral region which can be studied by optical spectroscopy. Thus, CF parameters can be deduced directly from the spectrum.
3. Different  $J$  levels are well separated.

Depending on the number of Stark components into which the  ${}^5D_0 \rightarrow {}^7F_j$  transitions are split, the symmetry at the  $\text{Eu}^{3+}$  site can be predicted [104], as presented in Table 10.

The observed number of bands could be fewer than predicted, since some transitions may appear too weak or due to the resonances between electronic and electronic-vibrational states [142].

${}^5D_0 \rightarrow {}^7F_0$  is allowed only in non-cubic crystallographic point groups which have no center of inversion. One has to be careful since  ${}^5D_1 \rightarrow {}^7F_3$  is overlapping with  ${}^5D_0 \rightarrow {}^7F_0$ , thus it is often wrongly identified. Number of  ${}^5D_0 \rightarrow {}^7F_0$  peaks may be indicative on the number of  $\text{Eu}^{3+}$  sites in a crystal, but only if they are all symmetry allowed [142].

Table 10. Number of CF components of different point group symmetry [102].

Point group	${}^7F_0$	${}^7F_1$	${}^7F_2$	${}^7F_3$	${}^7F_4$
$C_1$	1	3	5	7	9
$C_s$	1	3	5	7	9
$C_2$	1	3	5	7	9
$C_{2v}$	1	3	4	5	7
$C_i$	0	3	0	0	0
$C_{2h}$	0	3	0	0	0
$D_2$	0	3	3	6	6
$D_{2h}$	0	3	0	0	0
$D_{2d}$	0	2	2	3	3
$D_3$	0	2	2	4	4
$C_3$	1	2	3	5	6
$C_{3v}$	1	2	3	3	5
$C_{3h}$	0	2	1	3	4
$C_{3i}$	0	2	0	0	0
$D_{3d}$	0	2	0	0	0
$D_{3h}$	0	2	1	2	3
$C_4$	1	2	2	3	5
$C_{4h}$	0	2	0	0	0
$C_{4v}$	1	2	2	2	4
$D_{4h}$	0	2	0	0	0
$D_{4d}$	0	2	0	1	2
$S_4$	0	2	3	4	4
$D_4$	0	2	1	3	3
$C_6$	1	2	2	2	2
$C_{6v}$	1	2	2	2	2
$D_6$	0	2	1	2	1
$C_{6h}$	0	2	0	0	0
$D_{6h}$	0	2	0	0	0
$T$	0	1	1	2	2
$T_d$	0	1	1	1	1
$T_h$	0	1	0	0	0
$O$	0	1	0	1	1
$O_h$	0	1	0	0	0
$I_h$	0	1	0	0	0

## 2.5. Nanoscale PL structures

For designing a new equipment, crucial for modern applications, it is necessary to fully understand the influence of the geometry and morphology to the spectroscopic patterns of RE, especially for the nanoparticles [50]. Optical properties that change with particle size are emission lifetime, luminescence efficiency and concentration quenching [144].

In submicron architectures, (nanoparticles and thin films) the ratio of surface area to volume is high. [65], thus the surface properties become strongly relevant. E.g. on thin films of zirconia, most of the dopant ions do not enter the lattice of tetragonal zirconia to substitute  $Zr^{4+}$  ions. They are probably on the surface of  $ZrO_2$  crystallites, preventing their growth and providing the environment which favors the formation of the monoclinic zirconia [151]. As for the nanoparticles, 30 nm is the critical size below which pure tetragonal zirconia can be stabilized by the grain size alone [91].

Different excitation wavelengths can mean a different excitation process, thus this method can be used for identification of different  $Eu^{3+}$  sites in a crystal [152]. Excitations from host and CTB are nearly equal for larger particles. Liu at al. [146] reported that below the 23 nm in  $Gd_2O_3:Eu^{3+}$  the excitations by CTB are dominating.

Because nanoparticles are much smaller than the wavelength of light, their immediate surrounding environment needs to be considered to determine an effective index of refraction [153]. For nanocrystals, refractive index should be replaced by an effective refractive index, since only a fraction of the total volume is occupied by nanocrystals [130,144]:

$$n_{\text{eff}} = n_{\text{np}}x + (1 - x)n_{\text{med}} \quad (2.5.1)$$

where  $n_{\text{np}}$  and  $n_{\text{med}}$  are the refractive indexes of nanoparticles and surrounding media, respectively, and  $x$  is the filling factor representing the fraction of space occupied by the nanoparticles.

JO intensity parameters are different for nanoparticles and bulk materials. By reducing the particle size from 135 nm to 15 nm the quantum efficiency of the  $^5D_0$  band in  $Gd_2O_3:Eu^{3+}$  dropped for ca. 5 times, attributed to the enhancement of the nonradiative relaxation rate due to the large surface to volume ratio. The differences are due the

confinement effects on the vibrational states of impurity surface ions and the alteration of the electronic bands of the matrix [146]. Increase in luminescent efficiency was reported in cubic  $\text{Lu}_2\text{O}_3$ , where JO parameters were noticeably higher for nanocrystalline samples [144].

Nanothermometers are devices for temperature measurement with high spatial resolutions, employed in areas where conventional methods are less effective. They are needed in microelectronics, microoptics, photonics, microfluidics and nanomedicine. Nanothermometers can be used in temperature mapping of microcircuits or microfluids, or intercellular fluctuations [154]. The impact on the thermal sensitivity changes as follows: bulk material < nanowires < nanorods < nanoplates [32].

### 3. Experimental

#### 3.1. PEO

PEO method was chosen for creating the samples due to its wide industrial use, low price, speed and possibility of doping the created oxide films by RE ions. A 500 mL Pyrex beaker, with two 40 mm x 20 mm platinum plates was used for the formation of coatings, as presented in Fig. 53.

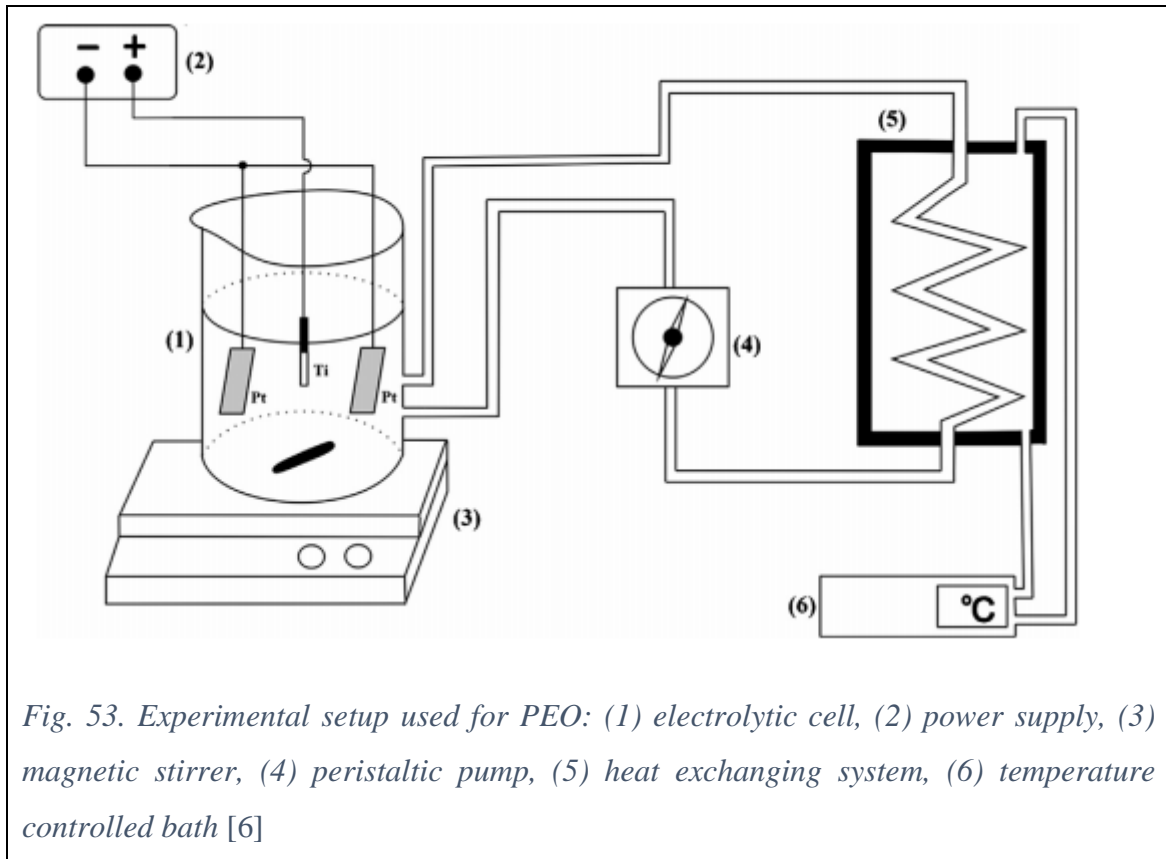


Fig. 53. Experimental setup used for PEO: (1) electrolytic cell, (2) power supply, (3) magnetic stirrer, (4) peristaltic pump, (5) heat exchanging system, (6) temperature controlled bath [6]

The starting material were titanium, zirconium, hafnium and niobium thin foils of dimensions: 15 mm x 5 mm x 0.25 mm for the hafnium foil and 25 mm x 10 mm x 0.15 mm for the rest. The material purity was 97%, 99.95%, 99.95% and 99.5% for Hf, Zr, Nb, and Ti foils, respectively. In Hf foil with 2.8%, the zirconium was the main impurity.

The foils were degreased in acetone, ethanol and then distilled water, and cleaned ultrasonically. Then the Ti, Nb, Zr and Hf foils were immersed into the electrolyte, consisting of water solution 10 g/L sodium phosphate dodecahydrate, 0.1 M phosphoric

acid, and 0.1 M boric acid + 0.05 M borax, and an aqueous solution of 20 g/L sodium phosphate dodecahydrate ( $\text{Na}_3\text{PO}_4 \cdot 12\text{H}_2\text{O}$ ), respectively. 4 g/L  $\text{Eu}_2\text{O}_3$  powder was added to the electrolyte for Hf foil, and 2 g/L for the rest. The pH of the electrolyte during the process with the Hf foil was 12.0, its conductivity was 10.7 mS/cm, and the temperature of the electrolyte during the PEO was maintained at  $(10 \pm 1)$  °C. PEO was carried out at constant current density of 300 mA/cm<sup>2</sup>, 150 mA/cm<sup>2</sup>, 200 mA/cm<sup>2</sup>, and 150 mA/cm<sup>2</sup>, for Hf, Ti, Nb and Zr foils, respectively, for 5, 10 and 15 minutes for Hf foil and 3, 5, and 10 minutes for other foils, for a total of 12 samples. The post-processing included rinsing in distilled water to prevent additional deposition of electrolyte components, and drying.

### 3.2. XRD, SEM, EDS, PL

X-Ray diffraction (XRD) was used to determine the phase composition of the sample. Measurements were made by Rigaku Ultima IV diffractometer in Bragg-Brentano geometry, with Ni-filtered  $\text{CuK}\alpha$  radiation ( $\lambda = 1.54178 \text{ \AA}$ ). The data were acquired over the  $2\theta$  scattering angle from 20° to 60° with acquisition time of 2°/min and 0.02° step. Rigaku PDLX 2 application software and COD database was used for peak identification.

A JEOL 840A scanning electron microscope (SEM) equipped with X-ray energy dispersive spectroscopy (EDS) was used to characterize the morphology and the chemical composition of the formed surface coatings.

Photoluminescence (PL) spectral measurements were taken on a Horiba Jobin Yvon Fluorolog FL3-22 spectrofluorometer at room temperature, with a 450 W xenon lamp as the excitation light source. The obtained spectra were corrected for the spectral response of the measuring system and the spectral distribution of the Xe lamp.

### 3.3. Heating/Cooling apparatus

Luminescence thermometry, in addition to a spectrofluorometer, requires an apparatus for sample heating/cooling. Temperature of the sample must be held stable during a measuring cycle of the spectrofluorometer, and sample temperature must be

measured by a precise reference thermometer [52]. Adequate commercial equipment is expensive, within the price range from several thousands to tens of thousands of USDs. The low material price was achieved by using widely available components, recycled material and by a careful design. Resistance thermometer sensor (RTD) was chosen as the reference detector, as it has higher accuracy and higher temperature stability than a thermocouple.

Built apparatus consists of several major parts: control/power unit (Fig. 54(a) to (g)), a very stable resistive heater with a large aluminum block (Fig. 54(h) and (i)), thermoelectric heater/cooler (TEC) for fast measurements (Fig. 54(j) to 1(m)), RTD (Fig. 56(a) to (f)), and an oven for the calibration of the RTD sensor (Fig. 56(i) to 3(k)).

### 3.3.1. Hot-plate in the range from room temperature to 400 °C

A heater that is low in price (ca. 10\$), is widely available and can achieve high temperatures is the ca. 1 kW radiant ceramic heating element for glass-ceramic hob stove. The hot-plate should be non-corrosive, with high thermal conductivity, high temperature stability, low price and low thermal emissivity on the given temperature range. The material that has the required properties is an aluminum alloy AlCuMgPb D5 Dural. Ø50 mm cylinder of bulk material was formed on the lathe to the shape of the conical frustum, in order to reduce the temperature gradient on the active surface (Fig. 56(g)). The weight and the heat capacity of the produced aluminum block are 1.8 kg and 1630 J/K, respectively. The high heat capacity increases temperature stability and reduces overshoot in achieving the desired temperature. The casing (Fig. 54(i)) is made by thermo-insulating foam, and additionally contains two empty chambers to prevent the heat going elsewhere but to the aluminum block. K-type thermocouple probe with M6 screw (Fig. 55(h)), typically used for 3D printers, is positioned in the aluminum block near the active surface.

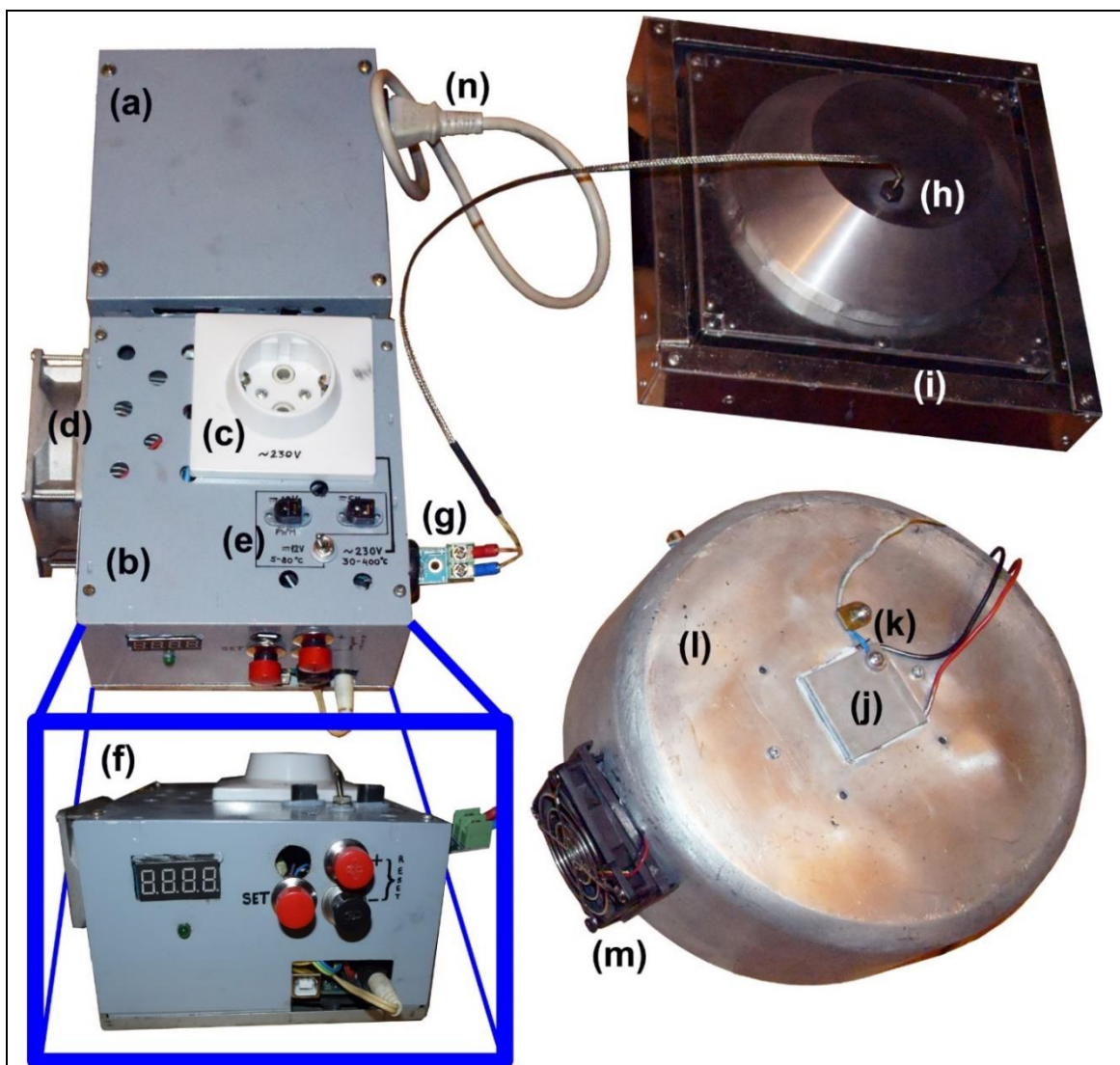


Fig. 54. Apparatus for heating and cooling samples. (a) ATX power supply, (b) control unit, (c) AC 230V port for hot-plate, (d) cooler with a fan, (e) port for 12V TEC, AC 230V and 12V mode switch, and 5V output for powering TEC fans, (f) control unit, front view, featuring LED display, control LED, control buttons and a USB port from the Arduino board, (g) thermocouple module, (h) thermocouple inserted into aluminum block, (i) double-wall aluminum casing of 230V hot-plate, (j) TEC, (k) thermocouple attached to TEC, (l) aluminum pot, (m) fan, (n) ATX power cord.

### 3.3.2. Hot/cold plate in the range from 0 °C to 80°C

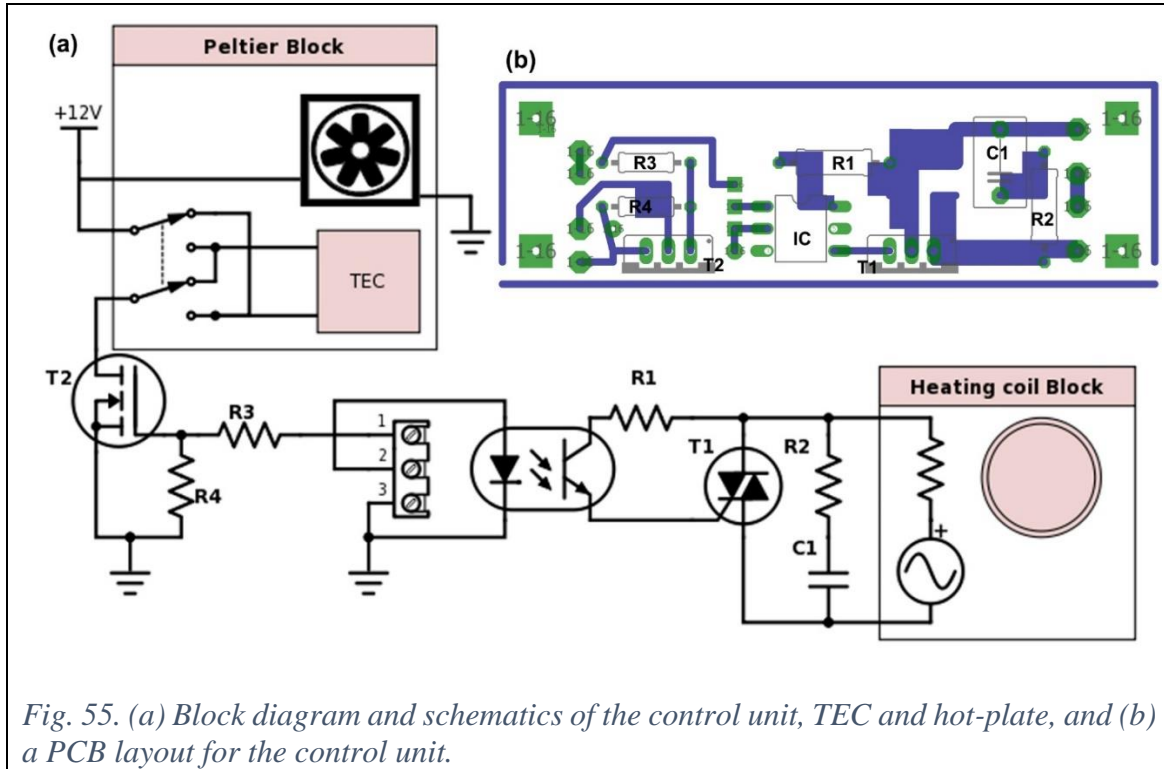
TEC is a solid-state heat pump that uses the Peltier effect to cool one and heat the other side of the element, where the cool and hot side depend on the polarity of the applied DC voltage. A maximum temperature difference of TEC is ca. 70 °C, thus the best performance can be achieved by keeping the unused side close to the room temperature.

Its advantages are small size, ease of control, DC 12 V operating voltage, and a low price. TEC 12715 has maximum 135 W power dissipation when powered by DC 12 V and a low price of ca. 3\$. One side of TEC is thermo-regulated by the active PC cooler, and a casing made from a large aluminum pot with 7 mm thick walls (Fig. 54(l)). On the active side a plate of dimensions 40 mm x 40 mm x 5 mm is placed (Fig. 54(j)) to improve the temperature stability. An additional PC 12V fan (Fig. 54(m)) attached to the casing increases the air flow and additionally stabilizes the TEC. On the top aluminum plate a K-type thermocouple (Fig. 54(k)) is attached as a feedback to the control unit.

### 3.3.3. Control/power unit

The control unit regulates both the hot-plate powered by AC 230V and the TEC. It consists of the following segments: ATX power supply (whose 12V powers the TEC element and 5V powers the microcontroller board), Arduino microcontroller board, pulse width modulation (PWM) switching board (Fig. 55(a)), and casing with switches, indicators and ports.

The benefits of the circuit of the PWM switching board presented here are: very low operating voltage (3-5V), a separation between high and low voltage circuitry by the opto-coupler, no mechanical parts, low size and a low price. The PCB with parts is given in Fig. 55(b). Parts list: opto-coupler MOC 3021, T1 – TRIAC BTA 16-600, T2 – MOSFET IRF 1010N, R1 – 360  $\Omega$  2 W, C1 – 0.01 $\mu$ F (optional), R2 – 39  $\Omega$  2 W (optional), R3/R4 = 1/10. TRIAC and MOSFET are attached to the active cooler (Fig. 54(d)).



The microcontroller board used was Arduino Uno (price ca. 5\$) with Atmel ATmega328P microcontroller. For measuring temperature via thermocouple sensor, MAX6675 module (Fig. 54(g)) with resolution of 0.25 °C on the 0-1024 °C temperature range and cold-junction compensation was used. TM1637 module is a 4-digit 7-segment LED with dots, utilized to display the temperature measured by the attached thermocouple.

The casing features control buttons (Fig. 54(f)) and ports (Fig. 54(c) and (e)). To match the code, given in Ref. [155], the pins on the Arduino Uno board should be attached as follows: pins 2 and 3 to the LED display, 4, 5 and 6 to the control buttons, 8, 9 and 10 are reserved for the thermocouple module, pin 11 is for 12V switching, pin 12 for 230V switching, A2 is for the control LED, 3.3V and 5V pins are for powering the display and thermocouple module, respectively.

By fitting the obtained temperatures to the applied PWM duty cycles, the following PWM duty cycle equations are obtained for the 230 V heater, TEC heating and cooling, respectively:

$$P[\%] = .8(1.015 * T_t - T + 1.5) + 0.00261 \cdot T_t^{1.57579} \quad (1)$$

$$P[\%] = 2.55 \cdot (T_t - T) - 15.09247 + .65495 \cdot T_t + .00535 \cdot T_t^2 \quad (2)$$

$$P[\%] = (T_t - T) + 103.7 - 5.35 T_t + .0633 T_t^2 \quad (3)$$

where  $T_t$  is the target temperature, and  $T$  is the current temperature as measured by the thermocouple. The manual for using the control unit is given in Ref. [156].

#### 3.3.4. Oven

Calibrating oven's top casing is made from a broken ATX power supply, and the bottom is made from a PC CD player's casing. The gaps are sealed and the walls insulated by chamotte. On the bottom, inside the CD player is the radiant ceramic heating element for glass-ceramic hob stove (Fig. 56(k)), thus it can be driven by the same control unit.

#### 3.3.5. RTD thermometer

The thermometer consists of three segments: microcontroller board with RTD read-out module, a casing with a display and a battery pack, and the probe. The chosen microcontroller board is Arduino Nano with Atmega328 microcontroller. MAX31865 module is a RTD analog-to-digital converter with 15b resolution, giving a 0.03 °C nominal temperature resolution to which RTD is connected via the 4-wire principle. pt100 Class B RTD by Heraeus is operable on the temperature range from -50 °C to 400 °C. The casing for the RTD sensor is made from chamotte (Fig. 56(a)) in order to withstand high temperatures. The window on the RTD casing (Fig. 56(b)), for the spectrofluorometer optic fiber bundle is made from quartz glass, which does not attenuate the UV light often used for RE excitation. The casing for the RTD is designed to provide a firm contact between the sensor and the sample's surface (Fig. 56(d) and (e)). By placing it on the hot/cold plate, it creates a miniature oven, reducing the undesired temperature gradient on the sample's surface.

RTD sensor in chamotte housing (Fig. 56(i)) was placed against the commercial RTD sensor (Fig. 56(j)) in the calibration oven. At various temperatures the read-out values were recorded and the corrections were made in the software code to match the readings by the commercial equipment. The complete software code for the microcontroller circuit is given in Ref. [155].

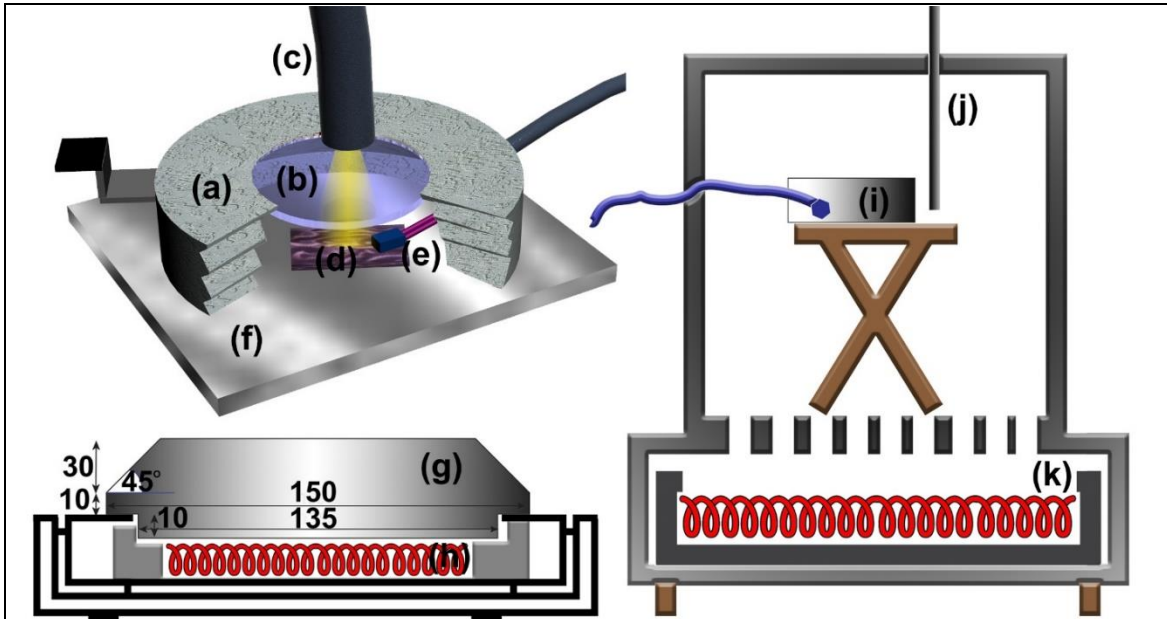


Fig. 56. RTD sensor bundle (top left), Hot-plate (bottom-left), oven (right). (a) Chamotte casing, (b) quartz glass, (c) fiber optic cable, (d) sample, (e) RTD sensor, (f) hot/cold plate, (g) aluminum block, (h) 1kW heater, (i) RTD sensor bundle, (j) commercial RTD sensor, (k) 0.5 kW heater.

### 3.3.6. Fiber optic bundle

The complete experimental setup for luminescence thermometry is presented in Fig. 57. The excitation beam and the resulting radiation is transmitted via an optical fiber bundle.

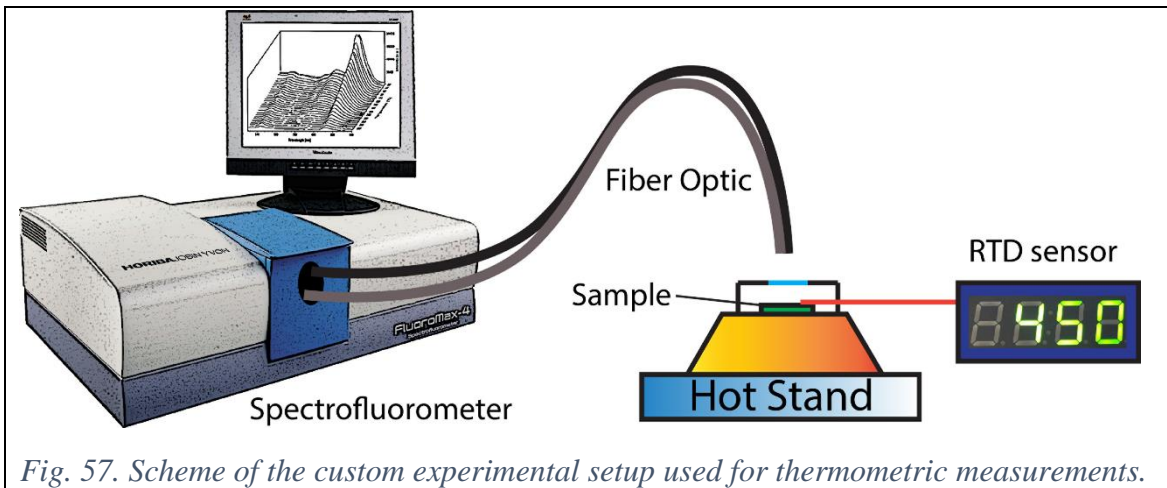


Fig. 57. Scheme of the custom experimental setup used for thermometric measurements.

## 4. Results and discussion

### 4.1. Morphology, chemical and phase compositions

#### 4.1.1. $\text{HfO}_2\text{:Eu}^{3+}$

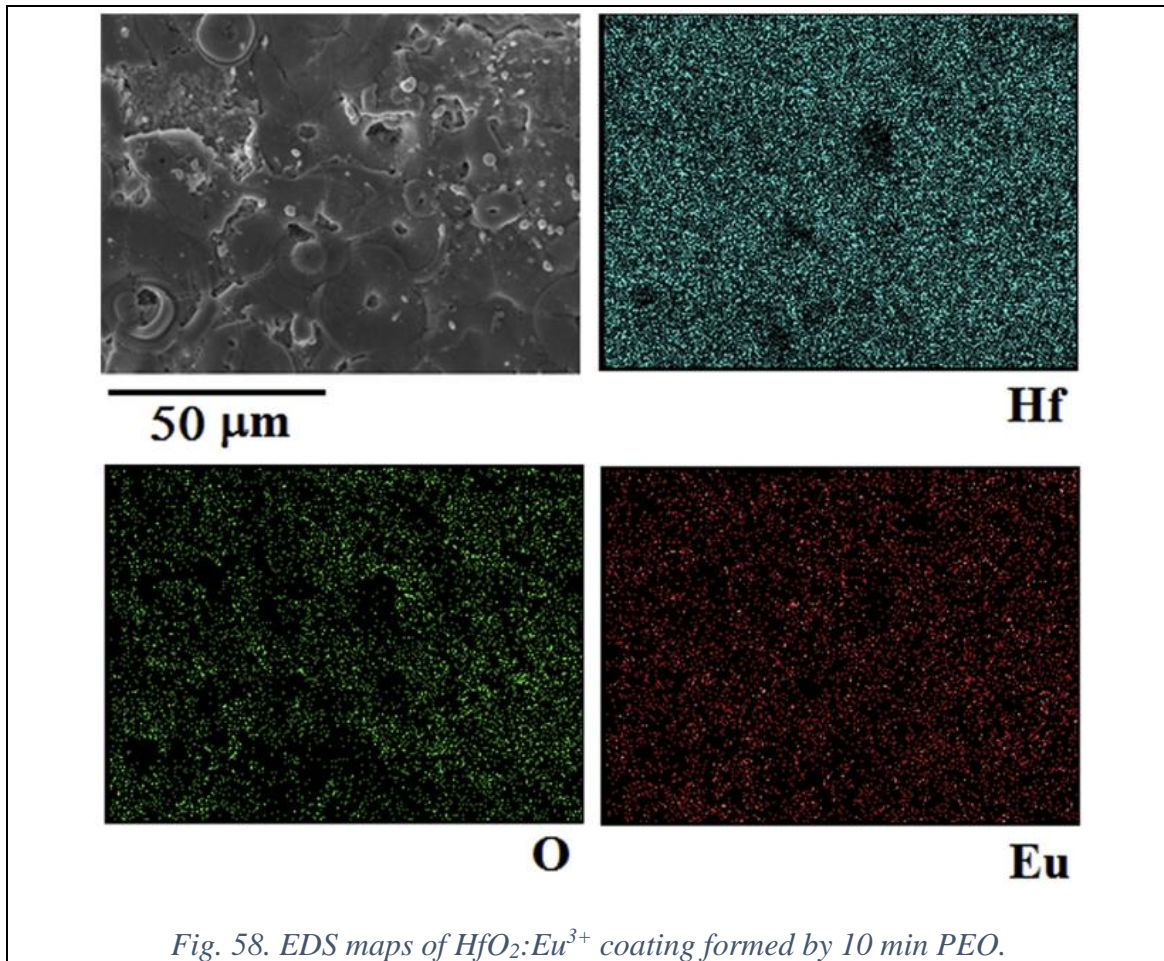
Top view and cross-sectional SEM micrographs of the coatings formed at various stages of PEO process are shown in Fig. 59. Numerous pores, cracks, and regions resulting from the rapid cooling of molten material decorate the surface of the coatings. Thickness of the coatings increases with PEO time and the average thickness of coating is approximately 7.1  $\mu\text{m}$  for the coatings formed after 5 min, 10.8  $\mu\text{m}$  for the coatings formed after 10 min, and 14.4  $\mu\text{m}$  for the coatings formed after 15 min. Results of EDS analyses of surface coatings in Fig. 59 are shown in Table 11. The elements identified in obtained PEO coatings are Hf, O, and Eu. All elements are rather uniformly distributed throughout the coatings (Fig. 58).

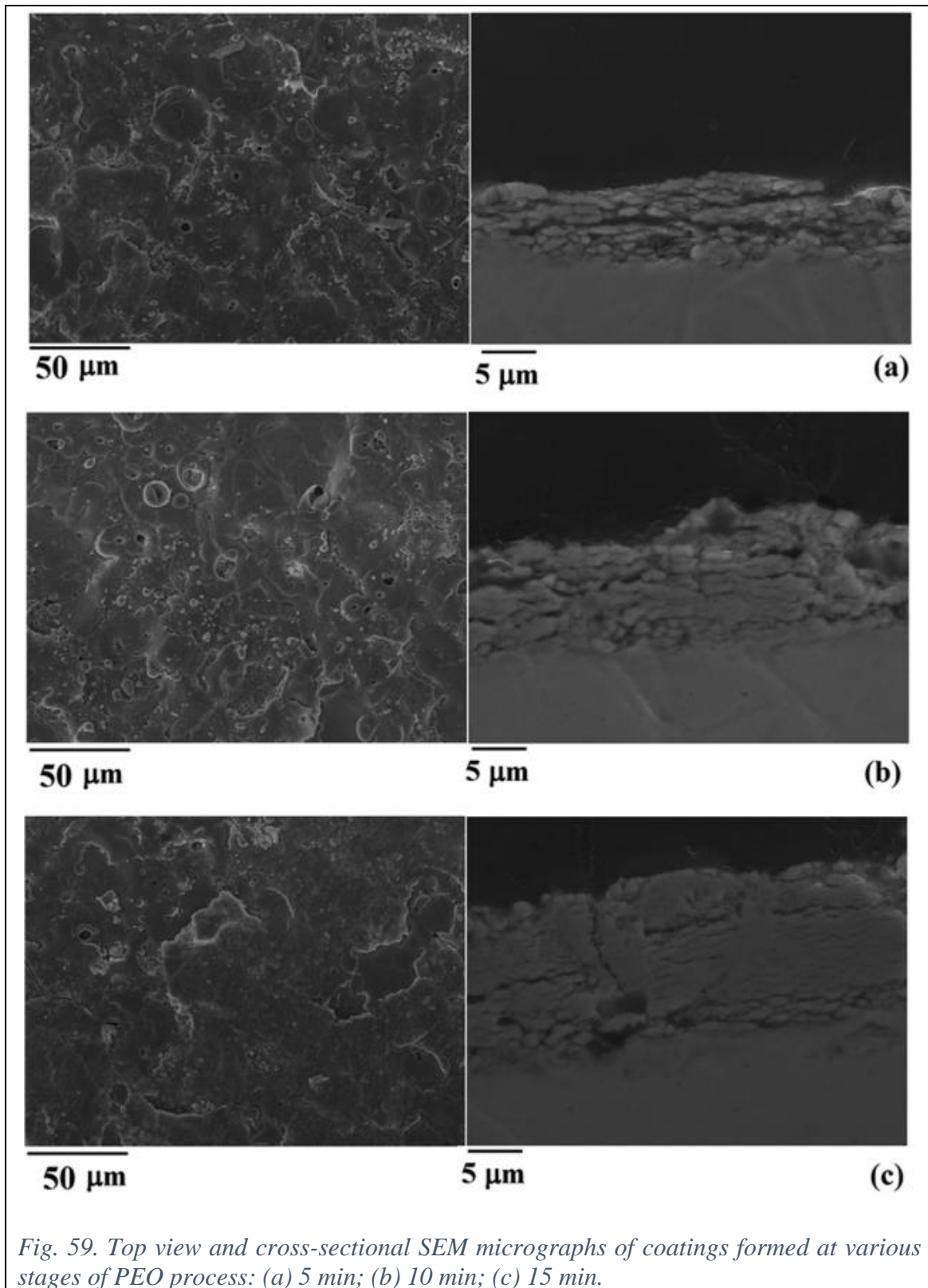
The elemental surface composition is closely related to the chemical mechanism of PEO process. Under locally high temperatures and pressures at sites of microdischarging, hafnium is melted out from the substrate.  $\text{Hf}^{4+}$  ions dissolved from the metallic Hf surface enter the microdischarge channels and react with  $\text{O}_2/\text{OH}$  ions from the electrolyte. Reaction products are ejected from active microdischarge channels onto the coating surface where they rapidly solidify in contact with the low temperature electrolyte. Finally, microdischarge channels get cooled and the reaction products are deposited onto its walls. This process repeats itself at a number of discrete locations over the coating surface, leading to an increase of the coating thickness. Incorporation of  $\text{Eu}_2\text{O}_3$  particles from the electrolyte is possible during the PEO process, through the electrophoretic and microdischarging mechanisms.  $\text{Eu}_2\text{O}_3$  particles have negative zeta potential in alkaline media [157] so it is expected that applied potential drives them towards the anode. Locally high temperature induced at the microdischarging sites, causes the deposition of  $\text{Eu}_2\text{O}_3$  particles on the surface of the formed oxide coating. Fig. 60 shows XRD patterns of PEO coatings formed after various PEO times. The coatings are crystallized and mainly composed of monoclinic  $\text{HfO}_2$  (reference JCPDS 43-1017). The average crystallite size of monoclinic  $\text{HfO}_2$ , calculated using Scherrer's equation from the strongest reflection (1,1,1) at  $2\theta = 28.4^\circ$ , is around 24 nm. Also, observed diffraction peak at around  $2\theta = 30.2^\circ$  matched (1,0,1) crystalline plane of

tetragonal  $\text{HfO}_2$  (reference JCPDS 08-0342). We were not able to detect any peaks corresponding to europium species in XRD patterns of formed PEO coatings, due to low concentration of uniformly dispersed  $\text{Eu}_2\text{O}_3$  particles in the surface coatings (Fig. 58). During the PEO process, molten material flows out of the microdischarge channels, contacts the surrounding low temperature electrolyte and rapidly solidifies as  $\text{HfO}_2$  at the coating/electrolyte interface, favoring the formation of monoclinic  $\text{HfO}_2$ . Predictably, monoclinic  $\text{HfO}_2$  is the main phase in the coating surface formed by the PEO process of hafnium.

Table 11. EDS analysis of  $\text{HfO}_2:\text{Eu}^{3+}$  PEO coatings.

PEO time (min)	Atomic (%)		
	O	Hf	Eu
5	76.94	22.77	0.29
10	77.36	22.16	0.48
15	77.63	21.75	0.62





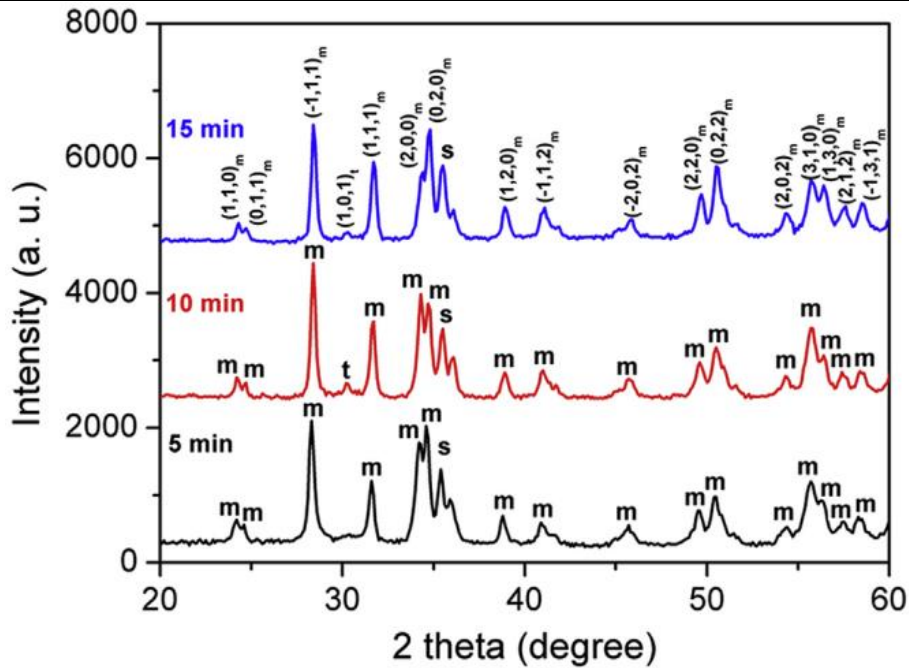


Fig. 60. XRD patterns of oxide coatings formed in various stages of PEO process (m - monoclinic  $\text{HfO}_2$ ; t - tetragonal  $\text{HfO}_2$ ; s - Hf substrate).

#### 4.1.2. $\text{Nb}_2\text{O}_5:\text{Eu}^{3+}$ and $\text{ZrO}_2:\text{Eu}^{3+}$

XRD patterns of  $\text{Eu}^{3+}$  doped  $\text{Nb}_2\text{O}_5$  and  $\text{ZrO}_2$  coatings are shown in Fig. 61.  $\text{Nb}_2\text{O}_5:\text{Eu}^{3+}$  coating is mostly composed of orthorhombic phase of  $\text{Nb}_2\text{O}_5$  (Fig. 61(a)), while monoclinic phase of  $\text{ZrO}_2$  is dominant in  $\text{ZrO}_2:\text{Eu}^{3+}$  coating (Fig. 61(b)). Peaks corresponding to europium species in XRD patterns of formed PEO coatings were not detect due to low concentration of uniformly dispersed  $\text{Eu}_2\text{O}_3$  particles in the surface coatings.

The  $\text{Eu}^{3+}$  concentrations in samples created by the 10 min PEO process are 1.42 at% and 0.44 at% in  $\text{Nb}_2\text{O}_5$  and  $\text{ZrO}_2$ , respectively.

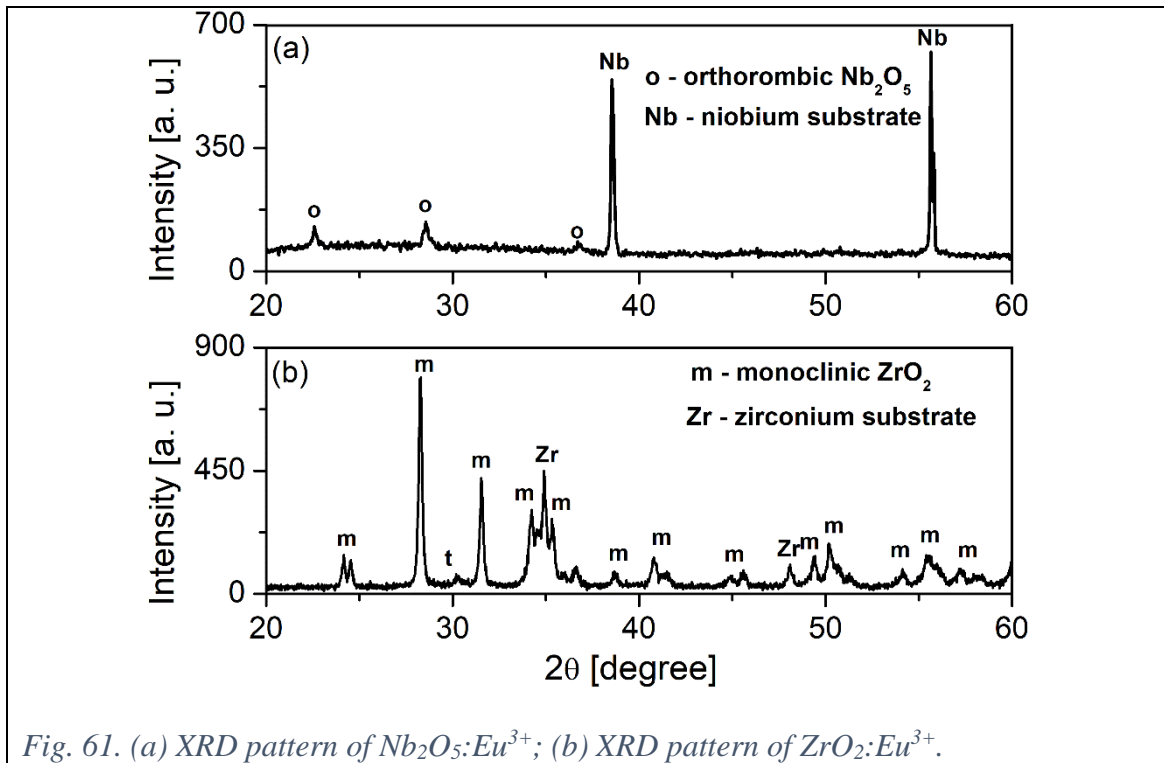


Fig. 61. (a) XRD pattern of  $\text{Nb}_2\text{O}_5:\text{Eu}^{3+}$ ; (b) XRD pattern of  $\text{ZrO}_2:\text{Eu}^{3+}$ .

#### 4.1.3. $\text{TiO}_2:\text{Eu}^{3+}$

XRD (Fig. 2) has revealed that the created  $\text{TiO}_2:\text{Eu}^{3+}$  coatings consists of anatase (space group  $I4_1/amd$  [158]) and rutile (space group  $P4_2/mnm$  [159]) phases (the former being the dominant one). The europium species are not visible which is due to the low concentrations. The concentration of incorporated europium species is 0.34% for the 10 min PEO process [6].

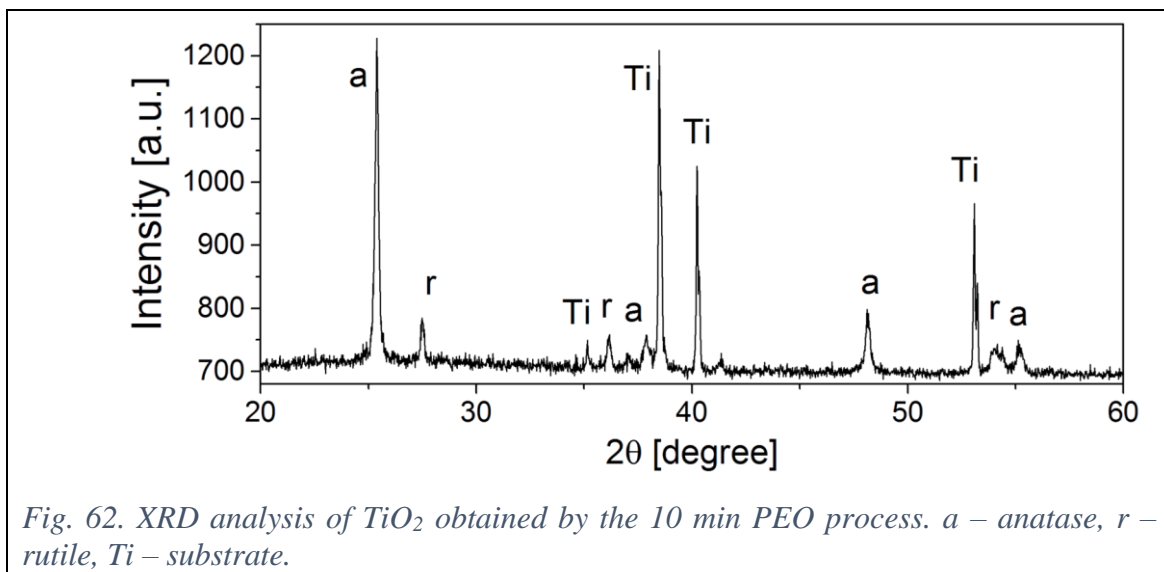


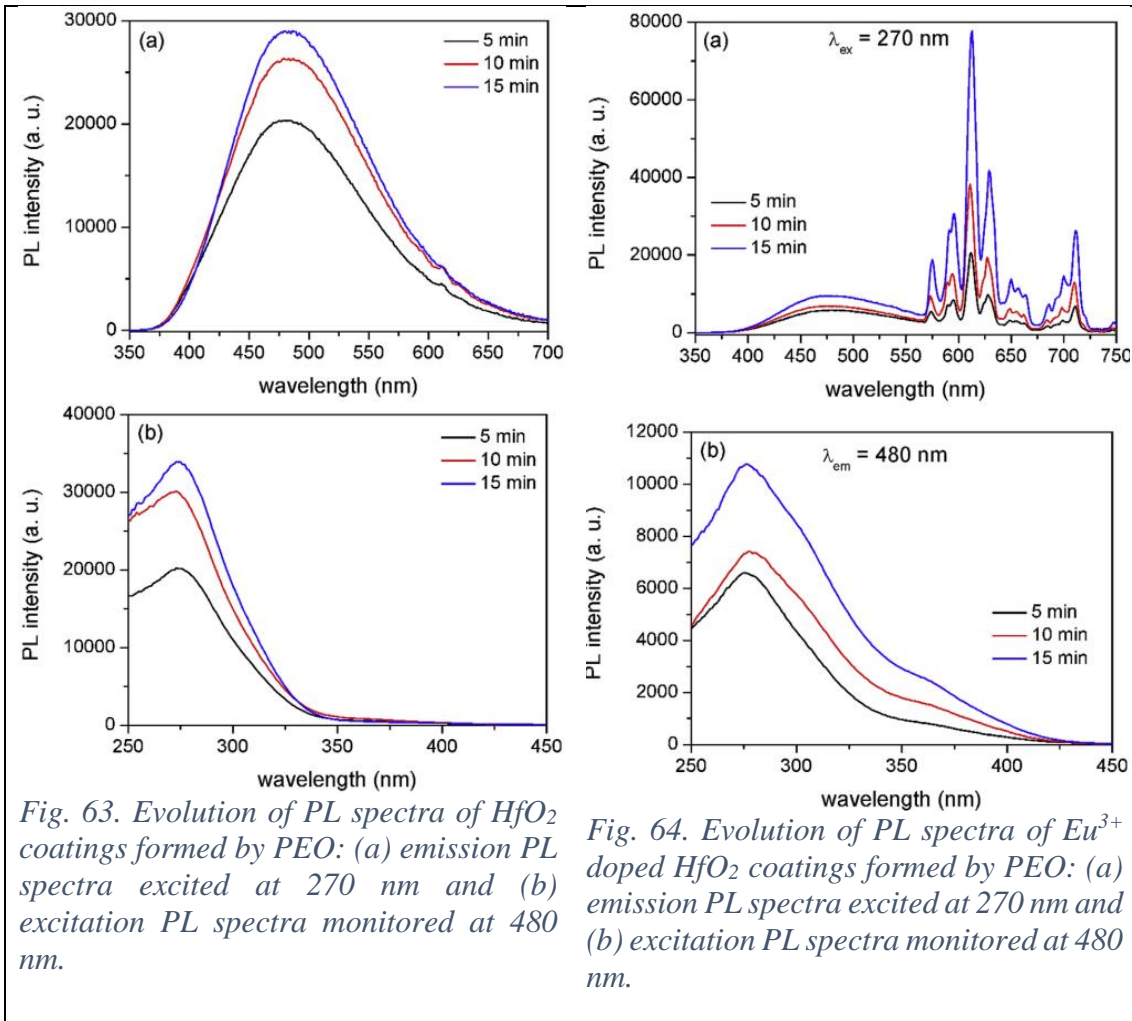
Fig. 62. XRD analysis of  $\text{TiO}_2$  obtained by the 10 min PEO process. a – anatase, r – rutile, Ti – substrate.

## 4.2. PL

### 4.2.1. HfO<sub>2</sub>:Eu<sup>3+</sup>

The PL of Eu<sup>3+</sup> doped HfO<sub>2</sub> coatings is a sum of PL originating from HfO<sub>2</sub> host and Eu ions incorporated into coatings. Fig. 63 shows typical PL emission and corresponding excitation spectra of HfO<sub>2</sub> coatings formed by PEO in the electrolyte without Eu<sub>2</sub>O<sub>3</sub> powder. Wide PL emission band is present in the visible region. It is generally proposed that PL of HfO<sub>2</sub> originates from optical transitions in PL centers which are defect centers related to oxygen vacancies [160]. The principal spectral maximum in emission PL spectra is positioned at around 480 nm, while its excitation spectra equivalent is at around 270 nm. PL intensity of obtained HfO<sub>2</sub> coatings increased with PEO processing time, which is related to an increase of oxygen vacancy defects [161]. The evolution of PL emission spectra of Eu doped HfO<sub>2</sub> coatings formed by PEO excited at 270 nm and the corresponding excitation spectra monitored at 480 nm are shown in Fig. 64. PL emission spectra feature two distinct regions. The first region represents characteristic blue PL band of HfO<sub>2</sub> with maximum at about 480 nm (see Fig. 63a). The second region features sharp emission bands in the orange-red region of visible spectrum which are related to 4f-4f transitions of Eu<sup>3+</sup> from the excited level <sup>5</sup>D<sub>0</sub> to the lower levels <sup>7</sup>F<sub>J</sub> (J = 0, 1, 2, 3, and 4). The bands are centered at around 575 nm, 595 nm, 613 nm, 649 nm, and 711 nm, which are assigned to the <sup>5</sup>D<sub>0</sub>→<sup>7</sup>F<sub>0,1,2,3,4</sub> transitions, respectively. PL intensity of the broad emission band of HfO<sub>2</sub> increases as a result of increased concentration of oxygen vacancy defects with PEO time, while increasing content of Eu<sup>3+</sup> ions incorporated into the coatings during the PEO process results in increasing PL intensity of the sharp emission bands (see Table 11). The PL excitation spectra in Fig. 64b have spectral maximum at around 270 nm. Excitation PL spectra of Eu<sup>3+</sup> doped HfO<sub>2</sub> coatings monitored at 613 nm, i.e. at the wavelength of the most intense peak in emission PL spectra (Fig. 64a), are shown in Fig. 65a. The excitation spectra can be divided into two regions: the broad band region from 250 nm to 350 nm and the series of sharp peaks in the range from 350 nm to 550 nm which correspond to the direct excitation of the Eu<sup>3+</sup> ground state <sup>7</sup>F<sub>0</sub> into higher levels of the 4f-manifold. These peaks are weak and only several main transitions were observed, such as <sup>7</sup>F<sub>0</sub>→<sup>5</sup>D<sub>4</sub> at 365 nm, <sup>7</sup>F<sub>0</sub>→<sup>5</sup>L<sub>7</sub> at 384 nm, <sup>7</sup>F<sub>0</sub>→<sup>5</sup>L<sub>6</sub> at 396 nm, <sup>7</sup>F<sub>0</sub>→<sup>5</sup>D<sub>3</sub> at 417 nm, <sup>7</sup>F<sub>0</sub>→<sup>5</sup>D<sub>2</sub> at 468 nm, <sup>7</sup>F<sub>0</sub>→<sup>5</sup>D<sub>1</sub> at 530 nm, and <sup>7</sup>F<sub>1</sub>→<sup>5</sup>D<sub>1</sub> at 537 nm. Since optical transitions of HfO<sub>2</sub> contribute very little to overall PL,

broad PL excitation band is mainly caused by the electron transfer between the completely filled 2p orbital of O<sub>2</sub> ions and the partially filled 4f orbital of the of Eu<sup>3+</sup> ions. This is confirmed by measuring excitation PL spectra monitored at 613 nm of Eu<sup>3+</sup> doped and pure HfO<sub>2</sub> coatings formed by 15 min PEO (Fig. 65b). A wide emission PL band of HfO<sub>2</sub> overlaps with the Eu<sup>3+</sup> excitation bands. PL emission band of pure HfO<sub>2</sub> coatings shows higher PL intensity compared to the Eu<sup>3+</sup> doped HfO<sub>2</sub> coatings formed under same conditions (see Fig. 63a and Fig. 64a). These results indicate the existence of non-radiative energy transfer from HfO<sub>2</sub> to Eu<sup>3+</sup> dopant. The similar model has been proposed for Eu<sup>3+</sup> doped ZrO<sub>2</sub> coatings [4].



PL emission spectra of Eu<sup>3+</sup> doped HfO<sub>2</sub> coatings, in the range from 550 nm to 750 nm, excited at the wavelength of the most intense peak in PL excitation spectra (<sup>7</sup>F<sub>0</sub>→<sup>5</sup>L<sub>6</sub> transition at 396 nm) are shown in Fig. 66a. The shape of PL emission spectra

is typical for  $\text{Eu}^{3+}$  ions in monoclinic surrounding. The intensity of peaks changes with the concentration of  $\text{Eu}^{3+}$ , i.e. time of PEO, but the peak positions remain practically unchanged. The most intense peak centered at around 613 nm corresponds to the electric dipole transition  ${}^5\text{D}_0 \rightarrow {}^7\text{F}_2$ . This transition is a hypersensitive transition (with respect to the local environment around the  $\text{Eu}^{3+}$  ion), and it is allowed only if  $\text{Eu}^{3+}$  ion occupies a site without an inversion center. The bands at around 624 nm and 629 nm also belong to the  ${}^5\text{D}_0 \rightarrow {}^7\text{F}_2$  transition. This multiple transition from  ${}^5\text{D}_0 \rightarrow {}^7\text{F}_2$  in monoclinic  $\text{HfO}_2$  can be associated with the lower local symmetry of  $\text{Eu}^{3+}$  ions. The peaks at about 590 nm and 595 nm are ascribed to permitted magnetic dipole transition  ${}^5\text{D}_0 \rightarrow {}^7\text{F}_1$ , which is independent of the local crystalline environment surrounding the active ions. In the case when  $\text{Eu}^{3+}$  ions occupy non-inversion symmetry lattice sites,  ${}^5\text{D}_0 \rightarrow {}^7\text{F}_2$  electric dipole transition becomes the most intense transition. If  $\text{Eu}^{3+}$  ions are located at the inversion symmetry site, then  ${}^5\text{D}_0 \rightarrow {}^7\text{F}_1$  magnetic dipole transition is the dominant one. The asymmetric ratio  $R$  between  ${}^5\text{D}_0 \rightarrow {}^7\text{F}_2$  and  ${}^5\text{D}_0 \rightarrow {}^7\text{F}_1$  transitions is used to measure the degree of distortion from inversion symmetry of the local environment surrounding  $\text{Eu}^{3+}$  ions in the host matrix. The asymmetric ratio between  ${}^5\text{D}_0 \rightarrow {}^7\text{F}_2$  and  ${}^5\text{D}_0 \rightarrow {}^7\text{F}_1$ , excited at 396 nm, is presented in Fig. 66b. The values of  $R$  were calculated using the equation 2.3.110. The asymmetric ratio increases slightly with increasing  $\text{Eu}^{3+}$  concentration, i.e. with PEO time. Reasonably high value of the asymmetric ratio indicates highly asymmetric environment around  $\text{Eu}^{3+}$  ions. Due to the mismatch of ionic radii and the charge imbalance between  $\text{Hf}^{4+}$  (71 pm) and  $\text{Eu}^{3+}$  (0.97 pm), the substitution of  $\text{Hf}^{4+}$  with  $\text{Eu}^{3+}$  ions in the crystalline lattice causes local disordering, resulting in reduced local symmetry. The observation of the  ${}^5\text{D}_0 \rightarrow {}^7\text{F}_0$  transition at 575 nm in PL emission spectra is an indication that the  $\text{Eu}^{3+}$  ion occupies a site with  $C_{nv}$ ,  $C_n$  or  $C_s$  symmetry.

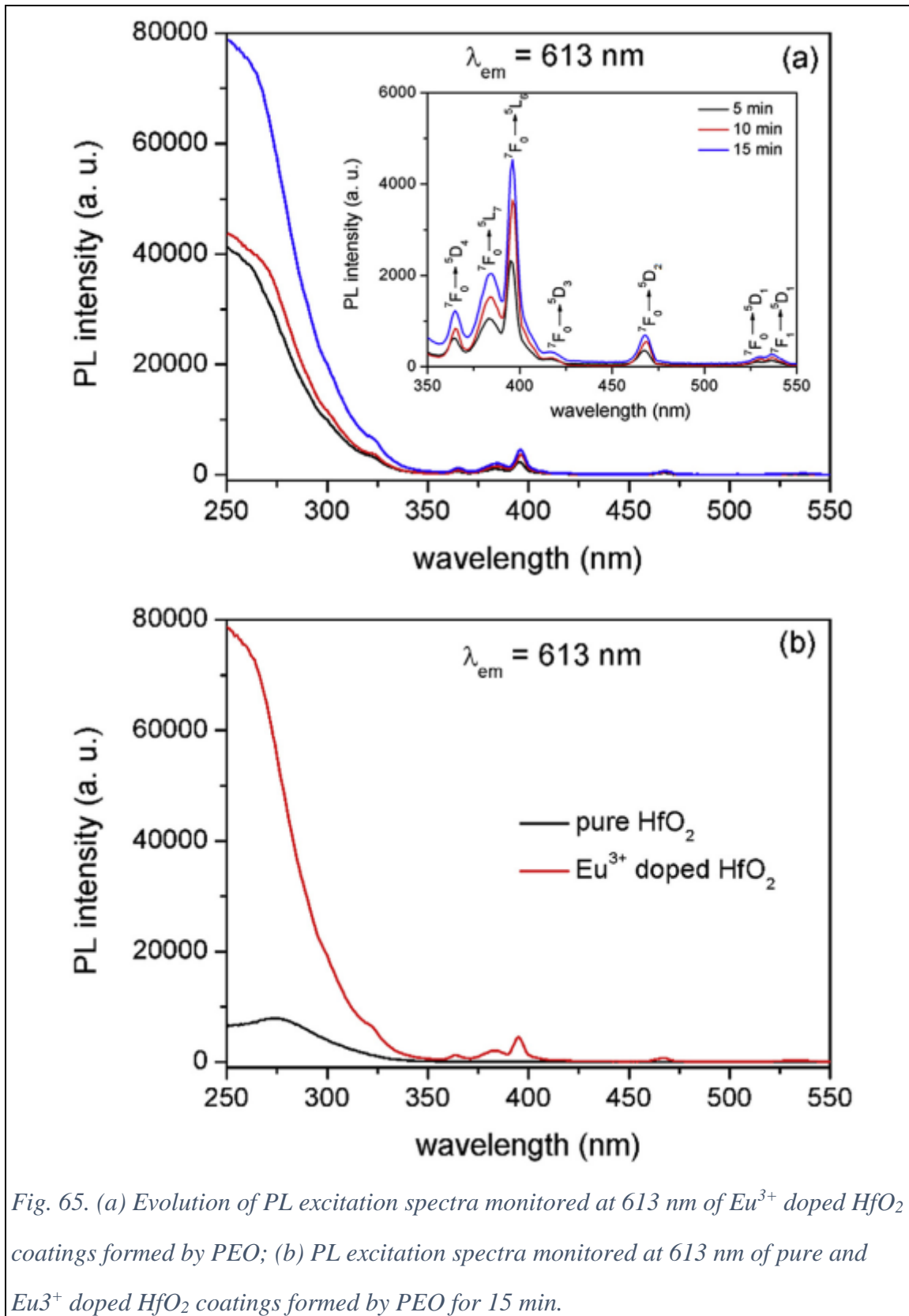


Fig. 65. (a) Evolution of PL excitation spectra monitored at 613 nm of  $\text{Eu}^{3+}$  doped  $\text{HfO}_2$  coatings formed by PEO; (b) PL excitation spectra monitored at 613 nm of pure and  $\text{Eu}^{3+}$  doped  $\text{HfO}_2$  coatings formed by PEO for 15 min.

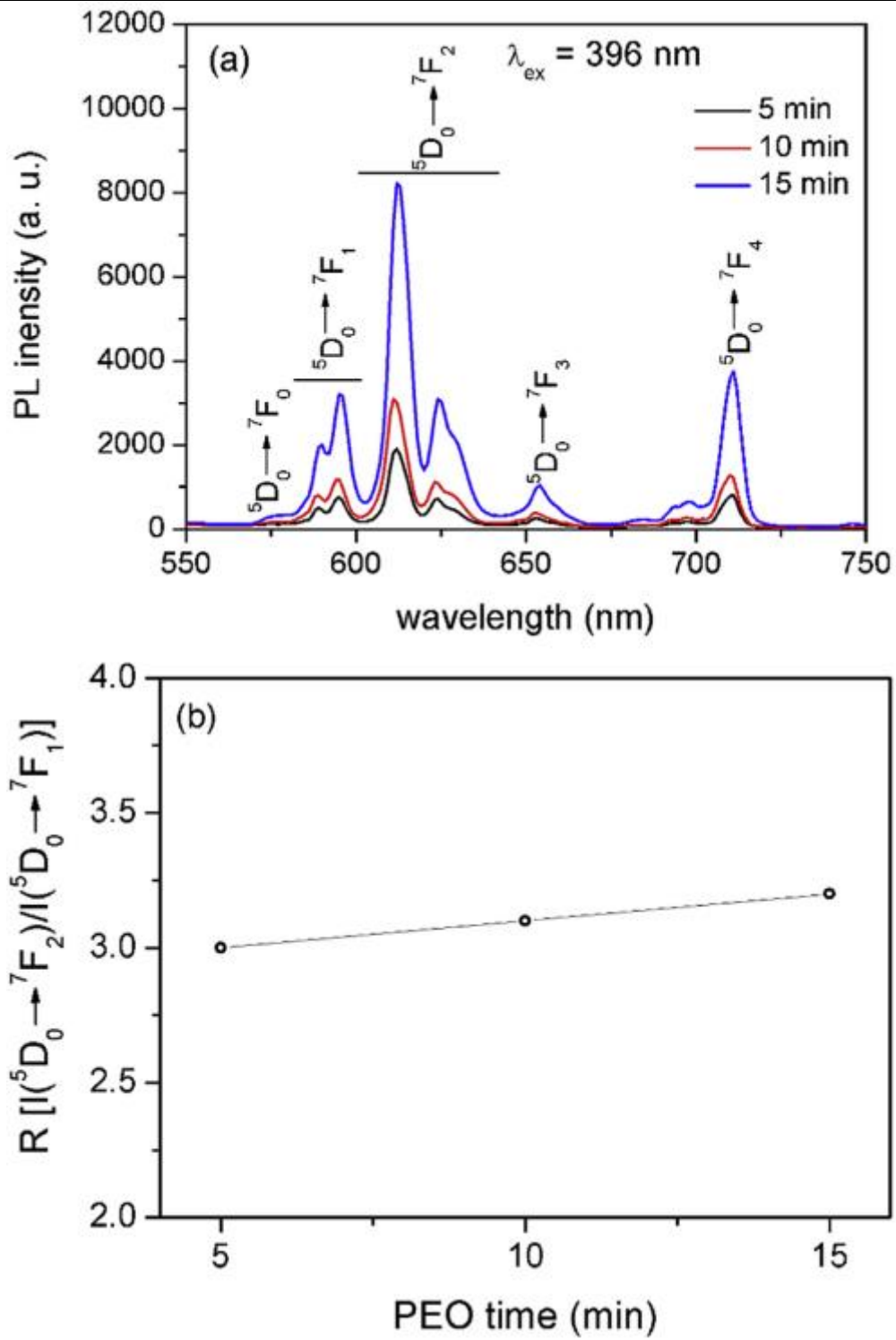
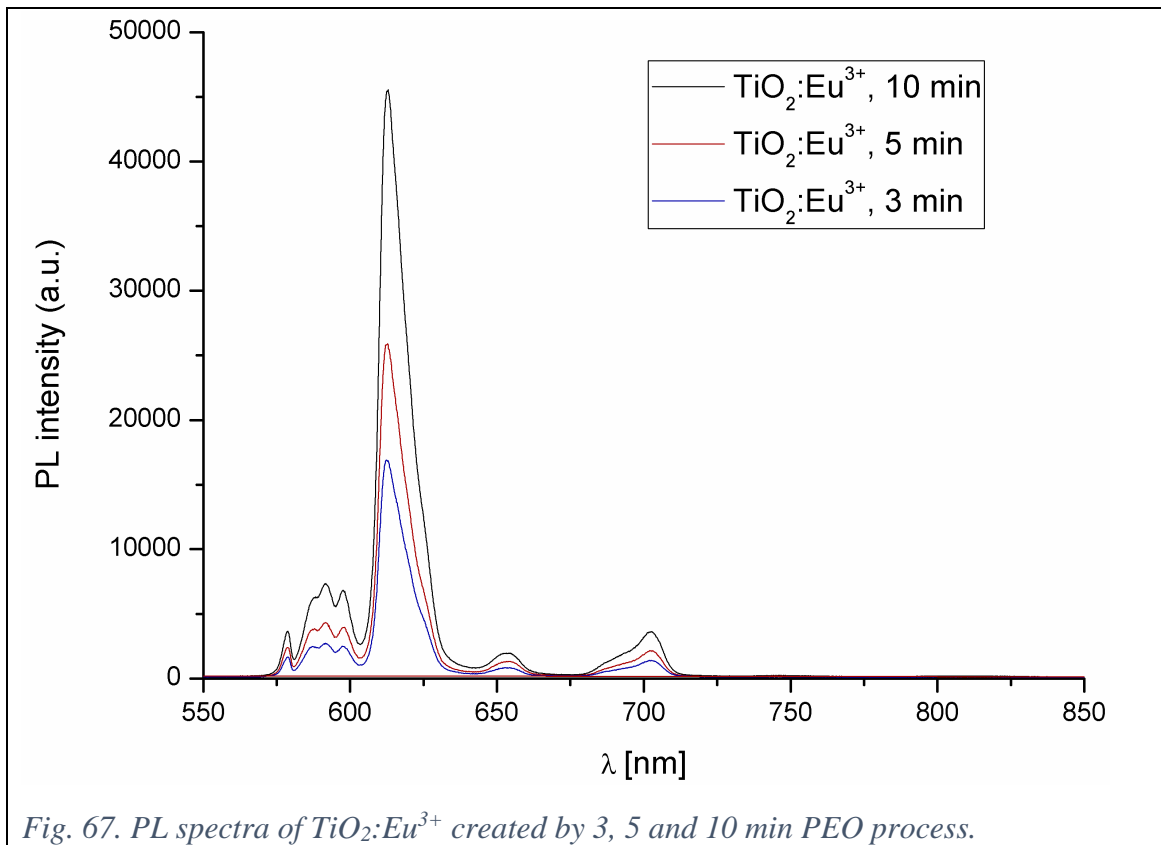


Fig. 66. (a) Evolution of PL emission spectra excited at 396 nm of  $\text{Eu}^{3+}$  doped  $\text{HfO}_2$  coatings formed by PEO; (b) The asymmetric ratio between  $^5\text{D}_0 \rightarrow ^7\text{F}_2$  and  $^5\text{D}_0 \rightarrow ^7\text{F}_1$ .

#### 4.2.2. $\text{TiO}_2:\text{Eu}^{3+}$ , $\text{Nb}_2\text{O}_5:\text{Eu}^{3+}$ and $\text{ZrO}_2:\text{Eu}^{3+}$

The emission spectra of Eu doped Ti, Nb and Zr oxides were recorded upon the excitation  ${}^7\text{F}_0 \rightarrow {}^5\text{L}_6$  by 393 nm beam and are presented in Fig. 67, Fig. 68, and Fig. 69, respectively. On the recorded range 550 – 850 nm, transitions  ${}^5\text{D}_0 \rightarrow {}^7\text{F}_{0,1,2,3,4}$  can be clearly identified. The transitions  ${}^5\text{D}_0 \rightarrow {}^7\text{F}_{5,6}$  were of low intensity and are thus not observed, except in  $\text{ZrO}_2:\text{Eu}^{3+}$  where a low intensity  ${}^5\text{D}_0 \rightarrow {}^7\text{F}_5$  can be seen at ca. 750 nm.



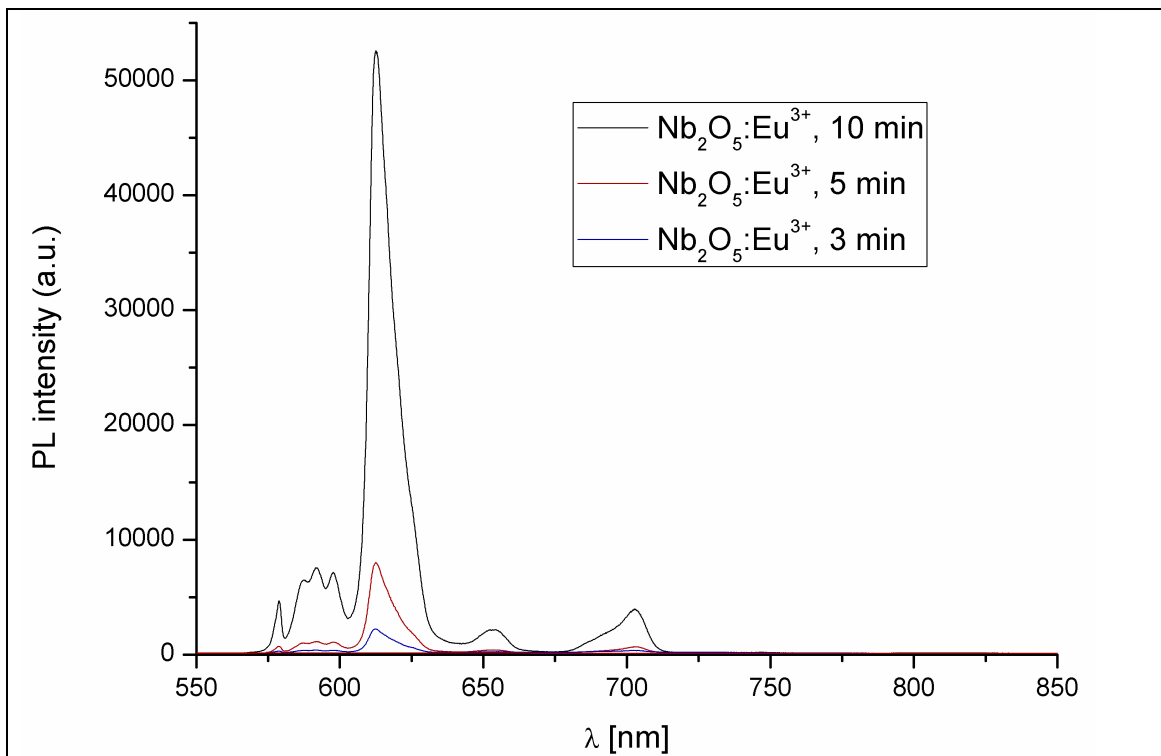


Fig. 68. PL spectra of Nb<sub>2</sub>O<sub>5</sub>:Eu<sup>3+</sup> created by 3, 5 and 10 min PEO process.

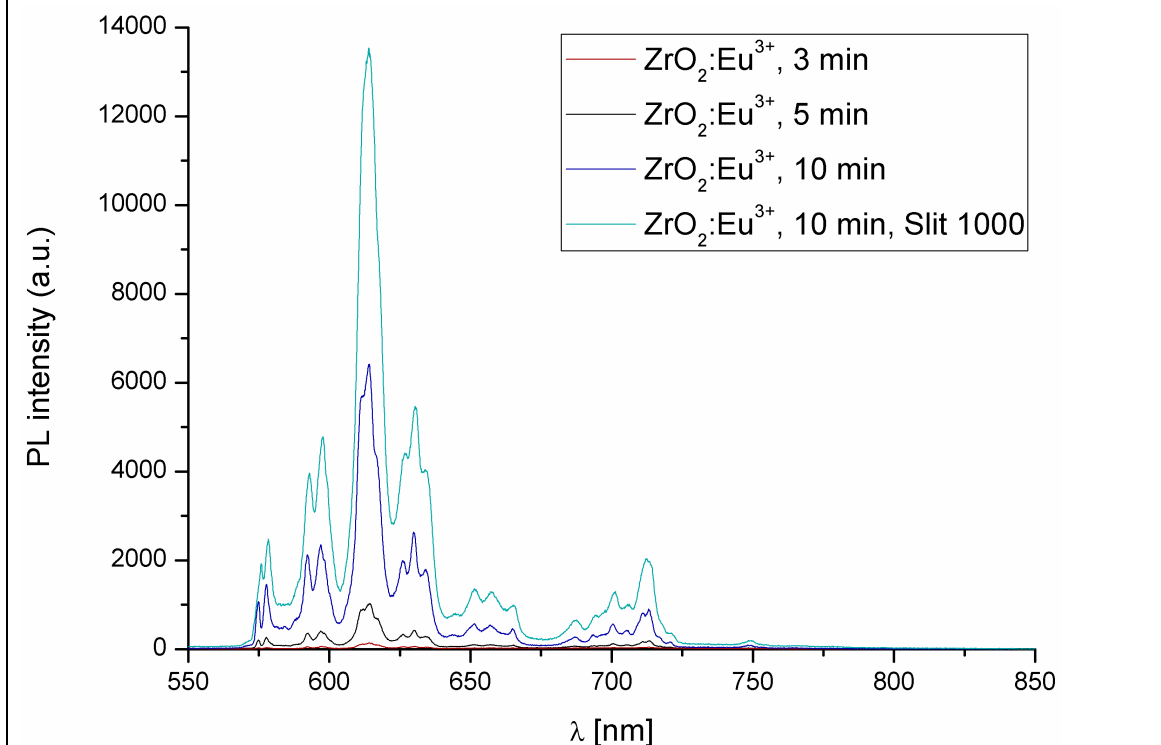


Fig. 69. PL spectra of ZrO<sub>2</sub>:Eu<sup>3+</sup> created by 3, 5 and 10 min PEO process.

### 4.3. Heating/Cooling apparatus

230V hot-plate was tested by setting the time interval to 30 min, at which the target temperature was risen up to 400 °C by 50 °C steps. The temperature was recorded every minute. The results show the speed in achieving the target temperature, the relatively low overshoot and the high stability of achieved temperature, which lies within the thermocouple readout error. The recorded temperatures are presented in Fig. 70(a).

TEC heating was tested by setting the 10 °C steps up to 100 °C, and 10 min time for each step. Testing of TEC cooling was done by the 5 °C step. The recorded temperatures for both modes of TEC operation are given in Fig. 70(b).

As it is assumed, the 230V hot-plate is slower, but more stable than TEC in the heating mode. Both modules achieved the desired temperatures, in the given temperature range, and have a good temperature stability on the whole operable range.

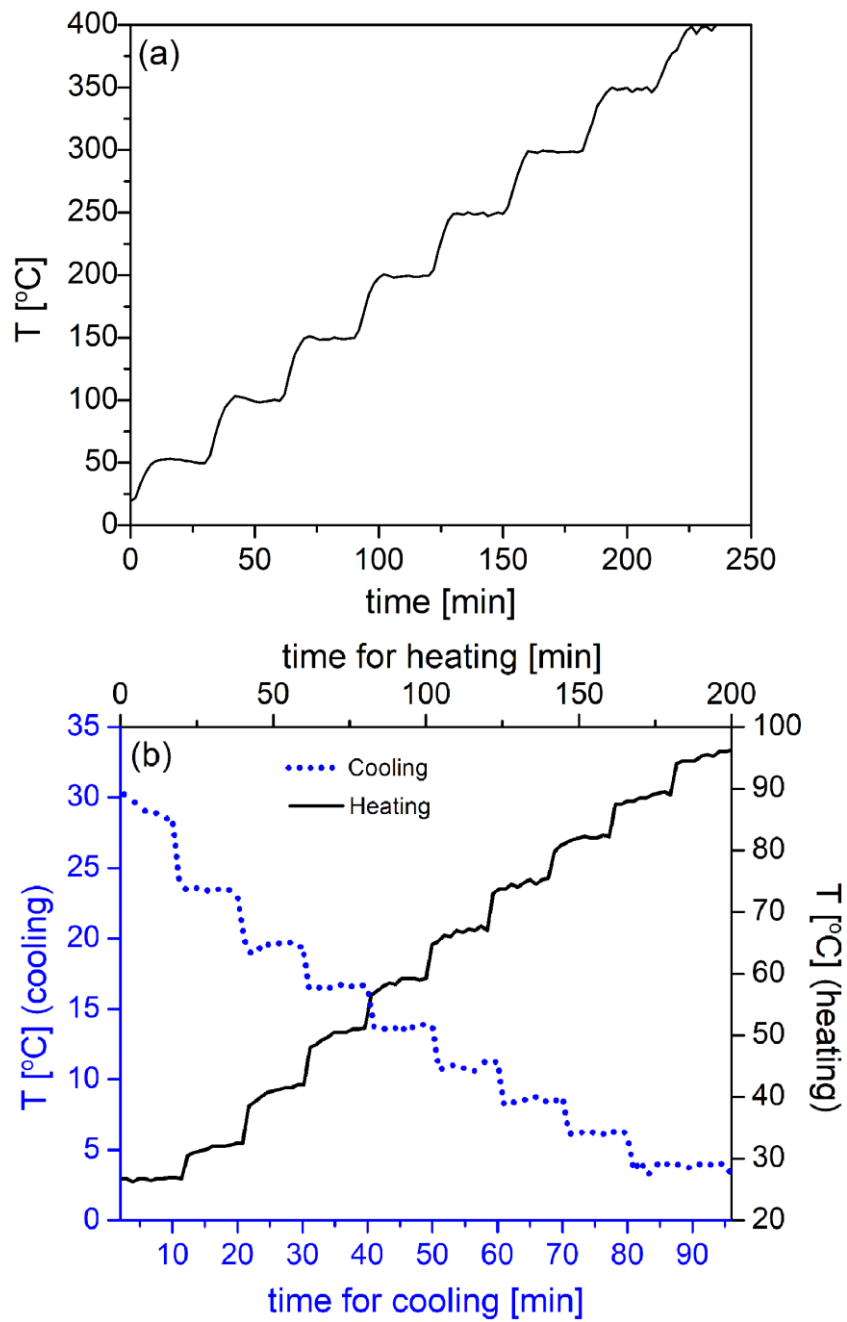


Fig. 70. Testing accuracy and speed of the (a) 230 V hot-plate, (b) 12V TEC.

## 4.4. LIR

### 4.4.1. $\text{Nb}_2\text{O}_5:\text{Eu}^{3+}$ and $\text{ZrO}_2:\text{Eu}^{3+}$

Temperature dependent PL emission spectra feature peaks at the same positions in  $\text{Nb}_2\text{O}_5:\text{Eu}^{3+}$  and  $\text{ZrO}_2:\text{Eu}^{3+}$  (see Fig. 6a and 6b, respectively). At 544 nm, the temperature independent peak created by  $^5\text{D}_1 \rightarrow ^7\text{F}_1$  transition is observed, with  $^5\text{D}_1 \rightarrow ^7\text{F}_2$  appearing as a shoulder peak to the right. Both samples show a much greater intensity of the hypersensitive  $^5\text{D}_0 \rightarrow ^7\text{F}_2$  than the magnetic dipole  $^5\text{D}_0 \rightarrow ^7\text{F}_1$  transition, which is in accordance with the low symmetry observed in the XRD patterns.

The intensity of the  $^5\text{D}_0 \rightarrow ^7\text{F}_2$  transition in  $\text{Nb}_2\text{O}_5:\text{Eu}^{3+}$  drops rapidly and in  $\text{ZrO}_2:\text{Eu}^{3+}$  drops slowly with increasing temperature. The  $\text{Nb}_2\text{O}_5:\text{Eu}^{3+}$  is recorded in 10 °C steps and on the range from the room temperature to 180 °C, and  $\text{ZrO}_2:\text{Eu}^{3+}$  in 50 °C steps in the range from room temperature to 272 °C. LIR experimental values and theoretical fits to the equation 2.1.12 are given in Fig. 71. B values obtained from the fit are 1.62 and 34.64 for  $\text{ZrO}_2:\text{Eu}^{3+}$  and  $\text{Nb}_2\text{O}_5:\text{Eu}^{3+}$  respectively.

In  $\text{Nb}_2\text{O}_5:\text{Eu}^{3+}$  and  $\text{ZrO}_2:\text{Eu}^{3+}$  the calculated relative sensitivities (from equation 2.1.6) are 3.17 %K<sup>-1</sup> and 3.07 %K<sup>-1</sup> at 290K, respectively. The absolute sensitivities (equation 2.1.5) are 0.0012 K<sup>-1</sup> at 453 K and 0.00012 K<sup>-1</sup> at 445 K for  $\text{Nb}_2\text{O}_5:\text{Eu}^{3+}$  and  $\text{ZrO}_2:\text{Eu}^{3+}$ , respectively.

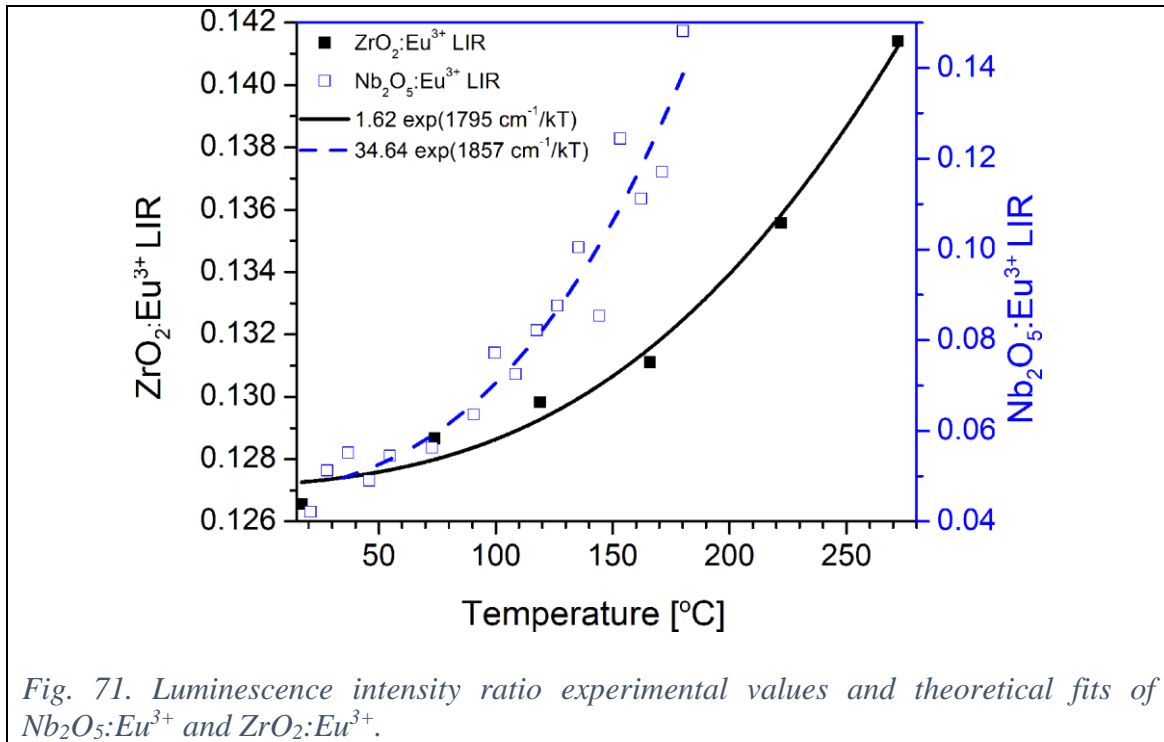


Fig. 71. Luminescence intensity ratio experimental values and theoretical fits of  $\text{Nb}_2\text{O}_5:\text{Eu}^{3+}$  and  $\text{ZrO}_2:\text{Eu}^{3+}$ .

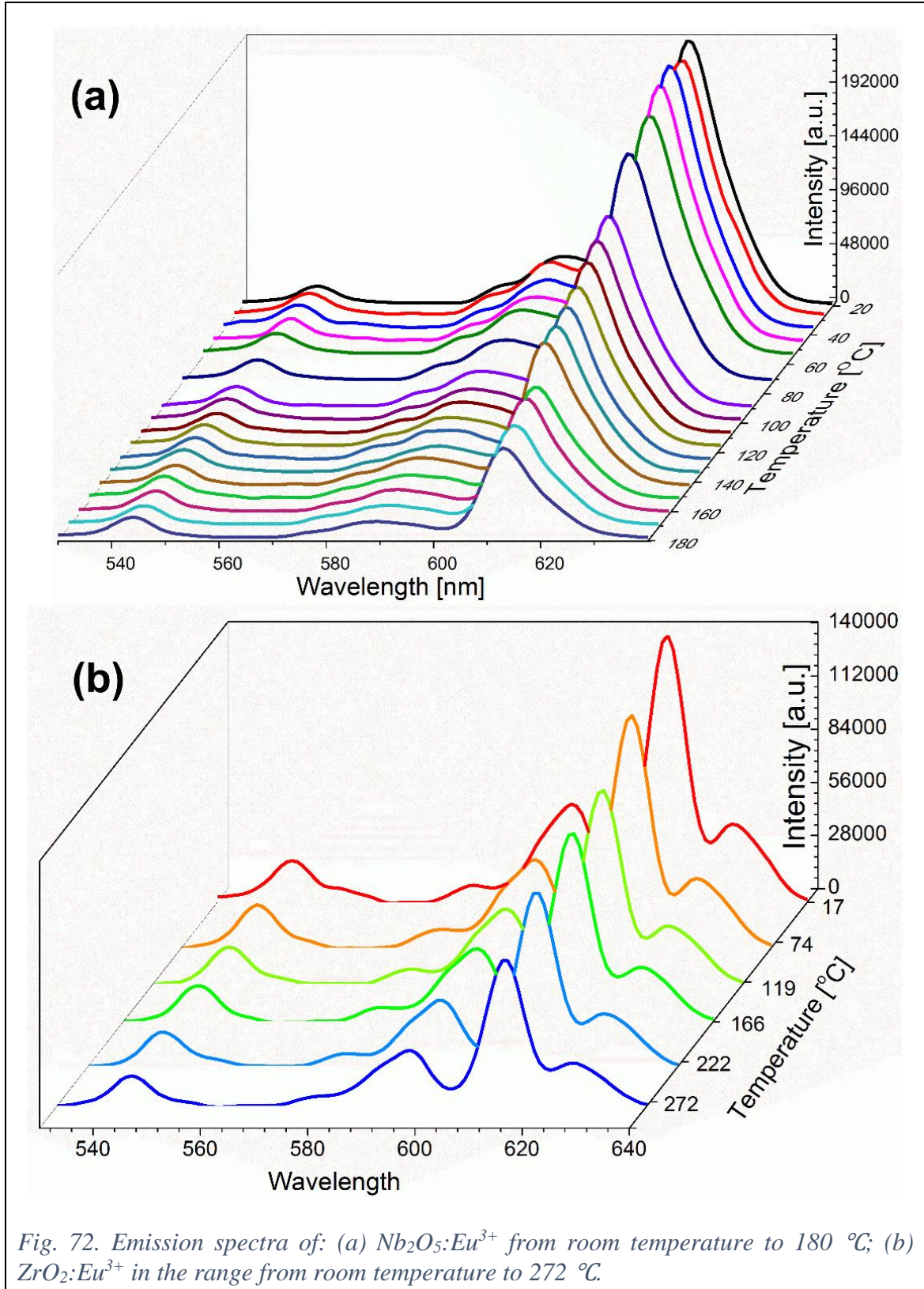


Fig. 72. Emission spectra of: (a)  $\text{Nb}_2\text{O}_5:\text{Eu}^{3+}$  from room temperature to 180 °C; (b)  $\text{ZrO}_2:\text{Eu}^{3+}$  in the range from room temperature to 272 °C.

#### 4.4.2. $\text{TiO}_2:\text{Eu}^{3+}$

PL spectra of  $\text{TiO}_2:\text{Eu}^{3+}$  was recorded over the temperature range from the room temperature to 260 °C. In our case the hypersensitive transition  ${}^5\text{D}_1 \rightarrow {}^7\text{F}_1$  is chosen as an internal reference, since the peak at ca. 543 nm has almost constant intensity on the measured temperature range. The other, also hypersensitive, transition chosen to measure LIR,  ${}^5\text{D}_0 \rightarrow {}^7\text{F}_2$ , dominates the spectrum in host matrices with low symmetries and with no inversion center (such is the case of  $\text{Eu}^{3+}$  doped titanium dioxide). In contrast to the  ${}^5\text{D}_1 \rightarrow {}^7\text{F}_1$  transition, the  ${}^5\text{D}_0 \rightarrow {}^7\text{F}_2$  transition is highly temperature dependent, and its intensity drops rapidly with the temperature increase (Fig. 73).

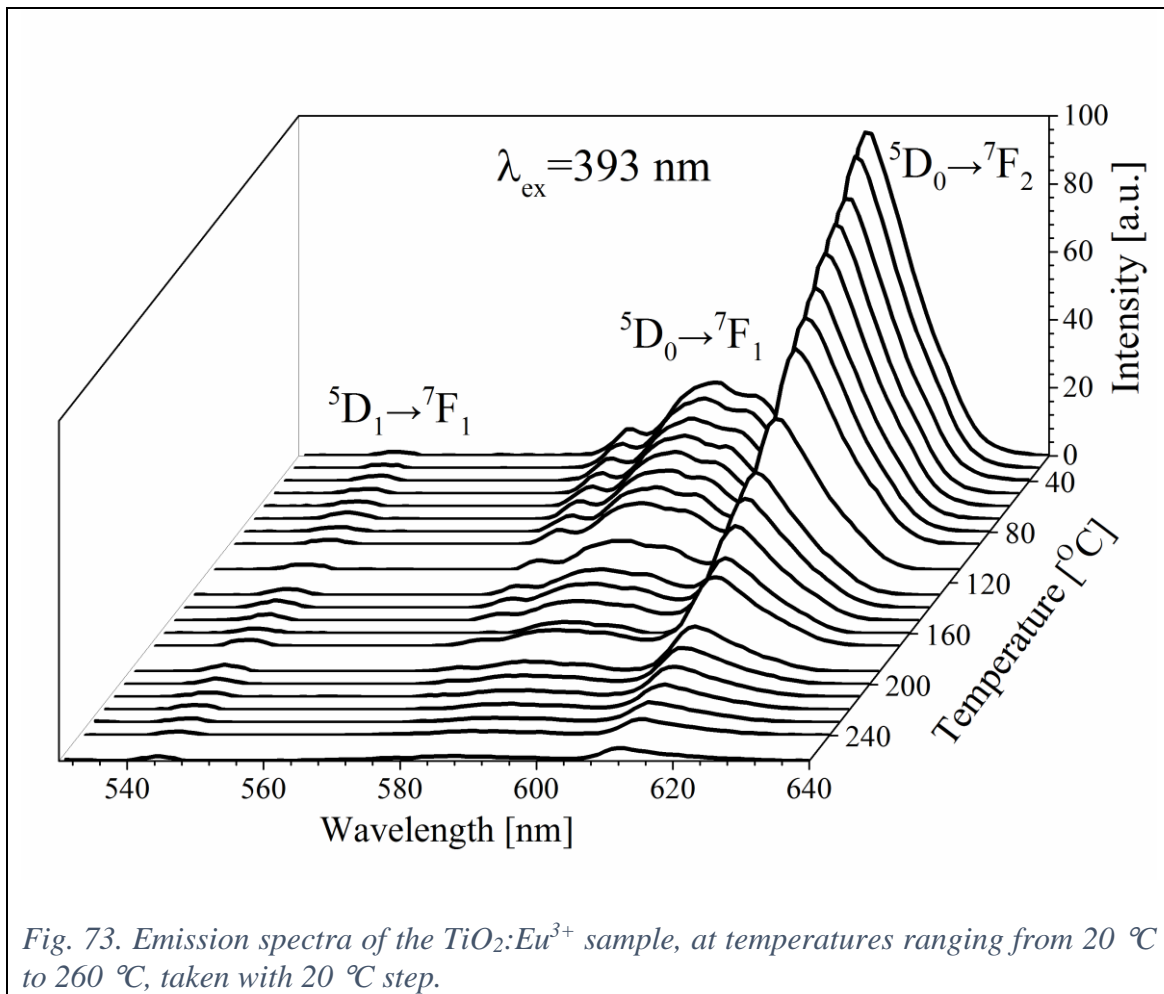
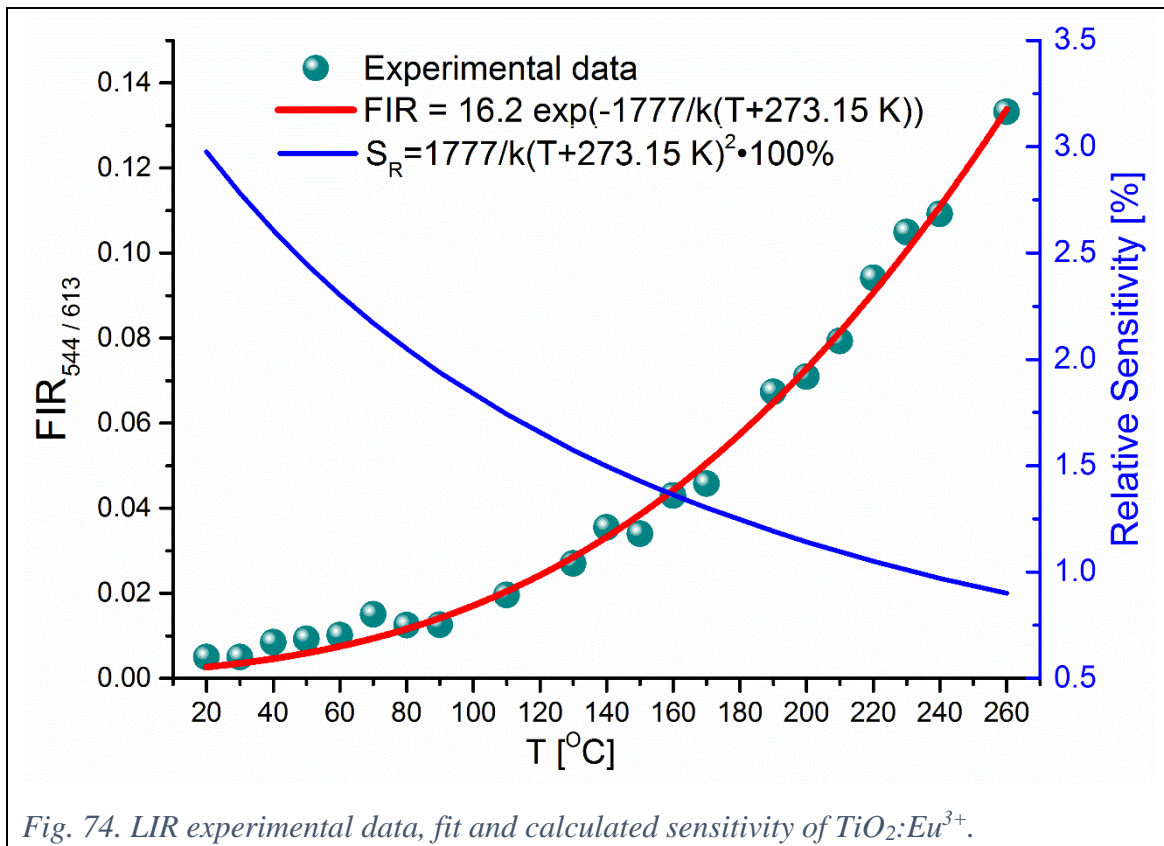


Fig. 73. Emission spectra of the  $\text{TiO}_2:\text{Eu}^{3+}$  sample, at temperatures ranging from 20 °C to 260 °C, taken with 20 °C step.

From the fit of the ratio of integrated emission intensities of  ${}^5\text{D}_1 \rightarrow {}^7\text{F}_1$  and  ${}^5\text{D}_0 \rightarrow {}^7\text{F}_2$  the values  $B = 16.2$  and  $\Delta E = 1777 \text{ cm}^{-1}$  are obtained (which is in agreement with the value given in Ref. [52]). Theoretical fit together with the relative sensitivity is

presented in Fig. 74. The value of relative sensitivity  $S_R = 3.43 \%K^{-1}$  at 293 K is higher than any sensitivity reported in Ref. [36].



## 4.5. JOES application software

### 4.5.1. Introduction

From the absorption or luminescence spectra, Judd-Ofelt theory (JO) has the ability to predict oscillator strengths, luminescence branching ratios, excited state radiative lifetimes, and estimates of quantum efficiencies, by using only three parameters. Thus, it has become a centerpiece in RE optical spectroscopy [33]. Unfortunately, the theory itself is complex, and the calculation by hand is a cumbersome process that can be easily overcome with an appropriate application software.

The usual way for calculating JO parameters of solids with doped trivalent RE ions is with the absorption spectra, and it involves a complicated algorithm, best described in Ref. [33], and supported by the RELIC application software [111].

Europium is unique among RE elements in a way that JO analysis can be done with the emission as well as with the absorption spectra. Apart from the simpler algorithm, PL methods are 3 orders of magnitude more sensitive than in absorption spectroscopy [17].

LUMPAC is a software package that can calculate JO parameters from the emission spectra, but it is limited to only two intensity parameters and it lacks the ability to calculate many JO derived quantities [162]. Recently, simple scripts using the MathCad 14<sup>®</sup> program have been presented from which one can easily obtain the  $\Omega_2$  and  $\Omega_4$  experimental intensity parameters by using the areas under the emission curves and energy barycenters of the  $^5D_0 \rightarrow ^7F_2$  and  $^7F_4$  transitions using the magnetic dipole  $^5D_0 \rightarrow ^7F_1$  one as the reference. However, MathCad 14<sup>®</sup> program is a commercial software and operates only on MS Windows. To overcome these limitations, the JOES software was created. Containing the vast database of refractive indexes, it requires only a single file to calculate Judd-Ofelt intensity parameters, branching ratios, radiative transition probabilities, barycenter energies, nonradiative transition probability, lifetimes, cross-sections, quantum efficiency and sensitization efficiency.

### 4.5.2. Refractive index

For better accuracy the refractive indexes should be obtained at the wavenumber of the peak's barycenter instead of applying the constant value for all transitions [55].

Unless a user enters the values manually, the program takes refractive indexes in two forms: Sellmeier's equations or calculated numerically, from values obtained from the refractive index database [163].

#### 4.5.3. Derived Quantities

Equations for radiative transition probability in the simplest form are:

$$A_{\lambda} = 8.034 \cdot 10^9 \cdot \tilde{\nu}_{\lambda}^3 n_{\lambda} (n_{\lambda}^2 + 2)^2 \Omega_{\lambda} U^{\lambda} \quad (4.5.1)$$

$$A_1 = 3.009 \cdot 10^{-12} \cdot \tilde{\nu}_1^3 n_1^3 \quad (4.5.2)$$

The equation for cross sections in  $\text{cm}^2$ , which is the function of the wavelength, given in nm, is:

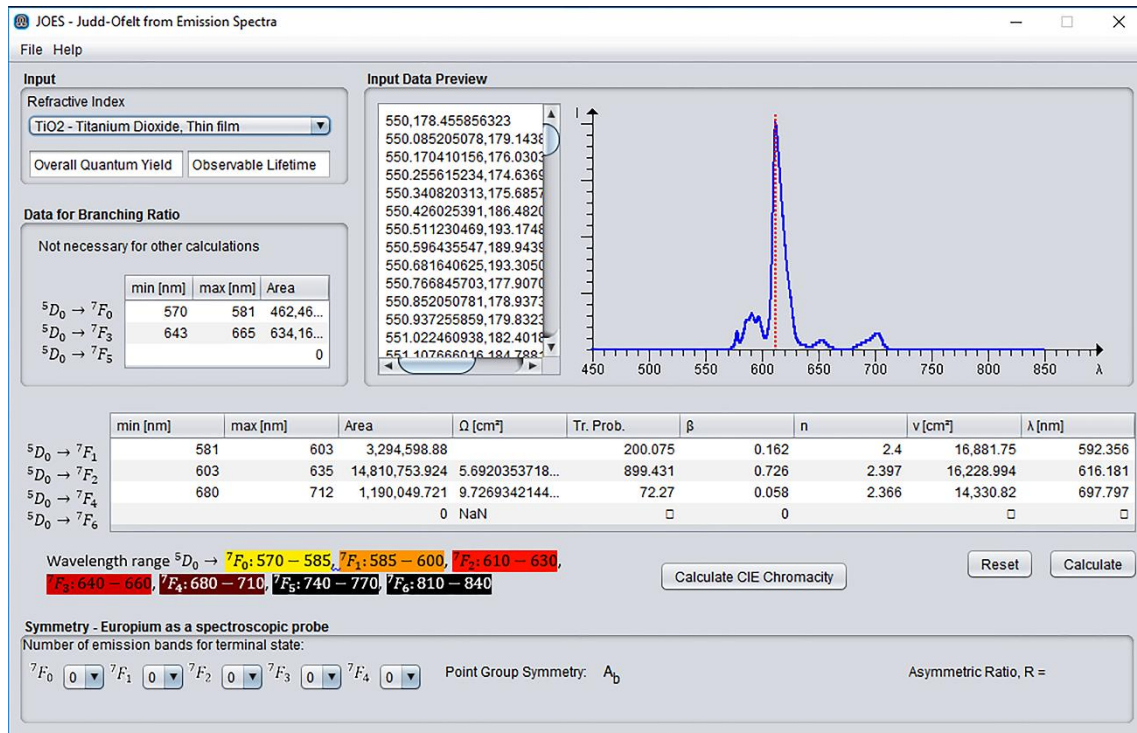
$$\sigma_{\kappa}(\lambda_p) = \frac{\lambda_p^4}{23.984 \pi \cdot n_p^2} \frac{\max I_{\kappa}}{\int I_{\kappa} d\lambda \cdot 10^{-7}} A_{\kappa} \cdot 10^{-31} \quad (4.5.3)$$

#### 4.5.4. UI

The UI of JOES is presented in Figure 75. After the input of the comma separated value (CSV) file, with points obtained from the spectrofluorometer (the CSV file can be exported from the Origin [164]), the graph and the table of intensities vs. wavelengths appear in the *Input Data Preview* panel. The user is asked to choose the material from the database with over 150 entries, or to manually input the refractive indexes in the table.

In the main table, peak bounds must be entered for all but the  ${}^5\text{D}_0 \rightarrow {}^7\text{F}_6$  transition, since it lies outside the visible spectrum and is very weak in many materials. The inputs for the *Overall Quantum Yield* and the *Observable Lifetime* are optional entries and are required only for calculations of the derived quantities. A complete set of results the program outputs to a text file. Instructions are provided in more detail in the help file within the application software.

(a)



(b)

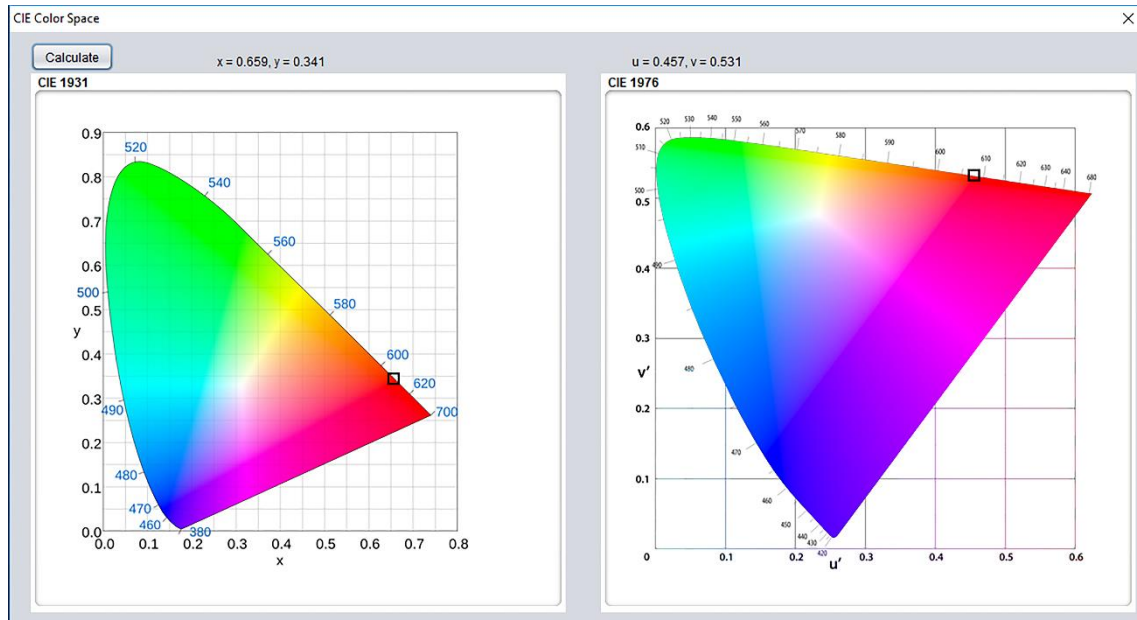


Figure 75. (a) UI of JOES, (b) UI for calculation and graphical plot of CIE 1931 and CIE 1976 chromaticity coordinates.

#### 4.5.5. JO analysis of HfO<sub>2</sub>, TiO<sub>2</sub>, ZrO<sub>2</sub> and Nb<sub>2</sub>O<sub>5</sub> doped with Eu<sup>3+</sup>

The data from JOES application software is presented in Table 12 and Table 13. The calculated data gives the information about the luminescent and structural properties of the material. JO parameters and the derived quantities obtained from the absorption spectrum are generally accepted to be accurate within 20% [118,143], from the emission spectrum within 10% [123]. By comparing the calculated with theoretical values for the branching ratio and radiative lifetime, it is evident that they match within the desired 10% for all three samples, which is an indication of the accuracy of the JOES application software.

Table 12. JOES output data for TiO<sub>2</sub>:Eu<sup>3+</sup>, ZrO<sub>2</sub>:Eu<sup>3+</sup> and Nb<sub>2</sub>O<sub>5</sub>:Eu<sup>3+</sup> at various PEO times [165].

Host	ZrO <sub>2</sub>			TiO <sub>2</sub>			Nb <sub>2</sub> O <sub>5</sub>		
PEO time [min]	10	5	3	10	5	3	10	5	3
Concentration [%]	0.44	0.33	0.17	0.34	0.20	0.15	1.42	1.11	0.62
$\Omega_2 \cdot 10^{20}$ [cm <sup>2</sup> ]	4.836	4.645	4.567	5.692	5.453	5.295	6.124	5.810	4.677
$\Omega_4 \cdot 10^{20}$ [cm <sup>2</sup> ]	1.306	1.857	4.812	0.972	1.069	0.963	1.022	1.350	2.712
$\beta_{\text{exp}} (^5\text{D}_0 \rightarrow ^7\text{F}_1)$	0.174	0.169	0.130	0.161	0.164	0.169	0.156	0.155	0.156
$\beta_{\text{exp}} (^5\text{D}_0 \rightarrow ^7\text{F}_2)$	0.606	0.565	0.426	0.726	0.706	0.709	0.734	0.696	0.560
$\beta_{\text{exp}} (^5\text{D}_0 \rightarrow ^7\text{F}_4)$	0.078	0.108	0.217	0.058	0.065	0.060	0.058	0.076	0.155
$\beta_{\text{th}} (^5\text{D}_0 \rightarrow ^7\text{F}_1)$	0.202	0.200	0.168	0.170	0.175	0.180	0.164	0.167	0.179
$\beta_{\text{th}} (^5\text{D}_0 \rightarrow ^7\text{F}_2)$	0.705	0.670	0.550	0.767	0.754	0.754	0.774	0.749	0.642
$\beta_{\text{th}} (^5\text{D}_0 \rightarrow ^7\text{F}_4)$	0.091	0.128	0.280	0.061	0.069	0.064	0.061	0.082	0.177
A ( <sup>5</sup> D <sub>0</sub> → <sup>7</sup> F <sub>1</sub> ) [s <sup>-1</sup> ]	143.5	143.4	143.5	200.0	200.4	200.3	183.2	183.3	183.6
	8	8	9	7	6	9	8	5	8
A ( <sup>5</sup> D <sub>0</sub> → <sup>7</sup> F <sub>2</sub> ) [s <sup>-1</sup> ]	499.2	479.0	469.5	899.4	861.8	837.2	863.2	819.2	658.3
	1	6	8	3	3	7	3	3	6
A ( <sup>5</sup> D <sub>0</sub> → <sup>7</sup> F <sub>4</sub> ) [s <sup>-1</sup> ]	64.54	91.96	239.3	72.26	79.63	71.63	68.07	90.22	182.2
			0						7
v ( <sup>5</sup> D <sub>0</sub> → <sup>7</sup> F <sub>1</sub> ) [cm <sup>-1</sup> ]	16811	16807	16811	16881	16892	16890	16883	16886	16896
v ( <sup>5</sup> D <sub>0</sub> → <sup>7</sup> F <sub>2</sub> ) [cm <sup>-1</sup> ]	16172	16167	16151	16228	16229	16231	16232	16234	16226
v ( <sup>5</sup> D <sub>0</sub> → <sup>7</sup> F <sub>4</sub> ) [cm <sup>-1</sup> ]	14211	14219	14239	14330	14339	14333	14323	14336	14363
$\tau_{\text{th}}$ [ms]	1.186	1.151	0.885	0.797	0.812	0.838	0.841	0.841	0.844
$\tau_{\text{calc}}$ [ms]	1.413	1.399	1.173	0.853	0.875	0.901	0.971	0.915	0.976
$\tau_{\text{obs}}$ [ms]	0.883	0.869	0.812	0.578	0.587	0.588	0.506	0.506	0.551
$\sigma (^5\text{D}_0 \rightarrow ^7\text{F}_1) \cdot 10^{22}$ [cm <sup>2</sup> ]	5.336	5.623	5.485	3.587	3.456	3.516	3.422	0.449	0.757
$\sigma (^5\text{D}_0 \rightarrow ^7\text{F}_2) \cdot 10^{22}$ [cm <sup>2</sup> ]	15.11	14.69	13.55	23.73	22.56	22.50	25.24	3.182	4.487
	8	3	4	1	5	4	1		
$\sigma (^5\text{D}_0 \rightarrow ^7\text{F}_4) \cdot 10^{22}$ [cm <sup>2</sup> ]	3.034	3.830	6.702	2.628	2.639	2.562	2.634	0.502	1.019
$\eta$	0.744	0.754	0.917	0.724	0.722	0.700	0.601	0.602	0.653
Asymmetric ratio	3.756	3.607	3.541	4.859	4.665	4.552	3.756	3.607	3.541

Table 13. Judd-Ofelt parameters and derived quantities for monoclinic hafnia doped with various  $\text{Eu}^{3+}$  concentrations.

Concentration [at%]	0.29	0.48	0.62
$\Omega_2 \cdot 10^{20} [\text{cm}^2]$	3.76	3.89	4.03
$\Omega_4 \cdot 10^{20} [\text{cm}^2]$	2.10	2.06	2.26
$\beta (^5\text{D}_0 \rightarrow ^7\text{F}_1)$	0.23	0.23	0.22
$\beta (^5\text{D}_0 \rightarrow ^7\text{F}_2)$	0.61	0.62	0.62
$\beta (^5\text{D}_0 \rightarrow ^7\text{F}_4)$	0.16	0.15	0.16
$A (^5\text{D}_0 \rightarrow ^7\text{F}_1) [\text{s}^{-1}]$	135.8	135.9	135.3
$A (^5\text{D}_0 \rightarrow ^7\text{F}_2) [\text{s}^{-1}]$	359.8	372.9	384.3
$A (^5\text{D}_0 \rightarrow ^7\text{F}_4) [\text{s}^{-1}]$	94.6	92.7	101.3
$\nu (^5\text{D}_0 \rightarrow ^7\text{F}_1) [\text{cm}^{-1}]$	16867	16872	16849
$\nu (^5\text{D}_0 \rightarrow ^7\text{F}_2) [\text{cm}^{-1}]$	16203	16215	16194
$\nu (^5\text{D}_0 \rightarrow ^7\text{F}_4) [\text{cm}^{-1}]$	14143	14147	14126
$\tau_{\text{exp}} [\text{ms}]$	1.67	1.64	1.58
$\tau_{\text{th}} [\text{ms}]$	1.69	1.66	1.61
$\sigma (^5\text{D}_0 \rightarrow ^7\text{F}_1) \cdot 10^{22} [\text{cm}^2]$	5.14	4.86	5.13
$\sigma (^5\text{D}_0 \rightarrow ^7\text{F}_2) \cdot 10^{22} [\text{cm}^2]$	13.07	12.97	13.49
$\sigma (^5\text{D}_0 \rightarrow ^7\text{F}_4) \cdot 10^{22} [\text{cm}^2]$	7.80	7.58	8.59

#### 4.5.6. Additional Features

Additionally, JOES application software can determine chromaticity from spectrum or exploit the  $\text{Eu}^{3+}$  ability to be used as a spectroscopic probe to determine the site symmetry.

##### 4.5.6.1. Spectroscopic probe

By counting the number of crystal-field components that can be observed for the transitions  $^5\text{D}_0 \rightarrow ^7\text{F}_J$ , the point group symmetry of the  $\text{Eu}^{3+}$  site can be determined, as described by K. Binnemans and C. Gorller-Walrand in Ref. [166] and in section 2.4.4. The user needs to enter the number of observed peaks for the given terminal state and the program output will provide the possible point group symmetry.

The problem with the site symmetry identification often arises due to the overlapping of the peaks. Often the weaker overlapping peak appears as a shoulder to the more intense peak. The other complication arises because of the overlapping with the transitions from higher excited states. This problem can be resolved by time-gated spectroscopy or by measuring at lower temperatures. Multiple symmetries in the program output mean that the information on the polarization of the transitions is required to assign a particular symmetry group, which is beyond this project's scope.

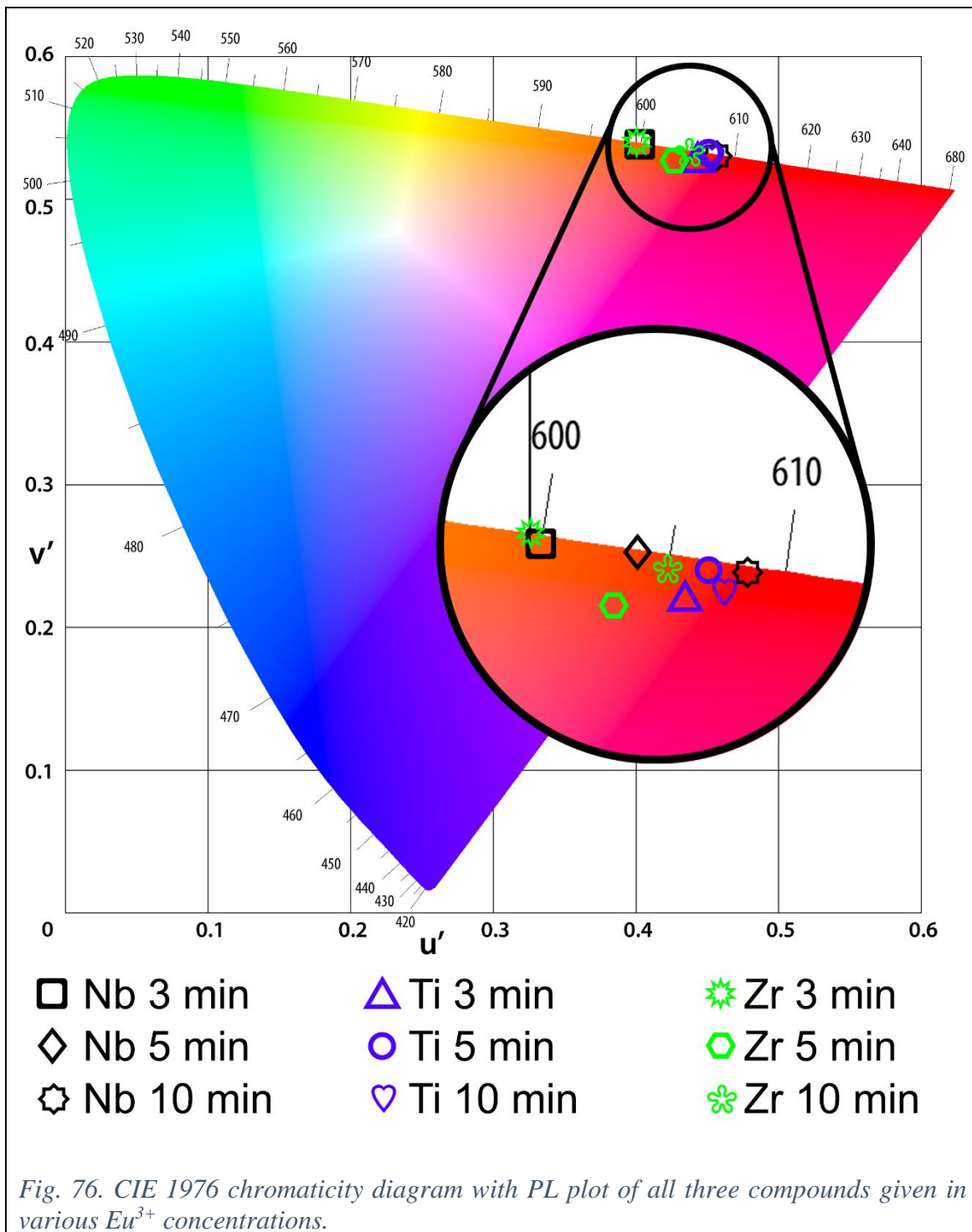
The asymmetric ratio gives a measure of the degree of distortion from the inversion symmetry of the local environment of the  $\text{Eu}^{3+}$  ion in a matrix [96]. It is equal to the ratio of integrated intensities of the hypersensitive and magnetic dipole transitions [142]. As the  $\text{Eu}^{3+}$  concentration increases, more lattices become deviated and lose symmetry. In all three hosts investigated in this paper, the asymmetric ratios calculated by JOES increase with increasing  $\text{Eu}^{3+}$  concentrations, as predicted by the theory (see Table 12).

#### 4.5.6.2. Chromaticity

After the spectrum data has been loaded into the JOES application software, the calculation of the Commission International De I-Eclairage (CIE 1931 and CIE 1976) coordinates are evaluated and plotted (Fig. 76). The color matching curves are approximated as given in Ref. [167] and calculated as explained in Ref. [168,169].

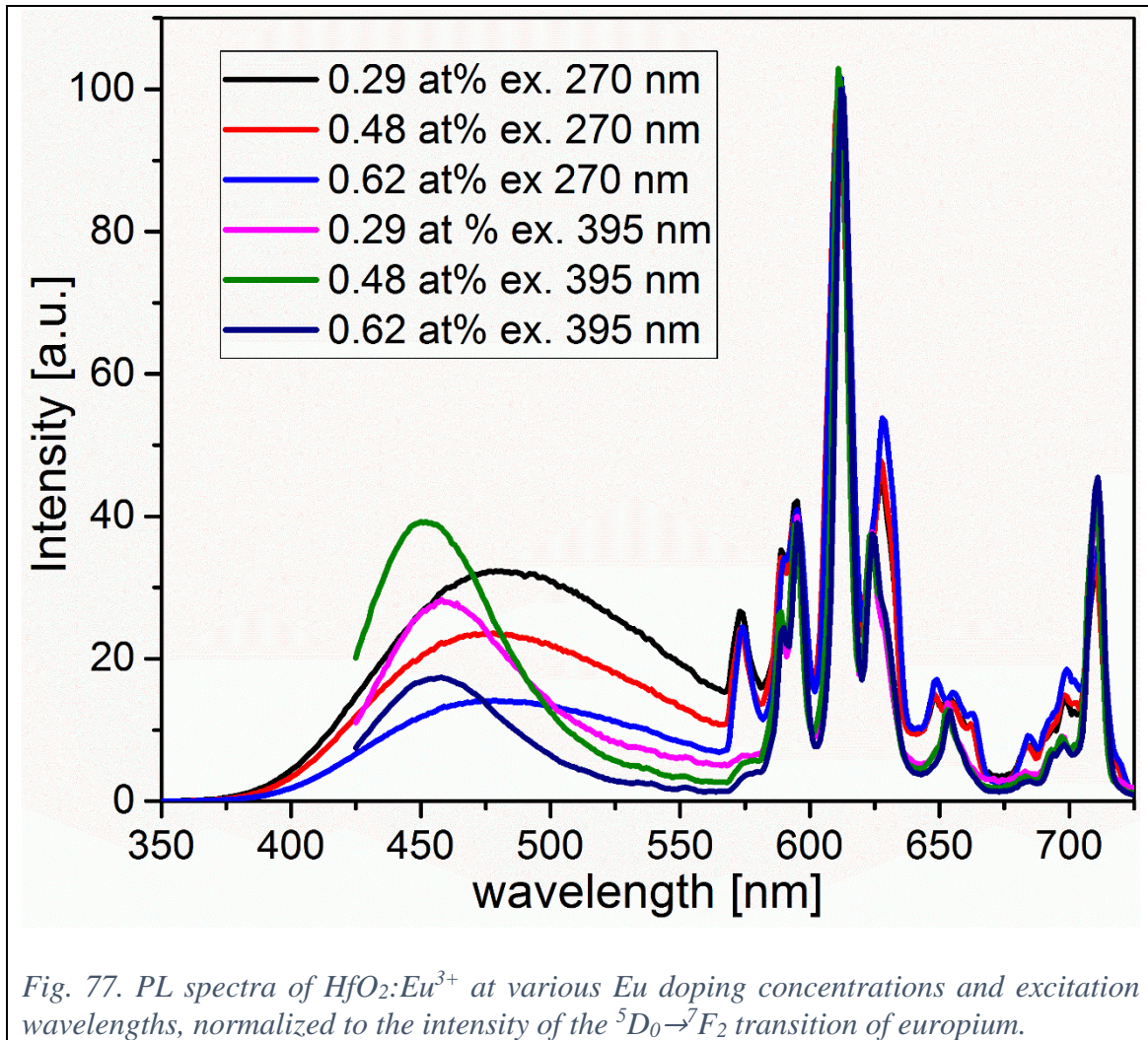
From the spectra of the  $\text{Eu}^{3+}$  doped  $\text{TiO}_2$ ,  $\text{ZrO}_2$  and  $\text{Nb}_2\text{O}_5$ , it is evident the existence of the chromatic shift towards higher wavelengths proportional to the europium concentration. The similar results are reported in Ref. [170]. These results indicate that all three materials can be used as a red phosphor for LED or display applications.

Since the desired PL color of the sample can be tuned for specific purposes, the CIE 1976 coordinates are calculated for  $\text{HfO}_2:\text{Eu}^{3+}$  as well. The chromaticity of PL of  $\text{HfO}_2:\text{Eu}^{3+}$  doped with 0.29, 0.48 and 0.62 at% europium concentrations, excited by 270 nm into the charge transfer band (CTB), and 395 nm  ${}^7\text{F}_0 \rightarrow {}^5\text{L}_6$  4f-4f transition were investigated. For spectral color comparison, the spectra with different excitation wavelengths and different  $\text{Eu}^{3+}$  concentrations have been normalized to the intensity of the  ${}^5\text{D}_0 \rightarrow {}^7\text{F}_2$  transition, and are presented in Fig. 77.



CIE 1976 coordinates were calculated by the JOES application software and are presented in Fig. 78.  $\text{HfO}_2:\text{Eu}^{3+}$  shows an expected shift to higher wavelengths with increasing doping concentration, due to the higher emission intensity that originates from the europium species comparing to PL of the host matrix. The material shows quite different PL properties when excited by 270 nm and 395 nm beams. The relatively low

host luminescence in 0.48 at% spectra excited by 395 nm is not expected, and is the reason behind the low v' CIE coordinate.



PL of pure  $\text{HfO}_2$  gives exactly the same color as from the RGB LED spectrum (obtained from Ref. [171]). The UV excitation of  $\text{HfO}_2:\text{Eu}^{3+}$  with lower europium concentrations shows a promising white LED applications of the material, as the color is almost purely white. Its chromaticity values are very close to the commercial YAG yellow phosphor excited by InGaN blue phosphor (spectrum obtained from Ref. [172]). The low temperature stability of the InGaN:YAG and very high temperature stability of the investigated material make the later even more appealing. However, the relatively high price of both hafnium and europium might limit their practical applications.

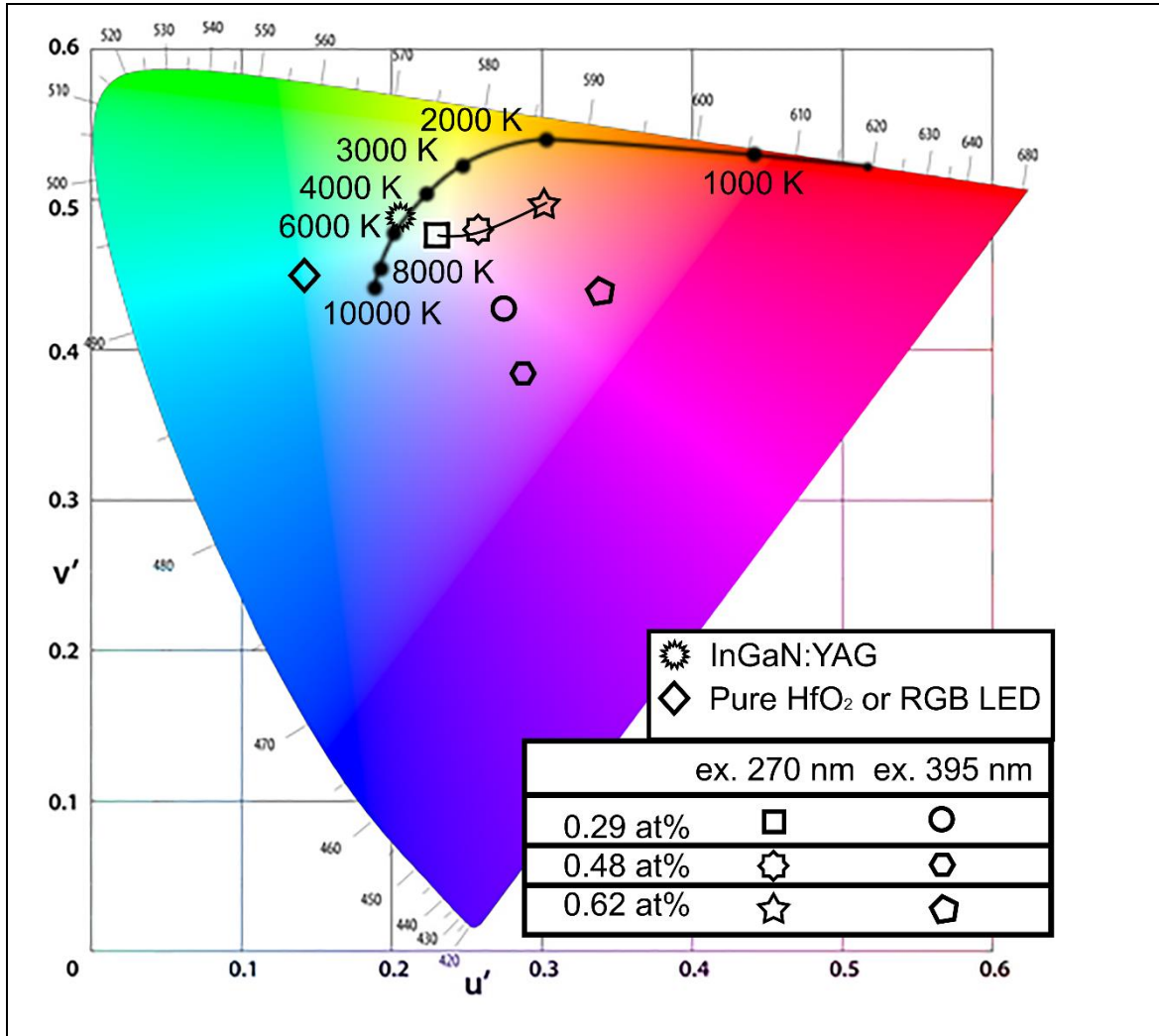


Fig. 78. CIE 1976 chromaticity diagram of 0.29, 0.48 and 0.69 at% HfO<sub>2</sub>:Eu<sup>3+</sup>, excited by 270 nm and 395 nm beams.

## 4.6. LIR and thermometry

### 4.6.1. Radiative transition probability and ED strength of ${}^5D_1$ emissions

With the data from the LIR analysis and the JO, more information about the hypersensitive  ${}^5D_1 \rightarrow {}^7F_1$  transition can be obtained. The transitions  ${}^5D_1 \rightarrow {}^7F_1$  and  ${}^5D_0 \rightarrow {}^7F_2$  will be abbreviated as  $H$  and  $L$ , respectively.

The temperature independent constant  $B = A_H \nu_H g_H / A_L \nu_L g_L$ , by using the equation 2.3.87 can now be expressed as:

$$B = \frac{n_H (n_H^2 + 2)^2 \nu_H^4}{n_L (n_L^2 + 2)^2 \nu_L^4} \frac{D_H}{e^2 \Omega_L U^L} \quad (4.6.1)$$

from where the dipole strength of the  ${}^5D_1 \rightarrow {}^7F_1$  transition, depending on the JO parameters and the temperature constant, can be evaluated. By substituting the values obtained for the  $\text{TiO}_2:\text{Eu}^{3+}$ , the dipole strength of the  ${}^5D_1 \rightarrow {}^7F_1$  transition equals to:  $D_H = 1.084 \cdot 10^{-42} \text{ esu}^2 \text{ cm}^2$ .

With the knowledge of the rate of spontaneous emission of the  ${}^5D_0 \rightarrow {}^7F_2$  emission, the rate of spontaneous emission of  ${}^5D_1 \rightarrow {}^7F_1$  can be directly calculated by the equation [173]:

$$A_H = \frac{B A_L \nu_L g_L}{\nu_H g_H} = 3171 \text{ s}^{-1} \quad (4.6.2)$$

The result indicates very high radiative transition probability, i.e. a fast decay rate, which is in accordance with an assumption that the higher excited states are less stable. The intensity of the  ${}^5D_1 \rightarrow {}^7F_1$  transition is given by:  $I_H = N_H g_H A_H h \nu_H$ , where  $N_H$  is the population of the  ${}^5D_1 \rightarrow {}^7F_1$  level. The ratio of populations:  $N_H / N_L = g_H / g_L \exp(-\Delta E / kT)$  at room temperature is equal to ca.  $6 \cdot 10^{-4}$ , which explains the low intensity of the  ${}^5D_1 \rightarrow {}^7F_1$  transition in the room temperature spectrum of  $\text{TiO}_2:\text{Eu}^{3+}$ .

### 4.6.2. LIR thermometric JO model

In order to proceed with introducing the theoretical model, RME of  ${}^5D_{2,1,0} \rightarrow {}^7F_{0-6}$  transitions of  $\text{Eu}^{3+}$  must be obtained. The average experimental values of Slater integrals and s-o coupling parameter for  $\text{Eu}^{3+}$  in various hosts, taken from Ref. [112,115,117] are:

$F_2 = 381 \text{ cm}^{-1}$ ,  $F_4 = 56 \text{ cm}^{-1}$ ,  $F_6 = 6 \text{ cm}^{-1}$ ,  $\zeta = 1331 \text{ cm}^{-1}$ . These values closely match those by Carnall et al. [103] and are in agreement with approximate relations for finding the Slater parameters:  $F_2 = 12.4(Z-34)$  [35],  $F_4 = 0.148(4)F_2$ ,  $F_6 = 0.016(1)F_2$ , and  $\zeta = 3.5F_2$  [107]. For the average Slater integrals and s-o coupling parameter, by using RELIC application software, RME of transitions that originate at  $^5D_{0,1,2}$  and end at the ground multiplet have been calculated and presented in Table 14.

*Table 14. Barycenter wavelengths, type of transition and calculated RME. Wavelengths for transitions outside of recorded scope 500 nm – 720 nm are taken from Ref. [118].*

Transition	$\lambda$ [nm]	Type	$U^2$	$U^4$	$U^6$
$^5D_0 \rightarrow ^7F_0$	583		0	0	0
$^5D_0 \rightarrow ^7F_1$	590	MD	0	0	0
$^5D_0 \rightarrow ^7F_2$	614	ED	0.0032	0	0
$^5D_0 \rightarrow ^7F_3$	654		0	0	0
$^5D_0 \rightarrow ^7F_4$	693	ED	0	0.0023	0
$^5D_0 \rightarrow ^7F_5$	744		0	0	0
$^5D_0 \rightarrow ^7F_6$	807	ED	0	0	0.0002
$^5D_1 \rightarrow ^7F_0$	527	MD	0	0	0
$^5D_1 \rightarrow ^7F_1$	537	ED	0.0026	0	0
$^5D_1 \rightarrow ^7F_2$	555	MD+ED	0.0008	0	0
$^5D_1 \rightarrow ^7F_3$	566	ED	0.0038	0.0019	0
$^5D_1 \rightarrow ^7F_4$	617	ED	0	0.0027	0
$^5D_1 \rightarrow ^7F_5$	659	ED	0	0.0007	0
$^5D_1 \rightarrow ^7F_6$	708	ED	0	0	0.0003
$^5D_2 \rightarrow ^7F_0$	466	ED	0.0009	0	0
$^5D_2 \rightarrow ^7F_1$	474	MD+ED	0.0002	0	0
$^5D_2 \rightarrow ^7F_2$	489	ED	0.0018	0.0015	0
$^5D_2 \rightarrow ^7F_3$	512	MD+ED	0.0024	0.0026	0
$^5D_2 \rightarrow ^7F_4$	536	ED	0.0020	0.0004	0
$^5D_2 \rightarrow ^7F_5$	567	ED	0	0.0016	0
$^5D_2 \rightarrow ^7F_6$	603	ED	0	0	0.0001

Slightly different values have been reported in glass hosts [118]. The values of the transitions calculated by Carnall et al. on  $\text{LaF}_3:\text{Eu}^{3+}$  [103] match to our RME. RME can also help in identifying the transition type, i.e. if the transition has RME different than zero, then it has an ED component. If the transition is MD allowed by the selection rules and has RME greater than zero, then it is the case of a mixed ED + MD transition.

Theoretical model that connects JO and LIR is an expression of LIR and thermometric figures of merit by JO parameters. This theoretical model not only extends the JO theory but also simplifies measurements and reduces its cost by requiring just a spectrofluorometer for the analysis. Thermometry measurements and data processing is an exhaustive and long process with requirement of expensive apparatus. In contrast to this model, thermometric measurements would require spectra at many temperature points, and special apparatus for heating/cooling samples. This theoretical model not only extends the JO theory but also simplifies measurements and reduces its cost by requiring just a spectrofluorometer for the analysis. In all lanthanides it can predict the best transitions for LIR thermometry on the given temperature range. Even more, the LIR thermometric figures of merit can be predicted for a given material from the JO parameters given in the literature, thus allowing the direct and fast evaluation of the best thermometric material and the best choice of its transitions for LIR.

An approximate application of this method for a single pair of transitions of upconversion phosphor  $\text{Yb}^{3+}/\text{Er}^{3+}$  has been presented in Ref. [19]. Ref. [173] gave the B parameter value from the two specific transitions. Here is presented an accurate, general solution, that can be applied to all RE ions and for all transitions allowed in the JO theory.

Emissions from energetically higher level will be labeled as high (H), and analogously from lower level (L). The selected emissions must have high enough intensity and must not significantly overlap with other transitions in the spectra.

The B parameter in equation 2.1.12 can be expressed through JO parameters, by using the equations 2.3.86,  $I = Nh\nu A$  and the Boltzmann distribution:

$$B = \left( \frac{\tilde{\nu}_H}{\tilde{\nu}_L} \right)^4 \frac{\chi_{ED}^H D_{ED}^H + \chi_{MD}^H D_{MD}^H}{\chi_{ED}^L D_{ED}^L + \chi_{MD}^L D_{MD}^L} \quad (4.6.3)$$

The relative sensitivity depends only on the separation of coupled energy levels, but B directly affects the absolute sensitivity (see equation 2.1.13):

$$S(T) = \frac{\Delta E}{kT^2} B \exp\left(-\frac{\Delta E}{kT}\right) \quad (4.6.4)$$

Now that B parameter can be obtained by JO parameters, the absolute sensitivity can be calculated from the JO parameters as well, by replacing B with equation 4.6.3.

The temperature at which the absolute sensitivity has maximum is given by:

$$T(\max S) = \frac{\Delta E}{2k} \quad (4.6.5)$$

By returning the value into the equation 4.6.4, the maximum sensitivity can also be derived from JO parameters and equation:

$$S_{\max} = \frac{4Bk}{e^2 \Delta E} \quad (4.6.6)$$

The temperature resolution (equation 2.1.7) is then given by:

$$\Delta T = \frac{kT^2 \cdot \sigma}{\Delta EB \exp(-\Delta E/kT)} \quad (4.6.7)$$

The standard deviation is often large for transitions that have large absolute sensitivities, thus counteracting the absolute sensitivities in the choice for the best transition for thermometric measurements.

Experimental B values, i.e. obtained by fitting the LIR data to equation 8, can differ from the theoretically calculated values. This can be due to the unresolved spectrum, or the researcher's choice to approximate the ratio of integrated intensities with the ratio of peak heights. The second source of error is the JO theory, which introduces an error of 20% if JO parameters are obtained from the absorption spectrum [118,143], or 10% if obtained experimentally from the emission spectrum [123]. However, by comparing the experimental values with theoretical values, the trend of experimental and theoretical B values must match.

This method is of even greater value for lanthanides other than europium. In the case of  $\text{Eu}^{3+}$ , where only two energy levels are thermally coupled, this method only reveals the transition with greatest sensitivity, but every transition's sensitivity has the maximum on the same temperature. As the result, a single transition can be chosen as the best transition for the material. If m number of levels are thermally coupled, sensitivity maximums would be on different T values, i.e. on m-1 places on the temperature scale. This would lead to the model predicting the best transition for a given temperature range. E.g.  $\text{Ho}^{3+}$  has three pairs of thermally coupled levels:  ${}^6\text{G}_6$ - ${}^5\text{F}_1$ ,  ${}^5\text{F}_{2,3}$ - ${}^3\text{K}_8$ ,  ${}^5\text{F}_4$ - ${}^5\text{S}_2$  [36], thus there are three different values of  $T_{\max}$ . Each of the

sensitivities can have maximum value on some temperature range, and thus the preferable transition to measure. LIR thermometric JO model can predict this behavior in any material doped with any lanthanide ion, from spectrum recorded solely at room temperature. Even more, the energy separation of  $^5D_1$  and  $^5D_0$  levels is the largest among the lanthanides, thus with the value of ca.  $1750\text{ cm}^{-1}$ , the thermalization is not complete. Thus, the prediction of thermometric figures of merit is more precise for other lanthanides, inversely proportional to the energy separation of thermalized levels.

## 5. Conclusion

PEO processing of hafnium in electrolyte containing  $\text{Eu}_2\text{O}_3$  powder is a suitable technique for the formation of  $\text{Eu}^{3+}$  doped  $\text{HfO}_2$  coatings. The main elemental components of formed coatings are Hf, O, and Eu which are uniformly dispersed all over the coatings' surface. The content of Eu detected in coatings increases with PEO time. The coatings are crystallized and mostly composed of monoclinic  $\text{HfO}_2$ . PL spectra of formed coatings feature well pronounced bands intrinsic to  $\text{HfO}_2$  and  $\text{Eu}^{3+}$  ions. Increase of PL with PEO time is related to an increase of oxygen vacancy defects and the content of  $\text{Eu}^{3+}$  in the coatings. PL emission band of  $\text{HfO}_2$  with a maximum at around 480 nm is related to oxygen vacancy defects. PL emission spectra of  $\text{Eu}^{3+}$  features sharp bands in the orange-red part of the spectrum which are related to f-f transitions of  $\text{Eu}^{3+}$  from excited level  $^5\text{D}_0$  to lower levels  $^7\text{F}_J$  ( $J = 0, 1, 2, 3, \text{ and } 4$ ). The emission of  $\text{Eu}^{3+}$  ions corresponding to  $^5\text{D}_0 \rightarrow ^7\text{F}_2$  transition is split into multiple peaks, suggesting that the environment around the  $\text{Eu}^{3+}$  ions in monoclinic  $\text{HfO}_2$  has lower local symmetry. PL excitation spectra, monitored at wavelength of the most intense peak in the emission PL spectra (613 nm), are characterized by a broad band extending from 250 nm to 350 nm, associated with the electron transfer transition from 2p orbital of  $\text{O}^{2-}$  ions to 4f orbital of  $\text{Eu}^{3+}$  ions, and the bands in the range from 350 nm to 550 nm which correspond to direct excitation of the  $\text{Eu}^{3+}$  ground state  $^7\text{F}_0$  into higher levels of the 4f-manifold. Electrical dipole transition  $^5\text{D}_0 \rightarrow ^7\text{F}_2$  is much more intense than the magnetic dipole transition  $^5\text{D}_0 \rightarrow ^7\text{F}_1$ , suggesting that  $\text{Eu}^{3+}$  ions are positioned in highly asymmetric environment.

JOES is the complete package for calculation of Judd-Ofelt parameters and derived quantities from the emission spectra of europium doped compounds. To our knowledge, it is the only application software that facilitates the complete study of this type, and is available free of charge at the web site: <https://sites.google.com/view/juddofelt/>, as well as its source files. Until now, there has been no Judd-Ofelt analysis on the materials prepared by the PEO process. The results obtained for the three investigated samples,  $\text{TiO}_2:\text{Eu}^{3+}$ ,  $\text{ZrO}_2:\text{Eu}^{3+}$  and  $\text{Nb}_2\text{O}_5:\text{Eu}^{3+}$  stand as the guarantee of the accuracy of the calculated results. This computational tool brings the power of the Judd-Ofelt theory without the necessary theoretical knowledge, and is offered to the other experimental research teams interested in luminescent systems.

Judd-Ofelt analysis of  $\text{TiO}_2:\text{Eu}^{3+}$ ,  $\text{ZrO}_2:\text{Eu}^{3+}$ ,  $\text{Nb}_2\text{O}_5:\text{Eu}^{3+}$  and  $\text{HfO}_2:\text{Eu}^{3+}$ , at various concentrations, has provided the values of the radiative transition probabilities, radiative lifetime, branching ratios and emission cross section of transitions originating from  $^5\text{D}_0$  level. The high  $\Omega_2$  parameter in all the samples is in accordance with the low site symmetry of  $\text{Eu}^{3+}$ . Large branching ratios and emission cross-sections are indications of the materials potential for lasing purposes of  $^5\text{D}_0 \rightarrow ^7\text{F}_2$  emission.

The calculated CIE chromaticity coordinates of  $\text{TiO}_2:\text{Eu}^{3+}$ ,  $\text{ZrO}_2:\text{Eu}^{3+}$ ,  $\text{Nb}_2\text{O}_5:\text{Eu}^{3+}$  and  $\text{HfO}_2:\text{Eu}^{3+}$  have been calculated. While  $\text{TiO}_2:\text{Eu}^{3+}$ ,  $\text{ZrO}_2:\text{Eu}^{3+}$  and  $\text{Nb}_2\text{O}_5:\text{Eu}^{3+}$  emit in the orange-red region, plot on the CIE diagram shows that hafnia doped with low concentration of europium species gives pure white emission when irradiated by UV light. Superior temperature and chemical stability of hafnia compared to the widely used white LED phosphors make it a favorable material for specific applications. High material price is the only limiting factor for its higher usage. The color can be fine-tuned to exactly match the ca. 6000 K black body radiation, by even further lowering the europium concentration, but to the expense of the phosphor's quantum efficiency. Unexpectedly lower  $v'$  chromaticity CIELUV coordinate was observed in the sample with 0.48 at% of  $\text{Eu}^{3+}$ , which is an indication of the existence of some other concentration dependent mechanism that quenches the hafnia substrate luminescence.

Testing of the custom-built apparatus showed the adequacy for using it for luminescence thermometry. The design presented here resulted in the material cost at a fraction of the cost of the commercial equipment, thus the blueprints and software are enabling the thermometry research to a wider group of laboratories. In addition, the provided software code is open-source and can be further modified to fully automate the process, which is a feature of the top-of-the-line commercial equipment.

The luminescence thermometry of the industry important materials, prepared by the PEO process, showed a good thermometric properties and marked  $\text{TiO}_2:\text{Eu}^{3+}$ ,  $\text{Nb}_2\text{O}_5:\text{Eu}^{3+}$  and  $\text{ZrO}_2:\text{Eu}^{3+}$  as potential temperature sensor materials. Thus, the new functionality to the already good protective coatings is added, with wide range of applications e.g. in aerospace industry or for temperature readouts on rotors.

By connecting the LIR and JO, a novel method for calculation of the radiative transition probability, radiative lifetime and dipole strength of the transitions originating from the  $^5D_1$  level has been introduced. This extension of the JO theory has been applied on the investigated sample, but can be applied to any  $\text{Eu}^{3+}$  doped material.

An extension of the Judd-Ofelt theory has been presented, a theoretical model which connects the Judd-Ofelt theory and the luminescence intensity ratio in a manner that the luminescence intensity ratio and thermometric figures of merit can be predicted from the Judd-Ofelt intensity parameters, revealing the best pair of 4f-4f transitions for thermometric measurements on the given temperature range. Thus, the values obtained by the conventional thermometric measurements, which require a complex, expensive equipment, lengthy measurements and data processing, can be predicted from a single spectrum taken at room temperature, easing the choice of a host material and a doped rare-earth element. In all lanthanides it can predict the best transition for the given temperature range.

## 6. References

- [1] B. Fultz, J.M. Howe, *Transmission electron microscopy and diffractometry of materials*, 2008. doi:10.1007/978-3-540-73886-2.
- [2] International Centre for Diffraction Data, (n.d.). <http://www.icdd.com> (accessed February 10, 2018).
- [3] N. Tadić, *Strukturna i optička karakterizacija fotokatalizatora na bazi TiO<sub>2</sub> i ZnO prahova dobijenih plazmenom elektrolitičkom oksidacijom*, University of Belgrade, 2014.
- [4] S. Stojadinović, R. Vasilić, Formation and photoluminescence of Eu<sup>3+</sup> doped zirconia coatings formed by plasma electrolytic oxidation, *J. Lumin.* 176 (2016) 25–31. doi:10.1016/j.jlumin.2016.03.012.
- [5] S. Stojadinovic, Plasma electrolytic oxidation of metals, *J. Serbian Chem. Soc.* 78 (2013) 713–716. doi:10.2298/JSC121126129S.
- [6] S. Stojadinović, N. Radić, B. Grbić, S. Maletić, P. Stefanov, A. Pačevski, R. Vasilić, Structural, photoluminescent and photocatalytic properties of TiO<sub>2</sub>:Eu<sup>3+</sup> coatings formed by plasma electrolytic oxidation, *Appl. Surf. Sci.* 370 (2016) 218–228. doi:10.1016/j.apsusc.2016.02.131.
- [7] A.L. Yerokhin, V. V Lyubimov, R. V Ashitkov, Phase formation in ceramic coatings during plasma electrolytic oxidation of aluminium alloys, *Ceram. Int.* 24 (1998) 1–6. doi:10.1016/S0272-8842(96)00067-3.
- [8] A.V. Apelfeld, A.A. Ashmarin, A.M. Borisov, A.V. Vinogradov, S.V. Savushkina, E.A. Shmytkova, Formation of zirconia tetragonal phase by plasma electrolytic oxidation of zirconium alloy in electrolyte comprising additives of yttria nanopowder, *Surf. Coatings Technol.* 328 (2017) 513–517. doi:10.1016/j.surfcoat.2016.09.071.
- [9] S. Stojadinović, R. Vasilić, Orange–red photoluminescence of Nb<sub>2</sub>O<sub>5</sub>:Eu<sup>3+</sup>, Sm<sup>3+</sup> coatings formed by plasma electrolytic oxidation of niobium, *J. Alloys Compd.* 685 (2016) 881–889. doi:10.1016/j.jallcom.2016.06.192.

- [10] S. Stojadinović, N. Tadić, A. Ćirić, R. Vasilić, Photoluminescence properties of  $\text{Eu}^{3+}$  doped  $\text{HfO}_2$  coatings formed by plasma electrolytic oxidation of hafnium, *Opt. Mater. (Amst)*. 77 (2018) 19–24. doi:10.1016/j.optmat.2018.01.014.
- [11] S. Stojadinović, N. Tadić, R. Vasilić, Photoluminescence of  $\text{Sm}^{3+}$  doped  $\text{ZrO}_2$  coatings formed by plasma electrolytic oxidation of zirconium, *Mater. Lett.* 164 (2016) 329–332. doi:10.1016/j.matlet.2015.11.056.
- [12] J. Brübach, C. Pflitsch, A. Dreizler, B. Atakan, On surface temperature measurements with thermographic phosphors: A review, *Prog. Energy Combust. Sci.* 39 (2013) 37–60. doi:10.1016/j.peecs.2012.06.001.
- [13] Stevan Stojadinović, Rastko Vasilić, Bećko Kasalica, Ivan Belča, and Ljubiša Zeković, Luminescence During the Electrochemical Oxidation of Aluminum, in: *Electrodepos. Surf. Finish. Fundam. Appl.*, 2014: pp. 217–239. doi:10.1007/978-1-4939-0289-7.
- [14] Ž. Antić, K. Prashanthi, S. Ćulubrk, K. Vuković, M.D. Dramićanin, T. Thundat, Effect of annealing conditions on structural and luminescent properties of  $\text{Eu}^{3+}$ -doped  $\text{Gd}_2\text{Ti}_2\text{O}_7$  thin films, *Appl. Surf. Sci.* 364 (2016) 273–279. doi:10.1016/j.apsusc.2015.12.137.
- [15] K.N. Shinde, S.J. Dhoble, H.C. Swart, K. Park, Basic Mechanisms of Photoluminescence, in: *Phosphate Phosphors Solid-State Light.*, Springer Berlin Heidelberg, Berlin, Heidelberg, 2012: pp. 41–60. doi:10.1007/978-3-642-34312-4.
- [16] J.R. Lakowicz, *Principles of Fluorescence Spectroscopy*, Springer US, Boston, MA, 2006. doi:10.1007/978-0-387-46312-4.
- [17] A. Townshen, *Principles of Instrumental Analysis*, *Anal. Chim. Acta.* 152 (1983) 314. doi:10.1016/S0003-2670(00)84936-3.
- [18] D.R. Tobergte, S. Curtis, *Methods in Cellular Imaging*, Springer, 2001. doi:10.1007/978-1-4614-7513-2.
- [19] Y. Yang, C. Mi, F. Jiao, X. Su, X. Li, L. Liu, J. Zhang, F. Yu, Y. Liu, Y. Mai, A Novel Multifunctional Upconversion Phosphor:  $\text{Yb}^{3+}/\text{Er}^{3+}$  Codoped  $\text{La}_2\text{S}_3$ , *J. Am.*

- Ceram. Soc. 97 (2014) 1769–1775. doi:10.1111/jace.12822.
- [20] J. Vuojola, T. Soukka, Luminescent lanthanide reporters: new concepts Luminescent lanthanide reporters: new concepts for use in bioanalytical applications, 2014. doi:10.1088/2050-6120/2/1/012001.
- [21] B. Quantum, An Introduction to Fluorescence Spectroscopy, Chem 312. (2007).
- [22] R. Wegerhoff, O. Weidlich, M. Kässens, Basics of Light Microscopy & Imaging, (2008).
- [23] P.T. So, C.Y. Dong, Fluorescence Spectrophotometry, *Encycl. Life Sci.* (2001) 1–4. doi:10.1038/npg.els.0002978.
- [24] C.R. Cornejo, Luminescence in Rare Earth Ion-Doped Oxide Compounds, in: *Lumin. - An Outlook Phenom. Their Appl.*, InTech, 2016. doi:10.5772/65185.
- [25] M. Gaft, R. Reisfeld, G. Panczer, *Modern Luminescence Spectroscopy of Minerals and Materials*, Springer, 2005.
- [26] Olympus, Light Sources, (n.d.). <https://www.olympus-lifescience.com/en/microscope-resource/primer/techniques/fluorescence/fluorosources/>.
- [27] Zeiss Microscopy, (n.d.). <http://zeiss-campus.magnet.fsu.edu> (accessed June 5, 2016).
- [28] G.C. Righini, M. Ferrari, Photoluminescence of rare-earth-doped glasses, *Riv. Del Nuovo Cim.* 28 (2005) 1–53. doi:10.1393/ncr/i2006-10010-8.
- [29] J.W. Hofstraat, M.J. Latuhihin, Correction of fluorescence spectra, *Appl. Spectrosc.* 48 (1994) 436–447. doi:10.1366/000370294775269027.
- [30] B.G. Wybourne, The fascination of the rare earths - then, now and in the future, *J. Alloys Compd.* 380 (2004) 96–100. doi:10.1016/j.jallcom.2004.03.034.
- [31] B.M. Walsh, Judd-Ofelt theory: principles and practices brian m. walsh, *Int. Sch. At. Mol. Spectrosc.* (2006) 403–433. doi:10.1007/1-4020-4789-4\_21.
- [32] L.D. Carlos, and F. Palacio, Thermometry at the nanoscale techniques and selected

- applications., 2016. doi:10.1039/9781782622031-FP007.
- [33] M.P. Hehlen, M.G. Brik, K.W. Krämer, 50th anniversary of the Judd–Ofelt theory: An experimentalist’s view of the formalism and its application, *J. Lumin.* 136 (2013) 221–239. doi:10.1016/j.jlumin.2012.10.035.
- [34] B.G. Wybourne, *Spectroscopic Properties of Rare Earths*, Interscience publishers, Argonne, IL (United States), 1965.
- [35] R. Reisfeld, *Optical Properties of Lanthanides in Condensed Phase, Theory and Applications*, *AIMS Mater. Sci.* 2 (2015) 37–60. doi:10.3934/matensci.2015.2.37.
- [36] M.D. Dramićanin, Sensing temperature via downshifting emissions of lanthanide-doped metal oxides and salts. A review, *Methods Appl. Fluoresc.* 4 (2016) 042001. doi:10.1088/2050-6120/4/4/042001.
- [37] D. MacIsaac, M.I. Roldán, R. Monterreal, A. Marzo, J. Ballestrín, J. Barbero, I. Cañadas, J. Rodríguez, D. Hernandez, G. Olalde, G. Bonnier, F. Le Frious, M. Sadli, J. Ballestrín, A. Marzo, I. Cañadas, J. Rodríguez, A. Ianiro, G. Cardone, D. Hernandez, G. Olalde, J.M. Gineste, C. Gueymard, K. Gruner, A.P. Freid, P.K. Johnson, M. Musella, R. Müller, J.E. Steinbrenner, R.D. Palumbo, H.R. Tschudi, M. Schubnell, I. Thermometers, P. a. a. Ni, R.M.M. More, F.M.M. Bieniosek, H. Yoneda, F.M.M. Bieniosek, O. Kamada, I. Alxneit, H.R. Tschudi, G. Morian, W.R. Barron, W. Corporation, F.O.R. Thermal, E. Storage, J. Barbero, I. Can, E. Alonso, C. Pérez-rábago, J. Gonzalez-aguilar, M. Romero, *Principles of Non-contact Temperature Measurement*, *J. Sol. Energy Eng.* 3 (2003) 1397. doi:10.1119/1.880392.
- [38] S.F. Collins, G.W. Baxter, S.A. Wade, T. Sun, K.T. V. Grattan, Z.Y. Zhang, A.W. Palmer, Comparison of fluorescence-based temperature sensor schemes: Theoretical analysis and experimental validation, *J. Appl. Phys.* 84 (1998) 4649–4654. doi:10.1063/1.368705.
- [39] P.R.N. Childs, J.R. Greenwood, C.A. Long, Review of temperature measurement, *Rev. Sci. Instrum.* 71 (2000) 2959–2978. doi:10.1063/1.1305516.
- [40] P.R.N. Childs, *Temperature*, in: P.R.N. Childs (Ed.), *Pract. Temp. Meas.*, Elsevier,

- Oxford, 2001: pp. 1–15. doi:10.1016/B978-075065080-9/50001-0.
- [41] D. Ross-Pinnock, P.G. Maropoulos, Review of industrial temperature measurement technologies and research priorities for the thermal characterisation of the factories of the future, *Proc. Inst. Mech. Eng. Part B J. Eng. Manuf.* 230 (2016) 793–806. doi:10.1177/0954405414567929.
- [42] X. Wang, O.S. Wolfbeis, R.J. Meier, Luminescent probes and sensors for temperature, *Chem. Soc. Rev.* 42 (2013) 7834. doi:10.1039/c3cs60102a.
- [43] Non-Contact Temperature Measurement: A Technical Reference Series Brought to You by OMEGA. IR Thermometers & Pyrometers, 1998. [http://www2.kelm.ftn.uns.ac.rs/literatura/si/pdf/Transactions\\_Vol\\_I.pdf](http://www2.kelm.ftn.uns.ac.rs/literatura/si/pdf/Transactions_Vol_I.pdf).
- [44] J.P. Feist, A.L. Heyes, Europium-doped yttria-stabilized zirconia for high-temperature phosphor thermometry, *Proc. Inst. Mech. Eng. Part L J. Mater. Des. Appl.* 214 (2000) 7–12. doi:10.1177/146442070021400102.
- [45] K.T. V. Grattan, B.T. Meggitt, eds., *Optical Fiber Sensor Technology*, Springer Netherlands, Dordrecht, 1999. doi:10.1007/978-94-017-2484-5.
- [46] X. Li, X. Li, X. Wang, L. Tong, L. Cheng, J. Sun, J. Zhang, S. Xu, B. Chen, Concentration- and temperature-dependent fluorescent quenching and Judd–Ofelt analysis of  $\text{Eu}^{3+}$  in  $\text{NaLaTi}_2\text{O}_6$  phosphors, *J. Mater. Sci.* 52 (2017) 935–943. doi:10.1007/s10853-016-0388-4.
- [47] B.R. Judd, Optical Absorption Intensities of Rare-Earth Ions, *Phys. Rev.* 127 (1962) 750–761. doi:10.1103/PhysRev.127.750.
- [48] G.S. Ofelt, Intensities of Crystal Spectra of Rare-Earth Ions, *J. Chem. Phys.* 37 (1962) 511–520. doi:10.1063/1.1701366.
- [49] Google Scholar, (n.d.). <https://scholar.google.com> (accessed January 1, 2018).
- [50] L. Smentek, Judd-Ofelt Theory - The Golden (and the Only One) Theoretical Tool of f-Electron Spectroscopy, in: *Comput. Methods Lanthan. Actin. Chem.*, John Wiley & Sons Ltd, Chichester, UK, 2015: pp. 241–268. doi:10.1002/9781118688304.ch10.

- [51] V. Lojpur, S. Čulubrk, M. Medić, M. Dramićanin, Luminescence thermometry with  $\text{Eu}^{3+}$  doped  $\text{GdAlO}_3$ , *J. Lumin.* 170 (2016) 467–471. doi:10.1016/j.jlumin.2015.06.032.
- [52] S.A. Wade, S.F. Collins, G.W. Baxter, Fluorescence intensity ratio technique for optical fiber point temperature sensing, *J. Appl. Phys.* 94 (2003) 4743. doi:10.1063/1.1606526.
- [53] M. McSherry, C. Fitzpatrick, E. Lewis, Review of luminescent based fibre optic temperature sensors, *Sens. Rev.* 25 (2005) 56–62. doi:10.1108/02602280510577852.
- [54] V. Lojpur, Željka Antić, R. Krsmanović, M. Medić, M.G. Nikolić, M.D. Dramićanin, Thermographic properties of  $\text{Eu}^{3+}$  and  $\text{Sm}^{3+}$  - doped  $\text{Lu}_2\text{O}_3$  nanophosphor, *J. Serbian Chem. Soc.* 77 (2012) 1735–1746. doi:10.2298/JSC121021140L.
- [55] C. Görller-Walrand, K. Binnemans, Chapter 167 Spectral intensities of f-f transitions, in: *Handb. Phys. Chem. Rare Earths*, 1998: pp. 101–264. doi:10.1016/S0168-1273(98)25006-9.
- [56] M.G. Nikolić, D.J. Jovanović, M.D. Dramićanin, Temperature dependence of emission and lifetime in  $\text{Eu}^{3+}$  - and  $\text{Dy}^{3+}$  -doped  $\text{GdVO}_4$ , *Appl. Opt.* 52 (2013) 1716. doi:10.1364/AO.52.001716.
- [57] S. Čulubrk, V. Lojpur, S.P. Ahrenkiel, J.M. Nedeljković, M.D. Dramićanin, Non-contact thermometry with  $\text{Dy}^{3+}$  doped  $\text{Gd}_2\text{Ti}_2\text{O}_7$  nano-powders, *J. Lumin.* 170 (2016) 395–400. doi:10.1016/j.jlumin.2015.06.006.
- [58] M. Dramićanin, Chapter 6 - Lanthanide and transition metal ion doped materials for luminescence temperature sensing, in: M. Dramićanin (Ed.), *Lumin. Thermom.*, Woodhead Publishing, 2018: pp. 113–157. doi:https://doi.org/10.1016/B978-0-08-102029-6.00006-3.
- [59] M.G. Nikolić, Ž. Antić, S. Čulubrk, J.M. Nedeljković, M.D. Dramićanin, Temperature sensing with  $\text{Eu}^{3+}$  doped  $\text{TiO}_2$  nanoparticles, *Sensors Actuators B Chem.* 201 (2014) 46–50. doi:10.1016/j.snb.2014.04.108.

- [60] Z. Cao, S. Zhou, G. Jiang, Y. Chen, C. Duan, M. Yin, Temperature dependent luminescence of Dy<sup>3+</sup> doped BaYF<sub>5</sub> nanoparticles for optical thermometry, *Curr. Appl. Phys.* 14 (2014) 1067–1071. doi:10.1016/j.cap.2014.05.020.
- [61] S.W. Allison, G.T. Gillies, Remote thermometry with thermographic phosphors: Instrumentation and applications, *Rev. Sci. Instrum.* 68 (1997) 2615–2650. doi:10.1063/1.1148174.
- [62] M.D. Dramićanin, *Luminescence Thermometry, Methods, Materials and Applications*, Woodhead Publishing, 2018. doi:https://doi.org/10.1016/B978-0-08-102029-6.00006-3.
- [63] M.R.N. Soares, C. Nico, D. Oliveira, M. Peres, L. Rino, A.J.S. Fernandes, T. Monteiro, F.M. Costa, Red light from ZrO<sub>2</sub>:Eu<sup>3+</sup> nanostructures, *Mater. Sci. Eng. B Solid-State Mater. Adv. Technol.* 177 (2012) 712–716. doi:10.1016/j.mseb.2011.10.010.
- [64] J.B. Kim, M.L. Weichman, D.M. Neumark, High-resolution anion photoelectron spectra of TiO<sub>2</sub><sup>-</sup>, ZrO<sub>2</sub><sup>-</sup>, and HfO<sub>2</sub><sup>-</sup> obtained by slow electron velocity-map imaging, *Phys. Chem. Chem. Phys.* 15 (2013) 20973. doi:10.1039/c3cp54084g.
- [65] V. Miikkulainen, M. Leskelä, M. Ritala, R.L. Puurunen, Crystallinity of inorganic films grown by atomic layer deposition: Overview and general trends, *J. Appl. Phys.* 113 (2013) 021301. doi:10.1063/1.4757907.
- [66] Y. Hui, B. Zou, S. Liu, S. Zhao, J. Xu, Y. Zhao, X. Fan, L. Zhu, Y. Wang, X. Cao, Effects of Eu<sup>3+</sup>-doping and annealing on structure and fluorescence of zirconia phosphors, *Ceram. Int.* 41 (2015) 2760–2769. doi:10.1016/j.ceramint.2014.10.091.
- [67] J.D. Buckley, *Stabilization of the phase transformations in hafnium oxide*, Iowa State University, 1968. <https://lib.dr.iastate.edu/rtd/3650>.
- [68] F.L. Martínez, M. Toledano-Luque, J.J. Gandía, J. Cárabe, W. Bohne, J. Röhrich, E. Strub, I. Mártil, Optical properties and structure of HfO<sub>2</sub> thin films grown by high pressure reactive sputtering, *J. Phys. D. Appl. Phys.* 40 (2007) 5256–5265. doi:10.1088/0022-3727/40/17/037.

- [69] F. Bohra, B. Jiang, J.-M. Zuo, Textured crystallization of ultrathin hafnium oxide films on silicon substrate, *Appl. Phys. Lett.* 90 (2007) 161917. doi:10.1063/1.2724925.
- [70] G.D. Wilk, R.M. Wallace, J.M. Anthony, High- $\kappa$  gate dielectrics: Current status and materials properties considerations, *J. Appl. Phys.* 89 (2001) 5243–5275. doi:10.1063/1.1361065.
- [71] A. Sharma, M. Varshney, H.J. Shin, K.H. Chae, S.O. Won, XANES, EXAFS and photoluminescence investigations on the amorphous Eu:HfO<sub>2</sub>, *Spectrochim. Acta - Part A Mol. Biomol. Spectrosc.* 173 (2017) 549–555. doi:10.1016/j.saa.2016.10.006.
- [72] A. Wiatrowska, E. Zych, L. Kpiński, Monoclinic HfO<sub>2</sub>:Eu X-ray phosphor, *Radiat. Meas.* 45 (2010) 493–496. doi:10.1016/j.radmeas.2009.12.017.
- [73] A.M. Raba, J. Bautista-Ruíz, M.R. Joya, Synthesis and Structural Properties of Niobium Pentoxide Powders: A Comparative Study of the Growth Process, *Mater. Res.* 19 (2016) 1381–1387. doi:10.1590/1980-5373-mr-2015-0733.
- [74] Y.Y. Shanshan Yao, Lihong Xue, Properties of Eu<sup>3+</sup> Luminescence in the monoclinic Ba<sub>2</sub>MgSi<sub>2</sub>O<sub>7</sub>, *Ceramics-Silikaty.* 55 (2011) 251–255. [http://www.ceramics-silikaty.cz/2011/pdf/2011\\_03\\_251.pdf](http://www.ceramics-silikaty.cz/2011/pdf/2011_03_251.pdf).
- [75] B. Milićević, V. Đorđević, K. Vuković, G. Dražić, M.D. Dramićanin, Effects of Li co-doping on properties of Eu<sup>3+</sup> activated TiO<sub>2</sub> anatase nanoparticles, *Opt. Mater. (Amst).* 72 (2017) 316–322. doi:10.1016/j.optmat.2017.06.029.
- [76] S. Gražulis, A. Daškevič, A. Merkys, D. Chateigner, L. Lutterotti, M. Quirós, N.R. Serebryanaya, P. Moeck, R.T. Downs, A. Le Bail, Crystallography Open Database (COD): An open-access collection of crystal structures and platform for worldwide collaboration, *Nucleic Acids Res.* 40 (2012) 420–427. doi:10.1093/nar/gkr900.
- [77] K. Momma, F. Izumi, VESTA 3 for three-dimensional visualization of crystal, volumetric and morphology data, *J. Appl. Crystallogr.* 44 (2011) 1272–1276. doi:10.1107/S0021889811038970.

- [78] X. Sang, E.D. Grimley, T. Schenk, U. Schroeder, J.M. Lebeau, On the structural origins of ferroelectricity in HfO<sub>2</sub> thin films, *Appl. Phys. Lett.* 106 (2015) 1–5. doi:10.1063/1.4919135.
- [79] C. Tiseanu, B. Cojocaru, V.I. Parvulescu, M. Sanchez-Dominguez, P.A. Primus, M. Boutonnet, Order and disorder effects in nano-ZrO<sub>2</sub> investigated by micro-Raman and spectrally and temporally resolved photoluminescence, *Phys. Chem. Chem. Phys.* 14 (2012) 12970. doi:10.1039/c2cp41946g.
- [80] P. Ghosh, A. Patra, Role of surface coating in ZrO<sub>2</sub>/Eu<sup>3+</sup> nanocrystals, *Langmuir*. 22 (2006) 6321–6327. doi:10.1021/la0604883.
- [81] S. Dhiren Meetei, S. Dorendrajit Singh, N. Shanta Singh, V. Sudarsan, R.S. Ningthoujam, M. Tyagi, S.C. Gadkari, R. Tewari, R.K. Vatsa, Crystal structure and photoluminescence correlations in white emitting nanocrystalline ZrO<sub>2</sub>:Eu<sup>3+</sup> phosphor: Effect of doping and annealing, *J. Lumin.* 132 (2012) 537–544. doi:10.1016/j.jlumin.2011.09.011.
- [82] Z. Fan, J. Deng, J. Wang, Z. Liu, P. Yang, J. Xiao, X. Yan, Z. Dong, J. Wang, J. Chen, Ferroelectricity emerging in strained (111)-textured ZrO<sub>2</sub> thin films, *Appl. Phys. Lett.* 108 (2016). doi:10.1063/1.4939660.
- [83] S.F. Wang, F. Gu, M.K. Lü, Z. Sen Yang, G.J. Zhou, H.P. Zhang, Y.Y. Zhou, S.M. Wang, Structure evolution and photoluminescence properties of ZrO<sub>2</sub>:Eu<sup>3+</sup> nanocrystals, *Opt. Mater. (Amst.)* 28 (2006) 1222–1226. doi:10.1016/j.optmat.2005.08.003.
- [84] X. Yin, Y. Wang, D. Wan, F. Huang, J. Yao, Red-luminescence enhancement of ZrO<sub>2</sub>-based phosphor by codoping Eu<sup>3+</sup> and M<sup>5+</sup> (M = Nb, Ta), *Opt. Mater. (Amst.)* 34 (2012) 1353–1356. doi:10.1016/j.optmat.2012.02.012.
- [85] R. Marin, G. Sponchia, E. Zucchetta, P. Riello, F. Enrichi, G. De Portu, A. Benedetti, Monitoring the *t* → *m* Martensitic Phase Transformation by Photoluminescence Emission in Eu<sup>3+</sup>-Doped Zirconia Powders, *J. Am. Ceram. Soc.* 96 (2013) 2628–2635. doi:10.1111/jace.12363.
- [86] J.D. McCullough, K.N. Trueblood, The crystal structure of baddeleyite

- (monoclinic  $\text{ZrO}_2$ ), *Acta Crystallogr.* 12 (1959) 507–511. doi:10.1107/S0365110X59001530.
- [87] H. Zhang, X. Fu, S. Niu, G. Sun, Q. Xin, Synthesis and characterization of  $\text{ZrO}_2\text{:Eu}$  nanopowder by EDTA complexing sol-gel method, *Mater. Chem. Phys.* 91 (2005) 361–364. doi:10.1016/j.matchemphys.2004.11.040.
- [88] Y.S. Vidya, K.S. Anantharaju, H. Nagabhushana, S.C. Sharma, H.P. Nagaswarupa, S.C. Prashantha, C. Shivakumara, Danithkumar, Combustion synthesized tetragonal  $\text{ZrO}_2\text{:Eu}^{3+}$  nanophosphors: Structural and photoluminescence studies, *Spectrochim. Acta - Part A Mol. Biomol. Spectrosc.* 135 (2015) 241–251. doi:10.1016/j.saa.2014.06.151.
- [89] B.K. Moon, I.M. Kwon, J.H. Jeong, C.S. Kim, S.S. Yi, P.S. Kim, H. Choi, J.H. Kim, Synthesis and luminescence characteristics of  $\text{Eu}^{3+}$ -doped  $\text{ZrO}_2$  nanoparticles, *J. Lumin.* 122–123 (2007) 855–857. doi:10.1016/j.jlumin.2006.01.308.
- [90] S.D. Meetei, S.D. Singh, Effects of crystal size, structure and quenching on the photoluminescence emission intensity, lifetime and quantum yield of  $\text{ZrO}_2\text{:Eu}^{3+}$  nanocrystals, *J. Lumin.* 147 (2014) 328–335. doi:10.1016/j.jlumin.2013.11.064.
- [91] P. Platt, P. Frankel, M. Gass, R. Howells, M. Preuss, Finite element analysis of the tetragonal to monoclinic phase transformation during oxidation of zirconium alloys, *J. Nucl. Mater.* 454 (2014) 290–297. doi:10.1016/j.jnucmat.2014.08.020.
- [92] E.N. Cerón, G.R. Gattorno, J. Guzmán-mendoza, M. García-hipólito, C. Falcony, Photoluminescence Response of  $\text{HfO}_2\text{:Eu}^{3+}$  Obtained by Hydrothermal Route, *2013 (2013)* 73–77.
- [93] R. Marin, G. Sponchia, M. Back, P. Riello, Determining europium compositional fluctuations in partially stabilized zirconia nanopowders: A non-line-broadening-based method, *Acta Crystallogr. Sect. B Struct. Sci. Cryst. Eng. Mater.* 72 (2016) 29–38. doi:10.1107/S2052520615021083.
- [94] J. Gonzalez, M.D.C. Ruiz, D. Pasquevich, A. Bohé, Formation of niobium-tantalum pentoxide orthorhombic solid solutions under chlorine-bearing

- atmospheres, *J. Mater. Sci.* 36 (2001) 3299–3311. doi:10.1023/A:1017911125106.
- [95] B.M. Gatehouse, A.D. Wadsley, The crystal structure of the high temperature form of niobium pentoxide, *Acta Crystallogr.* 17 (1964) 1545–1554. doi:10.1107/S0365110X6400384X.
- [96] H.-Q. Liu, L.-L. Wang, S.-G. Chen, B.-S. Zou, Optical properties of nanocrystal and bulk  $\text{ZrO}_2\text{:Eu}^{3+}$ , *J. Alloys Compd.* 448 (2008) 336–339. doi:10.1016/j.jallcom.2006.11.171.
- [97] A. Kitai, *Luminescent Materials and Applications*, 2008. doi:10.1002/9780470985687.
- [98] R. Gunawidjaja, T. Myint, H. Eilers, Stabilization of tetragonal phase in  $\text{ZrO}_2\text{:Eu}$  by rapid thermal heating, *Chem. Phys. Lett.* 515 (2011) 122–126. doi:10.1016/j.cplett.2011.09.004.
- [99] X. Li, B. Chen, R. Shen, H. Zhong, L. Cheng, J. Sun, J. Zhang, H. Zhong, Y. Tian, G. Du, Fluorescence quenching of  $^5\text{D}_J$  ( $J = 1, 2$  and  $3$ ) levels and Judd-Ofelt analysis of  $\text{Eu}^{3+}$  in  $\text{NaGdTiO}_4$  phosphors, *J. Phys. D. Appl. Phys.* 44 (2011). doi:10.1088/0022-3727/44/33/335403.
- [100] M. Ferhi, C. Bouzidi, K. Horchani-Naifer, H. Elhouichet, M. Ferid, Judd-Ofelt analysis of spectroscopic properties of  $\text{Eu}^{3+}$  doped  $\text{KLa}(\text{PO}_3)_4$ , *J. Lumin.* 157 (2015) 21–27. doi:10.1016/j.jlumin.2014.08.017.
- [101] E.G. Villabona-Leal, L.A. Diaz-Torres, H. Desirena, J.L. Rodríguez-López, E. Pérez, O. Meza, Luminescence and energy transfer properties of  $\text{Eu}^{3+}$  and  $\text{Gd}^{3+}$  in  $\text{ZrO}_2$ , *J. Lumin.* 146 (2014) 398–403. doi:10.1016/j.jlumin.2013.10.002.
- [102] K. Binnemans, Interpretation of europium(III) spectra, *Coord. Chem. Rev.* 295 (2015) 1–45. doi:10.1016/j.ccr.2015.02.015.
- [103] W.T. Carnall, H. Crosswhite, H.M. Crosswhite, Energy level structure and transition probabilities in the spectra of the trivalent lanthanides in  $\text{LaF}_3$ , Argonne, IL (United States), 1978. doi:10.2172/6417825.
- [104] S.S. Babu, P. Babu, C.K. Jayasankar, W. Sievers, T. Tröster, G. Wortmann, Optical

- absorption and photoluminescence studies of Eu<sup>3+</sup>-doped phosphate and fluorophosphate glasses, *J. Lumin.* 126 (2007) 109–120. doi:10.1016/j.jlumin.2006.05.010.
- [105] C.G. Ma, M.G. Brik, V. Kiisk, T. Kangur, I. Sildos, Spectroscopic and crystal-field analysis of energy levels of Eu<sup>3+</sup> in SnO<sub>2</sub> in comparison with ZrO<sub>2</sub> and TiO<sub>2</sub>, *J. Alloys Compd.* 509 (2011) 3441–3451. doi:10.1016/j.jallcom.2010.12.071.
- [106] N.M. Edelstein, *Electronic Structure of f-Block Compounds*, in: *Organometallics of the F-Elements*, Springer Netherlands, Dordrecht, 1979: pp. 37–79. doi:10.1007/978-94-009-9454-6\_2.
- [107] W.T. Carnall, P.R. Fields, K. Rajnak, *Electronic Energy Levels in the Trivalent Lanthanide Aquo Ions. I. Pr<sup>3+</sup>, Nd<sup>3+</sup>, Pm<sup>3+</sup>, Sm<sup>3+</sup>, Dy<sup>3+</sup>, Ho<sup>3+</sup>, Er<sup>3+</sup>, and Tm<sup>3+</sup>*, *J. Chem. Phys.* 49 (1968) 4424–4442. doi:10.1063/1.1669893.
- [108] A. Novoselsky, J. Katriel, R. Gilmore, Coefficients of fractional parentage in the L–S coupling scheme, *J. Math. Phys.* 29 (1988) 1368–1388. doi:10.1063/1.527930.
- [109] G.F.K. C. W. Nielson, *Spectroscopic coefficients for the pn, dn, and fn configurations*, (1963) xi, 275 p. file://catalog.hathitrust.org/Record/001983848.
- [110] D.D. Velkov, *Tables of multi-electron coefficient of fractional parentage for the p,d and f shells*, (2000).
- [111] M.P. Hehlen, *RELIC 1.0 (Rare Earth Level and Intensity Calculations) User Guide*, Los Alamos, NM (United States), 2013. doi:10.2172/1079556.
- [112] P. Hamm, J. Helbing, G. Liu, B. Jacquier, Thermo Spectronic, H.C. Swart, J.J. Terblans, O.M. Ntwaeaborwa, R.E. Kroon, E. Coetsee, I.M. Nagpure, V.V.V. Kumar, V.V.V. Kumar, V.V.V. Kumar, *Spectroscopic Properties of Rare Earths in Optical Materials*, 2005. doi:10.1007/3-540-28209-2.
- [113] V.Y. Irkhin, Y.P. Irkhin, *Electronic structure, correlation effects and physical properties of d- and f-metals and their compounds*, *Arxiv Prepr. Cond-Mat/9812072*. 2 (1998) 457. [http://www.imp.uran.ru/KTM\\_LAB/irkhin/irkhins/](http://www.imp.uran.ru/KTM_LAB/irkhin/irkhins/).

- [114] B.R. Judd, *Operator Techniques in Atomic Spectroscopy*, Princeton University Press, 1998. <http://www.jstor.org/stable/j.ctt7zvhhcb>.
- [115] Y.R. Shen, W.B. Holzapfel, Nephelauxetic effects on  $\text{Sm}^{2+}$  and  $\text{Eu}^{3+}$  in ternary MYX compounds, *Phys. Rev. B.* 52 (1995) 12618–12626. doi:10.1103/PhysRevB.52.12618.
- [116] M.J. Weber, T.E. Varitimos, B.H. Matsinger, Optical intensities of rare-earth ions in yttrium orthoaluminate, *Phys. Rev. B.* 8 (1973) 47–53. doi:10.1103/PhysRevB.8.47.
- [117] G.H. Dieke, H.M. Crosswhite, B. Dunn, Emission Spectra of the Doubly and Triply Ionized Rare Earths\*, *J. Opt. Soc. Am.* 51 (1961) 820. doi:10.1364/JOSA.51.000820.
- [118] M. Dejneka, E. Snitzer, R.E. Riman, Blue, green and red fluorescence and energy transfer of  $\text{Eu}^{3+}$  in fluoride glasses, *J. Lumin.* 65 (1995) 227–245. doi:10.1016/0022-2313(95)00073-9.
- [119] K. Gorrler-Walrand, Christiane; Binnemans, Chapter 155 Coordination Chemistry Division, Celestijnenlaan 200E, *Handb. Phys. Chem. Rare Earths.* 23 (1996) 121–283.
- [120] W.T. Carnall, P.R. Fields, K. Rajnak, Spectral Intensities of the Trivalent Lanthanides and Actinides in Solution. II.  $\text{Pm}^{3+}$ ,  $\text{Sm}^{3+}$ ,  $\text{Eu}^{3+}$ ,  $\text{Gd}^{3+}$ ,  $\text{Tb}^{3+}$ ,  $\text{Dy}^{3+}$ , and  $\text{Ho}^{3+}$ , *J. Chem. Phys.* 49 (1968) 4412–4423. doi:10.1063/1.1669892.
- [121] E. Preda, M. Stef, G. Buse, A. Pruna, I. Nicoara, Concentration dependence of the Judd–Ofelt parameters of  $\text{Er}^{3+}$  ions in  $\text{CaF}_2$  crystals, *Phys. Scr.* 79 (2009) 035304. doi:10.1088/0031-8949/79/03/035304.
- [122] C. Görller-Walrand, L. Fluyt, A. Ceulemans, W.T. Carnall, Magnetic dipole transitions as standards for Judd–Ofelt parametrization in lanthanide spectra, *J. Chem. Phys.* 95 (1991) 3099–3106. doi:10.1063/1.460867.
- [123] L. Đačanin, S.R. Lukić, D.M. Petrović, M. Nikolić, M.D. Dramićanin, Judd–Ofelt analysis of luminescence emission from  $\text{Zn}_2\text{SiO}_4:\text{Eu}^{3+}$  nanoparticles obtained by a polymer-assisted sol–gel method, *Phys. B Condens. Matter.* 406 (2011) 2319–

2322. doi:10.1016/j.physb.2011.03.068.
- [124] M.G. Brik, Ž.M. Antic, K. Vuković, M.D. Dramićanin, Judd-Ofelt Analysis of  $\text{Eu}^{3+}$  Emission in  $\text{TiO}_2$  Anatase Nanoparticles, *Mater. Trans.* 56 (2015) 1416–1418. doi:10.2320/matertrans.MA201566.
- [125] R.O. Freire, M.E. Mesquita, M.A. Couto dos Santos, N.B. da Costa, Sparkle model and photophysical studies of Europium  $\text{BiQO}_2$ -cryptate, *Chem. Phys. Lett.* 442 (2007) 488–491. doi:10.1016/j.cplett.2007.06.010.
- [126] S. Constantin, M.L. Stanciu, Calculation Of The Judd - Ofelt Parameters Of The  $\text{ZnAl}_2\text{O}_4:\text{Eu}^{3+}$ , *Ann. West Univ. Timisoara - Phys.* 56 (2012).
- [127] F. Huang, Y. Zhang, L. Hu, D. Chen, Judd–Ofelt analysis and energy transfer processes of  $\text{Er}^{3+}$  and  $\text{Nd}^{3+}$  doped fluoroaluminate glasses with low phosphate content, *Opt. Mater. (Amst.)* 38 (2014) 167–173. doi:10.1016/j.optmat.2014.10.019.
- [128] M.H. V. Werts, R.T.F. Jukes, J.W. Verhoeven, The emission spectrum and the radiative lifetime of  $\text{Eu}^{3+}$  in luminescent lanthanide complexes, *Phys. Chem. Chem. Phys.* 4 (2002) 1542–1548. doi:10.1039/b107770h.
- [129] D. Uma Maheswari, J. Suresh Kumar, L.R. Moorthy, K. Jang, M. Jayasimhadri, Emission properties of  $\text{Eu}^{3+}$  ions in alkali tellurofluorophosphate glasses, *Phys. B Condens. Matter.* 403 (2008) 1690–1694. doi:10.1016/j.physb.2007.09.089.
- [130] W. Luo, J. Liao, R. Li, X. Chen, Determination of Judd–Ofelt intensity parameters from the excitation spectra for rare-earth doped luminescent materials, *Phys. Chem. Chem. Phys.* 12 (2010) 3276. doi:10.1039/b921581f.
- [131] J. Papan, D.J. Jovanović, K. Vuković, K. Smits, V. Đorđević, M. Dramićanin, Europium(III)-doped  $\text{A}_2\text{Hf}_2\text{O}_7$  ( $\text{A} = \text{Y, Gd, Lu}$ ) nanoparticles: Influence of annealing temperature, europium(III) concentration and host cation on the luminescent properties, *Opt. Mater. (Amst.)* 61 (2016) 68–76. doi:10.1016/j.optmat.2016.04.007.
- [132] D.F. Eaton, Reference materials for Fluorescence measurement, *J. Photochem. Photobiol. B Biol.* 2 (1988) 523–531. doi:10.1016/1011-1344(88)85081-4.

- [133] W.L. Barnes, R.I. Laming, E.J. Tarbox, P.R. Morkel, Absorption and emission cross section of  $\text{Er}^{3+}$  doped silica fibers, *IEEE J. Quantum Electron.* 27 (1991) 1004–1010. doi:10.1109/3.83335.
- [134] A. V. Egorysheva, V.D. Volodin, A.A. Chistyakov, Y.A. Kuzishchin, V.M. Skorikov, T.D. Dudkina, Luminescence of europium-doped  $\text{BaO-Bi}_2\text{O}_3\text{-B}_2\text{O}_3$  glasses, *Inorg. Mater.* 46 (2010) 1384–1390. doi:10.1134/S0020168510120204.
- [135] W.T. Carnall, J.P. Hessler, F. Wagner, Transition probabilities in the absorption and fluorescence spectra of lanthanides in molten lithium nitrate-potassium nitrate eutectic, *J. Phys. Chem.* 82 (1978) 2152–2158. doi:10.1021/j100509a003.
- [136] S.A. Saleem, B.C. Jamalaiah, A.M. Babu, K. Pavani, L.R. Moorthy, A study on fluorescence properties of  $\text{Eu}^{3+}$  ions in alkali lead tellurofluoroborate glasses, *J. Rare Earths.* 28 (2010) 189–193. doi:10.1016/S1002-0721(09)60078-8.
- [137] S.K. Gupta, P.S. Ghosh, M. Sahu, K. Bhattacharyya, R. Tewari, V. Natarajan, Intense red emitting monoclinic  $\text{LaPO}_4\text{:Eu}^{3+}$  nanoparticles: host–dopant energy transfer dynamics and photoluminescence properties, *RSC Adv.* 5 (2015) 58832–58842. doi:10.1039/C5RA09076H.
- [138] W.C. Martin, R. Zalubas, L. Hagan, Atomic energy Levels - The Rare-Earth Elements, National Bureau of Standards, 1978.
- [139] R. Reisfeld, E. Zigansky, M. Gaft, Europium probe for estimation of site symmetry in glass films, glasses and crystals, *Mol. Phys.* 102 (2004) 1319–1330. doi:10.1080/00268970410001728609.
- [140] G.S. Ofelt, Structure of the  $f^6$  Configuration with Application to Rare-Earth Ions, *J. Chem. Phys.* 38 (1963) 2171–2180. doi:10.1063/1.1733947.
- [141] P.S. Peijzel, A. Meijerink, R.T. Wegh, M.F. Reid, G.W. Burdick, A complete 4f energy level diagram for all trivalent lanthanide ions, *J. Solid State Chem.* 178 (2005) 448–453. doi:10.1016/j.jssc.2004.07.046.
- [142] P.A. Tanner, Some misconceptions concerning the electronic spectra of tri-positive europium and cerium, *Chem. Soc. Rev.* 42 (2013) 5090. doi:10.1039/c3cs60033e.

- [143] N.B.D. Lima, J.D.L.J.D.L. Dutra, S.M.C. Goncalves, R.O. Freire, A.M. Simas, S.M.C. Gonçalves, R.O. Freire, A.M. Simas, Chemical Partition of the Radiative Decay Rate of Luminescence of Europium Complexes, *Sci. Rep.* 6 (2016) 21204. doi:10.1038/srep21204.
- [144] J.C. Boyer, F. Vetrone, J.A. Capobianco, A. Speghini, M. Bettinelli, Variation of Fluorescence Lifetimes and Judd-Ofelt Parameters between  $\text{Eu}^{3+}$  Doped Bulk and Nanocrystalline Cubic  $\text{Lu}_2\text{O}_3$ , *J. Phys. Chem. B.* 108 (2004) 20137–20143. doi:10.1021/jp0480504.
- [145] X.Y. Chen, G.K. Liu, The standard and anomalous crystal-field spectra of  $\text{Eu}^{3+}$ , *J. Solid State Chem.* 178 (2005) 419–428. doi:10.1016/j.jssc.2004.09.002.
- [146] C. Liu, J. Liu, K. Dou, Judd–Ofelt Intensity Parameters and Spectral Properties of  $\text{Gd}_2\text{O}_3:\text{Eu}^{3+}$  Nanocrystals, *J. Phys. Chem. B.* 110 (2006) 20277–20281. doi:10.1021/jp063075j.
- [147] M.R.N. Soares, C. Nico, M. Peres, N. Ferreira, A.J.S. Fernandes, T. Monteiro, F.M. Costa, Structural and optical properties of europium doped zirconia single crystals fibers grown by laser floating zone, *J. Appl. Phys.* 109 (2011) 2–6. doi:10.1063/1.3527914.
- [148] J. Pisarska, M. Sołtys, L. Zur, W.A. Pisarski, C.K. Jayasankar, Excitation and luminescence of rare earth-doped lead phosphate glasses, *Appl. Phys. B Lasers Opt.* 116 (2014) 837–845. doi:10.1007/s00340-014-5770-9.
- [149] X. Zhang, L. Zhou, Q. Pang, M. Gong, Synthesis, photoluminescence and Judd–Ofelt analysis of red  $\text{LiGd}_5\text{P}_2\text{O}_{13}:\text{Eu}^{3+}$  phosphors for white LEDs, *RSC Adv.* 5 (2015) 54622–54628. doi:10.1039/C5RA06680H.
- [150] R. Reisfeld, Excited States and Energy Transfer from Donor Cations to Rare Earths in the Condensed Phase, *Struct. Bond.* 30 (1976) 65–97.
- [151] W.-C. Liu, D. Wu, A.-D. Li, H.-Q. Ling, Y.-F. Tang, N.-B. Ming, Annealing and doping effects on structure and optical properties of sol-gel derived  $\text{ZrO}_2$  thin films, *Appl. Surf. Sci.* 191 (2002) 181–187. doi:10.1016/S0169-4332(02)00177-0.
- [152] A. Zhang, M. Lu, Z. Qiu, Y. Zhou, Q. Ma, Multiband luminescence of  $\text{Eu}^{3+}$  based

- on  $\text{Y}_2\text{Zr}_2\text{O}_7$  nanocrystals, *Mater. Chem. Phys.* 109 (2008) 105–108. doi:10.1016/j.matchemphys.2007.10.042.
- [153] T. Myint, R. Gunawidjaja, H. Eilers, Spectroscopic Properties of Nanophase Eu-Doped  $\text{ZrO}_2$  and Its Potential Application for Fast Temperature Sensing Under Extreme Conditions, *J. Phys. Chem. C.* 116 (2012) 21629–21634. doi:10.1021/jp307092b.
- [154] D.A. Gálico, I.O. Mazali, F.A. Sigoli, Nanothermometer based on intensity variation and emission lifetime of europium(III) benzoylacetate complex, *J. Lumin.* 192 (2017) 224–230. doi:10.1016/j.jlumin.2017.06.062.
- [155] A. Ćirić, Arduino code for thermometric measurements apparatus, (2018). doi:http://dx.doi.org/10.17632/ddb9cz7gm5.1.
- [156] A. Ćirić, Instructions for DIY Apparatus for Luminescence thermometry, (2018). <https://sites.google.com/view/apparatus-for-thermometry/> (accessed September 22, 2018).
- [157] R. Li, Z. Ji, C.H. Chang, D.R. Dunphy, X. Cai, H. Meng, H. Zhang, B. Sun, X. Wang, J. Dong, S. Lin, M. Wang, Y.-P. Liao, C.J. Brinker, A. Nel, T. Xia, Surface Interactions with Compartmentalized Cellular Phosphates Explain Rare Earth Oxide Nanoparticle Hazard and Provide Opportunities for Safer Design, *ACS Nano.* 8 (2014) 1771–1783. doi:10.1021/nn406166n.
- [158] T.. Weirich, M. Winterer, S. Seifried, H. Hahn, H. Fuess, Rietveld analysis of electron powder diffraction data from nanocrystalline anatase,  $\text{TiO}_2$ , *Ultramicroscopy.* 81 (2000) 263–270. doi:10.1016/S0304-3991(99)00189-8.
- [159] E. P. Meagher, G. A. Lager, Polyhedral thermal expansion in the  $\text{TiO}_2$  polymorphs: Refinement of the crystal structures of rutile and brookite at high temperature, *Can. Mineral.* 17 (1979) 77–85.
- [160] T. V Perevalov, V.S. Aliev, V.A. Gritsenko, A.A. Saraev, V. V Kaichev, E. V Ivanova, M. V Zamoryanskaya, The origin of 2.7 eV luminescence and 5.2 eV excitation band in hafnium oxide, *Appl. Phys. Lett.* 104 (2014) 71904. doi:10.1063/1.4865259.

- [161] S. Stojadinović, N. Tadić, R. Vasilić, Plasma electrolytic oxidation of hafnium, *Int. J. Refract. Met. Hard Mater.* 69 (2017) 153–157. doi:<https://doi.org/10.1016/j.ijrmhm.2017.08.011>.
- [162] J.D.L. Dutra, T.D. Bispo, R.O. Freire, LUMPAC lanthanide luminescence software: Efficient and user friendly, *J. Comput. Chem.* 35 (2014) 772–775. doi:[10.1002/jcc.23542](https://doi.org/10.1002/jcc.23542).
- [163] M.N. Polyanskiy, Refractive index database, (n.d.). <https://refractiveindex.info> (accessed March 5, 2018).
- [164] Origin, (n.d.). <http://www.originlab.com>.
- [165] A. Ćirić, S. Stojadinović, M. Sekulić, M.D. Dramićanin, JOES: An application software for Judd-Ofelt analysis from  $\text{Eu}^{3+}$  emission spectra, *J. Lumin.* 205 (2019) 351–356. doi:[10.1016/j.jlumin.2018.09.048](https://doi.org/10.1016/j.jlumin.2018.09.048).
- [166] K. Binnemans, C. Görller-Walrand, Application of  $\text{Eu}^{3+}$  ion for site symmetry determination, *J. Rare Earths.* 14 (1996) 173–180.
- [167] C. Wyman, P.-P. Sloan, P. Shirley, Simple Analytic Approximations to the CIE XYZ Color Matching Functions, *J. Comput. Graph. Tech.* 2 (2013) 1–11. <http://jcgt.org/published/0002/02/01/paper.pdf>.
- [168] C. Abraham, A Beginner's Guide to (CIE) Colorimetry, (2016). <https://medium.com/hipster-color-science/a-beginners-guide-to-colorimetry-401f1830b65a> (accessed April 3, 2018).
- [169] Lighting Research Center, Appendix A: Calculating chromaticity coordinates, NLPPIP - Specif. Reports. (n.d.). <http://www.lrc.rpi.edu/programs/nlpip/lightinganswers/lightsources/appendixa.asp> (accessed March 3, 2018).
- [170] A.N. Meza-Rocha, A. Speghini, M. Bettinelli, U. Caldiño, Orange and reddish-orange light emitting phosphors:  $\text{Sm}^{3+}$  and  $\text{Sm}^{3+}/\text{Eu}^{3+}$  doped zinc phosphate glasses, *J. Lumin.* 167 (2015) 305–309. doi:[10.1016/j.jlumin.2015.06.050](https://doi.org/10.1016/j.jlumin.2015.06.050).
- [171] I.L. Azevedo, M.G. Morgan, F. Morgan, The Transition to Solid-State Lighting,

Proc. IEEE. 97 (2009) 481–510. doi:10.1109/JPROC.2009.2013058.

- [172] S. Keeping, Phosphor Development Addresses Lower Efficacy of Warm-White LEDs, Electron. Prod. Mag. (2014). <https://www.digikey.com/en/articles/techzone/2014/may/phosphor-development-addresses-lower-efficacy-of-warm-white-leds> (accessed November 11, 2018).
- [173] A. Ćirić, S. Stojadinović, M.D. Dramićanin, Luminescence Intensity Ratio thermometry and Judd-Ofelt analysis of  $\text{TiO}_2:\text{Eu}^{3+}$ , Opt. Mater. (Amst). 85 (2018) 261–266. doi:10.1016/j.optmat.2018.08.065.

## 7. Biografija

Aleksandar Ćirić rođen je 26.05.1983. u Knjaževcu. Osnovnu školu završio je u Knjaževcu, a gimnaziju “HS Marietta” u Marietta, GA, SAD. Godine 2003. upisao je Fizički fakultet u Beogradu, smer Teorijska i eksperimentalna fizika. Diplomirao je na Fizičkom fakultetu Univerziteta u Beogradu 2015. godine na smeru Teorijska i primenjena fizika, sa temom: “Projektovanje i izrada višekanalnog kontrolera za programibilni LED izvor”. Iste godine upisuje postdiplomske doktorske studije na odseku Fizika, smer Primenjena fizika. Od tada osnovni predmet istraživanja Aleksandra Ćirića je luminiscencija i termometrija neorganskih materijala i Judd-Ofelt teorija.

Glavni rezultati objavljeni su u sledećim radovima:

1. S. Stojadinović, N. Tadić, **A. Ćirić**, R. Vasilić, Photoluminescence properties of  $\text{Eu}^{3+}$  doped  $\text{HfO}_2$  coatings formed by plasma electrolytic oxidation of hafnium, *Opt. Mater. (Amst)*. 77 (2018) 19–24. doi:10.1016/j.optmat.2018.01.014.
2. **A. Ćirić**, S. Stojadinović, M.D. Dramićanin, Luminescence Intensity Ratio thermometry and Judd-Ofelt analysis of  $\text{TiO}_2:\text{Eu}^{3+}$ , *Opt. Mater. (Amst)*. 85 (2018) 261–266. doi:10.1016/j.optmat.2018.08.065.
3. **A. Ćirić**, S. Stojadinović, M. Sekulić, M.D. Dramićanin, JOES: An application software for Judd-Ofelt analysis from  $\text{Eu}^{3+}$  emission spectra, *J. Lumin.* 205 (2019) 351–356. doi:10.1016/j.jlumin.2018.09.048.
4. **A. Ćirić**, S. Stojadinović, M.D. Dramićanin, Judd-Ofelt and chromaticity analysis of hafnia doped with trivalent europium as a potential white LED phosphor, *Opt. Mater.* 88 (2019) 392-395. doi: 10.1016/j.optmat.2018.11.056.

## 8. Prilog

### Prilog 1.

#### Izjava o autorstvu

Potpisani: Aleksandar Ćirić

broj indeksa: 8003/2015

#### Izjavljujem

da je doktorska disertacija pod naslovom

JUDD-OFELT THEORY AND THERMOMETRY OF EUROPIUM DOPED MATERIALS

- rezultat sopstvenog istraživačkog rada,
- da predložena disertacija u celini ni u delovima nije bila predložena za dobijanje bilo koje diplome prema studijskim programima drugih visokoškolskih ustanova,
- da su rezultati korektno navedeni i
- da nisam kršio autorska prava i koristio intelektualnu svojinu drugih lica.

Potpis doktoranda



U Beogradu 27.05.2019.

## Prilog 2.

### Izjava o istovetnosti štampane i elektronske verzije doktorskog rada

Ime i prezime autora: Aleksandar Ćirić

Broj indeksa: 8003/2015

Studijski program: Primenjena fizika

Naslov rada: JUDD-OFELT THEORY AND THERMOMETRY OF EUROPIUM  
DOPED MATERIALS

Mentor: prof. dr. Miroslav D. Dramićanin

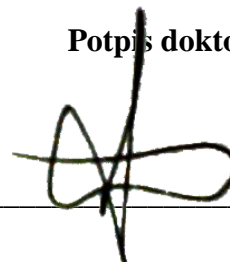
Potpisani: Aleksandar Ćirić

Izjavljujem da je štampana verzija mog doktorskog rada istovetna elektronskoj verziji koju sam predao za objavljivanje na portalu **Digitalnog repozitorijuma Univerziteta u Beogradu**.

Dozvoljavam da se objave moji lični podaci vezani za dobijanje akademskog zvanja doktora nauka, kao što su ime i prezime, godina i mesto rođenja i datum odbrane rada. Ovi lični podaci mogu se objaviti na mrežnim stranicama digitalne biblioteke, u elektronskom katalogu i publikacijama Univerziteta u Beogradu.

U Beogradu 27.05.2019.

Potpis doktoranda



### Prilog 3.

#### Izjava o korišćenju

Ovlašćujem Univerzitetsku biblioteku "Svetozar Marković" da u Digitalni repozitorijum Univerziteta u Beogradu unese moju doktorsku disertaciju pod naslovom:

JUDD-OFELT THEORY AND THERMOMETRY OF EUROPIUM DOPED MATERIALS

koja je moje autorsko delo.

Disertaciju sa svim prilogima predao sam u elektronskom format pogodnom za trajno arhiviranje.

Moju doktorsku disertaciju pohranjenu u Digitalni repozitorijum Univerziteta u Beogradu mogu da koriste svi koji poštuju odredbe sadržane u odabranom tipu licence Kreativne zajednice (Creative Commons) za koju sam se odlučio.

- ①. Autorstvo
2. Autorstvo – nekomercijalno
3. Autorstvo – nekomercijalno – bez prerade
4. Autorstvo – bez prerade
5. Autorstvo – deliti pod istim uslovima

U Beogradu 27.05.2019.

Potpis doktoranda

